DISS. ETH NO. 25004

ULTRA-FAST BEAM STEERING FOR NEXT GENERATION MOBILE COMMUNICATION

A thesis submitted to attain the degree of

DOCTOR OF SCIENCES of ETH ZURICH

(Dr. sc. ETH Zurich)

presented by

ROMAIN BONJOUR

M.Sc., Karlsruhe Institute of Technology

born on 03.12.1986

citizen of Lignières (NE)

accepted on the recommendation of

Prof. Dr. Juerg Leuthold, examiner

Prof. Dr. Luc Thévenaz, co-examiner

2018

CONTENT

Content

Content

ABSTRACT

In the next five years, the demand for wireless network capacity is expected to grow at least twice as fast as the one of wired networks [1]. Nowadays, end-users consume more data on mobile devices such as smartphones, tablets or laptops rather than on fixed computers. In parallel, the quantity of data used per session has increased tremendously, mainly driven by video-on-demand services. In order to cope with this increasing demand, new wireless communication schemes and technologies will be needed.

The capacity of any communication network can be increased by two means: by increasing the spectral efficiency or by leveraging larger bandwidth. Higher spectral efficiencies are achieved with concepts such as advanced modulation formats or polarization multiplexing. Yet, there is not much room for improvement as the currently implemented wireless systems are already extremely close to the theoretical Shannon limit. Leveraging more bandwidth is on the other side still an attractive option. There are two major possibilities to increase the bandwidth

1. More bandwidth can be leveraged by driving communication systems at higher carrier frequencies. While the industry is already moving from microwave (3-30 GHz) to millimeter frequencies (30-300 GHz), the next step could be to rely on terahertz frequencies (>300 GHz). The main challenge at terahertz frequency is however the additional free-space path losses which greatly limits the reach of the communication link.

2. For point-to-multipoint communication, as in radio access networks, the total bandwidth can be increased by reusing the same frequency bands multiple times. This can usually take two forms. First, the size of the mobile cells is reduced and therefore the bandwidth per square kilometer is increased. Second, space division multiplexing can be implemented to reuse the same bandwidth in different directions. Yet, the technologies to create multiple beams are difficult to implement as it requires a large number of closely integrated millimeter wave components.

In this work, the technical challenges to merge the benefits of space division multiplexing and millimeter wave are solved by performing many operations using photonic in place of electronic technologies. This research field, called microwave photonics, leverages the large bandwidth and the small footprint available in photonics in order to generate, process, and detect microwave signals.

As demonstrated in this thesis, microwave photonics not only enable successful demonstrations of the multi-beam steering at millimeter wave but also empower a new multiplexing scheme leveraging ultra-fast beam steering. This development, only available with photonics, provides at the same time multi-beam capacity and reduces the hardware requirements.

RÉSUMÉ

Au cours des cinq prochaines années, la demande en réseau sans fil devrait croître au moins deux fois plus vite que celle en réseaux filaires [1]. Les utilisateurs consomment de plus de données sur des appareils mobiles tels que les smartphones, les tablettes ou les ordinateurs portables plutôt que sur des ordinateurs fixes. Parallèlement, la quantité de données utilisées par session a considérablement augmenté, principalement à cause des services de vidéo à la demande. Afin de faire face à cette demande croissante, de nouveaux schémas et technologies sans fil seront nécessaires.

La capacité de n'importe quel réseau de communication peut être augmentée par deux moyens : soit augmentant l'efficacité spectrale, soit exploitant une plus grande bande passante. L'efficacité spectrale peut être augmentée avec des concepts tels que les formats de modulation avancés ou le multiplexage de polarisation. Cependant, la capacité ne pourra pas être significativement améliorée étant donné que les systèmes actuels sont déjà extrêmement proches des limites théoriques. Tirer parti d'une plus grande bande passante reste toutefois possible. Cela peut être accompli de deux manières :

1. La bande passante peut être augmentée en utilisant des fréquences porteuses plus élevées. L'industrie s'intéresse déjà aux fréquences micro-ondes (3-30 GHz) ainsi qu'aux fréquences millimétriques (30-300 GHz), la prochaine étape pourrait être de s'appuyer sur des fréquences térahertz (> 300 GHz). Le principal défi est cependant les pertes supplémentaires qui limitent grandement la portée des liaisons.

2. Pour les réseaux point à multipoint, la bande passante totale peut être augmentée en réutilisant plusieurs fois les mêmes bandes de fréquences. Cela peut prendre deux formes. Tout d'abord, la taille des cellules est réduite et par conséquent la capacité par kilomètre carré est augmentée. Deuxièmement, un multiplexage spatial peut être mis en œuvre pour réutiliser la même bande passante dans différentes directions. Les technologies permettant de créer de multiples faisceaux sont néanmoins difficiles à mettre en œuvre car elles nécessitent un grand nombre de composants étroitement intégrés.

Dans ce travail, les défis techniques pour combiner le multiplexage spatial avec les fréquences millimétriques sont résolus en effectuant de nombreuses opérations avec de la photonique à la place de technologies électroniques. Ce domaine de recherche, appelé « microwave photonics », tire parti de la large bande passante et de la faible empreinte disponible en photonique pour générer, traiter et détecter des signaux haute fréquence.

Cette thèse démontre que la photonique offre d'une part un balayage ultra-rapide d'onde millimétriques, mais permet également l'implémentation d'un nouveau système de multiplexage exploitant ce balayage ultra-rapide. Ce développement, uniquement disponible en photonique, offre à la fois les avantage du multiplexage spatial tout en réduisant les besoins en matériel.

ACHIEVEMENTS OF THIS WORK

In this thesis, signal processing components and wireless communication systems based on microwave photonic technologies have been developed and experimentally demonstrated. A summary of the achievements is presented here.

Tunable time delays with record low settling time.

True-time delays are key components in many microwave and optical communications subsystems. In particular true-time delays are employed in phased array antenna systems to steer beams without suffering from beam squint. During this thesis, a new implementation method of a continuously tunable true-time delay featuring a settling time in the order of tens of picoseconds has been introduced and demonstrated. Such a settling speed is about three orders of magnitude faster than state-of-the-art delay lines for microwave photonic phased arrays. The proposed solution relies on the splitting and combining of complementary phased shifted spectra (CPSS). It works for large bandwidth signals, has a low complexity, offers moderate losses, and can be fully integrated.

Introduction of time-to-space division multiplexing.

Ultra-fast beam steering has been employed to introduce a new multiplexing scheme called time-to-space division multiplexing. This scheme offers the advantage of massive MIMO systems while relying on cost-effective components. The proposed scheme relies on time to space mapping of the transmitted symbols by means of ultra-fast beam steering. This scheme has the potential of largely reducing the hardware complexity of mobile access networks while increasing the available bandwidth.

First array feeder enabling symbol-by-symbol steering.

An ultra-fast millimeter wave beam steering system with settling times below 50 ps has been demonstrated. A phased array antenna with two elements is employed to realize beam steering. The phased array feeder is implemented with the concept of complementary phased shifted spectra that provides, at the same time, ultra-fast tunability, broadband operation and continuous tuning. Our implementation is used to perform symbol-by-symbol steering. In our demonstration, the beam direction is switched between two sequentially transmitted symbols towards two receivers placed 30° apart. We show successful symbol-by-symbol steering for data streams as fast as 10 GBd. The suggested scheme shows that ultrafast beam steering is becoming practical and might ultimately enable novel high-bit rate multiple access schemes.

Achievements of this Work

Microwave photonic array feeder with record low footprint. An integrated microwave photonics phased array antenna feeder operating at 60 GHz with record-low footprint is demonstrated. Our design is based on ultra-compact plasmonic phase modulators (active area <2.5 μm^2) that not only provide small sizes but also ultra-fast tuning speed. In this design, the integrated circuit footprint is in fact only limited by the contact pads of the electrodes and by the optical feeding waveguides. Using the high speed of the plasmonic modulators, we demonstrate beam steering with less than 1 ns reconfiguration time, i.e. the beam direction is reconfigured in-between 1 GBd transmitted symbols.

Photonic wireless link with record high spectral efficiency.

A 70 Gb/s photonic-based wireless link at 60 GHz using a single RF carrier and a single polarization has been demonstrated. This high capacity is achieved by using 32QAM modulation with a symbol rate of 14 GBd. A robust pre-equalization technique is introduced and enables usage of bandwidths as high as 60 GHz. This work indicates that the consumer oriented 60 GHz band could be a viable alternative to more expensive E-band or sub-THz links for high capacity photonic wireless transmission, mobile backhauling and last-mile high-capacity connections.

1 INTRODUCTION

This chapter describes the scope of the thesis – next generation radio access networks. The goal is to introduce the readers to different aspects and needs of current and future mobile networks. This chapter also includes a brief explanation of the vision of this work: Time-to-space division multiplexing (TSDM) which is explained further in chapters 4 and 5.

1.1 The Mobile Bandwidth Challenge

The required throughput per square meter of any mobile network highly depends on the type of environment. Particularly high capacity will be required in hotspots such as public transport stations, stadiums, airports, or for special events, where a large number of closely located users will consume high definition video streams directly to their terminals [2]. Applications include viewing replays, custom angle watching, real-time conferencing or simply for video streaming.

A possible mobile hotspot scenario is depicted on Fig. 1.1, where a large number of users is waiting to board a plane in front of an airport gate. In this scenario, users will likely employ high bit rates per user for watching high definition video or for conference purposes. In such hotspot scenarios, very high cell capacity must be installed to cope with the demands. The important unit to consider in these cases is the throughput per square meter of the network in bits/s/m².
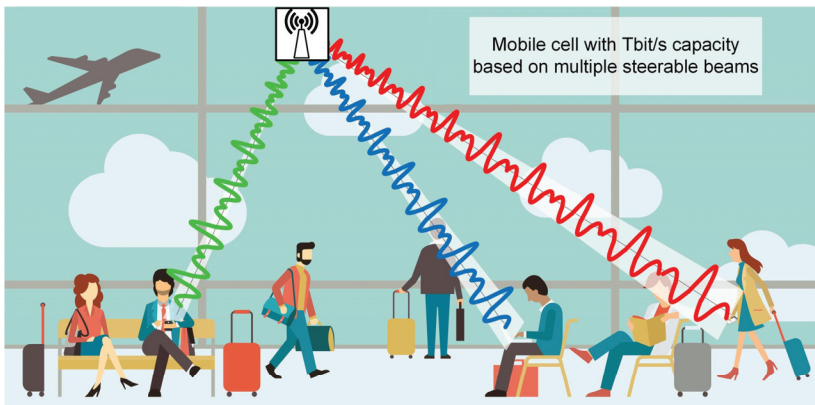

Fig. 1.1 - Example of a mobile hotspot where Tb/s cell capacity is required. In front of an airport gate, a large number of users is waiting to board the planes. In such a case, very high capacity per area is crucial to provide each user with a high bit rate connectivity required for activities such as high definition video streaming or conferencing.

Introduction

Network Capacity

In order to cope with the increasing demand of capacity in future mobile networks [1], different approaches are possible. These different schemes, summarized in the following section, are however limited by some fundamental theoretical limits [3, 4].

The maximum achievable capacity of a given communication channel can be estimated with the Shannon–Hartley theorem. It states that the **channel capacity** C of an additive white Gaussian noise channel is [3, 4]

$$C = B \cdot \log_2(1 + \text{SNR}) = B \cdot \log_2\left(1 + \frac{P}{N_0 B}\right) \tag{1.1}$$

with B the available channel bandwidth, SNR the signal-to-noise ratio, P the received power, and N_0 the noise power spectral density. First of all, it is crucial to note that increasing the bandwidth B does not always increase the capacity. Indeed, the noise power also increases with the bandwidth [5].

Eq. (1.1) is commonly used to estimate the maximum channel capacity in wire telecommunication. However, Eq. (1.1) is not perfectly suited to estimate the installed capacity of a wireless network as it does not provide any spatial information. Indeed, in Eq. (1.1) the "channel" is simply defined by its bandwidth, not by its applicable area. For a wire network, this is however satisfactory as the capacity "per wire" is of interest. If the capacity is to be increased above the theoretical limit, one can always add more wires in parallel to the original ones. Yet, this cannot be applied in wireless communication. Indeed, one cannot add a "wire". In the case of wireless communication, the channel has thus to be defined by its bandwidth and the area in which the channel is used. Thus, Eq. (1.1) can be extended to provide the **channel capacity per unit area** C_A as

$$C_A = \frac{B}{A} \cdot \log_2(1 + SNR) \tag{1.2}$$

with A the area in square meter in which the channel is used. By analyzing Eq. (1.2), it is clear that the capacity of a mobile network can be increased by

1. relying on more bandwidth B. This is the main motivation to shift from microwave to millimetre wave communication in future networks. However, as stated above, increasing the bandwidth usually increases the collected noise, thus the capacity gain may be limited [5].

2. using a given channel in a smaller area A. This method is strongly used in mobile communication and corresponds to a reduction of the mobile cell size from macro- (1-30km) or microcell (200-2000m) to picocells (4-200m) or even femtocells (<10m). [6]

3. increasing the SNR. This is often challenging to implement as the transmitted power is limited by regulations. Focusing the energy with beam steering is however an efficient solution.

1.2   State-of-the-Art on Next Generation Mobile Networks

As summarized above, the two most promising approaches to increase the capacity of mobiles network are to move to higher frequencies and to reduce the area in which a channel is used. There are however also some other alternatives [7-18]. The possible solutions can be regrouped into the following four categories

- **Millimeter wave** (mmWave) – The capacity of mobile networks can be increased by working at higher carrier frequencies [14-16, 19]. While current mobile access networks usually work below 5 GHz, the first mobile standards at 60 GHz or above have been defined already. More details on the advantages and challenges of this approach are given in section 1.2.1.

- **Massive MIMO**, or more generally a scheme based on **space division multiplexing** (SDM) – Reusing the same bandwidth is possible by reducing the cell sizes but also by splitting the cells in smaller angular sectors. The schemes that generate multiple beams in order to use spatial diversity can be regrouped under the term SDM. It can also be seen as the generation of virtual sectors in different directions [11, 12, 20, 21]. This method is compatible with mmWave technology, but the hardware becomes complex and costly [15]. More details on SDM are provided in section 1.2.2.

- **Device-centric architectures** – In today's systems, the mobile networks are based on the concept of "cells". A "cell" and the users are establishing an up and down-link, possibly in the same channel. With the reduction of the cell size and the resulting more frequent handovers between cells, this cellular design is becoming less and less effective as control data occupy a large part of the available bandwidth. In device-centric architectures, the device itself would initiate the connection to the best base station only when needed. All IP processing would alleviate the need of "registering" in the central office as currently needed. [7, 8]

- **Machine-to-machine communication** – In recent years, mobile networks were mainly used by users to make phone calls, text, or browse the Internet. Today, mobile networks are however also used by machines. The rise of the Internet of things (IoT) leads to new challenges and needs of the network. There is therefore a shift from a low number of users with large bandwidth needs towards a large number of things with low latency and real-time communication requirements. To meet this new demand and in parallel continue to serve current users, next generation mobile networks will have to designed with these additional specifications. [7, 9]

In the next two subsections, more details are provided on millimeter wave communication and space division multiplexing as these two next generation concepts are combined in the course of this work using microwave photonics.

1.2.1   Millimeter Wave Communications

The theoretical maximum bandwidth that can be used in a channel corresponds to twice the carrier frequency, see section 2.1 on fractional bandwidth for more details. As an example, a carrier at 2.5 GHz could in theory carry information occupying frequencies from 0 to 5 GHz. In reality, only a fraction of this bandwidth will be used for technical reasons and regulations, usually below 10%. Yet, keeping a constant fractional bandwidth of 10%, increasing the carrier frequency to higher bands provides a linear increase in bandwidth.

Different applications target different carrier frequencies. One of the key parameters when choosing the carrier frequency of a system is related to the attenuation of the signal by the atmosphere. Fig. 1.2 depicts the attenuation between 1 and 300 GHz at sea level for a humidity of 30%. The plot shows attenuations for three different rain rates. There are windows with low attenuation (0-50 GHz, 70-170 GHz, and 200-300 GHz) and windows in between with higher attenuation due to absorption by gases.

Typically, long-range point-to-point communication systems for mobile backhauling or satellite communications will use low attenuation windows to increase the reach. On the other hand, a point-to-multipoint access network will focus on high attenuation windows. This may sound surprising, but attenuation offers a large advantage: it intrinsically limits the size of the mobile cell and reduces the inter-cell interferences. The first millimeter wave communication standard (IEEE 802.11ad) is specifically designed at 60 GHz and aims to generate cell sizes with radius lower than 10m, i.e. femtocells.
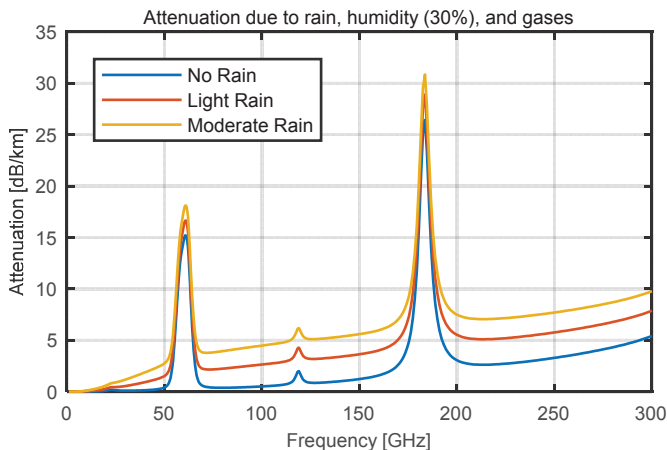

Fig. 1.2 - Atmospheric attenuation due to rain, humidity, and gases The attenuation of the atmosphere can be split in windows with low or high attenuation. Depending on the designed system, one may target low attenuation (to improve the range) or high attenuation (to reduce cell interferences). Raw data from MATLAB communication system toolbox.

Advantages

1. Larger bandwidth

The key advantage of moving to higher carrier frequencies is the larger available bandwidth. In recent mobile communication standards at millimeter wave frequencies, such as in IEEE 802.11ad-2012 (60 GHz), the bandwidth is 8 GHz split into four 2 GHz channels [22], a 20 fold improvement when compared to aggregated 4G LTE channels [23]. Using the four channels of the standard [22], the cell capacity C_{tot} can thus reach

$$C_{tot} = R_b \cdot n_{channel} \cdot n_{sector} = \sim 8\,\text{Gb/s} \cdot 4 \cdot 3 = \sim 96\,\text{Gb/s} \qquad (1.3)$$

with R_b the bitrate (here 2 GBd with QAM16 coding), $n_{channel}$ the number of channels, and n_{sector} the number of sectors, i.e. a mobile cell covering 360° is usually split in 3 sectors of 120°.

Recent research has shown far higher bitrates at mmWave frequencies, but mostly for point-to-point communication [24-27]. For the first generation of 802.11ad RAN, the envisioned applications are typically short range such as indoor communication or mobile docking (up to 10 m) and thus may avoid complex beam forming systems. On the other hand, outdoor applications will require higher reach and therefore a more sophisticated architecture.

2. Larger gain and smaller beamwidth

In current mobile access networks (both 4G LTE and Wi-Fi), the access points emit electromagnetic waves either in all directions, covering 360°, or in 120°, covering one of three sectors. Most of the energy is therefore not directed towards the active users. The intrinsic advantage is that the cells do not need to spatially locate the users. The downsides are however that 1) energy is lost and 2) the range is limited.

Current systems are planned this way not by design but by necessity. Indeed, as discussed further in section 2.2.1 on antenna fundamentals, an antenna with higher gain, i.e. with a higher "focusing effect" and thus a smaller 3 dB beamwidth, needs to have a large size. The size of an antenna, i.e. its aperture, is better given in relation to its designed carrier wavelength. As an example, in order to have an antenna with a 3 dB beamwidth of 10° (or a gain of 21 dBi), the antenna diameter must correspond at least to 5 wavelengths, see Eq. (2.46) for more details. In the case of a 2.5 GHz carrier frequency (wavelength ~12 cm), an antenna with a 10° beamwidth would need a diameter of ~60 cm. This cannot be implemented for various practical reasons. In the case of mmWave communication systems, the wavelength is however far smaller. Indeed, at 60 GHz, the wavelength is only 5 mm, thus an antenna with a 10° beamwidth would only need a diameter of 25 mm. High gain antennas are therefore practically implementable at mmWave.

As mmWave communication enables practical implementation of high gain antennas and therefore small beamwidth, more independent beams can be used in a given cell sector [28]. This thus enables SDM, see section 1.2.2.

Introduction

Challenges

1. Free space path losses

The main challenge in the design of mmWave communication systems is the large increase in free space path losses (FSPL) [3]. As detailed further in section 2.2.1, the FSPL corresponds to the losses due to the spherical propagation of a wave emitted by an isotropic antenna. The FSPL will be partially compensated by the antenna gains on both the transmitter and the receiver side. Yet, as depicted on Fig. 1.3, the FPSL increases quickly with the frequency. At the exemplary carrier frequency of 60 GHz, the losses are 68, 88, and 108 dB for propagation distances of 1, 10, and 100 m, respectively. These FPSL are 32 dB higher than those of a 2.5 GHz carrier (36 dB @ 1 m, 56 dB @ 10 m, and 76 dB @ 100 m). In order to keep the same power budget when changing the carrier frequency from 1.5 to 60 GHz, the additional 32 dB losses will have to be compensated by either higher gain antennas (+16 dBi on both the transmitter and the receiver) or by improving the power margin. Improving the power margin is however difficult as the maximum emitted power is regulated and due to the fact that higher frequency electronics will typically generate more noise. On the other hand, antennas with 16 dBi gain are feasible at mmWave and will moreover enable multiple beam capacity (the 3 dB beamwidth will be approximately 17°).

The losses due to FSPL will have to be added to the atmospheric losses, see Fig. 1.2. Yet, the values for the losses in Fig. 1.2 are given in dB/km and are already far smaller than the FPSL.
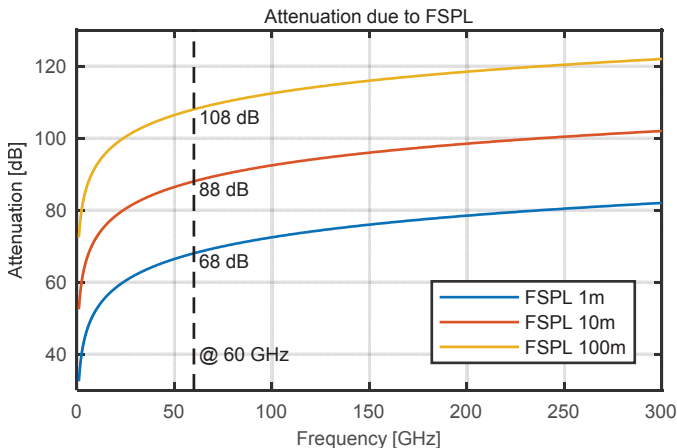
Fig. 1.3 - Attenuation due to free space path losses. The free space path losses increase quickly with the carrier frequency. At an exemplary frequency of 60 GHz, the losses are already as high as 68 dB after 1 m transmission. This is 32 dB higher than the losses of a microwave carrier at 2.5 GHz. These additional losses, that occur on top of the atmospheric losses, see Fig. 1.2, will have to be compensated by higher gain antennas on both the transmitter and the receiver sides.

2. Penetration loss

Another challenge with mmWave communication is the far higher penetration and reflection losses compared to microwave frequencies. At 28 GHz, a tinted glass already adds 40 dB losses [29]. In the discussion above on FSPL, a line-of-sight (LoS) communication link is assumed while the penetration (and reflection) losses are tied to a non-LoS link. Current microwave access networks rely on reflection and transmission to serve users that are not in LoS conditions. On top of this accessibility advantage, non-LoS components can be leveraged to perform MIMO processing and thus to reduce diverse fading effects.

Due to the higher penetration and reflection losses at mmWave, these two advantages will not be applicable. A mmWave link will 1) mainly rely on LoS communication and 2) MIMO processing is not applicable in the same sense as in microwave systems. A solution to mitigate the lack of non-LoS channel components is to use multi-hop relay [13]. This approach is based on quickly switching between different cells to keep a strong active LoS component.

3. Hardware implementation

In addition to the challenges due to the propagation of millimeter wave, technical challenges have to be resolved to successfully integrate mmWave components. At millimeter wave, the signal quality will be degraded when compared to microwave frequencies by the more difficult integration of low noise and power amplifiers, mixers, and the limited ADC/DAC resolutions [3, 30, 31].

An elegant solution may rely on microwave photonics (MWP) [32-35], where the millimeter wave signals are generated by optical heterodyning in a photodiode [36-38]. MWP enable larger bandwidth, lightweight structures, offer immunity to electromagnetic interference and larger inter-connection distances while simplifying the installation of the system [33]. Recently demonstrated photonic-based wireless links have shown impressive data rates in several frequency bands from 31 GHz up to 245 GHz carrier frequency.

4. Higher power consumption

As seen in Eq. (1.1) on the channel capacity, the capacity increases with the bandwidth only if the signal-to-noise ratio remains constant. As more noise will be collected in a larger bandwidth, the received power has to increase at the same rate as the bandwidth to keep the same SNR [39].

In addition, due to the larger power needed to keep a constant SNR, the components at mmWave are usually less efficient than those at microwave frequencies [39]. On top of this, if the larger FPSL and atmospheric losses cannot be compensated by the antenna gain, a larger power margin will be required.

1.2.2   Space Division Multiplexing

Another way of increasing the cell capacity by orders of magnitude is to use Space Division Multiplexing (SDM). SDM is based on reusing the same frequency band in various directions by forming spatially separated, non-interfering radio beams. If a user receives the signal from only one beam at a time, the advantages are twofold: first, the cell capacity is increased by the number of beams. Second, the full user equipment (UE) capacity can be used since neither time, code, nor frequency multiplexing is required.

In order to compare the various implementations of PAA, three main categories of feeders can be defined, see Fig. 1.4.

Fig. 1.4 - Comparison of phased array antenna concepts. (a) A simple PAA with one feeder (b) Analog PAA capable of multiple beam steering (c) DSP-based array feeder.

In Fig. 1.4(a), a simple feeder for a PAA is depicted. The signal $s_1(t)$ provided at the input of the PAA is transmitted in a direction defined by the phase or delay ΔT added in front of each antenna [40]. Such concepts allow for electronic scanning and longer reach, but they do not offer multi-beam capability and therefore cannot increase the cell capacity.

In Fig. 1.4(b), a PAA with multiple feeders is depicted. Many variations of this scheme can be found in the literature [41-45], united by the fundamental principle to add multiple feeder networks in parallel (depicted here with different colors). Such concepts enable larger capacity by creating fully independent multiple beams. Yet, the hardware requirements for a large number of beams make this approach complex and costly.

In Fig. 1.4(c), the most flexible multi-beam system is shown. This is usually referred to as massive MIMO or digital beamforming and relies on digital signal processing to form the different beams [11, 12, 20, 21, 28, 30, 39, 46]. The signals for each antenna with their requested delays are generated by a digital signal processing (DSP) stage with a large number of digital to analog converters (DAC). In [11], it is rightfully claimed that the cost and complexity of the hardware is not an unsurmountable issue. This statement unfortunately cannot be extended to mmWave frequencies [39].

1.2.3 Reaching Tb/s Cell Capacity

Cell capacity in Tb/s can be realized by combining millimeter wave with multiple beam solutions (such as SDM). Combining a mobile cell at mmWave fulfilling 802.11ad band definitions of 2.16 GHz (total bitrate of 96 Gb/s, see 1.2) and a multiple beam PAA supporting 11 independent beams would bring the total capacity above 1 Tb/s:

$$C_{tot} = R_b \cdot n_{channel} \cdot n_{sector} \cdot n_{beams}$$
$$= 8\ \text{Gb/s} \cdot 4 \cdot 3 \cdot 11 = 1056\ \text{Gb/s}$$

(1.4)

with n_{beams} the number of independent beams. By generating separated beams, each user can use the full channel capacity (8 Gb/s). In systems implementing SDM, the total cell capacity is increased by the number of beams. If more users would be located in the proximity of the cell, the capacity of each beam could still be shared by closely located users using time or frequency division multiplexing.

The step from single to multiple beams compatible with 802.11ad is depicted in Fig. 1.5. In Fig. 1.5(a), corresponding to a standard implementation, all the users in one sector have to share the bandwidth of one channel. Thus the capacity per sector is 32 Gb/s (4 bands · 8 Gb/s) and will be shared by time, code, or frequency division multiple access [47]. By generating separated beams as depicted in Fig. 1.5(b), each user can use the full channel bandwidth (8 Gb/s). The total cell capacity has now been increased by a factor of 3 (there are 3 beams per sector on the plot). If even more users would be located in the proximity of the cell, the capacity of each beam could still be shared by closely located users using time of frequency division multiplexing. Yet, the total capacity is increased.
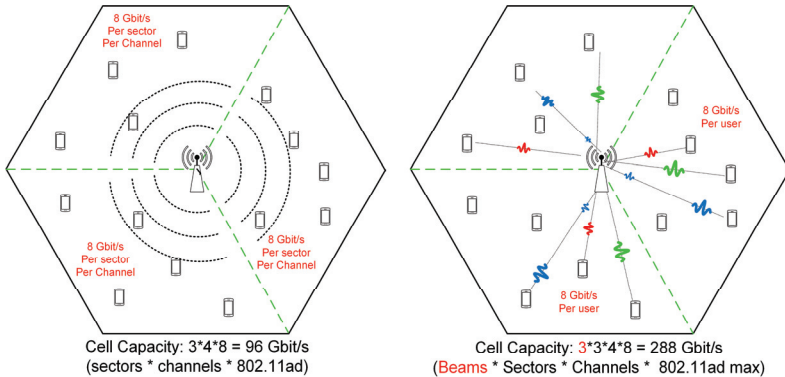

Fig. 1.5 - From single to multiple beams cells. (a) A standard mobile network cell is split in 3 or 4 independent sectors. In each sector, the capacity is shared between the users with time or frequency division multiple access. (b) Using multi-beam systems, users can be addressed with spatial division multiplexing and thus use the full capacity of the channels.

1.3   Vision Time-to-Space Division Multiplexing

As explained above, combining mmWave and space division multiplexing is an attractive solution for next generation radio access networks (NG RAN), but new architectures are needed to overcome the hardware complexity of approaches such as depicted in Fig. 1.4(b) relying on multiple analog feeders or Fig. 1.4 (c) relying on digital beamforming. A promising solution using the simple and cost effective single feeder of Fig. 1.4(a) but enabling the capacity of the more advanced approaches relies on a PAA with ultra-fast beam steering capabilities [48, 49] - a system in which the beam direction could be adjusted with extremely short settling times and allow for - what we call - time-to-space division multiplexing (TSDM) [49]. The key concept of TSDM is to emulate a multiple beam array by steering a single beam in between the transmitted symbols.

The vision of a NG RAN using TSDM and microwave photonic (MWP) as presented in this thesis (chapter 4 and 5) is summarized in Fig. 1.6 [49]. A transmitter located in the central office generates a radio-over-fiber (RoF) data signal and a steering control (SC) signal, see Fig. 1.6(a). The spectrum of the RoF signal is shown in Fig. 1.6(b). The desired microwave carrier frequency f_{RF} corresponds to the frequency difference between a reference and a carrier laser, f_1 and f_2. The data for the different UEs and the SC signals are generated by a digital signal processor (DSP) within the transmitter. The central office (CO) needs to know the exact position of the users to steer the signals correctly to the remote antenna unit (RAU) of the base station (BS). The RAU in the BS performs a time to space mapping of the symbols, emulating a system with multiple beams.

The RAU, see Fig. 1.6 (c), is built using a MWP PAA with ultra-fast tunable delay line elements [40]. The SC is transmitted to the RAU on a separate optical channel. The time delays for each element of the PAA are set in the feeder network of the RAU using the SC signal. As depicted in Fig. 1.6 (d), the UEs require first an RF front end to down-convert the wireless signals. A low pass filter is included to reduce the out-of-band noise. The signal processing can be performed in a low-cost receiver as the UEs only receive during their assigned time slots. As with other mmWave RAN schemes, the transmission from the BS to the UEs works well under line-of-sight (LoS) conditions.
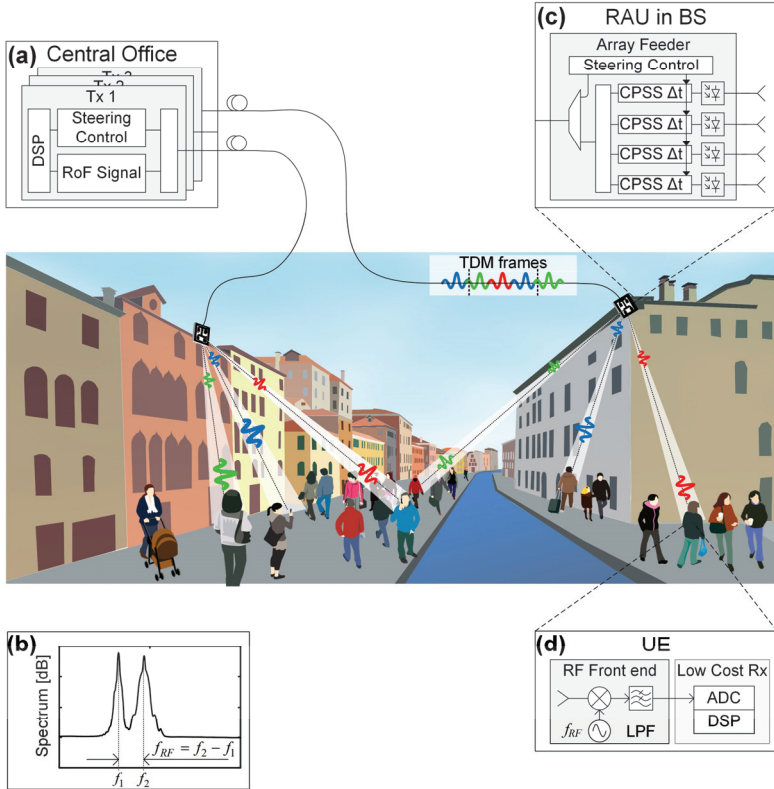
Fig. 1.6 - Concept of mmWave RAN based on TSDM. (a) The central office (CO) sends time division multiplexed (TDM) data frames to multiple users via a remote antenna unit (RAU). The radio-over-fiber signal is shown in (b). (c) The RAU uses the steering control signal sent from the CO to steer the time tributaries of the symbol based TDM signal to different directions, acting as a spatial demultiplexer. (d) The user equipment is based on a low-cost RF front end.

1.4 Organization of this Thesis

This cumulative thesis deals with the implementation of novel microwave photonic technologies into next generation mobile communication systems. Thus, it treats in parallel multiple research fields. Different aspects of this work are explained in the following different chapters.

In **chapter 2**, some theoretical and technological background is provided. The first objective of this chapter is to extend various theoretical aspects that are partially present in the published papers of this work. In particular, this chapter introduces the fundamentals of microwave photonics technologies and phased array antennas.

Chapter 3 presents two publications that demonstrate the implementation of photonic technologies for ultra-fast true-time delays. The demonstration of CPSS presented in this chapter not only define a new standard for some key parameters in the field of microwave photonics based true-time delay, it also serves as pillar for the development and demonstration of ultra-fast beam steering.

In **chapter 4**, the utilization of ultra-fast beam steering as enabler for a new type of multiple beam capable antenna is detailed. This chapter focuses on the concept of time-to-space division multiplexing (TSDM) and provides, with the help of full time domain simulations, guidelines and limits for TSDM implementation. The concept of time-space division multiplexing can offer the advantages of multiple beams systems while relying on simple, affordable hardware.

Two experimental demonstrations of time-to-space division multiplexing are regrouped in **chapter 5**. The first one relies on discrete off-the-shelf components and enables steering of radio beams in less than 100 ps. The second demonstration relies on a plasmonic-photonic integration of the array feeder and offers the smallest footprint ever demonstrated for such a technology. These two demonstrations prove that TSDM not only works in simulation but also experimentally.

In **chapter 6**, microwave photonics is used with a special pre-equalization technique to demonstrate a record high capacity and spectral efficiency for a 60 GHz wireless link. The work presented in this chapter shows that a cost-effective alternative to Terahertz frequencies can also enable 100 Gb/s communication for point-to-point wireless links.

In **chapter 7**, the achievements of this thesis are summarized and a short outlook on the future development of the technology is provided.

2 FUNDAMENTALS

This thesis deals with the demonstration of ultra-fast beam steering of millimeter wave signals using microwave photonics, hence multiple research fields were combined in the laboratory. Those research fields include among others: broadband optical communication, novel optical devices (plasmonic modulators), photonic integration, micro and millimeter systems, phase array antennas, digital signal processing, and microwave photonics.

The technological focus and novelty of this thesis is however on microwave photonics based phased array antennas. Therefore, the theoretical background provided in this chapter is limited and split into the following sections

- 2.1 Microwave Photonic. This section shows the fundamental concepts behind the utilization of photonic technologies for the generation and filtering of microwave signals.

- 2.2 Phased Array Antenna. This section explains the key aspects of phased array antennas such as beamforming and beamsteering are explained ranging from basic antenna characteristics to array tapering schemes.

- 2.3 Microwave Photonics for Phased Array Antenna. In this last section, the implications of phased array antenna systems based on microwave photonics are briefly discussed. This section focusses on the implementation of a photonic based array feeder and on the link budget of such systems.

The other aforementioned research fields, not detailed in this chapter, are covered in the various supervised semester [50-52], group [53, 54], or master thesis [55-58] and in numerous books [4, 5, 59-65]. The goal of this chapter is only to provide the specific knowledge useful for the understanding of this work.

2.1 Microwave Photonics

Microwave photonics (MWP) corresponds to the research field in which photonics is used to generate, process, and receive microwave or millimeter wave signals [66-70]. The key advantage of MWP is a larger available bandwidth compared to electronic systems. In standard microwave and millimeter wave technologies, the usable bandwidth is indeed often limited by the **fractional bandwidth** f_B, also called percent bandwidth, given as

$$f_B = \frac{B}{f_{RF}} \tag{2.1}$$

with the B the signal bandwidth and f_{RF} the carrier frequency. f_B ranges from 0, i.e. 0%, for small signal bandwidth (no signal at all for $f_B = 0$) to a theoretical limit of 2, i.e. 200% for $B = 2 \cdot f_{RF}$. The reason why the fractional bandwidth limits the performance of RF systems is related to the various wavelengths comprised in the signal. In a signal, the wavelength ranges from

$$\lambda_{min} = \frac{c}{f_{max}} = \frac{c}{f_{RF} + \frac{B}{2}} \quad to \quad \lambda_{max} = \frac{c}{f_{min}} = \frac{c}{f_{RF} - \frac{B}{2}} \tag{2.2}$$

with c the speed of light in the medium. The limitation in the design of microwave components comes from the ratio between the smallest and largest wavelength. A "**wavelength ratio**" R_λ can be defined as

$$R_\lambda = \frac{\lambda_{max}}{\lambda_{min}} = \frac{f_{RF} + \frac{B}{2}}{f_{RF} - \frac{B}{2}} = \frac{f_{RF} + \frac{f_B \cdot f_{RF}}{2}}{f_{RF} - \frac{f_B \cdot f_{RF}}{2}} = \frac{2 + f_B}{2 - f_B}. \tag{2.3}$$

The difference between standard electronic and MWP can be better understood by taking two examples. For both cases, assume that one wants to build a passband component such as an amplifier, a filter, or a mixer to process a signal with a bandwidth $B = 25$ GHz. This can be achieved using standard electronics directly at the targeted carrier frequency $f_{RF} = 60$ GHz or using MWP at an optical carrier frequency $f_{RF} \rightarrow f_{opt} \approx 192$ THz.

1. Using standard electronics, the fractional bandwidth is $f_B \approx 40\%$. Thus, the wavelength ratio is $R_\lambda = 1.5$. This means that the component has to be designed for a large range of wavelengths. This is already extremely challenging and corresponds to the usual working range of standard RF waveguides [71].

2. Using MWP, the fractional bandwidth is $f_B \approx 0.0001$. Thus, the wavelength ratio is $R_\lambda \approx 1$. The optical component is therefore relatively easy to build as it can be designed for a single wavelength.

In this section, some fundamental principles of MWP are provided for understanding the implementations specific to the experiment of this thesis. Broader overviews can be found in [66, 67, 70, 72-74].

2.1.1 Signal Generation

This section, presenting fundamental theory of signal generation using optical heterodyning, is partially based on work presented by M. Singleton in his master thesis [56].

Heterodyning is a technique where a signal at carrier f_1 and a single tone at $f_2 \neq f_1$ "beat" together to produce an upshifted signal at $f_1 + f_2$ and downshifted at $f_1 - f_2$. These two new signals are called "heterodynes". This is in contrast to homodyning, where $f_1 = f_2$ and in which the signal is shifted down to the baseband. Heterodyning is a technique which has been in widespread use since the early 20th century for radio, largely thanks to Armstrong's tunable super heterodyne [75]. In [75], heterodyning is combined with a band pass filter to downshift a high frequency signal radio signal to a more manageable intermediate frequency (IF), where it is further processed prior to shifting to the baseband.

With a suitable mixing device, the same effect can also be observed in the optical domain and therefore used to generated high frequency RF signals. The most common way to achieve this is to use a square law detector such as a photodiode [76, 77].

Photodiode Fundamentals

A photodiode (PD) is a device that converts optical energy (photons) into an electrical signal (electrons & holes). In order to perform this conversion efficiently, a PD must first convert as many photons as possible into electron-hole pairs. Second, these electron-hole pairs need to initiate a current [78]. In communications, four types of photodiodes are commonly used: PIN photodiodes, avalanche photodiode, Schottky photodetectors, and uni-travelling-carrier photodiodes [78]. In this subsection, a short summary of PIN PD is provided as it corresponds to the type of PDs used in this work. The equations provided below are, however, applicable for other types of photodiodes. This section is based on various sources [78-81].

Fig. 2.1 shows the cross section of a PIN (p-doped, intrinsic, n-doped) photodiode. It is reverse biased, with a negative voltage applied to the p$^+$ region with respect to the n$^-$ region. When an incident photon strikes the exposed surface of the intrinsic region, an electron-hole pair will be generated. Due to the applied bias, the electron will move towards the n$^-$ region, and the holes towards the p$^+$ region. This generates a current in a closed circuit.
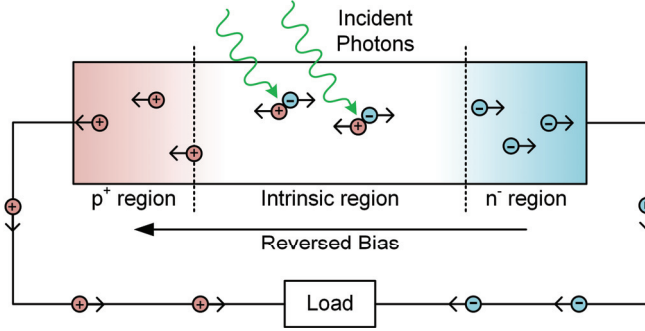
Fig. 2.1 - Simplified cross section of PIN photodiode.

The photocurrent generated by the PD depends on the "responsivity" of the PD. **The photocurrent I_{PD} is given by [78]**

$$I_{PD} = \Re \cdot P_{opt} \tag{2.4}$$

with $\Re$ the responsivity in [A/W] and P_{opt} the incident optical power. Typically, the responsivity of a PIN-PD ranges from 0.4-0.6 for Si based PD, 0.5-0.7 for Ge based PD, and 0.6-0.9 for InGaAs PD [79]. The incident optical power entering the photodiode is given by [78]

$$P_{opt} = A_{beam} \cdot I_{beam} = A_{beam} \cdot \frac{1}{2}\sqrt{\frac{\varepsilon_o \varepsilon_r}{\mu_0 \mu_r}} \cdot |E_{opt}|^2 = K \cdot |E_{opt}|^2 \tag{2.5}$$

with A_{beam} the effective area of the beam interacting with the PD, I_{beam} the beam intensity, E_{opt} the electromagnetic field amplitude of the incident beam, ε and μ the permittivity and permeability. K is a scalar taking into account the constants.

It is useful for the following section to rewrite Eq. (2.4) using Eq. (2.5) in order to replace the optical power by the electrical field amplitude [78]

$$I_{PD} = \Re \cdot K \cdot |E_{opt}|^2 \tag{2.6}$$

The responsivity is related to the quantum efficiency η of the PD using the following relation [78]

$$\eta = \frac{Generated\ electrons}{incident\ photons} = \frac{I_{PD}/q}{P_{opt}/hf} = \frac{hf}{q} \cdot \Re \cong \frac{1.24}{\lambda\,[\mu m]} \cdot \Re \tag{2.7}$$

with q the elementary charge, h the Planck constant, f the optical frequency, and λ the optical wavelength in $[\mu m]$.

Photodiode Signal-to-Noise Ratio

In optical communications, two different types of noises generated by the photodiodes have an impact on the output: shot noise and thermal noise. The 1/f noise, i.e. pink noise, and the dark current, i.e. spontaneous generation of electron-hole pairs, are indeed negligible in most of the cases [78, 80].

The shot noise is related to the quantum efficiency η. As not all photons are successfully converted into current, the output fluctuates. In fact, each photon has a conversion probability η. The average noise power due to the shot noise is given by [78]

$$\overline{\delta P_{\text{sn}}} = R_{\text{PD}} \cdot \overline{\delta I_{sn}}^2 \tag{2.8}$$

with R_{PD} the PD load and $\overline{\delta I_{\text{sn}}}$ the average shot noise current given by [78]

$$\overline{\delta I_{\text{sn}}} = \sqrt{2q\overline{I_{\text{PD}}}B} \tag{2.9}$$

where B is the electrical bandwidth of the photodiode. Note that if one wants to take into account the dark current in the noise calculation, $\overline{I_{\text{PD}}}$ should be replaced by $(\overline{I_{\text{PD}} + I_{\text{d}}})$ with $\overline{I_{\text{d}}}$ the dark current.

The thermal noise, or Johnson–Nyquist noise, is related to the thermal agitation of the charge carrier. Its average noise power is given by

$$\overline{\delta P_{\text{th}}} = R_{\text{PD}} \cdot \overline{\delta I_{\text{th}}}^2 \tag{2.10}$$

with the average thermal noise induced current δI_{th} given by [78]

$$\overline{\delta I_{\text{th}}} = \sqrt{\frac{4k_{\text{B}}TB}{R_{\text{PD}}}} \tag{2.11}$$

where k_{B} is the Boltzmann's constant and the T component temperature.

Note that thermal noise sometimes includes other noise sources. In these cases, the component temperature T is replaced by "a noise temperature", which is larger than the actual temperature of the component. This technique provides therefore an easy way of adding noise in a given system.

The signal-to-noise ratio (SNR) after a PIN photodiode is given by the ratio between the signal power and noise power [78], it is

$$\text{SNR}_{\text{PD}} = \frac{\text{signal power}}{\text{noise power}} = \frac{R_{\text{PD}} \cdot \overline{I_{\text{PD}}}^2}{R_{\text{PD}} \cdot \left(\overline{I_{\text{sn}}}^2 + \overline{I_{\text{th}}}^2\right)} = \frac{\overline{I_{\text{PD}}}^2}{\overline{\delta I_{\text{sn}}}^2 + \overline{\delta I_{\text{th}}}^2} \tag{2.12}$$

with R_{PD} the detector load. Replacing in Eq. (2.12) the results from Eq. (2.4), Eq. (2.9), and Eq. (2.11) lead to [78]

$$\text{SNR}_{\text{PD}} = \frac{\left(\Re \cdot \overline{P_{\text{opt}}}\right)^2}{2q\overline{I_{\text{PD}}}B + 4k_{\text{B}}TB/R_{\text{PD}}} = \frac{\left(\Re \cdot \overline{P_{\text{opt}}}\right)^2}{\left(2q\Re \cdot \overline{P_{\text{opt}}} + 4k_{\text{B}}T/R_{\text{PD}}\right) \cdot B} \tag{2.13}$$

The shot noise linearly depends on the input optical power. For low optical power the shot noise can be neglected, the PD is then used within a thermal noise limited mode. On the other hand, when the optical power is larger, the thermal noise can be neglected. This operation in a shot noise limited mode is preferably used as it provide a better SNR [78]. In this later case, the s**hot noise limited SNR of a PIN photodiode** is given by

$$\text{SNR}_{\text{PD}} = \frac{\Re \cdot \overline{P_{\text{opt}}}}{q \cdot 2B} \tag{2.14}$$

with $\Re$ the responsivity of the PD, P_{opt} the incident optical power, q the elementary charge, and B the electrical bandwidth of the photodiode.

Optical Heterodyning

Optical heterodyning is often used in microwave photonics as the fundamental process to generate signal. Optical heterodyning relies on the mixing of two optical laser lines, one encoded with data - one without, to produce a downshifted copy of the data at a frequency corresponding to the frequency differences. Optical heterodyning is explained further with the help of Fig. 2.2. A modulated laser source at an optical carrier frequency f_c is coupled with a reference laser at frequency f_{ref}. After coupling, both lasers are fed to the photodiode. Due to the square law detection process in the PD, a frequency difference term at $f_{RF} = f_c - f_{ref}$ is generated. A copy of the optical data on the carrier laser has thus been generated in the RF domain.
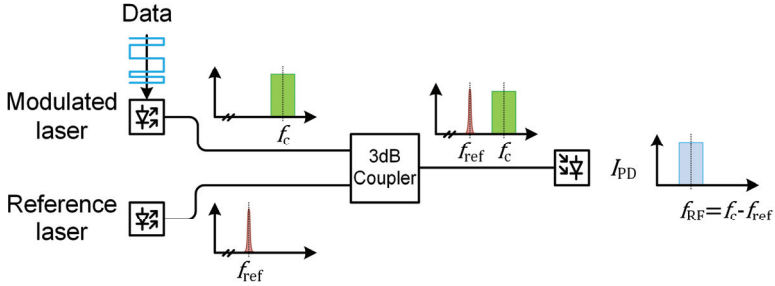

Fig. 2.2 - Optical heterodyning. A modulated optical carrier at frequency f_c is combined with a reference laser at frequency f_{ref}. Due to the square law detection process of the photodiode, a copy of the data signal at the lasers frequency difference $f_{RF} = f_c - f_{ref}$ is generated. For simplification, only the beating signal is plotted here after the PD, see Fig. 2.3 for more details.

Assuming slow varying envelope approximation which is typically true in optical communication [78], the field amplitude of the carrier is given by

$$E_c = c(t) \cdot \frac{\sqrt{P_c}}{\sqrt{K}} \cos(\omega_c t) \tag{2.15}$$

with $c(t)$ the complex data signal, P_c the average optical power, K a scalar as defined in Eq. (2.5), ω_c the angular frequency of the laser given by $\omega_c = 2\pi f_c$, and φ_c the laser phase shift. The reference laser field amplitude is given by

$$E_{ref} = \frac{\sqrt{P_{ref}}}{\sqrt{K}} \cos(\omega_{ref} t + \varphi_{ref} - \pi/2) \tag{2.16}$$

with P_{ref} the average optical power, ω_{ref} the angular frequency of the reference laser given by $\omega_{ref} = 2\pi f_{ref}$, and φ_{ref} the reference laser phase shift when compared with the carrier laser. The phase shift $-\pi/2$ is added to simplify the coupling of both lasers in the 3 dB coupler and will be thus neglected afterwards. The signal entering the PD is after the coupler given by

$$E_{opt} = \frac{E_c + i \cdot E_{ref}(with - \pi/2)}{\sqrt{2}} = \frac{E_c + E_{ref}(without - \pi/2)}{\sqrt{2}} \tag{2.17}$$

The photocurrent after the photodiode is, as defined in Eq. (2.6)

$$I_{\mathrm{PD}} = \Re \cdot \mathrm{K} \cdot \left[E_{\mathrm{opt}} \right]^2 \tag{2.18}$$

with $\Re$ the photodiode responsivity and K a constant, c.c. stands for complex conjugate. Using Eq. (2.17) in Eq. (2.18) lead to a photocurrent

$$\begin{aligned} I_{\mathrm{PD}} &= \Re \cdot \mathrm{K} \cdot \left[\frac{E_c + iE_{\mathrm{ref}}}{\sqrt{2}} \right]^2 = \frac{\Re \cdot \mathrm{K}}{2} \cdot [E_c + E_{\mathrm{ref}}]^2 \\ &= \frac{\Re \cdot \mathrm{K}}{2} \cdot \left[E_c{}^2 + E_{\mathrm{ref}}{}^2 + 2E_c E_{\mathrm{ref}} \right] \end{aligned} \tag{2.19}$$

Replacing Eq. (2.15) and Eq. (2.16) in Eq. (2.19) lead to

$$\begin{aligned} I_{\mathrm{PD}} &= \frac{\Re}{2} \cdot [c^2(t) \cdot P_c \cos^2(\omega_c t) + P_{\mathrm{ref}} \cos^2(\omega_{\mathrm{ref}} t + \varphi_{\mathrm{ref}})] \\ &+ \frac{\Re}{2} \cdot c(t) \cdot 2\sqrt{P_c}\sqrt{P_{\mathrm{ref}}} \cdot \cos(\omega_c t) \cdot \cos(\omega_{\mathrm{ref}} t + \varphi_{\mathrm{ref}}) \end{aligned} \tag{2.20}$$

Eq. (2.20) is further expanded using the trigonometric identities

$$\cos^2(\theta) = \frac{1 + \cos 2\theta}{2} \quad \text{and} \quad \cos\alpha \cdot \cos\beta = \frac{\cos(\alpha - \beta) + \cos(\alpha + \beta)}{2}$$

for the $\cos^2$ and cos·cos terms such that

$$\begin{aligned} I_{\mathrm{PD}} &= \frac{\Re}{2} \cdot \left[c^2(t) \cdot P_c \frac{1 + \cos 2\omega_c t}{2} + P_{\mathrm{ref}} \frac{1 + \cos(2\omega_{\mathrm{ref}} t + 2\varphi_{\mathrm{ref}})}{2} \right] \\ &+ \frac{\Re}{2} \cdot c(t) \cdot \sqrt{P_c}\sqrt{P_{\mathrm{ref}}} \cdot \frac{\cos\big((\omega_c - \omega_{\mathrm{ref}})t - \varphi_{\mathrm{ref}}\big)}{2} \\ &+ \frac{\Re}{2} \cdot c(t) \cdot \sqrt{P_c}\sqrt{P_{\mathrm{ref}}} \cdot \frac{\cos\big((\omega_c + \omega_{\mathrm{ref}})t + \varphi_{\mathrm{ref}}\big)}{2} \end{aligned} \tag{2.21}$$

Eq. (2.21) can be reorganized to identify easily the different types of signals that are generated by optical heterodyning such that

$$\begin{aligned} I_{\mathrm{PD}} &= \frac{\Re}{2} \cdot \left[c^2(t) \cdot \frac{P_c}{2} + \frac{P_{\mathrm{ref}}}{2} \right] && DC\ Terms \\ &+ \frac{\Re}{2} \cdot c(t) \cdot \sqrt{P_c}\sqrt{P_{\mathrm{ref}}} \cdot \cos\big((\omega_c - \omega_{\mathrm{ref}})t - \varphi_{\mathrm{ref}}\big) && RF\ Terms \\ &+ \frac{\Re}{2} \cdot c(t) \cdot \sqrt{P_c}\sqrt{P_{\mathrm{ref}}} \cdot \cos\big((\omega_c + \omega_{\mathrm{ref}})t + \varphi_{\mathrm{ref}}\big) && Opt.\ Terms \\ &+ \frac{\Re}{2} \cdot \left[c^2(t) \cdot \frac{P_c}{2} \cos 2\omega_c t + \frac{P_{\mathrm{ref}}}{2} \cos(2\omega_{\mathrm{ref}} t + 2\varphi_{\mathrm{ref}}) \right] && Opt.\ Terms \end{aligned} \tag{2.22}$$

Note that the factor $1/2$ is related to the 3 dB losses in the optical coupler.

The signals generated by optical heterodyning as defined by Eq. (2.22) can be identified graphically as depicted in Fig. 2.3. The red signals originate from detection of the reference lasers, the green signals from the data carrying laser, and the blue ones from the mixing term. Note the different current levels for an exemplary power ratio of $P_{ref} = 2 \cdot P_c$.
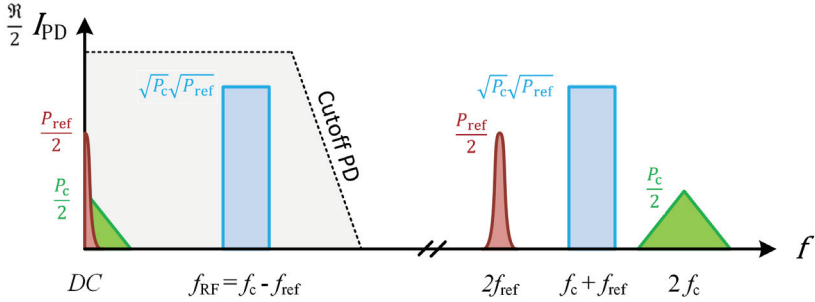

Fig. 2.3 - Signals generated by optical heterodyning.

The DC terms and the RF terms in Eq. (2.22) and Fig. 2.3 are below the frequency cutoff of the photodiode and thus appear in the photocurrent. The term at higher frequencies, i.e. at twice the laser frequencies, will not be present in the photocurrent and will only lead to heating of the device. Additionally, in the generation of wireless signals (at f_{RF}), the DC terms will be either filtered out by some components of the RF chain or at least by the transmitting antenna. Therefore, the RF photocurrent I_{RF} generated using optical heterodyning is given by

$$I_{RF} = \frac{\Re}{2} \cdot c(t) \cdot \sqrt{P_c}\sqrt{P_{ref}} \cdot \cos\big((\omega_c - \omega_{ref})t - \varphi_{ref}\big) \tag{2.23}$$

The **average RF power generated by optical heterodyning** is thus

$$P_{RF} = R_{PD} \cdot \overline{I_{RF}^2} = \frac{R_{PD} \cdot \Re^2 \cdot \bar{c}^2}{4} \cdot P_c \cdot P_{ref} \tag{2.24}$$

with R_{PD} the output impedance of the PD, $\Re$ its responsivity, $\bar{c}$ the average constellation power (0.5 for OOK, 1 for QPSK, …), and P_c and P_{ref} the optical powers of the carrier and reference laser, respectively. As a rule of thumb, Eq. (2.24) can be used with the following values for the various parameters: $R_{PD} = 50\Omega$, $\Re = 0.56$A/W, and $\bar{c} = 1$. Thus, the approximated RF power in [W] is

$$P_{RF} = \frac{50 \cdot 0.56^2 \cdot 1^2}{4} \cdot P_c \cdot P_{ref} \approx 4 \cdot P_c \cdot P_{ref} \tag{2.25}$$

As an example, if both the carrier and reference lasers have a power of 10 mW, the output RF power will be about 0.4mW.

The maximum power entering a photodiode is limited by the maximum ratings of the device. The allowed maximum power P_{max} corresponds to

$$P_{\text{max}} = P_{\text{ref}} + P_{\text{c}}. \tag{2.26}$$

In order to adapt Eq. (2.24), it is useful to define an optical power ratio R_{RoF} given as

$$R_{\text{RoF}} = \frac{P_{\text{ref}}}{P_{\text{c}}} \quad \rightarrow \quad P_{\text{c}} = R_{\text{RoF}} \cdot P_{\text{ref}}. \tag{2.27}$$

Replacing the power ratio given by Eq. (2.27) in Eq. (2.26) gives

$$P_{\text{max}} = P_{\text{ref}} + R_{\text{RoF}} \cdot P_{\text{ref}} = P_{\text{ref}} \cdot (1 + R_{\text{RoF}}) \quad \rightarrow \quad P_{\text{ref}} = \frac{P_{\text{max}}}{1 + R_{\text{RoF}}} \tag{2.28}$$

Using Eq. (2.27) and Eq. (2.28), the generated RF power of Eq. (2.24) can be rewritten as

$$\begin{aligned} P_{\text{RF}} &= R_{PD} \cdot \overline{I_{RF}}^2 = \frac{R_{PD} \cdot \Re^2 \cdot \bar{c}^2}{4} \cdot R_{\text{RoF}} \cdot P_{\text{ref}} \cdot P_{\text{ref}} \\ &= \frac{R_{PD} \cdot \Re^2 \cdot \bar{D}^2}{4} \cdot R_{\text{RoF}} \cdot \left(\frac{P_{\text{max}}}{1 + R_{\text{RoF}}}\right)^2 \end{aligned} \tag{2.29}$$

The RF output power for typical parameters ($P_{\text{max}} = 20\text{mW}$, $R_{PD} = 50\Omega$, $\Re = 0.5\text{A/W}$, and $\bar{c} = 1$) is plotted in Fig. 2.4. The plot shows that the maximum RF power will be generated for a power ratio $R_{\text{RoF}} = 1$, in other words when $P_{\text{ref}} = P_{\text{c}}$.
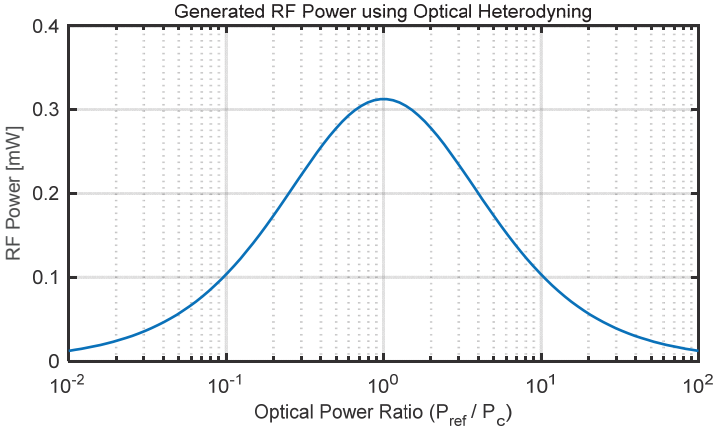

Fig. 2.4 - Generated RF Power using Optical Heterodyning. The maximum RF power is generated when the available maximum optical power (13 dBm in this case) is equally shared between the carrier and reference laser, i.e. when the optical power ratio is 1.

2.1.2   Signal Processing and Filtering

For signals with large fractional bandwidth, i.e. $f_B > 25\%$, designing passband component is extremely challenging due to the large wavelength range that have to be considered in the design of the component, see Eq. (2.3). Using microwave photonics, this challenge is solved easily as optical carrier frequencies are multiple orders of magnitude larger than the signal bandwidths. In the last 20 years, multiple types of filters have been implemented using MWP [82-86]. Next to the key advantage of larger available bandwidth, these proposed MWP based filters usually offer smaller integration footprint and faster tuning processes when compared to their electronic based counterparts.

As depicted in Fig. 2.5, extended from Fig. 2.2, a RF filter can be replaced by an optical filter. In this implementation, as use in this thesis, a RF filter placed after the photodiode, see Fig. 2.5(a), is replaced by an optical filter having the same frequency response and placed in front of the optical coupler, see Fig. 2.5(b). Note that the filter frequency response has to be centered around the optical carrier frequency instead of the RF carrier frequency. In both cases, Fig. 2.5(a) and (b), the output signal is equivalent.
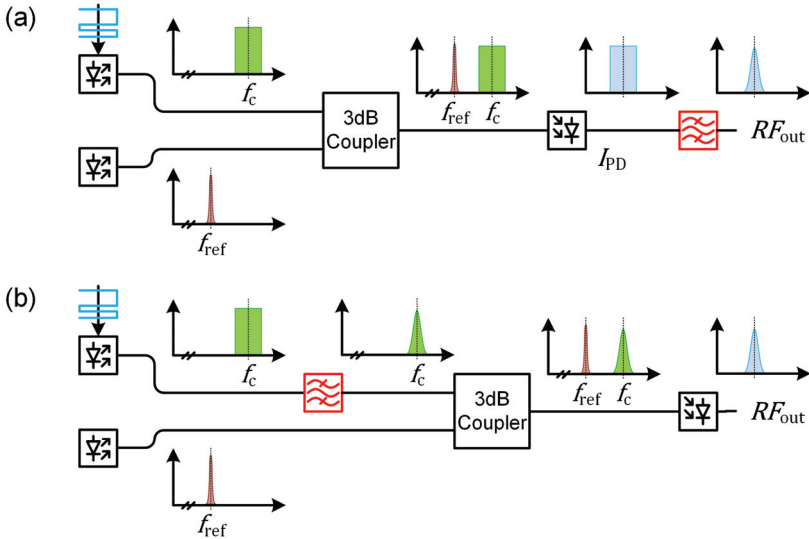

Fig. 2.5 - Filtering in microwave photonics. (a) An arbitrary bandpass RF filter is placed after the photodiode in the RF domain. Thus, it directly affects the output RF signal. (b) The RF filter of (a) can however be replaced by an optical filter placed in front of the coupler, i.e. in the optical domain, without affecting the output signal.

The equivalence between both implementations can be proven by analyzing the schemes of Fig. 2.5(a) and (b) in frequency domain. As seen in Eq. (2.19), the current $I_{\mathrm{PD}}(t)$ generated by the photodiode at the RF frequency is given, neglecting the various constants, by

$$I_{\mathrm{PD}}(t) \approx E_c(t) \cdot E_{\mathrm{ref}}(t) \tag{2.30}$$

with E_{c} and E_{ref} the field amplitude of the carrier and reference lasers, respectively. The output current thus corresponds to a time-domain multiplication of both signals. In frequency domain, see Eq. (2.30), the spectrum of the output RF current S_{PD} is

$$S_{\mathrm{PD}}(f) = \mathcal{F}\{I_{\mathrm{PD}}(t)\} \approx \mathcal{F}\{E_c(t) \cdot E_{\mathrm{ref}}(t)\} \tag{2.31}$$

and becomes, using the convolution theorem,

$$S_{\mathrm{PD}}(f) \approx \mathcal{F}\{E_c(t)\} * \mathcal{F}\{E_{\mathrm{ref}}(t)\} = S_c(f) * S_{\mathrm{ref}}(f) \tag{2.32}$$

with S_c and S_{ref} the carrier and reference lasers spectrums, respectively. In frequency domain, the spectrum of the photocurrent is given by a convolution of the individual spectrums of both lasers. Using a filter $\mathrm{H}(f)$, the RF implementation of Fig. 2.5(a) is therefore given by

$$S_{\mathrm{PD}}(f) \approx \mathrm{H}(f) \cdot [S_c(f) * S_{\mathrm{ref}}(f)] \tag{2.33}$$

while the optical implementation of Fig. 2.5(b) is

$$S_{\mathrm{PD}}(f) \approx [\mathrm{H}(f) \cdot S_c(f)] * S_{\mathrm{ref}}(f) \tag{2.34}$$

As the convolution is not associative with the multiplication, Eq. (2.33) and Eq. (2.34) cannot be considered as equal. The equivalence between the schemes of Fig. 2.5(a) and (b) is thus not valid for all cases. However, for the specific case of Fig. 2.5, one of the laser does not contain any data. Indeed, the reference laser is a single laser line which corresponds in frequency domain to a Dirac delta function (neglecting the laser linewidth). Thus

$$S_{\mathrm{ref}}(f) = \delta(f) \tag{2.35}$$

As the Dirac delta function is an identity operator in convolution, replacing Eq (2.35) in Eq. (2.33) and (2.34) lead in both cases to

$$S_{\mathrm{PD}}(f) \approx \mathrm{H}(f) \cdot S_c(f) \tag{2.36}$$

and shows that both scheme in Fig. 2.5 are equivalent if the linewidth of the reference laser is small (approximated by a single frequency).

In this thesis, dealing with phased array systems, MWP filters are limited to phase shifters (PS) and true-time delays (TTD). More details on frequency responses of PS and TTD can be found in section 3.2. Yet, the above equivalence between the RF and the optical domain can be applied to any type of filters. The choice of building an RF or an optical filter into a system will depends on the specific characteristics of the filters and on the goals of the design.

2.2 Phased Array Antennas

A phased array antenna (PAA) consists of a combination of multiple antennas, i.e. array elements, mounted together to form a multidimensional arrangement (1, 2, or 3D). Each array element or antenna transmits (or receives) similar signals and thus constructive or destructive interferences occur as discussed below.

While one usually first thinks of a PAA as a system in which the beam direction can be electronically steered, many applications of PAA rely on non-steerable systems. This distinction matters as a common terminology is not to be found in the literature. In the following sections and chapters, the following applies: the technologies used to change the beam direction are referred as *beamsteering* while *beamforming* is used when the shape of the beam (side lobe level, beamwidth, grating lobes, etc.) is adapted.

In this section, the fundamental concepts and theoretical background of PAA systems are presented. In particular, the following is treated:

- 2.2.1 Antenna Fundamentals
- 2.2.2 Array Factor & Array Pattern
- 2.2.3 Beamsteering
- 2.2.4 Geometry of Phased Array
- 2.2.5 Array Tapering

For all the aforementioned sub-sections on PAA fundamentals, the systems are considered in transmission mode. This matches the commonly accepted method found in many books on PAA [63, 64]. If not specified otherwise, the various equations provided in this section can however be employed for receiving PAA without modifications.

A substantial part of this section has been adapted from various work performed by, or under the supervision of, the author of this thesis. In these cases, the adapted work is cited at the beginning of the sub-sections.

2.2.1 Antenna Fundamentals

This subsection, presenting the fundamental theory of antennas and antenna patterns, is partially based on work presented by M. Singleton in his master thesis [56].

Near and Far-Field

The space surrounding a radiation source is commonly divided into three parts, each with different electromagnetic characteristics: the near-field, the Fresnel region, and the far-field (also called Fraunhofer region). There are no well-defined lines that divide these regions and indeed there exist a plethora of definitions which may be more appropriate for specific applications. Those defined in the IEEE Standard Definitions of Terms for Antennas [87] are listed in Table 2.1 and used in this thesis.

The near field region contains the reactive or "restorative", non-radiating fields, see Fig. 2.6. In this region the electric and magnetic fields are $\pi/2$ out of phase temporally and tend to be strong but quickly decay in strength with a factor $1/r^2$. The Fresnel region is somehow a transition region, where the radiating components begin to dominate, but the near field effects are still present. Further apart from the antenna the electric and magnetic fields are transverse, in-phase, and the intensity decays predictably with the inverse square law. This region is called far field (or Fraunhofer).

While there is some interest in the near field, as in near-field communications (NFC) for example, this work only deals with far field effects. The rest of this chapter thus exclusively deals with far fields effects.

Table 2.1 - Boundaries for near field, Fresnel region, and far field [87]., r corresponds to the distance from the source, D_A the size of the antenna, and λ the wavelenght.

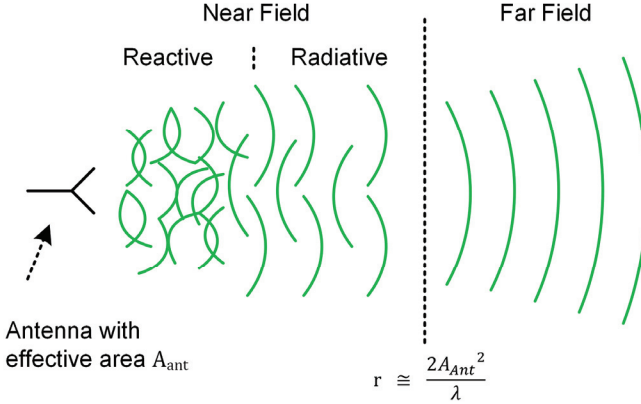| Region	IEEE distance	
Near field (reactive)	$r \; < \; 0.62 \sqrt{D_A^{\;3}/\lambda}$	(2.37)
Near field (Fresnel)	$0.62 \sqrt{D_A^{\;3}/\lambda} \; < \; r \; < \; \dfrac{2D_A^{\;2}}{\lambda}$	(2.38)
Far field (Fraunhofer)	$r \; > \; \dfrac{2D_A^{\;2}}{\lambda}$	(2.39)

Fig. 2.6 - Near and far field. The properties of electromagnetic fields change with distance from the antenna. Different regions, regrouped in near and far fields, are defined in which the behavior of the fields have to be predicted with different formalism.

Radiation

Disturbances in the local electromagnetic field about a charge or conductor produce a wave which will propagate away indefinitely from the source at the speed of light c until it encounters some obstacle, at which point the energy is absorbed or scattered. This is known as radiation, and it occurs due to the acceleration or deceleration of charge [9].

In a wire, radiation is typically produced by smooth bends, implying a constant acceleration normal to the direction of motion, and abrupt impedance discontinuities which cause reflections at the boundaries and thus a sharp, negative acceleration [9]. Furthermore, an oscillating source will also cause the charges within a conductor to oscillate, which is a periodic time varying acceleration.

For individual charges moving at nonrelativistic velocities, the Larmor formula shows that the **radiated power P_s [W] of a source** is given by [60]

$$P_s = \frac{q^2 a^2}{6\pi\varepsilon_0 c^3} \tag{2.40}$$

where q is the total electronic charge, a the acceleration of the charges, ε_0 vacuum permittivity, and c the speed of light. According to conservation of energy, energy cannot be created nor destroyed. In the case of radiation, the energy is taken from the momentum of the charged particle. This radiation reaction force is called "Abraham–Lorentz force".

Power Density

Assuming free-space propagation and as depicted on Fig. 2.7, the power density I_s in $[W/m^2]$, i.e. the power transmitted per area, of an isotropic source will decay according to the square law

$$I_s = \frac{P_s}{4\pi r^2} \tag{2.41}$$

with P_s the power emitted by the source, see Eq. (2.40), and r the distance from the source. Eq. (2.41) simply states that the power density decay corresponds to the increasing area of a sphere located at the position of the source and having a radius r.
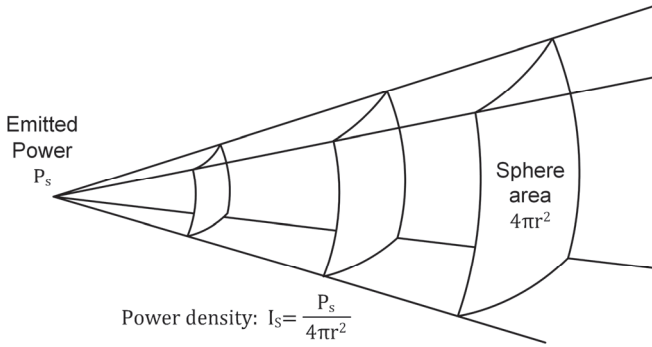

Fig. 2.7 - Inverse square law power decay The power density I_s decays at a rate inversely proportional to the surface of a sphere having a radius corresponding to the distance r.

Aperture of an Isotropic Antenna

An antenna can only act on electromagnetic fields in a limited area. This area, corresponding in a first approximation to the physical size of the antenna is called the antenna aperture. For the receiving case as an example, the larger the antenna aperture, i.e. its size, the more energy can be collected. For the particular case of an **isotropic antenna**, the **antenna aperture** or size A_{iso} is given as [88]

$$A_{iso} = \frac{\lambda_{RF}^2}{4\pi} \tag{2.42}$$

with λ_{RF} the wavelength.

The aperture of an isotropic antenna is always given by Eq. (2.42). Indeed, if an antenna with a larger aperture is used, the power would be transmitted to or received from a particular direction - The antenna would no longer be isotropic. In fact, the gain of an antenna is, to some extent, connected to its aperture size, see following sub-sections.

Free-Space Path Losses

Considering transmission between two isotropic antennas, the received power P_iso can be calculated by combining the power density at a specific distance, see Eq. (2.41), with the size of an isotropic receiver, see Eq. (2.42). The result is

$$P_\text{iso} = \frac{P_\text{s}}{4\pi r^2} \cdot \frac{\lambda_\text{RF}{}^2}{4\pi} = P_\text{s} \cdot \left(\frac{\lambda_\text{RF}}{4\pi \cdot r}\right)^2 \tag{2.43}$$

The losses occurring during the transmission, called the **free-space losses** ($FSPL$), are given by the ratio between transmitted and received power

$$FSPL = \frac{P_\text{s}}{P_\text{iso}} = \left(\frac{4\pi \cdot r}{\lambda_\text{RF}}\right)^2. \tag{2.44}$$

Note that the $FPSL$ are independent on the type of antennas. Indeed, the $FSPL$ provides link losses considering isotropic antenna (with a gain $G_\text{A} = 1$, by definition). In the link budget, the antenna gains will be added.

Antenna Directivity and Pattern

The directivity of an antenna is usually calculated in comparison to an isotropic antenna. An antenna with a directivity larger than 1, or 0 dBi, will thus have an antenna pattern with preferred directions. 0 dBi is per definition the gain of an isotropic antenna. Yet, the surface integral on a sphere around the antenna always matches the transmitted power P_S as an antenna never provides "power gain". It is in fact only a gain in comparison to an isotropic radiation. Having large directivity in a direction implies having lower directivity in other directions, see Fig. 2.8. In opposite to antenna gain, directivity does not include losses.

Antenna Pattern [dBi]

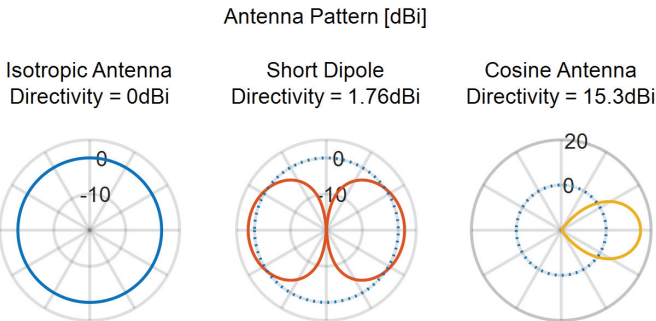| Isotropic Antenna	Short Dipole	Cosine Antenna
Directivity = 0dBi	Directivity = 1.76dBi	Directivity = 15.3dBi

Fig. 2.8 - Antenna pattern. By definition, an isotropic antenna has a directivity of 1, i.e. 0 dBi, and transmit energy in all the direction, see left part of the figure. The antenna pattern for two other antenna examples are plotted in reference to the isotropic antenna. For the case of a short dipole (middle), this lead to a directivity of 1.76 dBi. An exemplary cosine antenna (right) could have a directivity of 15.3 dBi when the energy is mainly received or transmitted in one direction.

Antenna effective Aperture

An antenna can only emit or receive energy in a physically limited aperture, i.e. area. In the case of lens or reflector-based antennas, the aperture is limited by the physical size of the lens or reflector. In the case of travelling wave antennas, e.g. horn antennas, the aperture size corresponds to the physical size of the waveguide. In addition, the losses (thermal, ohmic, etc.) have to be considered, thus the aperture of an antenna is defined as an antenna effective aperture A_{eff} comprising various losses and given as

$$A_{\text{eff}} = \epsilon_a \cdot A_{\text{phys}} \tag{2.45}$$

with ϵ_a the efficiency of the aperture (typically in the range 0.35-0.7 [89]) and A_{phys} the physical aperture size of the antenna. Note that for some antennas such as dipole of Yagi antenna, a "physical size" cannot be defined. A larger antenna can collect more power, but it also implies that the antenna pattern will not be isotropic. This is easier to understand for a transmitting antenna: If one wants to increase the power going in a specific direction, the power emitted in other directions has to be minimized. In order words, an antenna focuses the energy in a particular direction.

Antenna Gain

The antenna gain provides an information on the "focusing" effect of an antenna. It is comparable to the antenna directivity but comprises in addition the various losses such as the ohmic or thermal ones. The gain of an antenna is calculated in comparison with an isotropic radiator. The definition is made over the antenna effective aperture, see Eq. (2.45), and the aperture size of an isotropic antenna, see Eq. (2.42). Thus, the **antenna gain** is [62]

$$G_A = \frac{A_{\text{eff}}}{A_{\text{iso}}} = \frac{\epsilon_a \cdot A_{\text{phys}}}{\dfrac{\lambda_{\text{RF}}{}^2}{4\pi}} = \frac{4\pi \cdot \epsilon_a \cdot A_{\text{phys}}}{\lambda_{\text{RF}}{}^2} \tag{2.46}$$

As an example, if a wireless system engineer needs an antenna with a gain of 30 dBi at 60 GHz ($\lambda_{\text{RF}} = 5\text{mm}$), a horn antenna with a typical efficiency of 0.5 (for conical horn) will have an aperture size of

$$A_{\text{phys}} = \frac{G_A \cdot \lambda_{\text{RF}}{}^2}{4\pi \cdot \epsilon_a} = \frac{1000 \cdot 0.005^2}{4\pi \cdot 0.5} = 0.004 \text{ m}^2 = 4000 \text{ mm}^2$$

An aperture size of 4000 mm² corresponds to an antenna size D_A of

$$D_A = \sqrt{A_{\text{phys}}} = \sqrt{0.004} = 0.0632 \text{ m} = 63.2 \text{ mm}.$$

In other words, the antenna diameter will be $63.2/5 \cong 9$ time larger than the wavelength. This limitation is of interest in the design of a phase array antenna (PAA), see section 2.2.4. With a typical element spacing of $0.5 \cdot \lambda_{RF}$, the gain per antenna element is limited to approximately $4\pi \cdot \epsilon_a = 1.6$ dBi, see Eq. (2.46).

Friis Transmission Equation

The link budget of a wireless transmission is computed using the Friis transmission equation [88], see Fig. 2.9. This equation relates the output power after the receiving antenna to the power send through the transmitting antenna. It uses the definitions above of antenna gain (derived from the effective antenna aperture) and free-space path losses ($FSPL$). As explained with the help of Eq. (2.45) and Eq. (2.46), the various losses occurring in the antenna are already included in the antenna aperture efficiency, and thus in the antenna gain. In addition to the antenna losses, the atmospheric losses (absorption, scattering, etc.) must also be considered. The Friis transmission equation is given by [88]

$$P_{\text{Rx}} = \frac{P_{\text{Tx}} \cdot G_{A_{\text{Tx}}} \cdot G_{A_{\text{Rx}}}}{FSPL \cdot L_{\text{link}}} \tag{2.47}$$

where P_{Rx} and P_{Tx} are respectively the received and transmitted power, G_{A_Rx} and G_{A_Tx} are respectively the gain of the receiving and transmitting antenna, $FSPL$ the free-space path losses, and L_{link} the atmospheric losses. Note that $FSPL$ and L_{link} are in this definition larger than 1.

For simplicity, the Friis transmission equation, i.e. the **link budget**, is usually computed in decibel. In this case, Eq. (2.47) becomes

$$P_{\text{Rx}} = P_{\text{Tx}} + G_{A_{\text{Tx}}} + G_{A_{\text{Rx}}} - FSPL - L_{\text{link}} \tag{2.48}$$

With values in dBm or dBW for the power, dBi for the gains, and dB for the losses. $FSPL$ and L_{link} are positive values. In decibel, $FSPL$ is given by

$$FSPL = 20 \cdot \log_{10} \left(\frac{4\pi \cdot r}{\lambda_{\text{RF}}} \right) \tag{2.49}$$

Before the introduction of the Friis transmission equation in 1946 [88], the link budget of wireless system was calculated using field strength and aperture sizes. The calculation based on isotropic element has thus simplified the process.

Fig. 2.9 - Friis transmission equation. The link budget of a wireless link is computed with the Friis transmission equation. In the Friis equation, the gain of the antennas G_{A_Rx} and G_{A_Tx} is calculated in comparison with isotropic antenna elements, which simplify drastically the equation compared to the former field strength based calculations. The key advantage is that one can use the FSPL (in addition to the atmospheric losses) without having to consider the pattern of the antennas.

2.2.2 Array Factor & Array Pattern

The **array factor** provides information on the effect of the geometry of a phased array antenna (PAA) Different aspects have to be considered to compute the array factor. It includes the size of the array, the spacing and type of the antenna elements, and the array tapering (see section 2.2.5). The **array pattern** on the other hand describes the resulting radiation pattern of the full system when combining a specific PAA geometry (array factor) with the antenna elements (antenna radiation pattern).

The difference between array factor and array pattern is better explained with the help of Fig. 2.10. The array pattern (on the right) is in a first approximation the result of a multiplication between the antenna radiation pattern (on the left) and the array factor (middle). In this example, the antenna elements used as building blocks in the PAA are patch antennas with a half-power beamwidth (HPBW) of about 70°. The PAA itself, is an 4x1 uniform linear array (ULA) with a typical $\lambda/2$ element spacing, see section 2.2.4. The radiation pattern of the PAA system, i.e. the array pattern, is thus influenced by both the geometry of the array and by the characteristics of the antennas forming the PAA. Neglected in this section is the mutual coupling between antennas that can lead to an *active* array pattern quite different from the array pattern discussed in this section.

The distinction between array factor and array pattern is of particular importance when performing beamsteering. Indeed, the radiation pattern of the elements must cover the full steering range. In the example of Fig. 2.10, the PAA could not scan in a range larger than the ~70° antenna beamwidth.
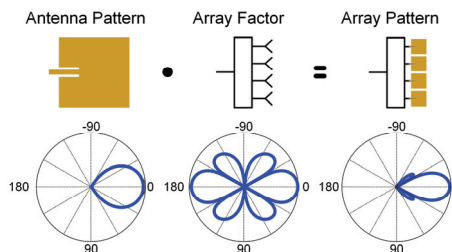

Fig. 2.10 - Antenna and array pattern. The array pattern of a PAA (right) is a combination of the single antenna radiation pattern (left), here a cosine antenna and the array factor (middle), here a 4x1 uniform linear array (ULA) [40].

Derivations of the Array Factor and Array Pattern

The derivations of the array factor and array pattern are here detailed starting with some coordinate definitions. As depicted in Fig. 2.11(a), the antennas of the PAA lie in the X-Y plane. Each antenna element i is located at a position $\mathbf{r_i}$ relative to the center of the array. In Fig. 2.11(b), the external coordinates are depicted with the far-field observation point $P(\mathbf{r})$, the elevation angle θ, and the azimuth angle ϕ. The derivations of the array factor and array pattern are performed by analyzing the signal received at the observation point $P(\mathbf{r})$.

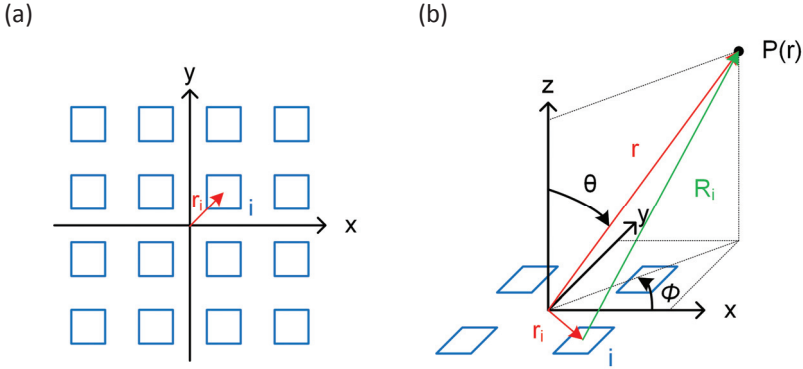(a)   (b)

Fig. 2.11 - Coordinate system definition for phased array systems. (a) The array is lying on the X-Y plane with each element defined by its position $\mathbf{r_i}$. (b) At the observation point $P(\mathbf{r}) = P(x,y,z) = P(|\mathbf{r}|,\theta,\phi)$, the sum of all the radiation coming from the i antennas have to be summed up. The distance between the i antenna and the observation point is defined by $\mathbf{R_i}$. [90]

Fig. 2.11(a) depicts an exemplary rectangular array with 4x4 antennas. Each antenna element i is defined by its antenna radiation pattern D_i and its position $\mathbf{r_i}$ in the array. The antenna pattern is given by

$$D_i(\theta,\phi) \qquad\qquad (2.50)$$

with θ and ϕ the elevation and azimuth angle, respectively. Different antennas such as dipole, horn antenna, or patch antenna have different pattern, see Fig. 2.8. The antenna pattern $D(\theta,\phi)$ provides an information about the angular dependency of the antenna directivity compared to a hypothetical isotropic antenna, i.e. an antenna radiating equally in all directions. The pattern of Eq. (2.50) is usually given in [dBi], i.e. gain of an antenna compared to an isotropic radiator with the same total power.

In most cases, PAAs are built with similar elements (antennas) and thus the antenna patterns can often be considered as equal for all elements, hence

$$D_i(\theta,\phi) \rightarrow D(\theta,\phi)$$

The received radiation at the observation point $P(\mathbf{r})$ can be calculated by adding the radiations coming from of all the elements forming the PAA.

First, the spherical wave E_s originating from each element is given by

$$E_s(\mathbf{R}_i) = \frac{1}{|\mathbf{R}_i|} e^{-ik|\mathbf{R}_i|} \tag{2.51}$$

with $\mathbf{R}_i$ the propagation vector from antenna element i and k the wavenumber.

As already stated, the received radiation amplitude E_P at the observation point is given by summing the radiation originating from all the antenna elements. In the summation, three factors have to be considered: 1) the spherical wave propagations with origins at each antenna elements, see Eq. (2.51), 2) the individual antenna radiation patterns $D_i(\theta, \phi)$, see Eq. (2.50), and 3) a complex weighting factor a_i used to tune the phase and amplitude of the waves in front of each antenna. Thus, E_P is given by [63]

$$E_P(\mathbf{r}) = \sum_i a_i \cdot D_i(\theta, \phi) \cdot \frac{1}{|\mathbf{R}_i|} e^{-ik|\mathbf{R}_i|} \tag{2.52}$$

Changing the value of the complex weighting factor a_i enable beamsteering, see below, and beamforming, see section 2.2.5 on array tapering.

Eq. (2.52) can be simplified by replacing the propagation vectors $\mathbf{R}_i$ by

$$\mathbf{R}_i = \mathbf{r} - \mathbf{r}_i \tag{2.53}$$

with $\mathbf{r} = [x, y, z]$ the position of the observation point P and $\overrightarrow{\mathbf{r}_i = [x_i, y_i, z_i]}$ the position of the i antenna element. As detailed in Appendix A, assuming $|\mathbf{r}| \gg |\mathbf{r}_i|$ and by using a first order Taylor approximation, the norm of Eq. (2.53) is simplified to

$$|\mathbf{R}_i| = |\mathbf{r}| - \hat{\mathbf{r}} \cdot \mathbf{r}_i \tag{2.54}$$

with $\hat{\mathbf{r}}$ the unit vector of $\mathbf{r}$. Using Eq. (2.54) in Eq. (2.52) leads to [63]

$$E_P(\vec{r}) = \sum_i a_i \cdot D_i(\theta, \phi) \cdot \frac{1}{|\mathbf{r}| - \hat{\mathbf{r}} \cdot \mathbf{r}_i} e^{-ik(|\mathbf{r}| - \hat{\mathbf{r}} \cdot \mathbf{r}_i)} \tag{2.55}$$

Eq. (2.55) can be further simplified. The propagation decay $1/|\mathbf{r} - \hat{\mathbf{r}} \cdot \mathbf{r}_i|$ is approximated by $1/|\mathbf{r}|$ as $|\mathbf{r}| \gg |\mathbf{r}_i|$ and can therefore be pulled out of the sum. In addition, the phase development $ik(|\mathbf{r}| - \hat{\mathbf{r}} \cdot \mathbf{r}_i)$ can be split with terms in and out of the sum. The received radiation E_P at the observation point is finally given by

$$E_P(\mathbf{r}) = \frac{e^{-ik|\mathbf{r}|}}{|\mathbf{r}|} \cdot \sum_i a_i \cdot D_i(\theta, \phi) \cdot e^{ik(\hat{\mathbf{r}} \cdot \mathbf{r}_i)} \tag{2.56}$$

Assuming identical antenna elements as usually true for PAA, $D_i(\theta, \phi)$ can be replaced by $D(\theta, \phi)$ and pulled out of the sum. The remaining term in the sum of Eq. (2.56) is defined as the **array factor** AF and given by

$$AF(\hat{r}) = AF(\theta, \phi) = \sum_i a_i \cdot e^{ik(\hat{r} \cdot r_i)}. \tag{2.57}$$

The radiation received at the observation point P is thus [63]

$$E_P(r, \theta, \phi) = \frac{e^{-ik|r|}}{|r|} \cdot D(\theta, \phi) \cdot AF(\theta, \phi) \tag{2.58}$$

The **array pattern** is given without the wave propagation, defined as

$$D_{PAA}(\theta, \phi) = D(\theta, \phi) \cdot AF(\theta, \phi) \tag{2.59}$$

Note that the radiation pattern $D(\theta, \phi)$ corresponds to the element radiation pattern in a PAA configuration. There is indeed a small difference in the antenna pattern when an antenna is used in a PAA or alone. This difference comes among other from cross-coupling between the elements.

Fig. 2.12 depicts the various patterns of an exemplary 8x1 PAA based on cosine antennas. On the left, the pattern of the antenna element is depicted. In this example, a cosine antenna is used. In the middle of the figure, the array factor for a uniform linear array (ULA) with 4 elements spaced by $\lambda/2$ is depicted. The array pattern, representing the radiation pattern of the full system, is depicted on the right. It corresponds to a multiplication of the antenna pattern with the array factor, see Eq. (2.59).
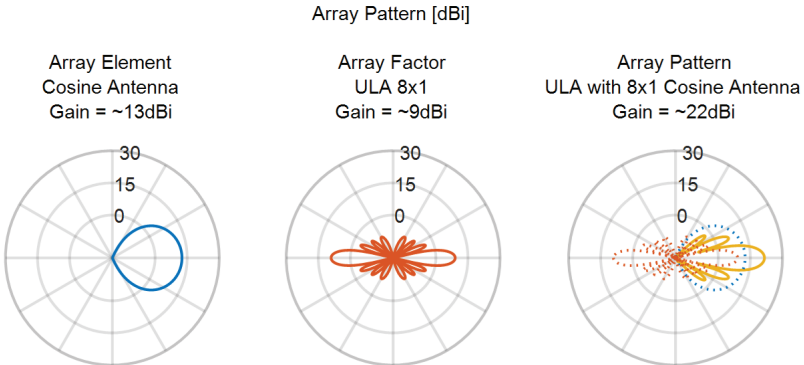

Fig. 2.12 - Pattern of a cosine antenna, a 8x1 isotropic array and a 8x1 cosine antenna array. On the left, a typical radiation pattern of a single cosine antenna is plotted. In the middle, a 8x1 array made of isotropic elements is plotted. As isotropic elements are used, this pattern corresponds to the array factor. Having an array of cosine antennas with the antenna pattern from the left in a 8x1 array with an array factor as in the middle plot, the resulting pattern, i.e. the multiplication of the antenna and the array will be as depicted on the right.

3 dB Beamwidth and Sidelobe Level

The most important characteristics of the array factor are the 3 dB beamwidth and the sidelobe level. Both are briefly discussed in this subsection.

The 3 dB beamwidth corresponds to the width of the beam at a 3 dB level below the array gain. In the example of Fig. 2.13, the array factor of a uniform linear array (ULA) with 16 antennas spaced by $\lambda/2$ is plotted. The beamwidth of 6.39° is the width of the beam at 9 dBi gain (the array gain is 12 dB). For a ULA, **the 3 dB beamwidth** Θ_{3dB} can be easily computed using [63]

$$\Theta_{3dB} = 0.88 \frac{\lambda_{\mathrm{RF}}}{D_{\mathrm{A}}} \cdot \frac{180}{\pi} \tag{2.60}$$

with λ_{RF}, the radio frequency wavelength and D_{A} the size of the array. D_{A} is given by $D_{\mathrm{A}} = N \cdot d$ with N the number of antennas and d the antenna spacing.

The second parameters, i.e. the sidelobe level, corresponds to the gain margin between the gain of the main lobe and the gain of the highest sidelobe. In the example of Fig. 2.13, the sidelobe level is 13.2 dB. The sidelobe level is of particular importance when a multi-beam system is built as it provides an information on the interferences that will originate from neighbor channels.

In the design of a PAA, the 3 dB beamwidth is tied to the sidelobe level. Indeed, when optimizing one, the other become worst. There is thus a trade-off that need to be found for a particular application.
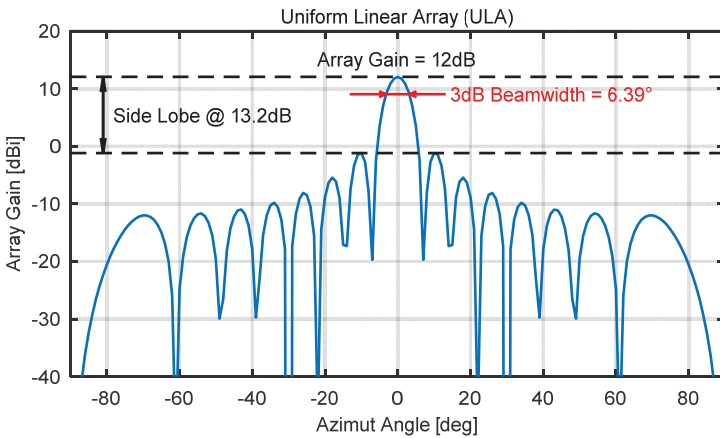

Fig. 2.13 - Array factor of a 16x1 uniform linear array (ULA). The 3 dB beamwidth corresponds to the width of the beam at a level 3 dB below the array gain. The sidelobe level corresponds to the gain difference between the main lobe and the highest sidelobe of the PAA:

2.2.3   Beamsteering

In order to change the direction of the beam, i.e. to perform beamsteering, the complex weighting factor a_i in the array factor can be adjusted. The easiest way to understand the principle of beamsteering is by analyzing Fig. 2.14. The direction of the wavefront after the PAA can be influenced by adding a path difference in front of each antenna elements. The path difference x to steer the beam in the direction θ with antenna spacing d is

$$x = d \cdot \sin \theta. \tag{2.61}$$

For array with more than 2 antennas, the value of x will be multiplied by the position of the elements. There are two fundamental ways to provide the path differences in front of the antennas.

1) Using true time delay (TTD). In this case, the required delay Δt is given by

$$\Delta t = \frac{x}{c} = \frac{d \cdot \sin \theta}{c}. \tag{2.62}$$

with c the speed of light in the medium. The advantage of TTD based PAA is that there is no frequency dependency in Eq. (2.62). Thus, all the frequency components will be steered in the same direction.

2) Using phase shifters (PS). In this case, the required phase shift φ is

$$\varphi = 2\pi \cdot \frac{x}{\lambda_{\mathrm{RF}}} = 2\pi \cdot \frac{d \cdot \sin \theta}{\lambda_{\mathrm{RF}}} \tag{2.63}$$

with λ_{RF} the wavelength of the carrier frequency. The main advantage of PS based PAA is the low implementation complexity. However, the PAA will perform well only for one frequency (corresponding to λ_{RF})
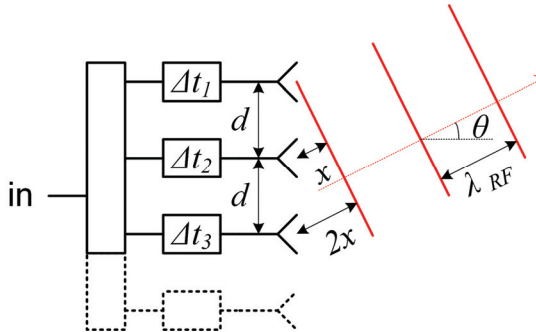

Fig. 2.14 - Principle of a phased array antenna (PAA). The input signal (in) is split into N array elements using a power splitter. In front of each antenna a time delay or a phase shifter is introduced in order to steer the direction of the beam. [40]

In the following subsection, generalized mathematical formulations are provided for PAA based on phase shifter and true time delays.

Generalized Equations for Phase Shifter & true Time Delays based PAA

A generalized calculation of the array weights for beamsteering can be derived by first recalling the array factor equation, i.e. Eq. (2.57),

$$AF(\hat{r}) = AF(\theta, \phi) = \sum_i a_i \cdot e^{ik(\hat{r} \cdot r_i)}.$$

The main lobe, i.e. the direction of the beam with most power, occurs when the sum is maximized. This happens when the phase of the complex weighting factor a_i are the conjugate of the phase related to the antenna element positions $k(\hat{r} \cdot r_i)$. This take place when

$$\forall i \quad \arg a_i = -k(\hat{r} \cdot r_i) \qquad (2.64)$$

In order to compute the required weights a_i, the definition of the wavenumber k is needed. k is given by

$$k = \frac{2\pi}{\lambda} = \frac{2\pi \cdot f}{c} \qquad (2.65)$$

with λ the wavelength, c the speed of light in the medium, and f the frequency. Replacing Eq. (2.65) in Eq. (2.64) leads to

$$\arg a_i = -\frac{2\pi \cdot f}{c} (\hat{r} \cdot r_i) \qquad (2.66)$$

From Eq. (2.66), is it clear that the argument of a_i is frequency dependent.

In the case of phase shifters based PAA, the **required phase shift** is usually computed for the carrier frequency f_{RF}, thus

$$\varphi_i = -\frac{2\pi \cdot f_{RF}}{c} (\hat{r} \cdot r_i) \qquad (2.67)$$

In the case of true time delay based PAA, the required time delay can be computed by using the Fourier transform of a time delay, i.e.

$$\mathcal{F}\{f(t - \Delta t)\} = e^{-2\pi \Delta t f} \cdot F(t). \qquad (2.68)$$

Using as phase response in Eq. (2.68) the relation from Eq. (2.66)

$$-2\pi \Delta t f = -\frac{2\pi \cdot f}{c} (\hat{r} \cdot r_i),$$

the **required time delay** in front of each antenna element is

$$\Delta t_i = \frac{(\hat{r} \cdot r_i)}{c} \qquad (2.69)$$

For both Eq. (2.67) and Eq. (2.69), the unit vector of the observation point direction could be replaced by the elevation θ and azimuth ϕ angle using

$$\hat{r} = \sin\theta \cos\phi \cdot \hat{x} + \sin\theta \sin\phi \cdot \hat{y} + \cos\theta \cdot \hat{z} \qquad (2.70)$$

Exemplary Array Factors

Using Eq. (2.57), the array factor for phase shifter based PAA can be computed with the help of Eq. (2.67) and for true time delay with Eq. (2.69). For both figures below, an 8x1 uniform linear array (ULA) with $\lambda/2$ element spacing is used. The design frequency f_{RF} is 60 GHz. The difference between phase shifters based PAA, see Fig. 2.15, and true time delay based PAA, see Fig. 2.16, is noticeable on the bottom of the figures, when steering the beam at 40° elevation angle. For the phase shifters, not all the frequencies go exactly to 40°, this error - not occurring for true time delay - is called beam squint and is further discussed in the following subsection.
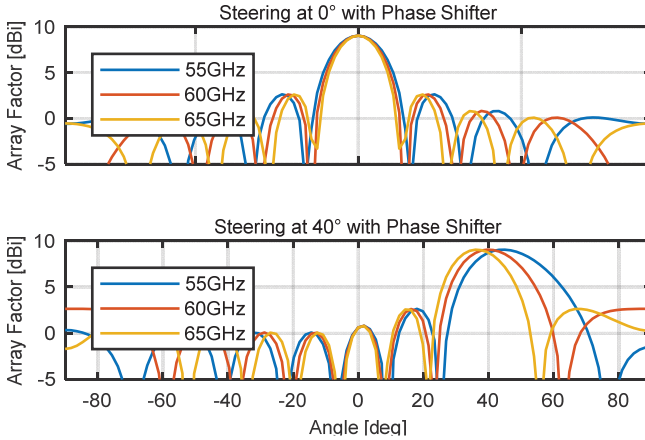
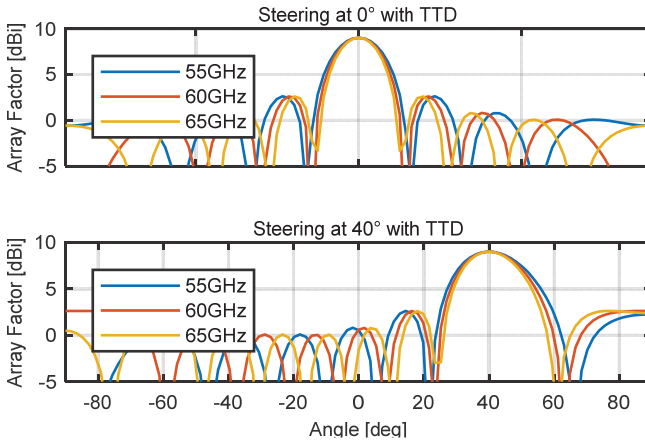

Fig. 2.15 - Array factor for phase shifters based PAA

Fig. 2.16 - Array factor for true time delay based PAA

Beam Squint

Beam squint is a steering error that occurs when using phase shifters (PS) in the PAA feeder. As seen in Eq. (2.67), the underlying problem is that PS based PAA can only be designed correctly for a single frequency. This is better described with the help of Fig. 2.17. It shown that only the design frequency, i.e. 60 GHz, is steered at exactly 45°. The pointing errors of the other frequencies are in this case non-negligible as they will limit the 3 dB bandwidth of the array. The pointing error is moreover dependent on the steering angle, this effect is depicted in Fig. 2.18.
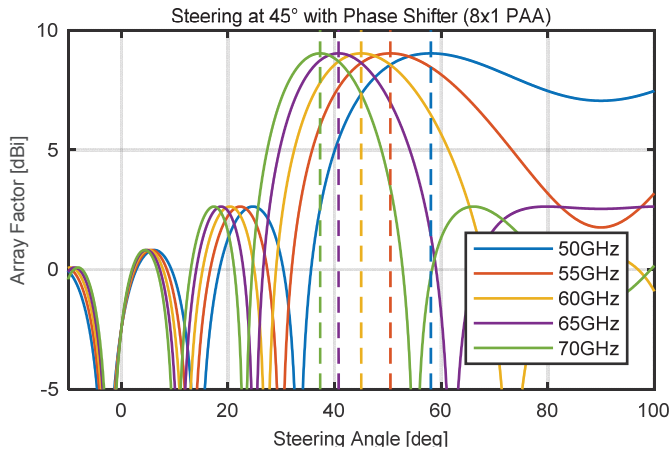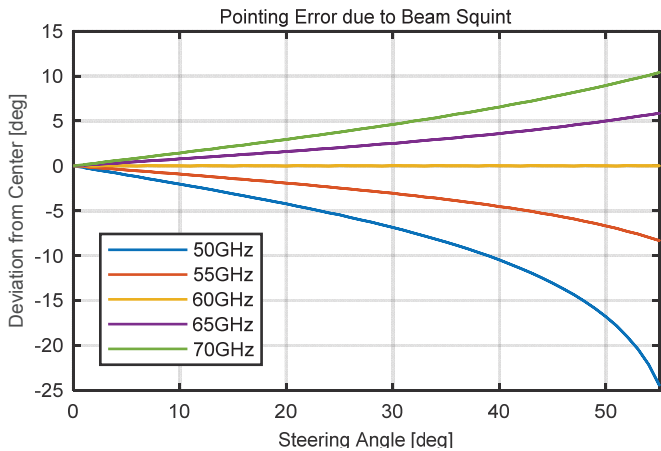

Fig. 2.17 - Beam squint at 45° steering.

Fig. 2.18 - Pointing error due to beam squint.

2.2.4 Geometry of Phased Array Antenna

The geometry of a PAA defines the position of the antenna elements. The elements can indeed be placed on a rectangular grid as described in the previous sections, but other geometries are also commonly used. In this section, the main geometries of PAA are summarized as they can be used to tune the gain, the side lobe level, and the beamwidth of the array factor.

Uniform Linear Array (ULA)

The most common geometry for PAA in text books is called uniform linear array (ULA). As depicted in Fig. 2.19, the elements are equispaced and placed on a 1D line. This geometry is extremely useful to understand the principles of PAA but is not often implemented as the array factor can only be controlled in one direction.
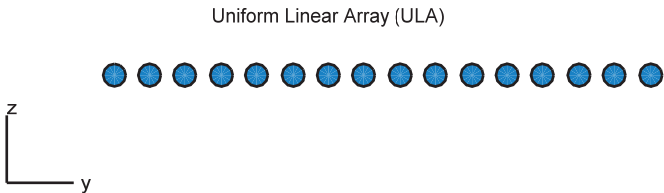

Fig. 2.19 - Geometry of a uniform linear array (ULA).

The corresponding array factor of such an array is shown in Fig. 2.20. With 16 antennas spaced by $\lambda/2$, the array gain is 12 dB, the 3 dB beamwidth 6.4°, and the side lobe level at -13.2 dB.
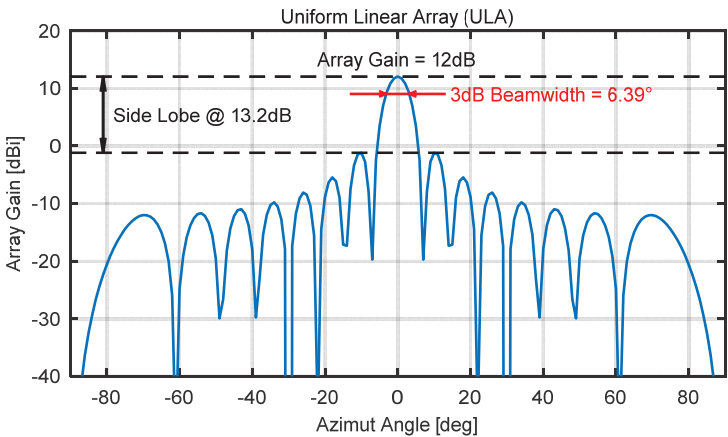

Fig. 2.20 - Array factor of a uniform linear array (ULA).

Uniform Rectangular Array (URA)

Another commonly seen array geometry is the uniform rectangular array (URA). In this case, the 16 antennas are placed on a rectangular grid. The geometry is depicted in Fig. 2.21.
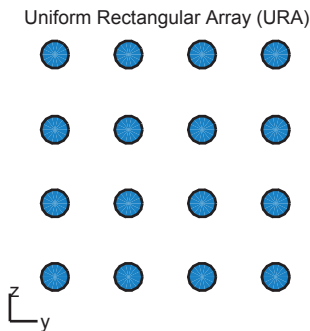

Fig. 2.21 - Geometry of a uniform rectangular array (URA)

The corresponding array factor is plotted in Fig. 2.22. It shows that compared to the ULA (previous section), the array gain is once again 12 dB. The reason is that, as before, constructive interferences between 16 elements take place. A factor 16 corresponds to 12 dB. For the 3 dB beamwidth, the main lobe is far larger with 26.3° (compared with 6.4° previously). In fact, this beamwidth corresponds to an 4x1 ULA as only 4 antennas are placed on one row or column of the array. The difference is however that this beamwidth is found along the elevation and azimuth angle of the array. The side lobe level is in this case 11.3 dB.
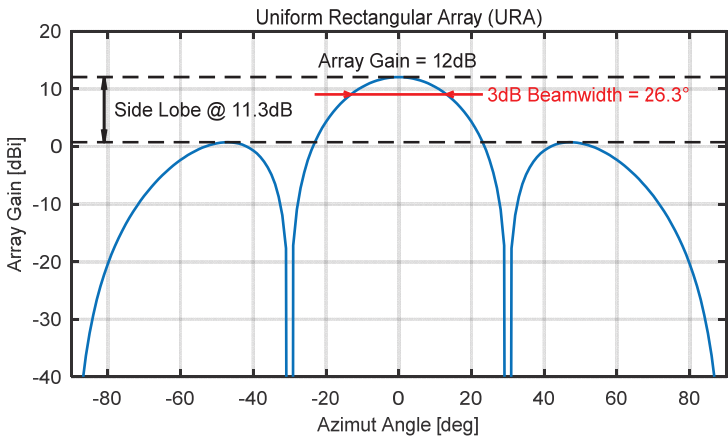

Fig. 2.22 - Array factor of uniform rectangular array (URA)

Uniform Rectangular Array with Triangular Grid (UTA)

To perform 2D steering with 16 antennas as achievable with ULA, see above, another geometry is commonly used. The main advantage of uniform rectangular array with triangular grid (UTA) is that the elements can please place closer to each other. The geometry is depicted in Fig. 2.23

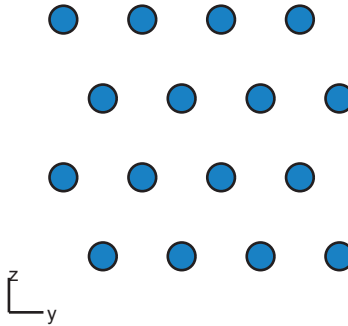Uniform Rectangular Array with Triangular Grid (UTA)

Fig. 2.23 - Geometry of uniform rectangular array with triangular grid (UTA)

In the UTA case, the array factor is depicted in Fig. 2.24. It provides when compared with the URA case at the same time a smaller beamwidth, i.e. 25.7° versus 26.3° for URA and a lower side lobe level, i.e. 12.8 dB versus 11.3 dB.
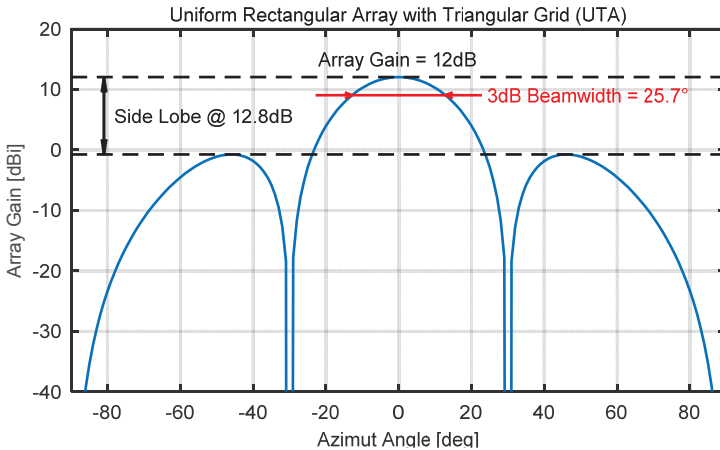

Fig. 2.24 - Array factor of uniform rectangular array with triangular grid (UTA)

Uniform Circular Array (UCA)

The 16 antennas can also be placed on a circle to perform 2D beamsteering. This geometry called uniform circular array (UCA) is plotted in Fig. 2.25.
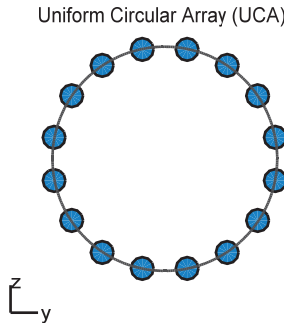
Uniform Circular Array (UCA)

Fig. 2.25 - Geometry of uniform circular array (UCA).

The array factor of a UCA is depicted in Fig. 2.26. Compare to the previous rectangular architecture is provides a smaller beamwidth of 20.6° but a worst side lobe. However, there is another fundamental difference in the array pattern. The beam width of 20.6° is achieved in all steering direction. Indeed, the beam is circular. In the URA and UTA, the beam shape is indeed closer to a square.
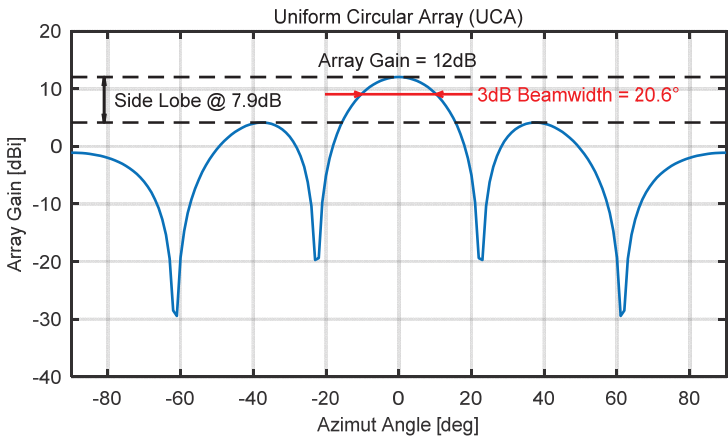

Fig. 2.26 - Array factor of uniform circular array (UCA).

Summary Array Geometry

In this section, the three common geometries described above used to perform 2D steering are summarized. The tree geometries

- Uniform rectangular array (URA),
- Uniform rectangular array with triangular grid (UTA), and
- Uniform circular array (UCA)

are characterized by the characteristic summarized in Table 2.2. Depending on the application, one or the other geometry may be preferable.

Table 2.2 - Summary of the array factor characteristics for URA, UTA, and

	URA	UTA	UCA
Array gain [dB]	12	12	12
Beamwidth [deg]	26.3	25.7	20.6
Side lobe level [dB]	11.3	12.8	7.9

In Fig. 2.27, the array factor of URA, UTA, and UCA are plotted on top of each other for an easier comparison. As stated in the previous section on UCA, the beam generated by a UCA has the additional advantage of beams circular while the beams of URA and UTA have a more rectangular shape. In all cases, the gain is 12 dB as the array are built with 16 antenna elements.
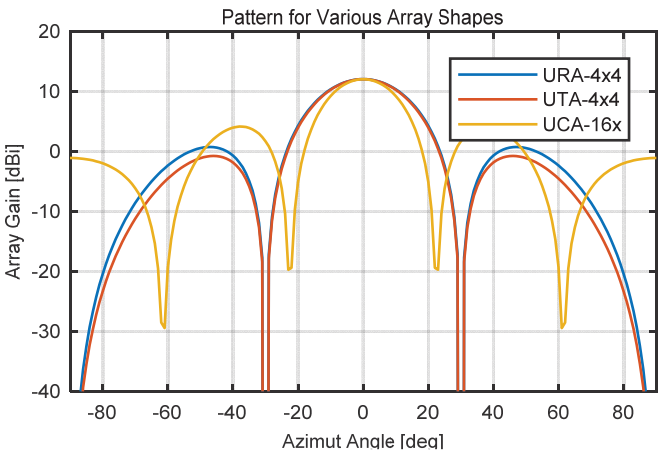

Fig. 2.27 - Array pattern for URA, UTA, and UCA.

2.2.5 Array Tapering

In addition to the choice of the various PAA geometries described in the previous section, the beamwidth and the side lobe level of a PAA can also be fine-tuned using array tapering. Array tapering consists of tuning the power distribution through the antenna elements. This technique is explained with the help of Fig. 2.28. On the left, a uniform rectangular array (URA) as used in the previous sections is depicted. In this case, all the elements of the array emit the same power. In more details, each element emits $1/16$ of the total power as there are 16 antennas in the array. The amplitude of the complex weighting factors a_i in Eq. (2.57) is thus set to $1/16$. On the right side of the figure, a rectangular array with non-uniform tapering is depicted. In this case, not all the complex weighting factor a_i have the same amplitude. By adapting the array tapering, it is possible to fine-tune the beamwidth and side lobe level of the array factor.

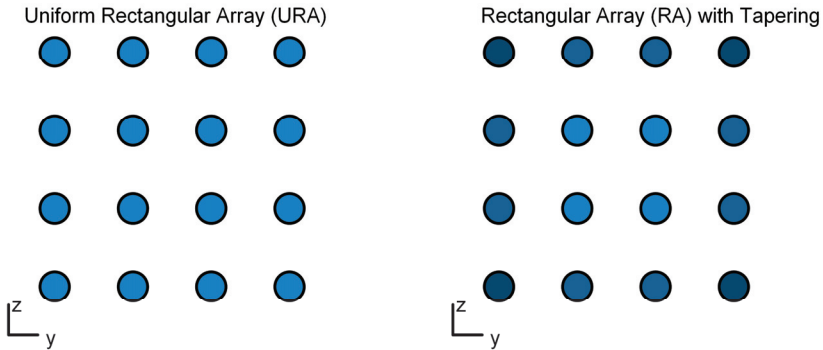Uniform Rectangular Array (URA) Rectangular Array (RA) with Tapering

Fig. 2.28 - Array tapering. The power emitted by the antennas of a PAA can be tuned depending on the antenna position. On the left, a standard uniform rectangular array is depicted with all elements having the same weight, i.e. they all transmit the same power. On the right, the element powers are tapered, i.e. the elements in the middle of the array transmit/receive more power than those on the edges.

There are many types of array tapering based on different power distribution. In the previous section, a simple "uniform" tapering has been used. The most common non-uniform tapering are Gaussian, binomial, and Dolph-Chebyshev.

In the following subsection, more details are provided for Dolph-Chebyshev array tapering as it enables simple tuning of the trade-off between beamwidth and side lobe level. It is also the tapering used in this thesis to optimize the array factor.

Dolph-Chebyshev Tapering

Dolph-Chebyshev array tapering is commonly used as it provides an easy way of tuning the trade-off between the 3 dB beamwidth and side lobe level. As discussed in section 2.2.2, only one of these two characteristics can be optimized in a PAA. The 3 dB beamwidth of a ULA has been given as

$$\Theta_{3dB} = 0.88 \frac{\lambda_{RF}}{D_A} \cdot \frac{180}{\pi}$$

with λ_{RF}, the radio frequency wavelength and D_A the size of the array. D_A is given by $D_A = N \cdot d$ with N the number of antennas and d the antenna spacing. The 3 dB beamwidth Θ_{3dB} of a ULA is fixed and cannot be tuned. This is different for Dolph-Chebyshev array tapering as the **3 dB beamwidth for Dolph-Chebyshev array tapering,** is given by [63]

$$\Theta_{DC\_3dB} = 0.18 \frac{\lambda_{RF}}{L} \sqrt{A_{SL} + 4.52} \cdot \frac{180}{\pi} \tag{2.71}$$

with A_{SL} the desired side lobe attenuation. As already mentioned, the advantage of Dolph-Chebyshev array tapering is that the trade-off between the 3 dB beamwidth Θ_{DC_3dB} and the sidelobe level A_{SL} can be adapted. If one wants a lower sidelobe level A_{SL}, the beam width will increase. The system designer will therefore be able to choose the ideal working point.

Another advantage of Dolph-Chebyshev tapering is that the side lobes have all the same level, defined by A_{SL}, see Fig. 2.29. The lower the sidelobe level, the broader the beamwidth.

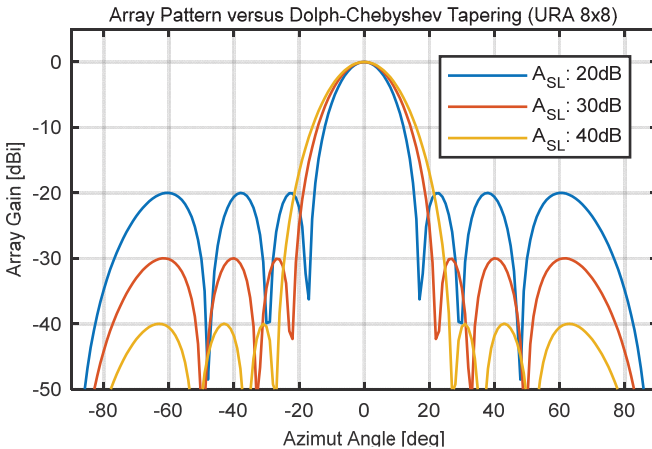In Fig. 2.30, the relation between beamwidth and sidelobe level is depicted for various array sizes.

Fig. 2.29 - Array factor for Dolph-Chebyshev array tapering. With Dolph-Chebyshev tapering, the sidelobe level can be adapted easily in order to optimize the PAA for a specific application.
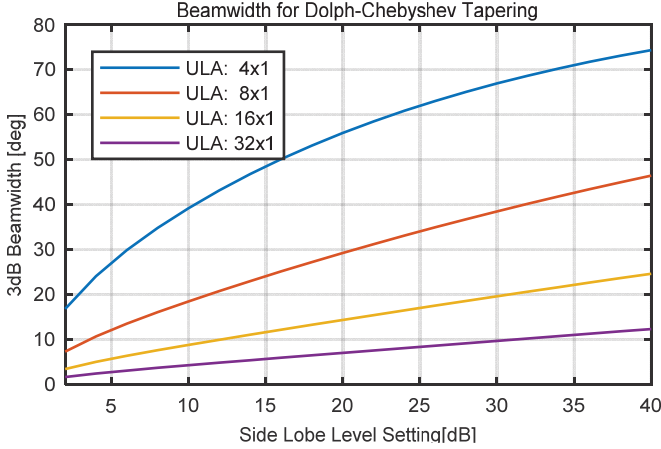
Fig. 2.30 - Beamwidth for Dolph-Chebyshev array tapering.

Beamwidth at Sidelobe Level

In multi-beam scenarios as used in this thesis, the definition of the beamwidth at a 3 dB level is not ideal. Indeed, it is better to consider the beamwidth at the sidelobe level as it directly provides an interference free spacing information between multiple users.

The beamwidth at the sidelobe level for Dolph-Chebyshev array tapering can be found by extending the theory provided in [65]. The **beamwidth at the sidelobe level** is given as

$$\Theta_{\text{DC\_SL}}(N) = 90 - \text{acos}\left(\text{acos}\left(\frac{1}{z_0(N, A_{\text{SL}})}\right) \cdot \frac{\lambda_{\text{RF}}}{\pi \cdot d}\right) \cdot \frac{180}{\pi} \tag{2.72}$$

with A_{SL} the desired side lobe attenuation. The "tapering function" z_0 is given by [65]

$$z_0(N, A_{\text{SL}}) = \cosh\left(\frac{2}{N-1} \text{acosh}(A_{\text{SL}})\right) \tag{2.73}$$

with N the number of antenna which in this case corresponds to the order of the Dolph-Chebyshev polynomial.

Optimization of Array Factor for multi-Beam Scenario

The beamwidth at side lobe level, is useful in multi-beam scenarios as it directly corresponds to the minimum angular spacing between users. Indeed, if one wants an exemplary interference free level below 30 dB between two users, a side lobe attenuation of $A_{\mathrm{SL}} = 30\ dB$ will be needed with a minimum user spacing of $\Theta_{\mathrm{DC\_SL}}/2$. This is however only true for two actives beams. In the case of more than two beams, interferences will originate from all the beams. In such a case, the desired interference free level, e.g. 30 dB, should corresponds to the sum of all possible interferences. If 5 beams are active, interferences could originate from the others 4 beams. This results in a needed side lobe attenuation A_{SL} per beam of 36 dB.

Two cases occur when optimizing the side lobe attenuation for multi-beams scenarios

1. Low side lobe attenuation $(A_{\mathrm{SL}} < 40\ \mathrm{dB})$. This means that the interferences sum is low and therefore barely noticeable, i.e. see discussion above. However, this also means that the beamwidth is large. In the received constellation, this look like "inter-symbol-interferences" as signals from the direct neighbors will be received in parallel. This ultimately limits the minimum users spacing.

2. High side lobe attenuation $(A_{\mathrm{SL}} > 20\ \mathrm{dB})$. In this case the interferences sum from all beams is very high. On the received constellation, this is similar to a higher noise level. This effect ultimately limits the signal-to-noise ratio.

Depending on the number of users and sector size, the ideal value for A_{SL} will change.

2.3 Microwave Photonics for Phased Array Antennas

Microwave photonics (MWP) can be applied to phased array antennas (PAA) in order to enable broadband feeders at millimeter waves. Electronic based feeders are usually limited in fractional bandwidth and in size. Performing the phase shifting or delaying or the signals using MWP thus provides two key advantages: 1) more bandwidth can be used, and 2) the feeder size is strongly reduced enabling multiple feeder on single chip [45].

Several MWP PAA architectures have been proposed lately. Such devices could be based on spatial light modulators (SLM) [91-95], ring-resonators [96-101], switched delays [102, 103], semiconductor optical amplifier (SOA) [104, 105], gratings [82, 83, 100, 106-110], dispersive fibers [111-116] and tunable phase shifters [117].

Yet, they all share the same fundamental principles - the signals are processed (phased shifted or delayed) using photonics and converted to mmWave signals using photodiode. In the receiving case, the incoming mmWave signals are first converted into the optical domain using modulator of directly modulated laser and further processed optically.

As phased array antennas based on microwave photonics are at the core of this cumulative thesis, state-of the art, theory, and principle of operation are therefore detailed in the various publications included in this work. More precisely

- An overview of the key principles of MWP based PAA is provided in the comparison paper of section 3.2 while section 3.1 described a new type of true-time delay called CPSS.

- In chapter 4, the low settling time of MWP PAA is used to perform ultra-fast beam steering, this enables a new multiplexing scheme called time-to-space multiplexing.

- In sections 5.1 and 5.2, two demonstrations of ultra-fast beam steering show practically the advantages of MWP based PAA.

In this section, a short theoretical background is provided on the following topics to complete the information provided in the publications

- In section 2.3.1, the power budget of a MWP communication system (see chapter 6 for a practical implementation) is discussed.

- In section 2.3.2, a typical MWP based PAA architecture is depicted and briefly discussed.

- In section 2.3.3, the power budget of a MWP systems is extended for phased array applications.

2.3.1 Power Budget of a MWP Link

As derived in section 2.2.1, the link budget of a radio communication link is computed using the Friis transmission equation, given in Eq. (2.48) as

$$P_{\text{Rx}} = P_{\text{Tx}} + G_{A_{\text{Tx}}} + G_{A_{\text{Rx}}} - FSPL - L_{\text{link}}$$

with P_{Tx} and P_{Rx} (dBm) the transmitted and received power, respectively, $G_{A_{\text{Tx}}}$ and $G_{A_{\text{Rx}}}$ (dBi) the gains of the Tx and Rx antennas, L_{link} the atmospheric losses (dB), and $FSPL$ the free space path losses (dB) given in Eq. (2.49) as

$$FSPL = 20 \cdot \log_{10}\left(\frac{4\pi \cdot r}{\lambda_{\text{RF}}}\right)$$

with r the link distance and λ_{RF} the mmWave carrier wavelength.
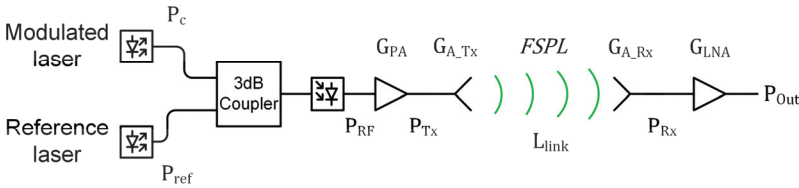

Fig. 2.31 - Power budget of a MWP wireless link. The power budget of a MWP wireless link is computed with the Friis transmission equation. In this thesis, only the transmitter is based on MWP and generate a RF power P_{RF} after the photodiode.

In this thesis, only the transmitter side is based on microwave photonics. Such a typical setup is depicted in Fig. 2.31. Two lasers, one encoded with data and one without, are combined. The optical power of the data carrying laser is P_c while the reference laser has an optical power of P_{ref}. After a 3 dB coupler, the RF signal is generated by optical heterodyning.

The generated RF power P_{RF}, as derived in section 2.1.1, is given by Eq. (2.24) as

$$P_{\text{RF}} = \frac{R_{PD} \cdot \mathfrak{R}^2 \cdot \bar{c}^2}{4} \cdot P_{\text{c}} \cdot P_{\text{ref}}$$

with R_{PD} the output impedance of the PD, $\mathfrak{R}$ its responsivity, $\bar{c}$ the average constellation power (0.5 for OOK, 1 for QPSK, …), and P_c and P_{ref} the optical powers of the carrier and reference laser in [mW], respectively.

The generated RF power can be converted in dBm using

$$
\begin{aligned}
P_{\text{RF}}[\text{dBm}] &= 10 \cdot \log_{10}\left(\frac{R_{PD} \cdot \mathfrak{R}^2 \cdot \bar{c}^2}{4} \cdot \frac{0.001}{1} \frac{P_{\text{c}}}{0.001} \cdot \frac{P_{\text{ref}}}{0.001}\right) \\
&= 10 \cdot \log_{10}\left(\frac{R_{PD} \cdot \mathfrak{R}^2 \cdot \bar{c}^2}{4} \cdot \frac{0.001}{1}\right) + P_{\text{c}}[\text{dBm}] + P_{\text{ref}}[\text{dBm}]
\end{aligned}
\tag{2.74}
$$

The first term of the equation (in the $\log_{10}$), can be grouped under a conversion efficiency factor ε_{RF}. Thus, the **RF power generated in MWP link** is

$$P_{RF}[dBm] = \varepsilon_{RF} + P_c[dBm] + P_{ref}[dBm] \qquad (2.75)$$

The "conversion efficiency factor" ε_{RF} depends on various parameters. While the photodiode responsivity will change in every setup, typical values can be used for the other variables. Using $R_{PD} = 50\Omega$, $\Re = 0.56A/W$, and $\bar{c} = 1$, conversion efficiency factors for various responsivity are provided in Table 2.3.

Table 2.3 - Conversion efficiency factor when generating signal using MWP.

$\Re$ [A/W]	0.2	0.3	0.4	0.5	0.6	0.7	0.8	0.9
ε_{RF} [dB]	-33.0	-29.5	-27.0	-25.1	-23.5	-22.1	-21.0	-19.9

Before transmission in the Tx antenna, a RF power amplifier (PA) with a gain G_{PA} is typically used to boost the RF output power up to the regulation limits (usually around 10 dBm). After transmission, a low-noise amplifier (LNA) with gain G_{LNA} is often used.

Using the above equations, the **received power through the link** is given as

$$P_{Out} = G_{LNA} + G_{A_{Tx}} - FSPL - L_{link} + G_{A_{Rx}} + G_{PA} + \varepsilon_{RF} + P_c + P_{ref} \quad (2.76)$$

with P_c and P_{ref} the optical powers of the carrier and reference laser in [dBm].

The FSPL and the atmospheric losses L_{link} depend on the transmission distance and the frequency. Typical values (without rain) are provided for a 60 GHz carrier frequency in Table 2.4.

Table 2.4 - Losses for a 60 GHz Link.

d [m]	10	20	50	100	200
$Losses$ [dB]	88	94	103	110	117

As a typical example, let's consider: a photodiode with maximum rating 13 dBm, thus ideally $P_c = P_{ref} = 10\,dBm$, a photodiode with 0.5 A/W responsivity ($\varepsilon_{RF} = -25\,dB$), a PA with $G_{PA} = 20\,dB$ gain, a transmission distance of 50 m (losses 103 dB), two antennas with $G_{A_{Rx}} = G_{A_{Tx}} = 25\,dB$ gain, and a LNA with a gain of $G_{LNA} = 30\,dB$. In such a case, the output power would be

$$P_{Out} = -8\ dBm$$

which would be enough to be detected by a storage oscilloscope.

2.3.2   Photonics based array feeder

A microwave photonic based phased array system would typically look like the one depicted in Fig. 2.32. A first laser is encoded with data while a second, not encoded, laser is set to have a frequency shift corresponding to the desired RF frequency, as explained is the section on optical heterodyning (2.1.1). But instead of sending both lasers directly into a photodiode as explained in section 2.1.1, both lasers are first power split in order to generated as many copies as there are antennas in the PAA. Each element of the array would then comprise the following components: first a phase shifter that is applied on the reference laser, a coupler to combine the data signal with the phase shifted copy of the reference laser, a photodiode to generate the signal and finally an antenna to transmit the generated RF signal.
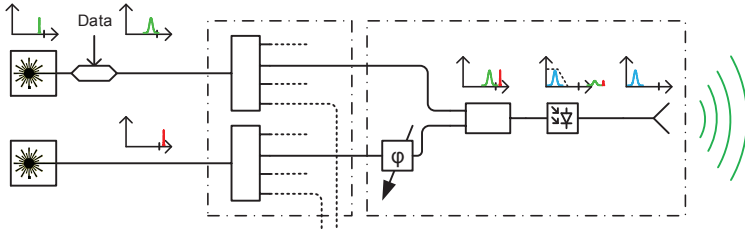

Fig. 2.32 - Microwave photonic based array feeder.

The current I_{RF} generated by heterodyning after each photodiode is given by Eq. (2.23) as

$$I_{\mathrm{RF}} = \frac{\Re}{2} \cdot c(t) \cdot \sqrt{P_{\mathrm{c}}}\sqrt{P_{\mathrm{ref}}} \cdot \cos\big((\omega_{\mathrm{c}} - \omega_{\mathrm{ref}})t - \varphi_{\mathrm{ref}}\big)$$

with $\Re$ the responsivity of the photodiode, D the data signal, P_{c} and P_{ref} the optical powers of the carrier and reference laser, respectively, ω_{c} and ω_{ref} the optical frequencies of the carrier and reference laser, respectively, and φ_{ref} the phase difference between both lasers. In the case of Fig. 2.32, the phase difference φ_{ref} between the lasers can be adjusted by the phase shifter. In order to steer the beam in the desired direction, the required phase shift in front of each antenna can be computed according to Eq. (2.67), derived in the section on array factor as

$$\varphi_i = -\frac{2\pi \cdot f_{RF}}{c}(\hat{\boldsymbol{r}} \cdot \boldsymbol{r}_i)$$

with f_{RF} the carrier frequency, c the speed of light, $\boldsymbol{r}_i$ the position of the antenna, and $\hat{\boldsymbol{r}}$ the desired pointing vector given by Eq. (2.70)

$$\hat{\boldsymbol{r}} = \sin\theta\cos\phi \cdot \hat{x} + \sin\theta\sin\phi \cdot \hat{y} + \cos\theta \cdot \hat{z}.$$

In reality, a MWP PAA would be more complicated to avoid the propagation of phase noise. Different schemes have been proposed but the fundamental principle remains the same.

2.3.3   Power Budget of a MWP Array Feeder

One of the key challenge in a MWP based phased array feeder is that 3 dB optical losses are converted in 6 dB less RF power during optical heterodyning. As a feeder usually split a given input signal power wise, the generated output power will therefore quickly diminish.

This is better explained by looking at Fig. 2.33. During the derivation on optical heterodyning in section 2.1.1, a setup such as in Fig. 2.33(a) was used. In such as case, the RF power after the PD was given by Eq. (2.24) as

$$P_{RF} = \frac{R_{PD} \cdot \mathfrak{R}^2 \cdot \bar{c}^2}{4} \cdot P_c \cdot P_{ref}$$

with R_{PD} the output impedance of the PD, $\mathfrak{R}$ its responsivity, $\bar{c}$ the average constellation power (0.5 for OOK, 1 for QPSK, ...), and P_c and P_{ref} the optical powers of the carrier and reference laser, respectively.
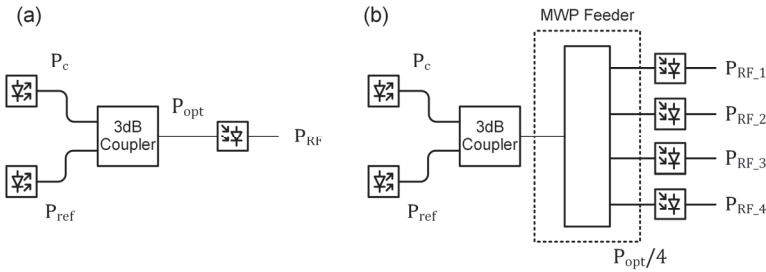

Fig. 2.33 - Power budget of a MWP PAA feeder.

In the case of the PAA feeder, as depicted in Fig. 2.33(b), the optical power in front of the photodiode is reduced by a factor inversely proportional to the number of antennas. If a feeder is built with 4 antennas, the power entering each photodiode is reduced by a factor 1/4. This factor 1/4 has to be applied on both the power of carrier reference laser. In a feeder for a PAA with N antenna element, the RF power generated by each photodiode P_{RF_i} is thus

$$P_{RF\_i} = \frac{R_{PD} \cdot \mathfrak{R}^2 \cdot \bar{c}^2}{4} \cdot \frac{P_c}{N} \cdot \frac{P_{ref}}{N} = \frac{R_{PD} \cdot \mathfrak{R}^2 \cdot \bar{c}^2}{4 \cdot N^2} \cdot P_c \cdot P_{ref}.$$

Thus, the RF power generated in each element is a factor $1/N^2$ smaller that is a case without array feeder. The **RF power transmitted by the array** P_{PAA} is the sum of the powers transmitted by all the elements, it corresponds to

$$P_{PAA} = N \cdot \frac{R_{PD} \cdot \mathfrak{R}^2 \cdot \bar{c}^2}{4 \cdot N^2} \cdot P_c \cdot P_{ref} = \frac{1}{N} \cdot P_{RF} \qquad (2.77)$$

The feeder power loss of $1/N$ will partially be compensated by the array gain. Yet, it should not be neglected as this effect does not occur in electronic based PAA

3 TRUE-TIME DELAY IMPLEMENTATION - THEORY AND CONCEPTS

Along the path to a successful demonstration of ultra-fast beam steering, multiple technological advancements in the field of microwave photonics were achieved and published. These demonstrated concepts not only supported the key achievement of this work, i.e. ultra-fast beam steering, but also brought the state-of-the-art in microwave photonics further.

This chapter is thus a collection of two publications that were published during this thesis. For each of the publications summarized below, novel concepts and new records have been set.

Section 3.1: Continuously Tunable True-time Delays with Ultra-low Settling Time

Section 3.2 presents the first publication of the author of this thesis. When starting in the field of microwave photonics (MWP), it was clear that 1) the large bandwidth of photonics offers large advantages if properly adapted to microwave systems. 2) that photonic processes are extremely fast, and 3) that novel concepts, not implementable with standard technologies, would be possible. In this first work, the focus had thus been set to tunable delay lines and thanks to the proposed technique called complementary phased shifted spectra (CPSS), we could demonstrate a delay line concept offering at the same time large bandwidth, ultra-fast settling times, and continuous tuning.

Section 3.2: Comparison of Steering Angle and Bandwidth for various Phased Array Antenna Concepts

Considering the key advantage of the proposed CPSS concept (section 3.2), its ultra-fast settling time, it quickly becomes clear that MWP could enable beam steering at speeds never reached before. Yet, before implementing this technology into a phased array feeder, a comparison technique for ultra-fast beam steering components has been developed. The comparison results, presented in section 3.2, show that while CPSS offer big advantages, a first system demonstration should better rely on a simpler yet limited phase shifter approach.

3.1 Continuously Tunable True-time Delays with Ultra-low Settling Time

Section 3.1 has been published in [RB1]:

Continuously tunable true-time delays with ultra-low settling time

R. Bonjour, *et al.*, *Opt. Express,* vol. 23, no. 5, pp. 6952-6964, 2015.

For consistency with the rest of this thesis, some variables have been adapted from the original publication.

Abstract: Ultra-fast, continuously tunable true-time delays are key components in many microwave and optical communications subsystems. In this paper, we introduce and demonstrate a new implementation method of a continuously tunable true-time delay featuring a settling time in the order of tens of picoseconds. Our solution relies on the splitting and combining of complementary phased shifted spectra (CPSS). It works for large bandwidth signals, has a low complexity, offers moderate losses, and can be fully integrated.

3.1.1 Introduction

Ultra-fast, continuously tunable true-time delays (TTDs) are a missing building block in many subsystems such as phased array feeder networks [13, 102, 118, 119] in microwave photonics [120, 121]; for clock synchronization, or synchronization of time division multiplexing tributaries in optical communication systems [122]; as a tunable delay element in coherence tomography [123], or light detection and ranging (LIDAR) [124]. An ideal TTD should be continuously tunable, have a large operating bandwidth, and offer small settling times. In addition, TTDs should provide the largest possible transparency – i.e. they should operate across a large wavelength range, work with any modulation format and any protocol.

Today, many implementations of tunable TTDs exist for various applications. Such devices are often based on ring-resonators [96-99], spatial light modulators (SLM) [91-95], switched delays [102, 103], dispersive fibers [111-116], and fiber gratings [83, 106-108]. All these schemes have different features: Ring-resonator based time delays, for instance, offer continuous tunability and low footprint [96-99]. They rely on the group delay appearing at resonant frequencies but are tuned using slow thermal effects and still have large losses. Spatial light modulators (SLM) can mimic true-time delays by generating an arbitrary filter shape [91-95]. However, the application range is constrained by the limited speed. Other existing solutions are based on switches [102, 103, 125]. Yet, they only offer discrete time delay steps [126]. Highly dispersive fibers [111-116] or fiber-grating based structures [83, 106-108] can also provide tunable delays even for very large delays. However,

as the delay is adjusted by tuning the laser frequency, precisely tuned lasers are needed, which makes these schemes costly if it should be scaled for larger number of units [97]. So far, continuous, fast and transparent tuning has been demonstrated using constant phase shifts rather than implementing true-time delays [127]. Yet, schemes applying a constant phase shift on all spectral components only allow for either beam steering of narrow band signals or steering in a narrow angle in phased array antenna (PAA) [97]. Thus, there is a need for a scheme that offers large bandwidth, ultra-low settling times, transparent operation, and low loss simultaneously.

In this paper, we introduce and demonstrate an ultrafast, continuously tunable true-time delay with a simple configuration that operates across a large bandwidth. The settling time of our approach is only limited by the speed of standard optical phase-modulators and could thus be on the order of tens of picoseconds. Here, we show that true-time delays of up to a quarter-symbol duration can be implemented with little degradation of the signal quality.

The paper is organized as follow. In a first section, we clarify the main differences between phase shifters and true-time delays, we introduce the concept and the theory of complementary phase shifted spectra (CPSS) – our new approach to mimic the behavior of true-time delays. Finally, we use simulations and experimental demonstrations to support the claims.

3.1.2 Phase Shifters and true-Time Delays

In various applications, true-time delays (TTD) are approximated by phase shifters (PS). Such phase shifter (PS) schemes have for instance been used to implement phased array feeders [63]. To explain the new concept more clearly, we first work out the main differences between a TTD approximated by a PS scheme and an ideal TTD. We also discuss the resulting errors in the frequency response of a phase-shifter scheme with respect to a TTD.

The effect of a PS on a signal is to add a phase offset φ in the frequency domain. The resulting output signal a_φ then is

$$a_\varphi(t) = \int_{-\infty}^{\infty} \widehat{A_o}(f) \cdot e^{j\varphi} \cdot e^{j2\pi ft} df \tag{3.1}$$

where $\widehat{A_o}$ is the complex spectrum of an incoming signal $a_o(t)$, t is the time and f is the frequency. The frequency response H_φ of the phase shifter in Eq. (3.1) is

$$\mathrm{H}_\varphi(f) = e^{j\varphi} \tag{3.2}$$

This can also be rewritten as a magnitude $\mathrm{M}(f)$ and phase response $\varphi(f)$,

$$\mathrm{M}(f) = 1 \quad \text{and} \quad \varphi(f) = \varphi = \text{const} \tag{3.3}$$

The important aspect is that the phase shift is constant in the frequency domain such that each frequency component experiences the same phase shift φ, i.e. there is no frequency dependence in Eq. (3.2).

In contrast, when applying a true-time delay Δt, the output signal $a_{TTD}(t)$ is

$$a_{\mathrm{TTD}}(t) = a_0(t - \Delta t), \tag{3.4}$$

which can be expressed using a Fourier transform as

$$\mathcal{F}[a_0(t - \Delta t)] = \widehat{A_o}(f) \cdot e^{-j2\pi\Delta t \cdot f}, \tag{3.5}$$

The frequency response of the TTD can be identified in Eq. (3.5) and is

$$\mathrm{H}_{\mathrm{TTD}}(f) = e^{j2\pi\Delta t \cdot f}, \tag{3.6}$$

or

$$\mathrm{M}(f) = 1 \quad \text{and} \quad \varphi(f) = -2\pi\Delta t \cdot f, \tag{3.7}$$

An ideal TTD thus has a unitary magnitude response $\mathrm{M}(f)$. In the phase response $\varphi(f)$, the TTD introduces a linear slope, directly related to the delay time Δt.

An ideal true-time delay unit together with its frequency response is plotted in Fig. 3.1. In all our illustrative plots, we display input and output signals in a time domain representation, in a frequency domain representation (with the magnitude and phase spectrum), and in a phasor representation. For the sake of simplicity, we have chosen signals with a rectangular shaped spectrum and thus sinc shaped time signals. The initial relative phases are zero for all spectral components of the input signal. In Fig. 3.1, the sinc shaped input signal is fed into the ideal TTD of Eq. (3.6). After passing the unit, the signal is delayed in time with respect to the input, see the insets of the output in Fig. 3.1. The magnitude spectrum of the output signal is unchanged whereas its phase spectrum has picked up a linearly increasing phase shift. The phasor representation of the output also displays the effect of a TTD on three different spectral components f_1, f_2, and f_3. It shows how they are offset by an equispaced phase after the TTD.

When a TTD is approximated by a PS, a phase response error occurs. We now estimate the error by comparing the phase response of a PS from Eq. (3.2) with the phase response of a TTD given in Eq. (3.6). We compare the error for a signal operating at a carrier frequency f_{RF} where all spectral components are phase shifted by φ_{off} with a PS to a signal delayed by a TTD by $\Delta t = -\varphi_{\text{off}}/2\pi f_{\text{RF}}$. The values have been chosen such that the carrier frequency f_{RF} experiences the same delay in both cases. The phase error $\varepsilon(f)$ versus frequency then is

$$\varepsilon(f) = \arg[\text{H}_\varphi(f)] - \arg[\text{H}_{\text{TTD}}(f)] = \varphi_{\text{off}} + 2\pi\Delta t \cdot f \tag{3.8}$$

Replacing the delay Δt by $\varphi_{\text{off}}/2\pi f_c$ leads to

$$\varepsilon(f) = \varphi_{\text{off}} + 2\pi \frac{-\varphi_{off}}{2\pi f_c} \cdot f = \varphi_{\text{off}} \cdot \left(1 - \frac{f}{f_{\text{RF}}}\right) \tag{3.9}$$

The total phase error that a signal with a bandwidth B will experience can be computed by comparing the error for the lowest frequency $f_{\text{min}} = f_{\text{RF}} - B/2$ and the highest frequency $f_{\text{max}} = f_{\text{RF}} + B/2$

$$\varepsilon_{\text{tot}} = |\varepsilon(f_{\text{max}}) - \varepsilon(f_{\text{min}})| = |\varphi_{\text{off}}| \cdot \frac{f_{\text{max}} - f_{\text{min}}}{f_c} = |\varphi_{off}| \cdot f_{\text{B}} \tag{3.10}$$

where f_{B} is the fractional bandwidth, i.e. the ratio between the signal bandwidth $B = f_{\text{max}}$-f_{min} and the carrier frequency f_{RF}.

It can be seen that for a low fractional bandwidth signal ($f_{\text{B}} \ll 1$), the phase error remains small. Therefore, the maximum error is negligible and consequently the approximation may be considered correct. This is the case in optical communication as the laser frequencies are orders of magnitude higher than the signal bandwidths. But for radio-over-fiber applications with large fractional bandwidths, this assumption is no longer valid. Any device aiming to mimic the effect of a TTD in application with large fractional bandwidth should thus have a frequency response as close as possible to the ideal true-time delay given by Eq. (3.6), Fig. 3.1.
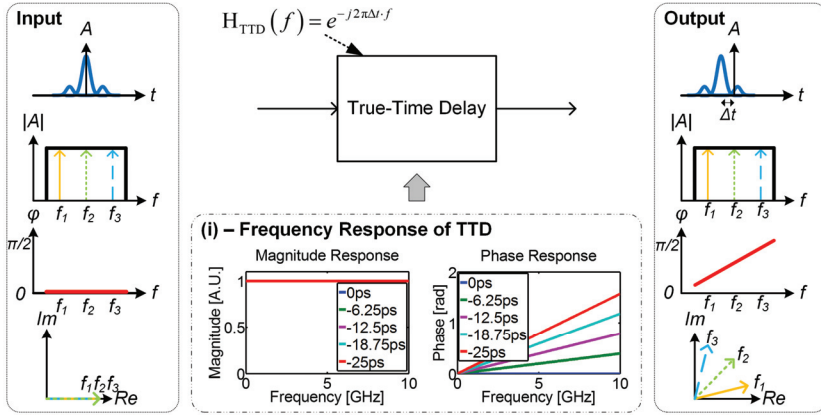
Fig. 3.1 - Effect of an ideal TTD onto a signal. The input signal, depicted in the time domain, in the frequency domain (with its magnitude and phase spectrum), and with a phasor representation, is delayed by a TTD and generates an output signal (also shown by its time, frequency and phasor representation on the right-hand side). The distinct features of the TTD are the flat magnitude response and the perfect linear phase response according to Eq. (3.6) and (3.7). Both of which are shown at the bottom. Assuming a signal bandwidth of $B = 10\ GHz$, the delay applied in this example corresponds to $\Delta t = -\Delta\varphi/(2\pi B) = -\pi/(4\pi 10^9) = -25ps$. A set of simulated frequency responses of a TTD are plotted in the inset (i) for delay varying between 0 ps and -50 ps.

3.1.3 Complementary Phase Shifted Spectra for true-Time Delays

In our proposed scheme, we mimic the characteristics of TTD by a new method that we call complementary phase shifted spectra (CPSS). In this scheme depicted in Fig. 3.2, the input signal is first split by means of a filter into two complementary spectra. After adding a relative phase offset on one arm, the two spectra are recombined. We will show that the frequency response obtained by this technique is a good approximation to a TTD while the tuning speed is fast and only limited by the speed of the built-in phase modulator.

The true-time delay adapted in the CPSS method comprises of three stages: First, complementary spectra are generated by a filter. In our example shown in Fig. 3.2, we use filters with triangular spectral shapes. The amplitude spectra of the lower and upper arms are shown as insets (i) and (ii) in Fig. 3.2, respectively. In the second stage, the signal on the lower arm is guided through a phase modulator and picks up a phase offset that we will call the CPSS phase. In the phasor representation, such a phase shift corresponds to a rotation of all the phasors by e.g. $\pi/2$. Finally, the two spectral parts are recombined in a coupler. The resulting phase for the individual spectral components can now be determined by adding the phasors from the two arms in the complex plane. The output signal after combining the fields in the coupler is plotted in time, in frequency (magnitude and phase spectrum), and in a phasor representation. The phase spectrum inherits its frequency dependence from the frequency dependent splitting ratio between the two spectra. By comparing this result with the output of an ideal time delay, Fig. 3.1, it is clear that the proposed method is a good approximation to an ideal TTD. If another CPSS phase offset is applied in the phase-modulator section of the CPSS module, the phasors in Fig. 3.2(ii) will have a different angle. Therefore, the addition of (i) and (ii) in the complex plane will lead to another delay, i.e. there will be a lower phase difference between f_1 and f_3.

In Fig. 3.2(iii), a set of simulated magnitude and phase response of the CPSS delay module are plotted for the triangular shaped filters of Fig. 3.2 for different CPSS phases. Fig. 3.2 also shows some frequency dependence in the magnitude response. Such non-ideal response functions can be mitigated by using more optimized filters for the generation of the two complementary spectra or by using multiple instances of CPSS.

An advantage of the suggested scheme is that the tuning speed may be in the GHz because it is only limited by the frequency response of the modulator. Another advantage of this scheme is that any time delay in the working range of the module ($\pm \pi/2$) can be generated, since the phase offset can be controlled continuously using the phase modulator. If no phase shift is applied on the second signal, the device will not delay the signal while a negative phase shift will lead to a delay in the opposite direction.

To avoid destructive interferences, the CPSS phase should preferably not be tuned above $\pm \pi/2$. Consequently, the maximum delay that can be generated by the CPSS method is $\Delta t_{\max} = \pm 1/4B$, as explained below.
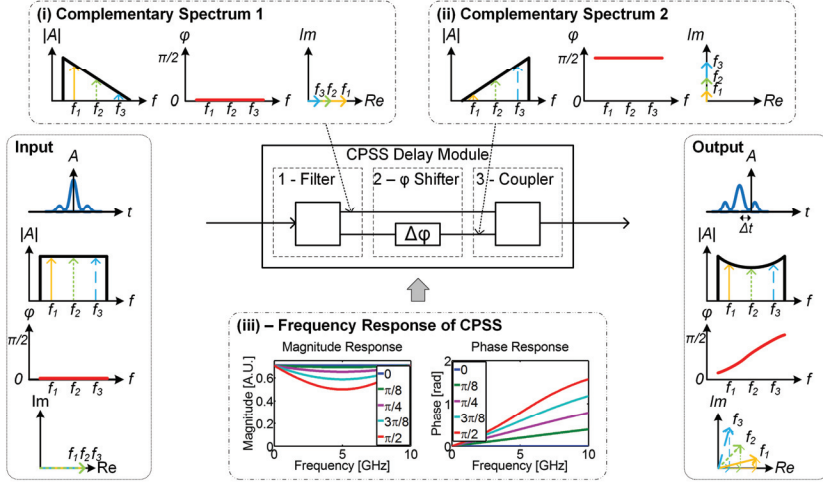
Fig. 3.2 - New true-time delay (TTD) scheme by means of a complementary phased shifted spectra (CPSS). In this method an input signal (shown in the time, frequency and phasor representation on the left) is first guided into a first filter stage that creates the two complementary signals shown in subfigures (i) and (ii). While one of the signal is unchanged (i), the second one (ii) is phase shifted by a phase modulator. By combining (i) and (ii) in the coupler using complex addition, each frequency components interferes. This results in a new output signal shown in the time, frequency and phasor representation on the right-hand side. By comparing this output signal with the output signal of an ideal TTD, Fig. 3.1, one can see that the CPSS based delay module provides a good approximation of a true-time delay. The frequency dependent phase shifts obtained with this method is indeed almost linear in frequency. The inset (iii) shows the magnitude and phase responses of this configuration for different CPSS phases.

Frequency response of CPSS

In this section, the frequency response H_{CPSS} of the CPSS module described above is derived by applying a transfer matrix for each of the three stages in the CPSS filter

$$H_{CPSS} = T_{Coupler} \cdot T_\varphi \cdot T_{Filter} \tag{3.11}$$

The first element T_{Filter} can be described by a set of two filters with a linear magnitude response (triangular shaped spectrum). The filter response functions $H_1(f)$ and $H_2(f)$ generating the complementary spectra are defined by

$$H_1(f) = 1 - \frac{f - f_{RF} + B/2}{B} \quad and \quad H_2(f) = \frac{f - f_{RF} + B/2}{B} \tag{3.12}$$

where B is the bandwidth of the incoming signal, f_{RF} the carrier frequency, and f the frequency (f takes any values between $f_{RF} - B/2$ and $f_{RF} + B/2$ leading to outputs between 0 and 1).

Using the functions from Eq. (3.12) to describe the filter response T_{Filter}, Eq. (3.2) to describe the phase-shifter section T_φ together with ideal values for a standard 50:50 coupler $T_{Coupler}$ we find

$$
\begin{aligned}
H_{CPSS}(f, \varphi) &= \begin{bmatrix} \dfrac{1}{\sqrt{2}} & \dfrac{1}{\sqrt{2}} \end{bmatrix} \cdot \begin{bmatrix} 1 & 0 \\ 0 & e^{-j\varphi} \end{bmatrix} \cdot \begin{bmatrix} 1 - \dfrac{f - f_{RF} + B/2}{B} \\ \dfrac{f - f_{RF} + B/2}{B} \end{bmatrix} \\
&= \frac{1}{\sqrt{2}} \cdot \left(1 - \frac{f - f_{RF} + B/2}{B} \right) + \frac{1}{\sqrt{2}} \cdot e^{-j\varphi} \cdot \left(1 - \frac{f - f_{RF} + B/2}{B} \right)
\end{aligned}
\tag{3.13}
$$

The magnitude and phase responses of this module are plotted in Fig. 3.2(iii). This somewhat simplistic CPSS filter provides a very good match to the ideal filter response of a TTD. Deviations from the TTD response can only be seen in a drop of the magnitude in the center and some small modulation in the phase response. While not perfect, the phase response has a strong linear component which results in a true-time delay in the spirit of Fig. 3.1. The slope of the phase response can be controlled by setting the CPSS phase in the phase-shifter. The larger the slope, the larger the true-time delay.

3.1.4   Implementation using Delay Interferometer

So far, the proposed solution for an implementation of a TTD was explained with linear amplitude filters. However, such filters are difficult to produce. Yet, many filters can be used that generate complementary spectra and therefore might be suitable for an implementation of TTD by means of the CPSS method. For instance, a delay interferometer (DI) is a simple and reasonable implementation of such a filter. A DI is a standard component that can be implemented in many ways. E.g. as a free space solution element (e.g. [128]), as an integrated photonic chip (e.g. [129]) or by optical fibers (e.g. [130]) depending on the specific purpose of the application. A DI has two outputs with a sine frequency response on one of them and a cosine frequency response on the second one [128]. By adjusting the frequency response of the DI to its 50:50 operation point, two complementary spectra are generated. A CPSS implementation with a DI (CPSS-DI) is depicted in Fig. 3.3. The signals at the two outputs of the DI are plotted as insets (i) and (ii). Their amplitude responses are complementary. A phase offset is then applied to one of the output signals of the DI (ii) before the signals are recombined in the last stage. Simulated frequency responses of this implementation are plotted as insets (iii) of Fig. 3.3 for different CPSS phases.
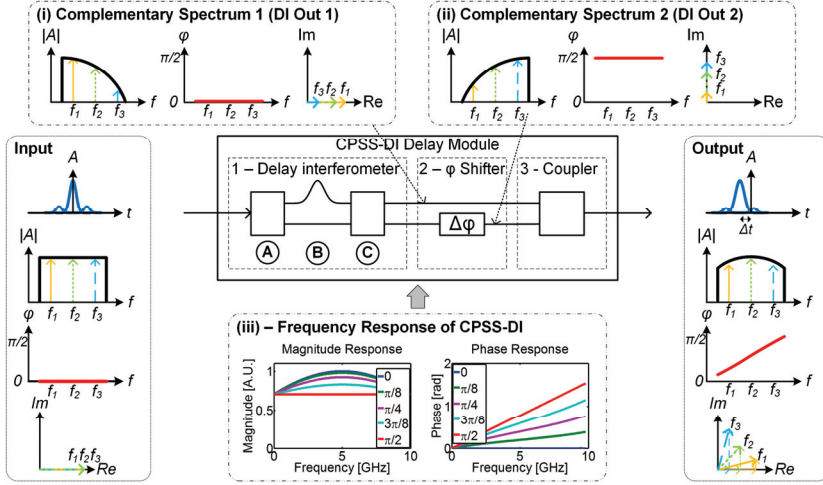
Fig. 3.3 - Implementation of a TTD by a CPSS module based on a delay interferometer (DI). A signal is split into two complementary spectra (i) and (ii) by a DI. The DI is tuned to its 50:50 operation point. A phase-offset is then added to one of the DI outputs by means of a phase modulator. The two signals in the arms are then recombined in a coupler. The inset (iii) shows the magnitude and phase responses of this configuration for different CPSS phases. Using a DI as input filter, the phase response is close to be perfectly linear as needed for a time delay line.

Frequency Response of CPSS-DI

The frequency response of the CPSS-DI module can be computed by replacing the filter response T_{Filter} in Eq. (3.11) by the matrix transfer function of the delay interferometer i.e. by replacing T_{Filter} by a sequence of an input splitter T_A, a delay line T_B and a 2x2 output coupler T_C

$$H_{CPSS-DI} = T_{Coupler} \cdot T_\varphi \cdot T_{Filter} = T_{Coupler} \cdot T_\varphi \cdot T_C \cdot T_B \cdot T_A$$

$$= \begin{bmatrix} \frac{1}{\sqrt{2}} & \frac{1}{\sqrt{2}} \end{bmatrix} \cdot \begin{bmatrix} 1 & 0 \\ 0 & e^{-j\varphi} \end{bmatrix} \cdot \begin{bmatrix} \frac{-j}{\sqrt{2}} & \frac{1}{\sqrt{2}} \\ \frac{1}{\sqrt{2}} & \frac{-j}{\sqrt{2}} \end{bmatrix} \cdot \begin{bmatrix} 1 & 0 \\ 0 & e^{-j2\pi B - j\pi/2} \end{bmatrix} \cdot \begin{bmatrix} \frac{1}{\sqrt{2}} \\ \frac{1}{\sqrt{2}} \end{bmatrix} \quad (3.14)$$

In Eq. (3.14), a phase shift of $-\pi/2$ is added to the delay line T_B in order to align the frequency response of the DI to its 50:50 operation point. After replacing the fixed delay Δt by the free spectral range (FSR), $FSR = 1/\Delta t$ we obtain for Eq. (3.14),

$$H_{CPSS-DI}(f) = \frac{1}{2\sqrt{2}} \cdot \left(-j + e^{\frac{-j2\pi f}{FSR} - \frac{j\pi}{2}} \right) + \frac{e^{j\varphi}}{2\sqrt{2}} \cdot \left(1 - j \cdot e^{\frac{-j2\pi f}{FSR} - \frac{j\pi}{2}} \right) \quad (3.15)$$

The frequency response of a CPSS based on a delay interferometer, Eq. (3.15), is plotted in Fig. 3.3(iii) for different CPSS phase shifts. It can be seen that the

phase response is close to perfectly linear and corresponds to an ideal true-time delay. On the other hand, the magnitude response is not perfect. This leads to two unwanted effects: First the average power may change by up to 1.5 dB when tuning the delay, acting as a small intensity modulation. However, the intensity modulation of 1.5 dB is lower than what is offered by comparable approaches based on ring resonator filters [131] which have already proven their effectiveness. Second, the magnitude response is not flat for all the delays. The outer frequency components may be attenuated by up to 3 dB compared to the center frequency. It should however be noticed that the delayed signal is undistorted, whereas the undelayed signal is slightly bandpass filtered. If such small distortions should be an issue, active compensation by an intensity modulator could be used to mitigate these effects.

Simulation

To confirm the working principle of the CPSS-DI implementation, simulations were performed with VPI Transmission Maker ©. An optimal FSR of 20 GHz, corresponding to twice the bandwidth of a 10 Gb/s signal, was used along with a 20 GHz Gaussian band pass filter (2nd order). Fig. 3.4 depicts the resulting eye diagrams for the maximum and minimum CPSS phase shift on the phase modulator ($\pm \pi/2$) - covering therefore the whole delay range. The simulation shows how a symbol can be delayed across a 25 % of its symbol duration with good signal quality.
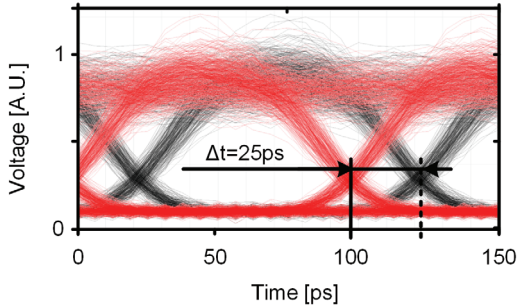
Fig. 3.4 - Simulation of a true-time delay of 25 ps induced by changing the phase between $\pm \pi/2$ in the CPSS filter module. The simulations have been performed for an OOK at 10 Gb/s with a SNR of 11 dB. The pulse is delayed by one quarter of the symbol duration when detuning the phase from the minimum (-$\pi/2$) to the maximum phase shift ($\pi/2$). The simulation has been performed with VPI Transmission Maker ©.

3.1.5   Experimental Setup

In order to perform a quick and simple demonstration of the CPSS method, we have built a fiber-based setup [127, 132, 133]. An on-off-keying (OOK) signal is first generated in a 10G transmitter using a PRBS sequence generator and a Mach-Zehnder optical modulator. The input signal then enters the first

stage of the CPSS module which is implemented by a polarization maintaining fiber (PMF) based delay interferometer. In such a DI, the linearly polarized input is split with a polarization controller (A) onto the fast and slow axis of the PMF (B). At the output of the PMF, a second polarization controller (C) is used to combine the fast and slow signals that are delayed with respect to each other. The alignment of the two output signals is then arranged such that one of the signals is aligned to the main axis of the subsequent LiNbO$_3$ phase modulator. As the second axis of the modulator is also slightly active, the applied voltage has to be larger than the specifications in order to produce the desired CPSS phase offset between the complementary signals. The signals then enter the third stage of the CPSS unit i.e. the coupler which is realized with a polarizer aligned at 45 ° between the phase modulator axes. Thus, the output signal detected in a receiver is a combination of the two complementary phase shifted spectra. As a polarizer aligned at 45° filters out half of the power on both polarization, 3 dB losses are added to the system. These additional losses are however not intrinsic to the CPSS method and could be removed in another implementation.

The FSR of the DI generating the complementary spectra is a critical parameter as it defines the maximum delay that a CPSS setup can produce, see section below. In our experimental setup, the length l_{PMF} of the PMF defines the FSR of the delay interferometer and is computed using

$$FSR = \frac{c}{l_{PMF} \cdot \Delta n} \tag{3.16}$$

where c is the speed of light and Δn the refractive index difference between the polarizations. With $\Delta n = \lambda/l_B$ [134] where l_B is the beat length (3.5 mm for SM.15-P-8/125-UV/UV-400) and λ the wavelength (1550 nm). The PMF should thus be 33.9 m long to match the signal bandwidth of 10 GHz (*FSR*=20 GHz).
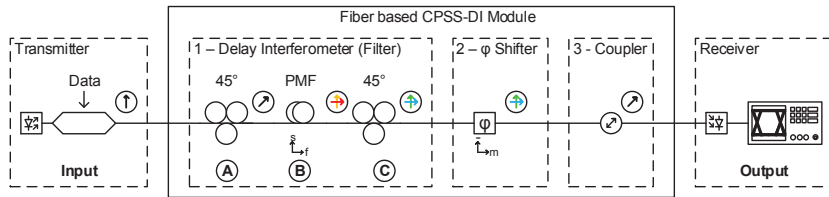

Fig. 3.5 - Fiber based TTD implemented by a CPSS-DI module relying on polarization diversity for implementing a delay interferometer. In the transmitter, an optical signal is encoded with a 10 Gb/s OOK. The signal is then launched into a polarization maintaining fiber based delay interferometer i.e. the filter creating the complementary phase-shifted spectra. In the interferometer, the input signal is first split into two polarizations (A). Then, one polarization is delayed with respect to the other by the birefringence of the fiber (B). Finally, the slow and fast signals are recombined (C) to produce the two complementary outputs in different polarizations. The two complementary signals are then fed into a LiNbO3 phase modulator that induces a certain phase offset onto the signal in the active axis only. Finally, the signals are recombined in the third stage and fed into a receiver for characterization

Results

Using the fiber based implementation described in the previous section, measurements were performed in order to demonstrate the TTD concept. Due to the availability of a fiber with 40 m rather than 33.9 m only, we performed the experiment with a FSR of about 17 GHz rather than 20 GHz. This means that the resulting delay range will be slightly higher (29.5 ps) than the expected 25 % of the symbol duration (25 ps @ 10 Gb/s) but also that the signal quality will decrease for the largest CPSS phases.

Fig. 3.6 shows the received eye diagrams (a) to (c) of a 10 Gb/s on-off keying signal for CPSS phases of -π/2, 0 and +π/2, respectively. A total delay range of 31.9 ps is found when varying the phase shift between ± π/2, corresponding to the expected value of 29.5 ps.
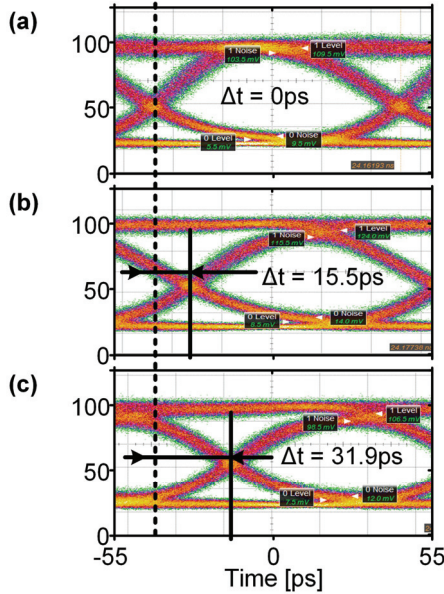
Fig. 3.6 - Experimental results showing a TTD of up to 31.9 ps only detuned by shifting the phase in the CPSS-DI module. (a-c) Eye diagrams of a 10 GB/s OOK signal with CPSS phases of -π/2, 0, and π/2, respectively.

Fast tunability is demonstrated in Fig. 3.7 by switching between two CPSS phase shifts (± π/4) every 33 μs. The switching time is limited by the 30 MHz function generator that was used to drive the phase modulator (Keysight 33520B). The resulting delay range of 18.3 ps is slightly larger than the expected 14.8 ps (half of the 29.5 ps calculated above). This is mainly due to the impedance mismatch between the phase modulator at 30 MHz and the output impedance of the function generator. As the two eye diagrams can be

distinguished, it can be concluded that the proposed method not only allows to delay signals but that the settling time is only limited by the phase modulator and its driving electronics.
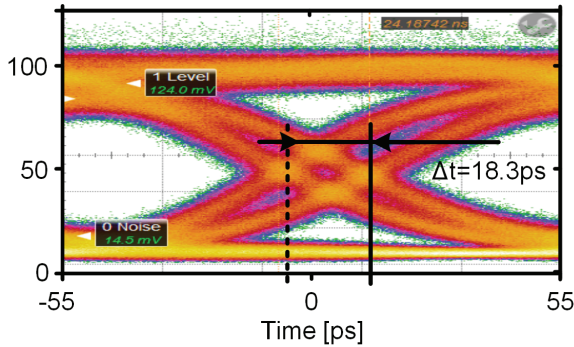

Fig. 3.7 - Demonstration of fast true-time delay tunability by means of a CPSS-DI fiber based delay line. The CPSS phase is switched at a rate of 30 MHz between ± π/4. The resulting delay range is 18.3 ps for this configuration (FSR=17 GHz).

Comparisons between measured and simulated signal qualities are shown in Fig. 3.8 for the different resulting delays. Experiments and simulations shows some similar trends but are not perfectly fitted. The mismatch is due to the limited stability of the fiber DI which was detuning the system over time. We are currently implementing a CPSS delay line with active adjustment of the DI. This should then fully mitigate the detuning issue and therefore shows better performances.
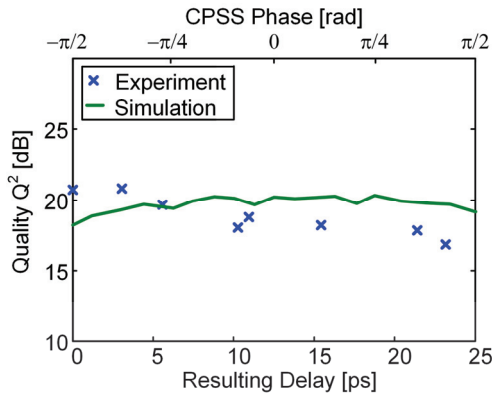
Fig. 3.8 - Comparison of signal quality for various true-time delays for both simulations and experiments. The simulations predict that the signal quality will be maintained throughout the true-time delay tuning range. The experimental results are slightly worse. In our setup we mainly attribute this to the instability of the fiber based DI arrangement.

3.1.6 Discussions

The proposed solution results in a frequency response that is close to an ideal true-time delay. For this reason, the scheme can handle any modulation format. A constraint of the proposed method is that the maximum delay time is limited. Indeed, for any specific spectral bandwidth B, the phase difference cannot exceed ±π/2. This follows from the phasor representation in Fig. 3.2. If the phase of a signal in one arm over the phase in the other arm should become larger then ±π/2, destructive interferences occur. The maximum delay range can thus be computed using Eq. (3.6)

$$\varphi(f) = -2\pi\Delta t \cdot f \rightarrow \Delta t = \frac{-\Delta\varphi}{2\pi\Delta f} \tag{3.17}$$

where Δf is the operation range of the CPSS module. The useable frequency range is about half the FSR of the DI. Ideally, the signals bandwidth $B \leq \Delta f$. In the CPSS scheme the maximum phase difference should not be larger than $\Delta\varphi \cong \pi \, (\pm \pi/2)$ and for a signal with a maximum bandwidth of $B = \Delta f$ that can carry at best symbols of length $T_S = 1/2B$ one can deduce a maximum true-time operation range of

$$\Delta t_{\max} = \frac{\pi}{2\pi B} = \frac{1}{2B} = \frac{1}{4}T_S \tag{3.18}$$

Thus, the effective tunable delay is in the order of 25 % of the symbol duration. Better pulse shaping such as Nyquist could increase this range by up to 50 % ($T_S = 1/B$). This is a sufficiently large delay for most applications. In fact, in most systems where an ultra-fast tunable delay unit is needed, the requested delay range is related to the carrier frequency and not to the signal bandwidth. Moreover, if a larger delay is required, many systems could be cascaded (after optimization of the filter shapes).

The discussions were made so far with baseband signals. For the case of a pass band signal as in a phased array antenna or other microwave photonics applications, two implementations are possible. First, the free spectral range of the DI can be adapted to cover the full radio-over-fiber bandwidth (the RF carrier and the data). This is an easy to implement approach. However, it will result in quite limited delay range, as can be seen by Eq. (3.18). Second, a more advanced implementation would phase offset the reference laser by means of a second phase modulator while the CPSS approach is only applied to the laser carrying data. This technique called Separate Carrier Tuning (SCT) [135] is compatible with CPSS and thus can extend the working range of the method.

3.1.7   Conclusion

We have introduced a true time delay module based on complementary phase shifted spectra (CPSS). We have shown ultra-fast tunability with settling times only limited by the underlying optical phase modulator technology. To the best of our knowledge, our experimental demonstration is already three orders of magnitude faster over other methods that offer large bandwidth and continuous tunability. The CPSS method should enable settling times in the order of tens of picosecond, i.e. another three order of magnitude improvement over what has been shown in this work. Another advantage of our method is that it can be directly integrated on a photonic chip and thus may allow for an integration of more complex systems. The suggested method may serve new applications in a wide range of fields from beam steering for next generation mobile communication networks to all optical clock recovery and could bring new opportunities for both network provider and users.

3.2 Comparison of Steering Angle and Bandwidth for various Phased Array Antenna Concepts

Abstract: In this paper we compare different integratable ultra-fast tunable true-time delay concepts with respect to their performances in a phased array system. The performances of the schemes are assessed with respect to the supported range, i.e. the range within which beam steering for a given fractional bandwidth can be achieved with a gain flatness better than 3 dB. We also compare the array gain as of function of steering angle and fractional bandwidth.

3.2.1 Introduction

Increasing the carrier frequency of wireless communication systems towards millimeter waves is a viable path to cope with the growing demand of bandwidth [13, 121, 136]. However, this comes at the price of larger free space path losses [21] which in return might limit the system reach. This drawback can be compensated by implementing highly directive beam steering systems based on phased array antennas (PAAs) [120]. Directive beams not only offer a larger reach but also provide more flexibility and reduced crosstalk.

Unfortunately, millimeter wave PAAs based on electronic technologies are difficult to build due to the large fractional bandwidth requested. Yet, promising solutions are based on microwave photonics (MWP), i.e. solutions in which the signal processing is made with photonic technologies instead of electronics. Many MWP architectures have been proposed. Such devices could be based on ring-resonators [96-99], spatial light modulators (SLM) [91-95], switched delays [102, 103], dispersive fibers [111-116], gratings [82, 83, 106-109], semiconductor optical amplifier (SOA) [104, 105] and tunable phase shifters [137]. All these schemes have different features optimized for specific applications, but none provides at the same time a large bandwidth, low settling times, continuous tunability, and integratability on silicon platforms. As a matter of fact, it is difficult to provide a fair comparison between phased array antenna systems due to a lack of a common metric to assess the systems.

In this paper, we compare various integratable broadband phased array concepts based on complementary phased shifted spectra [138, 139] with the performances of both an ideal true-time delay system and a phase-shifter

based solution. We assess the quality of the array concepts using two parameters from our MATLAB simulations: the supported range, within which the gain flatness is better than 3 dB, and the array gain as a function of the fractional bandwidth and steering angle.

3.2.2   Fundamentals of Phased Array Antenna

A PAA is a set of coordinated antenna elements arranged in space to produce favorable radiation characteristics. For common linear and planar geometries, the array radiation pattern is defined by the number of elements, their periodicity and their relative phases [63]. If the phase of each individual antenna can be tuned electronically or mechanically, the direction of the beam can be controlled arbitrarily, i.e. beam steering is achieved.

In practice a source signal is equally split and fed into N tunable time delay elements, Fig. 3.9. The requested delay to steer the power by an angle of θ with respect to the horizontal axis is directly related to the antenna element spacing d. From Fig. 3.9, one can see that for a steering angle of θ, a path offset x is required for two adjacent antennas. At the speed of light c, this path offset corresponds to a time delay $\Delta t = -x/c = -\sin\theta \cdot d/c$, and ultimately translates into a frequency dependent phase shift

$$\varphi(f) = -2\pi\Delta t \cdot f \tag{3.19}$$

The ideal true time delay transfer function of a single antenna i with an appropriate delay Δt_i is thus $H_{\mathrm{TTD}}(f, \Delta t_i) = \exp(-j2\pi\Delta t_i \cdot f)$ [63, 138]; an ideal phased array feeder network is build up of such delay elements. If the phase response of the delay lines does not fulfill Eq. (3.19), an effect called beam squint results, where different frequencies are steered in different directions.
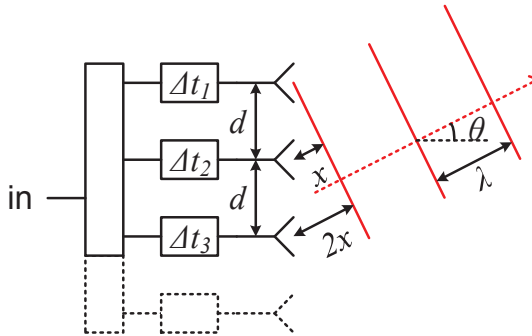

Fig. 3.9 - Principle of a phased array antenna (PAA). The input signal (in) is split into N array elements using a power splitter. In front of each antenna a time delay is introduced in order to steer the direction of the beam.

One of the main parameters of a PAA is the array pattern. As depicted in
Fig. 3.10, the array pattern (right) is found by multiplying the individual
antenna pattern (left) with the array factor (middle), defined as the resulting
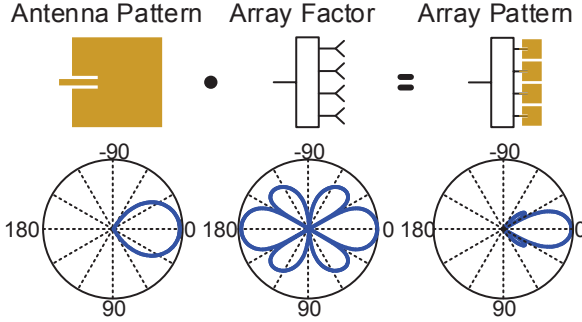interference pattern from ideal isotropic radiation elements.

*Fig. 3.10 - Antenna and array pattern. The radiation pattern of a PAA (right) is a combination of
the single antenna pattern (left), here a cosine antenna and the array factor (middle), here a 4x1
uniform linear array (ULA).*

Subsequently, we only include the array factor in our discussion as the
emphasis is on the performances of feeder networks build with tunable delay
elements. To compute the array factor, different formalisms can be used. This
work is based on the definition by Mailloux [63], reusing the same
nomenclature and coordinates. The array factor is therein computed using

$$F(\theta,\phi) = \sum_i a_i \cdot e^{-jk(\hat{r}\cdot\vec{r}_i)}$$

(3.20)

with a_i the complex coefficient of element i located at $\vec{r}_i$, k the
wavenumber, and $\hat{r}$ the direction vector defined by the elevation angle θ
and the azimuth angle ϕ. The array factor can be extended to support
multiple frequencies by replacing the complex coefficient a_i with the
frequency response of the delay elements so that one then can write

$$F_H(\theta,\phi,f) = \sum_i H_i(f,\Delta t_i) \cdot e^{-jk(\hat{r}\cdot\vec{r}_i)}.$$

(3.21)

with the delay value Δt_i defined by the requested steering direction and by
the element position $\vec{r}_i$. Note that the frequency response $H_i(f,\Delta t_i)$
depends also — as a result of some optimizations of the delay line — on the
carrier frequency f_{RF} and the signal bandwidth B. For simplicity this has been
omitted in the notation.

3.2.3 Comparison Method

In this chapter, we describe the method by which we assess the performance of the various PAA feeder networks. The method is set up to provide with a single plot information on the steering range, the available fractional bandwidth, the intrinsic losses, and the unwanted power modulation. As we only focus on the feeder network, effects from the antenna, the integration losses, the coupling losses, and the photodiode or modulator are excluded.

Our comparison method includes the following steps:

1) Calculation of the scattering parameter S21 between the array and the receiver as a function of the steering angle and fractional bandwidth for any of the true-time concepts introduced below. For this we calculate the delay Δt that is needed to steer the beam in the direction θ from the PAA at the point P1 to P2, see Fig. 3.11(a). Using Eq. (3.21) one then calculates the transmission for each set of θ and fractional bandwidth $f_B = B/f_{\mathrm{RF}}$. The scattering parameter S_{21} in [dB] is then computed using

$$S_{21_{f_B}}(\theta, f) = 20 \cdot \log_{10}\left[\mathrm{abs}\left(F_{\mathrm{H}}(\theta, 0, f)\right)\right] \tag{3.22}$$

For the sake of simplicity, we only vary the elevation angle and do not perform any azimuthal steering and thus set the azimuthal angle ϕ to 0°.
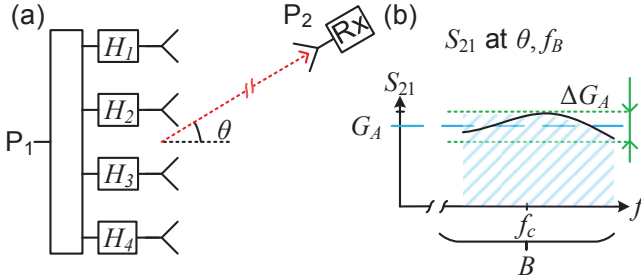
Fig. 3.11 - Feeder comparison method. (a) Phased array antenna with a set of delay element represented by their frequency response H_i. The scattering parameter S_{21} represents the transmission from P_1 to P_2 and is computed as a function of the fractional bandwidth f_B and a steering angle θ. (b) Visualization of array gain G_A and gain flatness ΔG_A definition. They are derived from the S_{21} transmission at each f_B and θ. The real shape of S_{21} will strongly depends on the feeder network, the representation in (b) is exemplary.

2) The gain flatness ΔG_A and the array gain G_A for a particular steering angle and fractional bandwidth f_B are derived from the scattering parameter $S_{21}(\theta, f)$, see Fig. 3.11(b). The gain flatness ΔG_A is defined as the variation of the gain within the bandwidth B

$$\Delta G_{A_{f_B}}(\theta) = \max_{f \in B} S_{21_{f_B}}(\theta, f) - \min_{f \in B} S_{21_{f_B}}(\theta, f) \tag{3.23}$$

The array gain G_A corresponds to the average gain within the signal bandwidth B around the carrier frequency f_c

$$G_{A_{f_B}}(\theta) = \frac{1}{B} \cdot \int_{f_c-B/2}^{f_c+B/2} S_{21_{f_B}}(\theta, f) df \qquad (3.24)$$

Exemplarily we have plotted in Fig. 3.12 the gain flatness ΔG_A and array gain G_A of a PAA with a particular implementation of a true-time delay as outlined in section 3.2.4. For the sake of compatibility with applications we are plotting the steering range $R = 2 \cdot \theta$ rather than the steering angle θ. In a perfect world with an ideal array feeder one would expect a perfectly flat gain flatness function with $\Delta G_A = 0$ dB (no distortion) and array gain G_A with the maximum ideal array gain independent of the steering range and fractional bandwidth. It can be seen that gain flatness degrades disproportionally when either the steering range or fractional bandwidth exceeds a certain value. The same can be seen on the array gain.
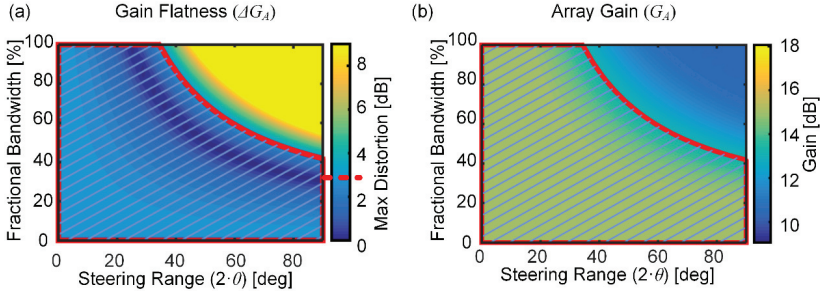
Fig. 3.12 - Gain flatness ΔG_A and array gain of a PAA based on the CPSS-SCT-I true-time delay concept, see section 3.2.4. (a) Gain flatness in dB plotted as a function of the fractional bandwidth and steering range. For any given set of f_B and θ, the plot provides information on the maximum distortion that a spectral component within the bandwidth of a signal may encounter. In the dashed area below the red curve, the gain flatness is better than 3 dB. Below we will call it the supported range. (b) Phased array gain shows anticipated gain for a signal with a specific fractional bandwidth within a steering window. To help identify the area with little distortions and a high gain we have directly copied the supported range from Eq. (3.25) into this plot.

3) The supported range (SR) is defined as the area within which the gain flatness is better than 3 dB. In our example in Fig. 3.12 this range is represented by the dashed area below the red curve. This range is defined by

$$SR = \left\{ (\theta, F_B) \mid \Delta G_{A_{f_B}}(\theta) \leq 3dB \right\} \qquad (3.25)$$

The area defined by SR should be as large as possible. In the results chapter further below, we only plot the array gain and the supported range as depicted in Fig. 3.12(b). The important information on the gain flatness can be derived from the shaded area within the plot.

In addition to the quality of the steering estimated by the supported range, specific solutions could provide additional advantages. Benefits such as low steering settling time, continuous tuning, or direct integration on a photonics integrated circuit (PIC) are not included in this discussion.

3.2.4   Different Implementations of Feeder Networks

In this chapter we introduce the frequency responses of various microwave photonic PAA delay elements: First, an ideal true-time delay (TTD) is introduced as a reference. Next a phase-shifter based concept and four variations of a delay interferometer element based concept are detailed. All of the delay interferometer based true-time delays rely on complementary phase shifted spectra (CPSS) as recently introduced in [138, 139]. In the different equations and drawings, the inputs should be considered as ideal lasers, one carrying data and one acting as a reference. The frequency difference between both lasers corresponds to the microwave carrier that will ultimately be generated in the photodiode and be fed to the antenna [13]. The baseband copies of the signals after the photodiode are filtered out by the antenna. The different frequency responses are plotted for a signal with carrier frequency f_c and bandwidth B. Also, we will give special attention to signals with a fractional bandwidth of 25% for which we mark the frequency range by a red dashed area. To simplify the comparison, the results are not summarized here but in the next chapter.

Ideal True-Time Delays

In the best case, each delay element of the feeder network is based on ideal true-time delay (TTD) lines. The basic scheme of an ideal TTD line is depicted in Fig. 3.13(a). The scheme shows how an optical signal (blue solid line) carrying the data together with a reference carrier (green solid line) in the optical domain are combined. The initial phase of both the data and reference signal are depicted as dashed red line in a retarded coordinate system. The two signals are then fed into a TTD which applies a delay Δt to any spectral component. The frequency response of an ideal true time delay is given by [63, 138]

$$\mathrm{H_{TTD}}(f, \Delta t) = \mathrm{e}^{-\mathrm{j}\,2\pi\Delta t\cdot f} = \mathrm{e}^{-\mathrm{j}\,\varphi(f)} \tag{3.26}$$

where f is the frequency and Δt the delay. From Eq. (3.26) one can see that applying a TTD onto a signal will have no effect on the amplitude but lead to a linear phase shift with frequency (the red dashed line has now a slope). Subsequently, the two signals are fed into a photodiode where the signal is down-converted to the RF domain and then fed to the antenna. The power and phase response of such an ideal TTD are depicted in Fig. 3.13(b). The important point to note here is the linear relation of the phase with the frequency. Any deviation from this ideal response will result in a distortion.
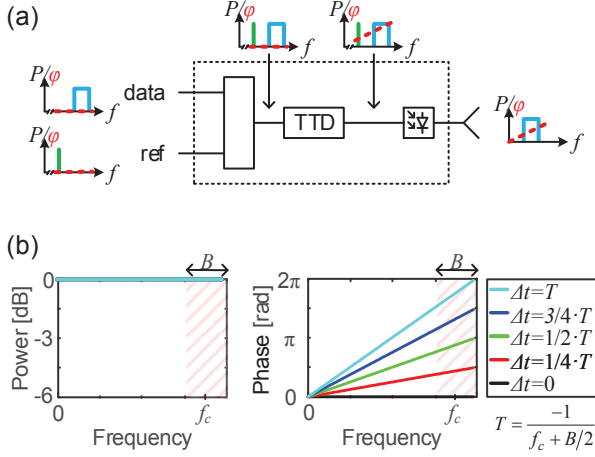
Fig. 3.13 - PAA feeder using ideal true-time delay (TTD). (a) An array element based on TTD consists of a combiner for both lasers, the ideal TDD and finally the photodiode and antenna. (b) The power (left) and phase (right) response are ideal in this case.

In microwave photonics such a TTD can be realized using tunable mechanical delay lines, spatial light modulator schemes [10-14], or a switched network [15, 16]. Such systems provide good steering quality but won't be fast and continuous at the same time. The question then is how such systems can be implemented? An answer may come from optical communications. The optical communications industry has created in the last few years quite a few ultra-fast tunable building blocks for the encoding of signals. These elements offer fast intensity and phase modulation up to highest speed. Finally, and most importantly, for schemes to be practical they should be compatible with photonic integrated circuits (PIC). We will now introduce some integratable concepts relying on fast tunable elements before we compare them in chapter 5 with respect to their performance.

TTDs Approximated by Phase Shifters

PAA feeder networks can be built using phase shifters instead of true-time delays [127]. Phase shifters apply the same phase on all the frequency components and are therefore not a perfect approximation to the ideal true-time delays [138]. Due to this approximation, the PAA will steer different frequencies in different directions, an effect called beam squint. The frequency response of a phase shifter can be derived from Eq. (3.26) by replacing f with the carrier frequency f_{RF} such that the frequency response simplifies to

$$H_\varphi(f, \Delta t) = e^{-j2\pi\Delta t \cdot f_{RF}} \tag{3.27}$$

As f_{RF} is a fixed variable, the output of Eq. (3.27) is frequency independent.

A scheme of an array element employing simple phase shifters is depicted in Fig. 3.14(a), with the phase shifter applied on the data laser only. The power response of the array element itself is always 0 dB. The phase response corresponds to constant phase offset that is applied to all frequencies equally. This is quite different from the ideal phase response (dashed lines) of a TTD and therefore results in a large phase error, Fig. 3.14(b). As a result, one will end up with a beam squint that decreases the array performance.
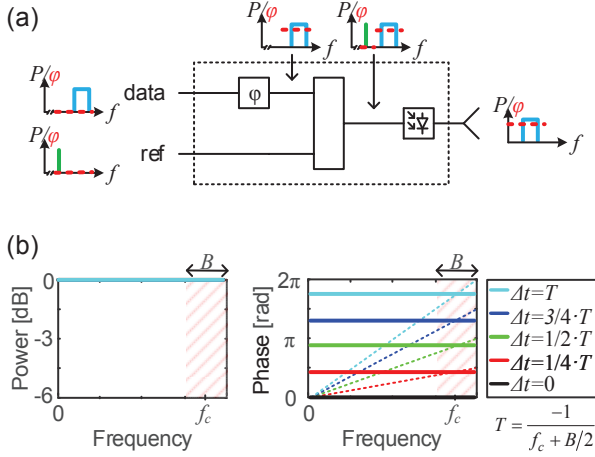
Fig. 3.14 - PAA feeder based on a TTD approximated by phase shifters. (a) Array element consisting of a phase modulator, a combiner and a photodiode that down-converts the optical signals into an RF signal before being fed to the antenna. (b) The TTD delay approximated by phase shifters features an ideal power frequency response (left) without any loss compared to its ideal counterpart. Yet the phase response (solid lines in right plot) shows quite some errors when compared to the ideal TTD (dashed lines). This will lead to a beam squint in the PAA.

TTDs Approximated by Complementary Phased Shifted Spectra (CPSS)

In this section, we use as an approximation to the TTD a delay interferometer in cascade with a phase-shifter. The concept was named complementary phased shifted spectra (CPSS) [138] – a name that best describes the operation principle of the scheme. The scheme is depicted in Fig. 3.15. The CPSS delay lines perform the TTD operation in three steps: First, complementary spectra are generated by a filter by means of a delay interferometer (DI). The amplitude spectra of the lower and upper arms are shown as insets of Fig. 3.15 in the dotted boxes (i) and (ii), respectively. In a second step, the signal on the lower arm is guided through a phase modulator and picks up a phase offset. In the complex representation, such a phase-shift corresponds to a rotation of all the phasors by e.g. $\pi/2$. Finally, the two spectral parts are recombined in a coupler. The resulting phase for the individual spectral components can now be determined by adding the phasors in the complex plane. This results in the time and phasor

representations of the combined field at the output. The phase response, see inset Fig. 3.15(iii), inherits its frequency dependence from the frequency dependent splitting ratio between the two spectra.
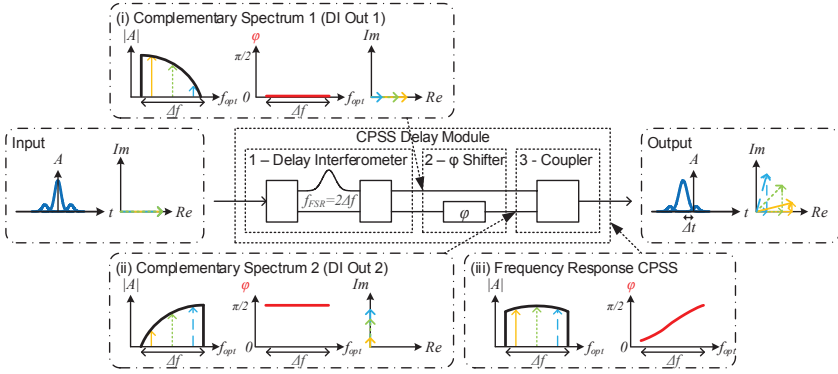

Fig. 3.15 - Principle using a complementary phase shifted spectra (CPSS) filter. The approximation of the time delay in CPSS is achieved using three steps: First, the signal is split in complementary spectrum (CS). Second, one CS is phase shifted. Third, both signals are recombined.

The frequency response of the DI used in the following sections is modified from [138] to represent the outputs of the upper and lower arms in the form of real-valued expressions

$$H_{DI}(f, f_{FSR}) = \begin{bmatrix} \cos\left(\dfrac{2\pi \cdot f}{f_{FSR}}\right) \\ \sin\left(\dfrac{2\pi \cdot f}{f_{FSR}}\right) \end{bmatrix} \tag{3.28}$$

where f_{FSR} is the free spectral range (FSR) of the interferometer. FSR is best chosen as twice the bandwidth of the signal on which the delay is applied. The frequency response of a whole CPSS delay line used in the array element is [138]

$$H_{CPSS}(f, \Delta t) = \begin{bmatrix} \dfrac{1}{\sqrt{2}} & \dfrac{1}{\sqrt{2}} \end{bmatrix} \cdot \begin{bmatrix} 1 & 0 \\ 0 & e^{-j2\pi\Delta t \cdot \Delta f} \end{bmatrix} \cdot H_{DI}(f, f_{FSR} = 2f_{RF} + B) \tag{3.29}$$

where the FSR of the DI is chosen to cover twice the full radio-over-fiber signal bandwidth, i.e. $f_{FSR} \cong 2\Delta f = 2f_{RF} + B$.

A simple array element based on the CPSS filter is shown in Fig. 3.16(a). It shares the same architecture as the true-time delay in Fig. 3.15(a). First, the two lasers are combined. Second, the delay is applied on both signals. Third, the RF or microwave signal is generated by photonic mixing and, finally, transmitted with an antenna.

The resulting power and phase responses are plotted in Fig. 3.16(b). Remarkably, the phase response is close to be ideal leading to an almost

squint-free operation. However, there are power fluctuations in the power response, which will degrade the signal quality. It is noteworthy though that the frequency response is ideally flat for the largest delay $T = \pm 1/(4f_{RF} + 2B)$ and only shows band-pass characteristics for small delays.
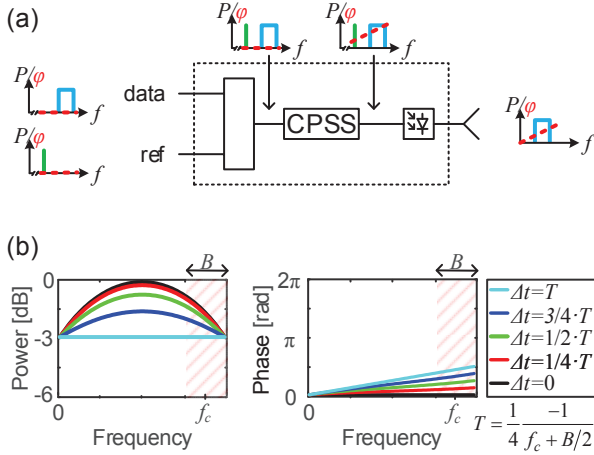

Fig. 3.16 - PAA feeder based on a TTD approximated by a CPSS filter. (a) The configuration of a TTD approximated by a CPSS filter is similar to scheme used for the TTD. First, both lasers are combined, then a delay is applied on the full radio-over-fiber bandwidth and finally the signal reaches the photodiode and antenna. (b) The power response (left) is neither flat nor without losses but the variations remain small. The CPPS scheme however provides close to ideal TTD phase responses with a linear dependence on the frequency.

TTDs Approximated by CPSS with Intensity Matching (CPSS-I)

The implementation of a simple CPSS array feeder as detailed in the previous section doesn't support an overly large set of fractional bandwidth and steering angles, as can be seen in the results chapter below. And while the phase response is close to be ideal, leading to an almost squint-free operation, there are power fluctuations in the power response that degrade the signal quality. Advanced implementations can improve the performances though. Two techniques can be used: First, the gain variation can be cancelled by an additional intensity modulator after the delay line, this is the technique detailed in this section. Second, the delay range and thus the steering angles can be extended by a technique called separate carrier tuning (SCT) [140, 141], see the following section.

The concept, here referred to 'intensity matching', uses an additional intensity modulator or a tunable attenuator on each array element to adjust the output power for each antenna. Thus, the gain variation can be cancelled by controlling the attenuation, at the cost of increasing the feeder loss. If needed, amplifiers can compensate this loss.

The concept of using CPSS-I in array elements is depicted in Fig. 3.17(a). Compared to Fig. 3.16(a), an intensity modulator is added after the CPSS delay line. The frequency response of a CPSS-I is found by normalizing Eq. (3.29). The normalization factor is given by

$$I_{\text{match}}(f, \Delta t) = \frac{B}{\sqrt{2} \int_{f_c - B/2}^{f_c + B/2} \left| H_{\text{CPSS}}(f, \Delta t, f_{\text{RF}}, B) \right| df} \tag{3.30}$$

where the factor $1/\sqrt{2}$ is inserted to normalize to a -3dB power loss. 3dB are the power losses of CPSS in the worst case. The frequency response of CPSS-I is therefore given by combining Eq. (3.29) and (3.30)

$$H_{\text{CPSS-I}}(f, \Delta t) = I_{\text{match}}(f, \Delta t) \cdot H_{\text{CPSS}}(f, \Delta t). \tag{3.31}$$

The resulting frequency response is plotted in Fig. 3.17(b). The phase is unchanged compared to the CPSS implementation, while the average power losses are always -3dB. The output power could thus be adjusted with an amplifier having constant gain.
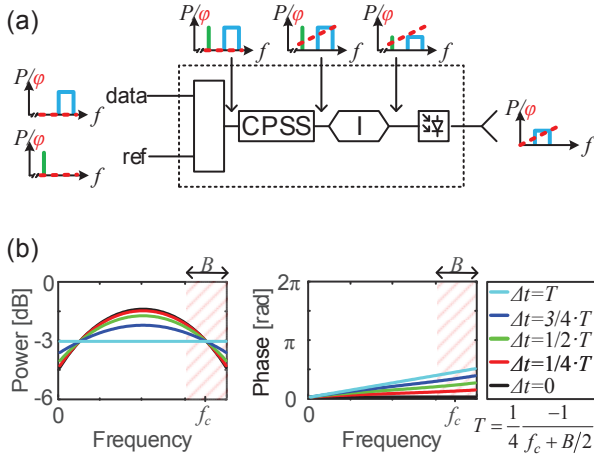
Fig. 3.17 - PAA feeder using CPSS-I. (a) An array element based on CPSS-I consist of the CPSS scheme from Fig. 3.16 and an additional intensity modulator. (b) The power response (left) is not flat but does now provide the same average power penalty of -3 dB for all delays. The phase response is close to ideal response of a TTD.

TTDs Approximated by CPSS with Separate Carrier Tuning (CPSS-SCT)

The second advanced concept improving the performances of the CPSS system is based on separate carrier tuning (SCT) [140, 141]. In CPSS, as in other interferometer based concepts, the achievable time delay is inversely proportional to the bandwidth on which the filter is applied [138], i.e. the smaller the bandwidth, the bigger the delay range. Using CPSS, the maximum achievable delay is given by $\Delta t_{max} = \pm 1/4\Delta f$, with Δf the passband within which the filter provides a reasonably good phase response. The delay interferometer must be chosen such that it can process the full signal bandwidth within this band. The total free-spectral range of a delay interferometer thus is $f_{FSR} \cong 2\Delta f$. Now, in order to increase the induced delay Δt_{max} one must reduce Δf. One can reduce the bandwidth Δf if the fractional bandwidth is small. Such a situation is found when the reference laser and the data signal are sufficiently far away so that they can be dealt with separately. More precisely, one may delay and adjust the phase of the reference laser with a phase shifter and adjust the delay of the data signal by the CPSS method. In the following, this technique is referred as CPSS-SCT.

The difference between CPSS and CPSS using SCT is illustrated in Fig. 3.18. For the simple implementation of a CPSS filter, the FSR of the DI is chosen to be twice the full radio-over-fiber bandwidth, that is to say $f_{FSR} \cong 2\Delta f = 2f_{RF} + B$, see Fig. 3.18(a). In the case of the CPSS-SCT scheme, the CPSS concept is only applied to the data signal and the FSR of the DI is chosen with $f_{FSR} \cong 2\Delta f = 2B$. I.e. the FSR can thus be chosen fairly small. In the CPSS-SCT the phase of the reference laser is then adjusted with a separate phase shifter, see Fig. 3.18(b). Since the slope of the filter passband is now quite large with respect to the radio-over fiber bandwidth the obtainable delay is increased accordingly, i.e. from $\Delta t_{max} = \pm 1/(4f_{RF} + 2B)$ to $\Delta t_{max} = \pm 1/4B$. In our example with a fractional bandwidth of 25%, the delay range would therefore be enhanced by a factor of 4.
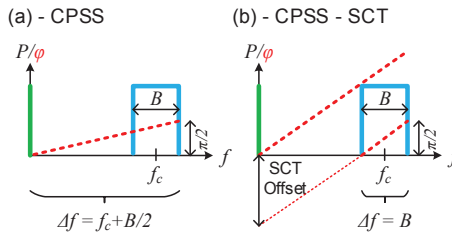

Fig. 3.18 - Separate carrier tuning applied to CPSS. (a) Phase response of a CPSS filter when the pass band of the DI is chosen such that both the RF-carrier and the data around f_c are within the FSR of the DI. In other words, for the simple CPSS case, the filter is applied on the full radio-over-fiber bandwidth providing a limited phase slope, i.e. delay. This is due to the limitation of the CPSS concept that cannot generate phase shifts larger than $\pi/2$. (b) Phase response of a CPSS-SCT filter scheme. The phase slope is increased by first applying the CPSS concept only on the data signal and second by adjusting the phase of the reference carrier by a phase shifter. This way larger slopes and thus larger total delays can be induced.

An array element using the CPSS-SCT scheme is plotted in Fig. 3.19(a). The CPSS delay is applied only on the data laser while an additional phase modulator is used to apply the SCT offset on the reference laser. Once both lasers are combined they are directly sent to the photodiode, generating the microwave signals. The frequency response of the CPSS-SCT scheme can be derived from Eq. (3.29) by replacing the FSR of the DI with $2B$ instead of $2f_{RF} + B$, by shifting the DI response, and by adding the SCT phase offset to the ref carrier

$$
H_{CPSS-SCT}(f, \Delta t) = e^{j2\pi\Delta t \cdot (f_{RF} - B/2)} \cdot \begin{bmatrix} \dfrac{1}{\sqrt{2}} & \dfrac{1}{\sqrt{2}} \end{bmatrix} \cdot \begin{bmatrix} 1 & 0 \\ 0 & e^{-j2\pi\Delta t \cdot B} \end{bmatrix}
$$
$$
\cdot H_{DI}\left(f - f_{RF} + B/2\,,\, 2B\right)
$$

(3.32)

The resulting frequency response is plotted in Fig. 3.19(b) for a filter optimized with a fractional bandwidth of 25%. The power response within the bandwidth of interest, i.e. the dashed area, is similar to the power response we have seen from the CPSS filter [138]. The phase response in the dashed area is close to ideal (dashed lines). The tunable delay range is increased by a factor four compare to the simple CPSS implementation.
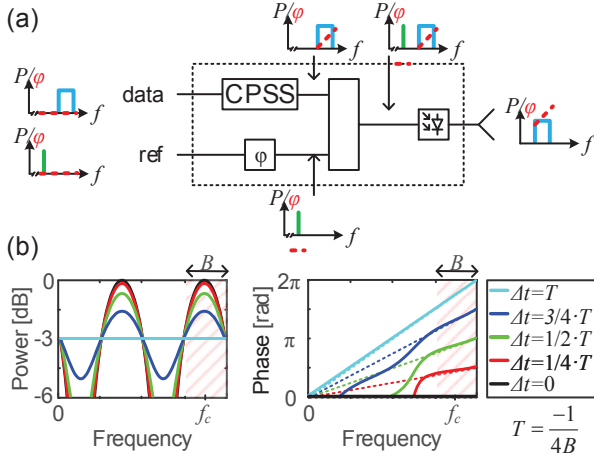
Fig. 3.19 - PAA feeder using CPSS-SCT. (a) An array element based on the CPSS-SCT scheme is built by applying the CPSS scheme on the laser carrying data and, in parallel, adjusting the phase of the reference laser by another phase shifter. Both lasers are then combined and enter the photodiode. (b) The power response (left) shows variation of about 1.5 dB in the bandwidth of interest while tuning the delay. The phase error (right) is close to the ideal case.

TTDs Approximated by CPSS with Intensity Matching and Separate Carrier Tuning (CPSS-SCT-I)

Both techniques, intensity matching and separate carrier tuning, can be combined to build a CPSS feeder network providing at the same time a low gain variation and a large supported steering range while still leveraging the ultra-fast tunability of CPSS. The array element depicted in Fig. 3.20(a) is a combination of the SCT concept of Fig. 3.19(a) and the intensity matching solution of Fig. 3.17(a). The frequency response is therefore a combination of Eq. (3.31) and a modified version of Eq. (3.30):

$$H_{\text{CPSS}-\text{SCT}-\text{I}}(f, \Delta t) = I_{\text{match}-\text{SCT}}(f, \Delta t) \cdot H_{\text{CPSS}-\text{SCT}}(f, \Delta t). \qquad (3.33)$$

The resulting power and phase responses are plotted in Fig. 3.20(b). The average power loss is now always -3dB, while the phase response in the bandwidth of interest remains excellent.
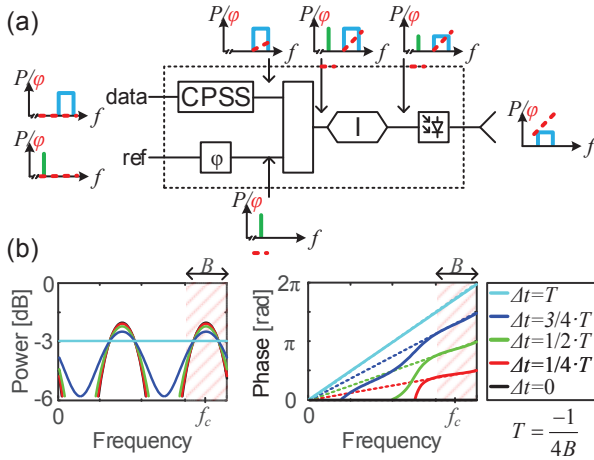
Fig. 3.20 - PAA feeder using CPSS-SCT-I. This array element is built by combining the CPSS-SCT scheme of Fig. 3.19(a) with an additional intensity modulator. (b) The power response (left) is not yet flat in but the average power is -3 dB across the whole spectrum. The phase response within the data-signal bandwidth is still close to the ideal.

3.2.5   Simulation Results and Discussions

In this section we compare the TTD concepts from section 3.2.4 following the procedure described in section 3.2.3. The comparison results are first computed for an 8x8 uniform rectangular array (URA). Fig. 3.21 shows the six plots of the array gains for the six true-time delay concepts discussed in the previous chapter. The important supported range has been added to the array gain plot as well. It is clearly marked by the red dashed curve.

The achievable gain by an ideal 8x8 TTD feeder is 18.1 dB corresponding to the dark blue color. For the ideal TTD feeder, the supported range covers the entire area without any limitations, see Fig. 3.21(a). The concept relying on phase shifters shows a surprisingly good performance. Indeed, the supported range extends over a large section of the plot and only suffers from limitations due to the beam squint for large angle or large fractional bandwidth, see Fig. 3.21(b). The supported ranges for the CPSS and CPSS-I, Fig. 3.21(c) and
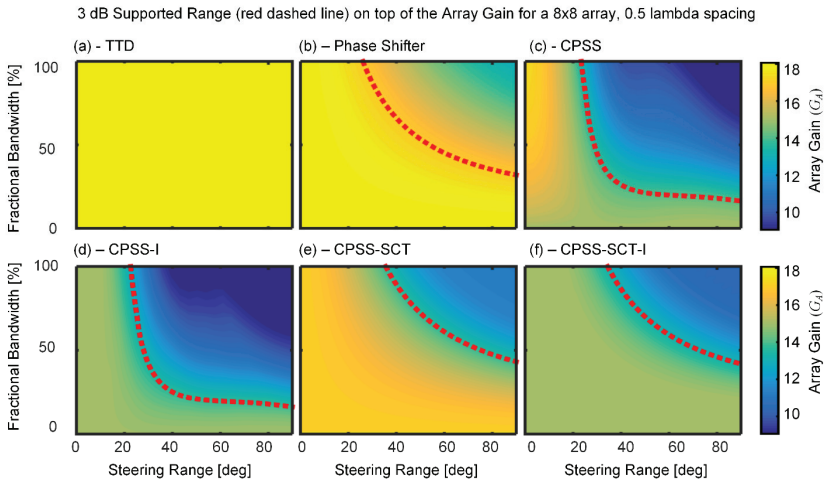
Fig. 3.21 - Comparison of the array gain for all the feeder types. Calculations were performed for a rectangular uniform array of 8x8 elements with an element spacing of $\lambda/2$. We only plot the array gain as the gain flatness is included in the calculation of the supported range, i.e. any point below the red dashed line (a) Ideal true-time delay (TTD). An ideal gain of 18.1 dB is found for all angles and all fractional bandwidths. (b) Phase shifter. The supported range doesn't cover the full area. A small gain variation is found though. (c) CPSS. The simple CPSS implementation doesn't provide a large supported range but offers squint-free operation due the ideal phase response of the delay lines, see Fig. 3.16. (d) CPSS-I. The resulting supported range is equivalent to (c), but the gain variations are largely reduced. (e) CPSS-SCT. The supported range is large, but the gain variations may limit the application range. (f) CPSS-SCT-I. In this advanced case, combining SCT and intensity matching, the results show the largest supported range. In addition, the gain variation is small. This large operation range comes however at the expense of a reduced gain.
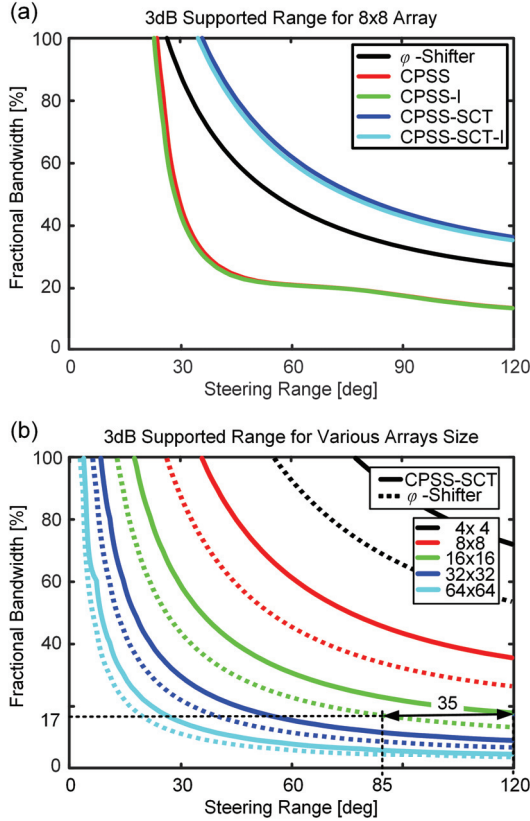
91

Fig. 3.22 - Comparison summary. (a) Comparison of the supported range for different feeder types in an 8x8 array. The results clearly show that CPSS-SCT outperforms all the other schemes. However, the simple implementation of CPSS, despite being squint free, doesn't perform better than the phase-shifter (b) Supported range difference between CPSS-SCT and phase shifter based PAA feeder for various array sizes. The supported range of CPSS-SCT and the simple phase-shifter is plotted for different array sizes. The results highlight the clear steering advantages of CPSS-SCT. For a V-band communication link using frequencies from 54 to 64 GHz, i.e. a fractional bandwidth 17%, a 16x16 array based on CPSS-SCT only requires three systems to cover the full 360° of a mobile cell.

Fig. 3.21(d) respectively, are smaller. Both the CPSS and CPSS-I have the same phase response and thus look similar. The array gain maps show an improved performance of the CPSS-I over the CPSS scheme thanks to the additional intensity matching. The array gain is indeed flatter. The largest supported range with the most flat array gain is found for the CPSS-SCT-I implementation, Fig. 3.21(f). The CPSS-SCT and the CPSS-SCT-I scheme are similar, see Fig. 3.21(e) and Fig. 3.21(f). In fact, the supported range — the largest of the practicable compared solutions — is similar for both implementations. The array gain variations of CPSS-SCT-I in the supported range are lower than in the CPSS-SCT case, though.

In order to compare the different types of feeder network directly, the supported ranges are combined into a single figure. The results, plotted in Fig. 3.22(a), show that the CPSS-SCT scheme outperforms any other concept by providing the largest supported range. It also can be seen that intensity matching on both CPSS and CPSS-SCT doesn't reduce the supported range significantly. It also shows that a simple CPSS feeder doesn't provide any better steering range over the simple phase shifter concept. A CPSS beam steering concept could however still be useful in e.g. applications where beam squint cannot be tolerated, such as those for which inter-cell-interference would play a major role.

The influence of the array size on the supported range for both the CPSS-SCT and the simple phase-shifter concept is investigated in Fig. 3.22 (b). It can be seen that for fractional bandwidths between 20 and 50%, a PAA feeder based on CPSS-SCT provides larger steering range for all the array sizes. Taking as example, a V-band communication link using frequencies from 54 to 64 GHz, i.e. a fractional bandwidth of 17%, a 16x16 phased array system based on CPSS-SCT will provide about 35° more steering range. This performance improvement reduces the number of systems required to cover the full 360° in a mobile cell from 5 down to 3 units.

3.2.6   Conclusion

In this paper, we have performed simulations to compare the performances of different integratable phased array feeder concepts. The comparison is made using two key parameters. The largest steering range for the broadest fractional bandwidths is found for a solution relying on complementary phased shifted spectra (CPSS) with separate carrier tuning (SCT) filters. The simpler scheme relying on phase shifters also offers a relatively large steering range though. An important aspect of the schemes discussed in this paper is that all of them can be monolithically integrated in silicon and may provide ultra-fast steering when properly implemented with fast phase modulators.

3.2.7   Acknowledgment

4 ULTRA-FAST BEAM STEERING FOR MOBILE COMMUNICATION

Ultra-fast beam steering systems could be used in many fields such as communication, sensing, or radar. Depending on the particular application, the tuning speed of the steering direction is one of the most important features.

In particular for applications in communication as investigated in this thesis, ultra-fast beam steering enables a new multiplexing scheme, see Fig. 4.1. On the left side, a typical current implementation of an access network using time division multiplexing (or frequency division multiplexing) is depicted. There are two intrinsic limitations in this widely used architecture:

1. The users have to retrieve all the transmitted data and use digital processing resources to recover their dedicated information.

2. Energy is lost as the information for a given user is spread across the whole cell sector.

With a steering system fast enough to change the beam direction in-between the transmitted symbols, a new multiplexing scheme as depicted on the right of the figure is possible. The idea is to send symbols only to the targeted users. This technique ultimately

1. reduces the costs,
2. reduces the energy consumption,
3. attenuates electromagnetic interferences, and
4. Improves the bandwidth utilization.

This chapter hence focuses on the utilization of ultra-fast beam steering in a novel multiplexing scheme called time-to-space division multiplexing (TSDM). After a description of TSDM based on the work submitted to IEEE transactions on wireless communication, the influence of various parameters is discussed.
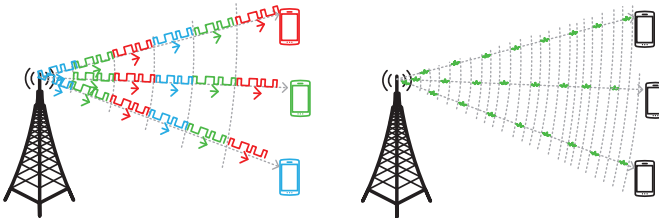

Fig. 4.1 - Time division multiplexing versus space-to-time division multiplexing. On the left, a typical mobile network architecture is depicted. Two of the limitations are that first users have to consume digital processing resources to retrieve their own data in the received information. Second, energy is waste as it is sent to users not needing it.

4.1 Time-to-Space Division Multiplexing for Tb/s Mobile Cells

Abstract: Space division multiplexing increases the capacity of mobile cells by reusing the frequencies in various directions. Yet, today's concepts scale badly to millimeter wave and therefore cannot provide Tb/s capacity. In this paper, we introduce time-to-space division multiplexing as a novel scheme to steer multiple beams simultaneously to different users. The main benefit of the proposed method relies in the fact that simple hardware can be used to generate the beams. In other word, it provides the advantages of space division multiplexing without relying on the complex array feeders that are usually required. Thanks to this advantage, the proposed technique can be easily combined with millimeter Wave systems as recently demonstrated.

4.1.1 Introduction

Space division multiplexing (SDM) and millimeter wave communication - if applied together – could offer Tb/s of wireless capacity [18, 21]. Yet, an affordable solution to merge the advantages of both technologies is very challenging to be found [7]. SDM requires either massive hardware in the form of multiple phased-array antennas or large digital signal processing (DSP) capacities. Yet, DSP is particularly expensive at highest speed such as those needed to encode millimeter wave signals. If Tb/s wireless links are to become practical new solutions that rely on low complexity and low-cost hardware will be needed [14].

Among the most promising implementations of next generation radio access networks (NG RAN), two trends can be distinguished: First, concepts relying on current 4G-LTE microwave frequencies (2.4, 5 GHz) with approaches such as massive multiple input, multiple output (MIMO) [11, 12] or smarter networks [7, 13]. Second, concepts based on millimeter wave (mm-Wave) technologies [14-16, 18, 142]. In the case of massive MIMO [11], e.g. E. Larsson *et al.* take advantage of low-cost, reliable, and mass producible components to generate multiple beams, but suffer from the limited bandwidth available at microwave frequencies. On the other hand, mm-Wave technologies leverage the large bandwidth available at mm-Wave bands to considerably increase the bitrate. However, the increased cost and complexity of the components diminish the benefits and often prevent the implementation of advanced concepts such as massive MIMO. Nonetheless, combining advanced system architectures such as massive MIMO or smarter networks with mm-Wave technologies could potentially combine the

benefits of both approaches to provide both a larger bandwidth and spatial diversity at the same time [20]. Yet, merging both approaches has shown to be challenging with current designs due to the large number of mm-Wave components in the base band units (BBU), the remote radio head (RRH), and the user equipment (UEs) [11, 46].

In this paper, a next generation (NG) RAN scheme relying on already published ultra-fast mm-Wave beam steering demonstrations is presented [48, 49]. The scheme, which is termed time-to-space division multiplexing (TSDM), increases the capacity of a mobile cell while simultaneously drastically reducing the hardware requirements on the UEs. In other words, TSDM enables multiple beam steering capabilities comparable to concepts such as known from massive MIMO [11] or multiple beam array feeders [143], but with a fraction of the hardware requirements at mm-Waves. Leveraging the advantages of TSDM, we propose the design of a mobile cell with an aggregated capacity above 1 Tb/s, meeting the frequency band specifications of the IEEE 802.11ad standard.

The paper is organized as follows: First, the requirements of a cell with Tb/s capacity is described. Second, the fundamental principles of TSDM are explained. After presenting results of a system level simulation the paper is concluded by summarizing the key aspects of TSDM.

4.1.2   Towards Tb/s Mobile Cells

The required throughput per square meter of a mobile network is highly dependent on the type of environment. Particularly, high capacity will be required in hotspots such as public transport stations, stadiums, airports, or special event venues, where a large number of closely located users may consume high definition video streams directly to their terminals. In such hotspot scenarios, a very high cell capacity must be installed to cope with the demands. The important unit to consider here is the throughput per square meter. Some of the current major trends to improve this metric rely on reducing the size from macro to picocells, better reuse of the available bandwidth, or the installation of smarter network schemes to reduce cell interference [7]. However, these solutions do not increase the capacity by several orders of magnitude, as would be required for the above-mentioned hotspots. In this chapter, two of the major envisioned solutions to increase the capacity by orders of magnitude are reviewed: Namely millimeter wave communication and space division multiplexing (SDM). Ultimately, it is concluded that Tb/s cell capacity is achievable using existing hardware compatible with actual standard by combining both mm-Wave and SDM in the same system.

Millimeter Wave Communications

In communication standards at millimeter wave frequencies, such as IEEE 802.11ad-2012 (60 GHz), the channel bandwidths can be as high as 2.16 GHz [22]. The maximal physical data rate defined therein is 6.757 Gb/s for a chip

rate of 1.76 GBd, using an OFDM 64-QAM modulation scheme and a 13/16 low-density parity-check code (LDPC) [22]. To simplify the discussions in this paper, a symbol rate R_s of 2 GBd (still fitting in the 2.16 GHz channel bandwidth) instead of 1.76 GBd is considered. Combined with a 4 bit/symbol modulation (16QAM) a bit-rate R_b of 8 Gb/s is encoded in the channels.

In the band definitions of the IEEE 802.11ad standard, up to four channels n_{channel} at various carrier frequencies can be used [22]. The cell capacity C_{tot} is thus given by

$$C_{\text{tot}} = R_b \cdot n_{\text{channel}} \cdot n_{\text{sector}} \qquad (4.1)$$

Using a bit-rate R_b of 8 Gb/s, 4 channels, and 3 sectors, the aggregated capacity is 96 Gb/s.

Recent research has shown even higher bitrates at millimeter wave frequencies, but mostly for point-to-point communication [24-27, 144, 145]. Yet, one of the main limiting factors for NG RAN at millimeter wave frequencies is the increased free space path loss that either reduces the reach of the access network or forces the utilization of beam steering systems. For the first generation of 802.11ad RAN, the envisioned applications are mostly short range such as indoor communication or mobile docking (up to 10 m) and thus may avoid complex beam forming systems. On the other hand, outdoor applications will require higher reach and therefore a more sophisticated architecture.

Advanced Beam Forming

Another way of increasing the cell capacity by orders of magnitude is to use SDM. SDM is based on reusing the same frequency band in various directions by forming spatially separated, non-interfering radio beams [21]. This corresponds to the creation of virtual cell sectors with adaptive coverage. If a user receives the signal from only one beam at a time, it results in two advantages: first, the cell capacity is increased by the number of spatially separated beams. Second, the full UE capacity can be used since neither time, code, nor frequency multiplexing is required. Hence, there is a need of phased array antenna (PAA) concepts capable of simultaneous and independent steering of multiple antenna beams. In order to compare the various implementations of PAA, three main categories of feeders can be defined, see Fig. 4.2.

In Fig. 4.2 (a), a simple feeder for a PAA is depicted. The signal $s_1(t)$ provided at the input of the PAA is transmitted in a direction defined by the phase or delay Δt added in front of each antenna [40]. Such concepts allow for electronic scanning and longer reach, but they do not offer multi-beam capability and therefore cannot increase the cell capacity. PAAs can be implemented as electronic or microwave photonic schemes. Using electronic array feeders, the feeding signal $s_1(t)$ is usually directly modulated onto the wireless carrier. The delay element ΔT is then implemented as a radio-frequency component [146-148]. In the case of a microwave photonic array

feeder, the feeding signal $s_1(t)$ is encoded onto an optical carrier. The delay element is then usually implemented as a photonic component [48, 110, 143]. Right after applying the delay, the optical signal is down-converted to the wireless domain by heterodyning with an optical local oscillator.

In Fig. 4.2(b), a PAA with multiple feeders is depicted. Many variations of this scheme can be found in literature, united by the fundamental principle to add multiple feeder networks in parallel (depicted here with different colors). Such concepts enable larger capacity by creating fully independent multiple beams. Yet, the hardware requirements for a large number of beams make this approach complex and costly.

In Fig. 4.2(c), the most flexible multi-beam system is shown. This is usually referred to as massive MIMO or digital beamforming and relies on digital signal processing to form the different beams. The signals for each antenna with their requested delays are generated by a digital signal processing (DSP) stage with a dedicated digital to analog converters (DAC). In [11], it is rightfully claimed that the cost and complexity of the hardware is not an unsurmountable issue at microwave frequencies. This statement unfortunately cannot be extended to mm-Waves frequencies. [21]

Fig. 4.2 - Comparison of phased array antenna concepts. (a) A simple PAA with one feeder (b) Analog PAA capable of multiple beam steering (c) DSP-based array feeder with DACs to generate the waveforms in front of the antennas.

Systems based on Fig. 4.2(b) are usually limited to a few beams while systems based on Fig. 4.2(c) are limited by the number of antennas that can be integrated with reasonable cost and complexity. For both Fig. 4.2(b) and Fig. 4.2(c), the first advantage is that the cell capacity is increased by the number of beams generated at the PAA. Assuming a system capable of generating 10 separate beams, the cell capacity will at best increased by a factor of 10. Another advantage is that the complexity of the UEs does not change with the number of beams - low-cost components can still be used at the UE.

Reaching Tb/s Cell Capacity

Cell capacity in Tb/s can be realized by combining mm-Wave with multiple beam solutions as depicted in Fig. 4.2. Merging a mobile cell at mm-Wave fulfilling 802.11ad (bitrate 96 Gb/s, see above) and a SDM system supporting 11 beams could bring the capacity C_{tot} to

$$C_{\text{tot}} = R_b \cdot n_{\text{channel}} \cdot n_{\text{sector}} \cdot n_{\text{beams}} \qquad (4.2)$$

With a bit-rate R_b of 8 Gb/s, 4 channels, 3 sectors, and 11 beams, the aggregated capacity is now 1056 Gb/s.

By generating separated beams, each user can use the full channel capacity (8 Gb/s). In systems implementing SDM, the total cell capacity is increased by the number of beams. If more users are located in the proximity of the cell, the capacity of each beam could still be shared by closely located users using time or frequency division multiplexing.

4.1.3   Time-to-Space Division Multiplexing

In RANs such as 4G LTE and most of the IEEE 802.11 wireless protocols, multiple UEs share the same transmission channel using time division multiplexing (TDM) and/or frequency division multiplexing (FDM). This requires components with processing capabilities corresponding to the full capacity of the base station. A drawback of this scheme is that only a fraction of the receiver's capabilities is exploited. On the other hand, space division multiplexing (SDM) implementations do not suffer from this limitation: in SDM-based mobile networks, the total cell capacity can be increased without changes to the UEs by parallelizing multiple streams.

As explained in the last section, combining mm-Wave and multiple beam steering is an attractive solution for 5G RAN, but new architectures are needed to overcome the hardware complexity or high costs of approaches such as those depicted in Fig. 4.2(b) and (c) [21]. A promising solution with the hardware of Fig. 4.2(a) but the capacity of the more advanced approaches relies on a PAA with ultra-fast beam steering capabilities [48, 49] - a system in which the beam direction could be adjusted with extremely short settling times and allow for – what we call - time space division multiplexing (TSDM) [49].

The concept of TSDM is to emulate a multiple beam system by steering a single beam in between the transmission of each symbols. To perform this operation, a PAA with low settling times is needed.

Steering Multiple Beams with Simple PAAs

The principle of TSDM is illustrated in Fig. 4.3. First, the signals for the different user equipment (UE) are time-division multiplexed (TDM) symbol-by-symbol. This feeding TDM signal could be, depending on the implementation of the feeder, in baseband, passband, or encoded onto an optical carrier. The different colors in Fig. 4.3(I) represent the time slots allocated to the different beams. The TDM sequence is subsequently transmitted to the PAA in the base station (BS). In a realistic scenario, the transmission would likely rely on radio-over-fiber [18].

In the BS, see Fig. 4.3(II), a control signal synchronized with the incoming data stream is used to perform time-to-space mapping to redirect the different tributaries in their time slots, to a specific direction. Using this symbol-by-symbol steering, the different UEs receive signals that correspond to a return-to-zero modulation scheme, see left part of Fig. 4.3(III). Therefore, a low-pass filter can be applied to the signal without causing inter-symbol-interference (ISI).

As can be seen from the signals after the low-pass filter, right part of Fig. 4.3(III), the sequence assigned to each user is received at a symbol rate 3 times smaller than the one of the transmitter. In other words, TSDM enables steering of multiple beams with a PAA built using a simple array feeder.
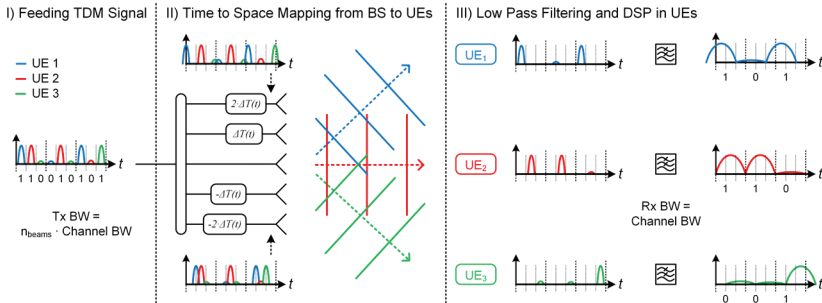
Fig. 4.3 - Principle of time-space division multiplexing (TSDM). I) Signals for the different user equipment (UE) of the base station (BS) are encoded using symbol-based time division multiplexing (TDM). II) The BS performs a time to space mapping using symbol-by-symbol steering. III) The UE down-converts the mm-Wave signals and performs a low-pass filtering (LPF). The signal after the LPF is similar to the one received with other space division multiplexing (SDM) schemes. Note that the signals in front of the antennas are passband signals, for the sake of readability only the envelope of the signals are plotted.

Replacing Low-Pass Filters by Band-Pass Filters

To stay compatible with channel specifications and low-end commercial UEs e.g. defined in 802.11ad, the low-pass filters from Fig. 4.3(III) can be replaced by band-pass filters (BPF) in front of the antennas in the BS. Such a scheme with BPF is depicted in Fig. 4.4. The difference compared to Fig. 4.3 lie in the

part II of the figures. To understand the working principle with BPF instead of LPF, a reminder of the signal characteristics in SDM system is needed. As shown in Fig. 4.2 (b) & (c), the signals transmitted by the antenna in SDM systems are a superposition of multiple inputs with various delays. This superposition is either performed with an analog combiner in front of the antenna or within the digital processor. In the case of Fig. 4.4(II) with BPF, this superposition of the signals is achieved by the time broadening effect that occurs when using a filter with bandwidth smaller than the one of the signal.

In fact, the filter bandwidth matches the channel bandwidth (2GHz using 802.11ad) while the bandwidth of the TDM signal corresponds to the number of slots (n_{slots}) times the channels bandwidth. The effect of the time broadening is similar to a moving average, thus the various TDM slots are added on top of each other, see black shape in Fig. 4.4(II). The UEs in Fig. 4.4(III) do no longer need to have a special LPF. Thus, the transmitted beams are fully comparable to those of a standard SDM system and respect the frequency bands definitions.

The main advantage of this approach compared to a multiple feeder solution, shown in Fig. 4.2(b), or massive MIMO, shown in Fig. 4.2 (c), is that the PAA only relies on a single simple feeder, see Fig. 4.2 (a). Neither complicated wiring nor a large quantity of expensive hardware is required.
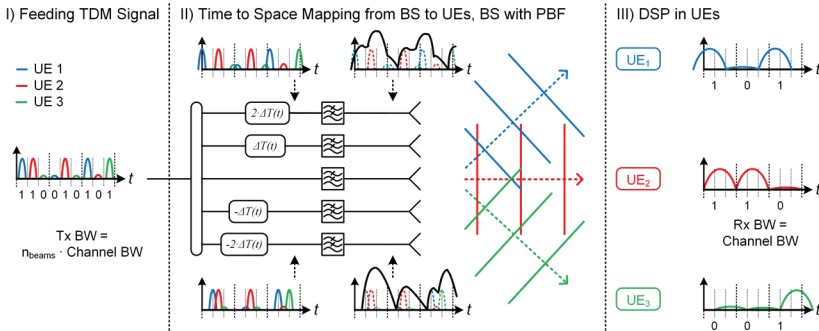
Fig. 4.4 - TSDM scheme with filtering in the base station (BS). In contrast to Fig. 4.3, where the filtering is performed in the UEs, the filtering now takes place in the base station. Band-pass filters (BPF) are placed in front of each antenna to match the bandwidth of the channel. Such a filter with a bandwidth smaller than the transmitted signal bandwidth usually leads to inter-symbol-interference (ISI) and distorts the signals. Yet, in the TSDM case, ISI matches the desired effect. Indeed, in SDM schemes as shown in Fig. 1.4(b) and (c), signals for various beams are added on top of each other in front of the antennas. Such an addition of different signals also take place through ISI - through a time broadening, the symbols extend into their neighbours and information is added. Note that the signals in front of the antennas are passband signals, for the sake of readability only the envelope of the signals are plotted.

Conditions for proper Operation of TSDM

Time-to-space division multiplexing (TSDM) enables multiple beam steering with low complexity PAA. However, there are two intrinsic limitations and corresponding conditions that must be respected a TSDM system. In this section, these limitations are summarized for a PAA build with true time delays (TTD). Further insight can be found in section 4.2. The first limitation is simply related to the fact that the angular width of the beam must be small enough to avoid interference between adjacent users. This is a limitation common to all SDM beam steering schemes. The second limitation is related to the memory-less nature of the TTDs used in the PAA feeder. In other words, the first symbol entering the TTD must be the first one leaving. This limitation is further explained with the help of Fig. 4.5. For the sake of clarity, the signals are depicted here as baseband signals (i.e. we plot the envelope of the signals) while in reality they are passband signals. If the beam is to be scanned between two directions (blue and red), the required feeder delay Δt is proportional to the relative angular separation $\Delta\theta$ between the two directions multiplied by the antenna spacing d. For the antennas at the edge of the PAA, the required delay is therefore $p \cdot \Delta t$ with p the position of the antenna ($p = 0$ at the center of the PAA). To avoid inter-symbol interference between the blue and red time slots, $p \cdot \Delta t$ should be smaller than $RZ \cdot T_s$ with RZ the return-to-zero duration and T_s the transmitter symbol duration. Due to this limitation, the relative steering angle $\Delta\theta$ between two beams is limited to small angular steps. To provide the highest capacity despite these limitations, design rules should be followed. First, the beam should be steered continuously from one edge of the sector to the other and then reset at the initial angle. Second, the transmitter pulse should feature a return-to-zero characteristic.

In the case of a PAA build with phase shifters, an analog limitation is to be found, see section 4.2 for more details.
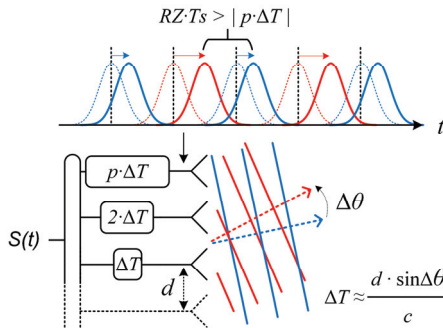
Fig. 4.5 - Maximum delay in the PAA feeder. The largest required delay $p \cdot \Delta t$ in the PAA feeder on the outmost antenna should stay smaller than the symbol duration T_s multiplied by an off-time factor RZ. Having smaller angular step $\Delta\theta$ between users makes this limitation easier to avoid.

1) The beamwidth condition

The beamwidth condition simply implies that the angular width of the beam should be smaller than the coverage of the sector divided by the number of users. Indeed, in a cell sector covering 120° with 10 independent beams, the beamwidth must be smaller than 12° to avoid interference. This condition, which defines a minimum number of antennas N required in the PAA, is given by

$$N \geq 1 + \frac{2 \cdot \mathrm{acosh}(A_{\mathrm{SL}})}{\mathrm{asech}\left(\cos\left(\sin\left(\frac{\Theta_{\mathrm{sector}}}{n_{\mathrm{users}}}\right) \cdot \frac{\pi \cdot d}{\lambda_{\mathrm{RF}}}\right)\right)} \tag{4.3}$$

where A_{SL} is the desired side lobe attenuation at the position of the adjacent user when using Dolph-Chebyshev tapering, Θ_{sector} is the size of the sector in radians, n_{users} is the number of equispaced users using the cell sector, d is the antenna element spacing and λ_{RF} is the wavelength of the mm-Wave carrier frequency f_{RF}. See section 4.2.1 for more detail on Eq. (4.3)

2) The symbol transition condition

The symbol transition condition implies that the requested delay to steer the beam should limit the ISI to a maximum of 3dB between adjacent time slots. As an example, if one uses a 50% RZ scheme in the transmitter, the maximal delay allowed between two consecutive symbols corresponds to 50% of the symbol duration. The condition can be calculated using

$$N \leq 1 + \frac{RZ \cdot T_{\mathrm{S}} \cdot c}{d \cdot \left|\sin\left(\frac{\Theta_{\mathrm{sector}}}{2 \cdot n_{\mathrm{users}}}\right)\right|} \tag{4.4}$$

where RZ is the return-to-zero duration $0 < RZ < 1$ (0.5 for 50% RZ), T_{S} is the symbol duration at the transmitter data rate and c is the speed of light. See section 4.2.2 for more detail on Eq. (4.4)

3) The frame transition condition

The third condition, i.e. the frame transition condition, corresponds to the pause in transmission that should be inserted while steering the beam back to the initial angle. In fact, the requested delay to steer the beam back from one end of the cell sector to the other is related to the sector size, e.g. 120°, and to the array size. Indeed, the larger the array and the steering angle, the larger the requested delays. If this requested delay is larger than the symbol duration, one must pause the signal transmission by inserting empty time slots in order to avoid interference. The frame transition condition can be stated as

$$N \leq 1 + \frac{(n_{\mathrm{slots}} - n_{\mathrm{users}}) \cdot T_{\mathrm{S}} \cdot c}{d \cdot \left|\sin\left(\frac{(n_{\mathrm{user}} - 1) \cdot \Theta_{\mathrm{sector}}}{2 \cdot n_{\mathrm{user}}}\right)\right|} \tag{4.5}$$

where l_{frame} is the length in symbols of the transmitted frames (including both active and "empty" users). See section 4.2.3 for more detail on Eq. (4.5).

To make TSDM simpler and easier to implement, we define two aspects of the transmitted signal generation. First, the symbols for the different beam directions are grouped in frames comprising both the symbols to be transmitted and the pauses from the frame transition condition. There are thus time slots at the transmitter that are filled by user data and others that are empty. For example, a frame could comprise 4 user slots out of 5 time slots. Second, the transmitter pulse shape corresponds to a return-to-zero modulation scheme. At the first glance, it seems that the spectral efficiency of the mobile cell is reduced as RZ and empty slots are implemented. However, this reduction of spectral efficiency only applies to the feeding signal in front of the array, not to the wireless signals. Indeed, the spectral efficiency related to the low bandwidth wireless channels is not impacted by the frame configuration as each individual beams could be mapped to a specific wireless channel bandwidth. The reduction of the spectral efficiency of the feeding signal only implies that a larger bandwidth will be required in the backbone network. Yet, the limitations in cell capacities comes from the wireless channel, not from the backbone network.

4.1.4   TSDM-based Mobile Cell

In Fig. 4.6, the three conditions stated above are exemplarily plotted for a configuration with 5 time slots in the frame. The figure shows the supported area (green) in which the TSDM scheme will work when using a 10 GBd transmitted signal with 50 percent RZ in a 60 GHz carrier cell covering 120°. The ideal working point corresponds to 4 equispaced users and requires at least 13 antennas. In addition, the results show that RZ50% is not needed for the system to perform correctly, as the ideal working point requires only a RZ of 21.6%. The array weights are tapered with a Dolph-Chebyshev side lobe level of 30 dB. Serving 4 active users implies a cell capacity increase by a factor 4. In Fig. 4.6(b), the corresponding transmitted frame is depicted. Fig. 4.6(c) describes the beam switching scheme. In the simplest case, the beam will be steered from the left to the right from users 1 to 4. Once the beam has been scanned through the sector, an additional slot is used to return to the initial angle.

The system has been optimized for three frame length configurations. The results, summarized in Table 4.1, show how to shape the frames in order to increase the cell capacity by a factor of 4, 8, and 11. The total cell capacity in Gb/s corresponds to the sector capacity in GBd multiplied by the number of sectors per cell (3 for 120° cells), the number of possible carrier frequencies (4 in 802.11ad-2012), and the spectral efficiency (4 b/s/Hz using 16-QAM).

Table 4.1 - Optimization of frame configuration.

	4x Capacity	8x Capacity	Tb/s Cell
Tx Rate [GBd]	10	22	36
Return-to-Zero	25%	50%	66%
Frame length	5	11	18
Active users	4	8	11
Rx Rate [GBd]	2	2	2
Antennas (1D)	13	23	37
Channel [GBd]	8	16	22
Total Cell [Gb/s]	384	768	1056
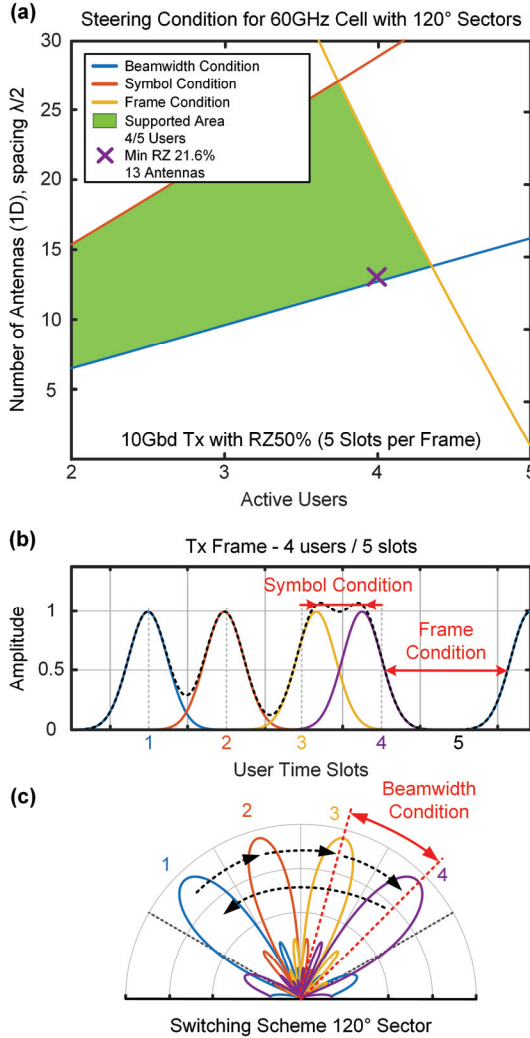
Fig. 4.6 - Conditions for TSDM. (a) Steering condition for a TSDM system comprising 5 time slots per frame. The ideal working point is found having 4 active users for a PAA built with 13 antennas. (b) The frame of a typical TSDM system consists of active users (here 4) followed by empty time slots (here 1). The empty time slots help fulfilling the frame condition while the return-to-zero scheme relaxes the symbol transition condition. (c) The beam direction in TSDM is best steered from one edge of the sector to the other, stopping at each active user. One time slot is used to go back from user 4 to user 1. The plot also depicts the beamwidth condition (the beamwidth must be smaller than the angular separation of the users).

Reaching Tb/s

The principle of TSDM has been experimentally demonstrated in [48] and [49]. However, these demonstrations were limited in array size and aggregated cell capacity. To demonstrate that the required capacity per sector can be reached with TSDM, simulations have been performed. For this purpose, a time-domain simulation framework supporting symbol-by-symbol beam steering has been implemented. It comprises the following key features: For the generation of the feeding TDM signal, multiple DeBruijn sequences are multiplexed onto the various tributaries. The calculation of the delay lines is made with finite impulse response (FIR) filters. Here, the development was very specific as the requested delays are changing for each transmitted symbols, thus, the FIR filter is updated for each symbol from a lock-up table supporting various types of delay lines. The array transmission is computed considering the applied delays and various array shapes (typically rectangular), taperings (typically Dolph-Chebyshev), and element patterns (typically isotropic). The 3 dB beamwidth is typically 120° divided by "n_users". The channel is only modeled through its free-space path losses, this assumption holds as focused beam are used. The filtering is performed either in pass-band in front of the antennas of the array or in the baseband in the receivers. In the receivers, standard digital signal processing is performed such as timing estimation, carrier recovery, and equalization.

In this section we present simulation results for a TSDM scenario. Fig. 4.7(a) depicts the error vector magnitude (EVM) results for a cell reaching a capacity of 1056 Gb/s - using 16-QAM, see Eq. (4.2). In this simulation, a PAA with 37 elements is used at 60 GHz to distribute 11 of 18 time slots towards 11 users placed equidistantly between -55° and 55° (i.e. covering a 120° cell sector with users spaced 10° apart). 18 times slots require a symbol rate of 36 GBd in the transmitter and a roll-off factor of 1 is used as it is best when delaying signals. An optimized Dolph-Chebyshev array tapering with side lobe level of 32 dB is implemented to reduce the inter-user interferences. The receivers are using 2 GHz bands and receive 16-QAM signals at 2 GBd (8 Gb/s), thus filters with low-roll-off (0.05) are implemented. The results show EVM values (rms) around 6 percent for all users. The EVM values are here limited by the signal distortion resulting from symbol-by-symbol steering. As other noise sources are not considered, the resulting EVM can be considered as the inherent TSDM penalty.

In Fig. 4.7(b) the impact of the bandwidth of the filter of the receiver is investigated. It can be seen that the first minimum EVM is reached at a receiver low-pass filter bandwidth of 2 GHz. The 2 GHz is matched with the 2 GBd transmission capacity of each of the 5, 11 or 18 tributaries of the of 10, 22, and 36 GBd TDM signal. The first minimum occurs at 2 GHz when the Nyquist ISI criterion is met. With smaller filter bandwidths (<2 GHz), the EVM increases to 60 percent where demodulation is no longer possible. At integer multiple of a 2 GHz filter bandwidth, the EVM is also small as the Nyquist ISI criterion is partially fulfilled Using filter bandwidths other than integer multiples of the received symbol rate results in a decrease in signal quality due to the introduced inter-symbol-interference.
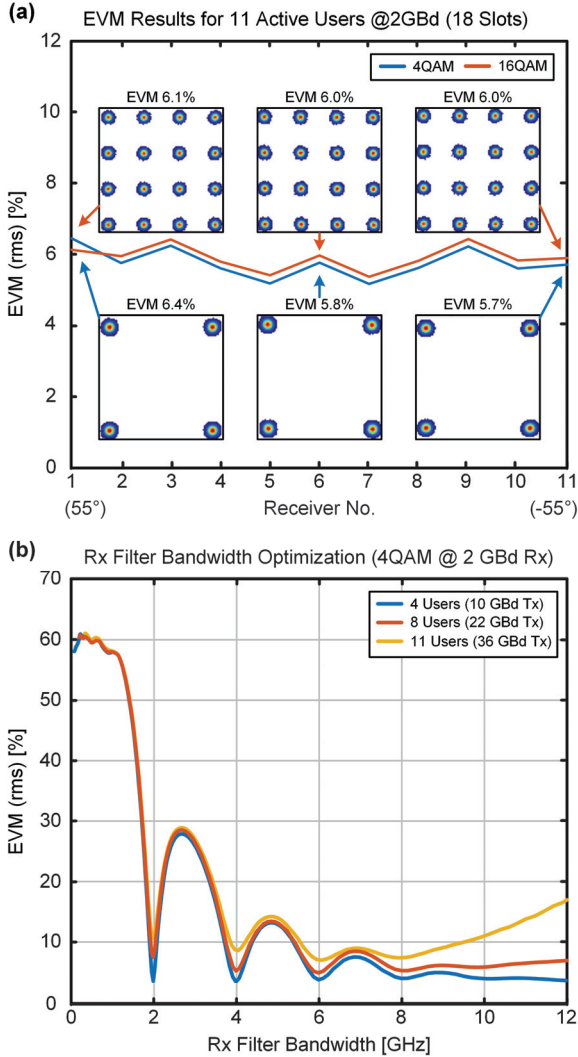
(a)

(b)

Fig. 4.7 - Simulation Results. (a) EVM for a TSDM system with 11 active users reaching an aggregated capacity of 1056 Gb/s (16-QAM). The EVM (~6 percent) only accounts for the distortion due to TSDM and can therefore be considered as a noise-equivalent penalty of the proposed concept. (b) The ideal low-pass filter bandwidth in the receivers is given by $1/n_{slots}$ with n_{slots} being the number of time slots in the transmitted frames and Tx_{BW} the bandwidth of the feeding TDM signal. In the three cases, the ideal receiver filter bandwidth is 2 GHz (20% of 10 GBd, 9% of 22 GBd, and 5.5% of 36 GBd), fulfilling the Nyquist ISI criterion.

While this work focuses on a 60GHz carrier frequency, the TSDM concept is frequency independent. As mentioned, the key advantage of TSDM is the low complexity and potentially low cost of the array feeder compared to alternative approaches. However, this advantage is rational only if the carrier frequency is large enough. Indeed, at low frequencies (<10 GHz), the costs and complexity to implement concept such as massive MIMO seems to be a surmountable challenge.

OFDM Implementation

In most mobile communication standards, the highest bitrates are reached by switching from single carrier (SC) to multi-carrier data formats, more specifically orthogonal frequency division multiplexing (OFDM) is commonly used. In the example of 802.11ad, the maximum bit rate is based on 512 subcarriers using a 64QAM modulation scheme. In this sub-section, the implementation of TSDM for OFDM data format is detailed as it requires special considerations comparing to the SC case explained in the previous sections.

As depicted on Fig. 4.8, OFDM is compatible with TSDM if the multiplexing is performed at the correct rate. As an example, we have depicted the situation where 2 OFDM sequences are TDM multiplexed to one TSDM frame. In our example, the OFDM symbols of two users (Fig. 4.8(a) and Fig. 4.8(b)) are generated and time division multiplexed sample by sample in the central office, see Fig. 4.8(c). The system rate in Fig. 4.8(c) is twice as high as the one of Fig. 4.8(a) and Fig. 4.8(b). The signals transmitted to the PAA, see Fig. 4.8(c), would thus be unreadable with standard OFDM techniques as two OFDM symbols are interleaved. Yet, after the sample based beam steering occurring in the PAA, Fig. 4.8(e), the two original sequences (a and b) will be mapped to separate directions (f) and (g). The steering control signal is, in this simplified case, rectangular, see Fig. 4.8(d). In the UEs, low pass filtering could also be implemented to restore the original OFDM sequence. Fig. 4.8(h) and Fig. 4.8(i) show that the received symbols would fully match the transmitted sequences (a) and (b) with proper filter design. As for the single carrier case, the LPF could also be replaced by a BPF placed in the PAA to be fully compatible with commercial receivers. Note that the ultra-fast beam steering is performed at the sample rate of the OFDM frame, not at the slower symbol rate. In Fig. 4.8, OFDM symbols comprising 8 samples are used. If one would change the beam direction after the OFDM symbols only, the capacity of the cell would match the capacity of the users. Indeed, the feeding signal would have to match the receiver sample rate.

The generated beams with an OFDM scheme, considering a BPF implementation, are fully comparable to those generated with other SDM schemes. Thus, OFDM in a TSDM based feeder could also be leveraged to mitigate fading.
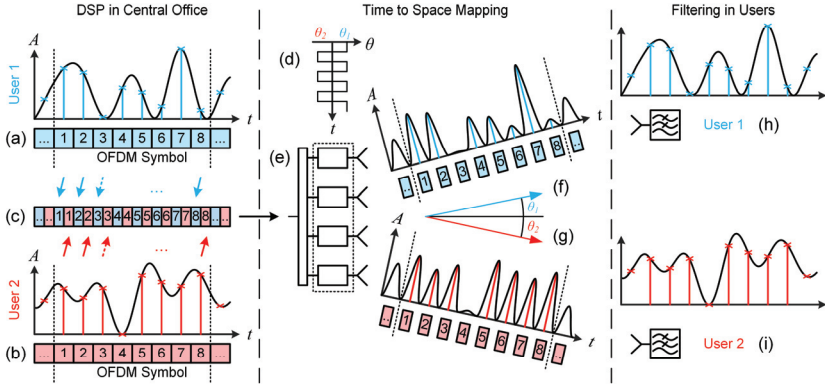
Fig. 4.8 - OFDM Implementation of TSDM. As opposed to the single carrier implementation, TSDM with OFDM sequences has to be performed at the sampling rate of the sequence. (a-c) Two OFDM symbols are generated for two users (red and blue) and consecutively interleaved sample-by-sample. (d-g) The PAA performs a sample based ultra-fast steering to send the two sequences in different directions. (h-i) The UEs only receive one of the data streams and can recover the original OFDM symbols after low pass filtering.

TSDM Challenges

The main challenge specifically tied to TSDM lies in the fabrication of the microwave array feeder that performs the time-to-space mapping in the RAU. However, the experimental demonstrations presented in [48] and [49] have already proven the feasibility of this approach. TDSM also shares limitations with other SDM approaches, yet standard solutions can be reused

- To steer the beam towards one specific user, the position of the user must be known in the transmitter. In a first approach, the users could collaborate with the cell by providing channel state information back to the transmitter. Yet, an easier way of solving this issue with TSDM would consist of having fixed beam directions, equidistantly split through the sector. The system would then perform standard handover between the generated virtual pico-cell.

- Even though uplink bandwidth requirements are usually lower than those of downlinks, a future-proof RAN concept should still increase the capacity of the uplink. In this paper, the downlink scheme is discussed primarily. Yet, TSDM could also be used in the uplink. In this case, the users would continuously transmit in the full 2 GHz bandwidth while the RAU would scan through the sector to perform a direction-based sampling.

- The practical implementation of an electronic system with very large fractional bandwidth is extremely challenging when using electronic systems. In the exemplary simulation, the feeding TDM signal has a

bandwidth of more than 36 GHz for a targeted carrier frequency of 60 GHz. To avoid this challenge and thus reduce the complexity, the demonstrations in [48] and [49] rely on microwave photonic processing in the array feeder. Yet, in less extreme cases with a lower number of beams of or a smaller channel bandwidth, TSDM could be implemented using electronic subsystems

4.1.5   Conclusion

In this paper, time-to-space division multiplexing (TSDM) has been presented as a solution to increase the capacity of future radio access network (RAN) without affecting the user equipment (UE) requirements. Simulations have been performed to demonstrate a mobile cell reaching an aggregated capacity over 1 Tb/s while fulfilling the frequency band restrictions of the IEEE 802.11ad standard. The capacity is augmented by generating multiple beams from the remote antenna unit (RAU) in the RAN.

TSDM can thus be considered as a space division multiplexing (SDM) concept that enhances the spectral efficiency by generating multiple beams in different directions. The same capacity enhancement could also be reached with multiple feeders based phase array antenna (PAA) or with a digital signal processing (DSP) based PAA. Yet, both approaches are complex to implement for mm-Wave communication systems. TSDM offers therefore a solution in which

- The complexity of the PAA is reduced to a single array feeder without the need of complex feeding schemes.

- The cell capacity can be adapted easily. If a user with higher-end equipment is in the sector, it could also use a higher capacity. On the other hand, if fewer users are in the cell, the transmitter symbol rate can be adapted to reduce the resources usage without influencing the user requirements.

- TSDM is compatible with OFDM by performing a sample-by-sample steering at the system rate of the OFDM scheme.

- TSDM could generically be applied to any type of analog input signals. The requirement is that each of the analog inputs, meant to be transmitted in various direction, should be sampled at least with the Nyquist sampling rate.

4.1.6   Appendix A

The appendix A of the original paper entitled "Derivation of TSDM Operating conditions" has been moved in section 4.2 of this thesis for clarity.

4.2   Derivation of TSDM Operating conditions

To mitigate inter-symbol interference (ISI), the design of a TSDM system must respect three conditions:

A. The beamwidth condition: it states that a PAA must have a minimum number of antenna to be able to generate a beamwidth smaller than the angular distance between adjacent users.

B. The symbol transition condition: it implies that the number of antenna of the PAA, i.e. its size, is limited by the maximum delay applicable on two consecutive symbols.

C. The frame transition condition: it implies that a pause has to be performed at the end of a frame transmission in order to scan the beam from its outmost angle back to its original transmission angle.

In the following, these three conditions are derived. Then, in subsection 4.2.4, the conditions for a given TSDM configuration are demonstrated visually.

4.2.1   The Beamwidth Condition

As explained above, the beamwidth condition states that "*a PAA must have a minimum number of antenna in order to be able to generate a beamwidth smaller than the angular distance between adjacent users*". This condition is relatively straight-forward to understand. Indeed, if 10 users should share a 120° sector, the beamwidth generated by the PAA should be smaller than $120/10 = 12°$. The equation associated with this condition is found with the following steps. First, assuming a Dolph-Chebyshev tapering of the PAA, the beamwidth $\Theta_{\mathrm{DC\_SL}}$ at a side lobe level A_{SL} is given by [65]

$$\Theta_{\mathrm{DC\_SL}}(N) = \frac{\pi}{2} - \mathrm{acos}\left(\mathrm{acos}\left(\frac{1}{z_0(N, A_{\mathrm{SL}})}\right) \cdot \frac{\lambda_{\mathrm{RF}}}{\pi \cdot d}\right) \tag{4.6}$$

where N is the number of antennas, λ_{RF} is the wavelength of the millimeter wave carrier frequency f_{RF}, and d is the antenna spacing and z_0 defined in [65]. Fig. 4.9 shows a typical array pattern when using Dolph-Chebyshev array tapering. When decreasing the desired side lobe level A_{SL}, the beamwidth becomes larger. In the definition of equation (4.6), the beamwidth is defined as the width where the array gain corresponds to the side lobe level, as opposed to the more common 3 dB definition.

Therefore, the number of user n_{users} that could share a sector of size θ_{sector} is given by:

$$n_{\text{users}} = \frac{\theta_{\text{sector}}}{\Theta_{\text{DC\_SL}}(N)} \tag{4.7}$$

Rearranging (4.7) according to Appendix B leads to **the beamwidth condition**:

$$N \geq 1 + \frac{2 \cdot \text{acosh}(A_{\text{SL}})}{\text{asech}\left(\cos\left(\sin\left(\frac{\theta_{\text{sector}}}{n_{\text{users}}}\right) \cdot \frac{\pi \cdot d}{\lambda_{\text{RF}}}\right)\right)} \tag{4.8}$$

where:

A_{SL} is the desired side lobe attenuation with the Dolph-Chebyshev tapering,

θ_{sector} is the size in [rad] of the sector,

n_{users} is the number of user using the cell sector,

d is the antenna element spacing, and

λ_{RF} is the wavelength of the millimeter wave carrier frequency f_{RF}.
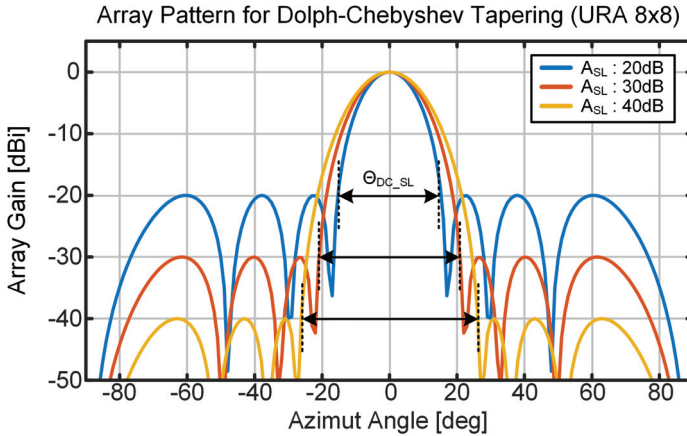
Fig. 4.9 - Array pattern with various Dolph-Chebyshev array tapering

4.2.2 The Symbol Transition Condition

The symbol transition condition implies that "the number of antenna of the PAA, i.e. its size, is limited by the maximum delay applicable on two consecutive symbols". The underlying problem leading to this limitation can be better understood with the help of Fig. 4.10. In Fig. 4.10 an exemplary PAA with N antennas is depicted. It is used to steer the beam towards two users (green and blue) at angle θ_i and θ_{i+1}, respectively. In Fig. 4.10 and in the following discussion, a PAA with a feeder based on time delay is firstly discussed. At the end of this sub-section, the case of a phase shifter driven PAA is analyzed.

The delays needed in the feeder to steer the beam can be computed for the different user i and for the various antenna positions p using

$$\Delta t_{p,i} = \frac{d_p \cdot \sin(\theta_i)}{c} \tag{4.9}$$
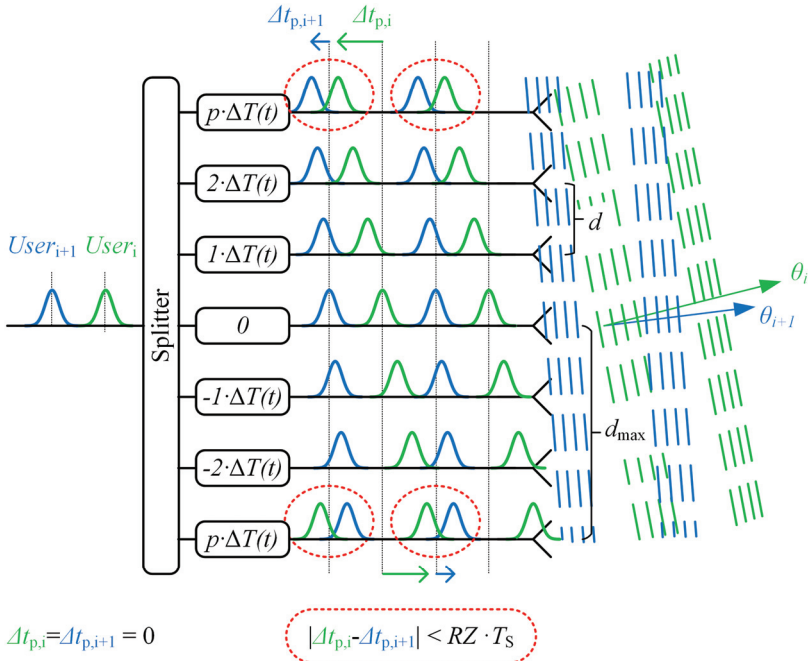
Fig. 4.10 - Symbol transition condition. (a) Delays needed to steer the beam towards two users located at θ_1 and θ_2. (b) Data signal with symbol rate T_S before entering the array feeder. (c) After the TTD in the array feeder, the symbol should not overlap too much to avoid ISI.

with d_p the position of the antenna defined by

$$d_p = p \cdot d \quad \text{with} \quad p \in \left[\frac{-(N-1)}{2}, \frac{(N-1)}{2}\right], p \in \mathbb{Z} \tag{4.10}$$

where d is the antenna elements spacing.

For ideal operation of the PAA, the delays computed with equation (4.9) will have to be applied using TTDs. However, a limitation arises while performing symbol-by-symbol steering: The introduced delay on a symbol can be as large as the spacing between two symbols. Considering a data signal as depicted in Fig. 4.10 with a symbol duration T_S, two consecutive symbols can only be delayed as long as ISI is not an issue. The maximum allowed time delay difference between adjacent users, occurring at antenna position $p = \pm (N-1)/2$, is limited to

$$\left|\Delta t_{p,i} - \Delta t_{p,i+1}\right| \leq RZ \cdot T_S \tag{4.11}$$

where RZ is the return-to-zero duration with $0 < RZ < 1$. The RZ duration depends on the type of pulse shape that is used and its resilience against ISI. Ideally, a return-to-zero (RZ) modulation scheme [59] should be used. As example, if one uses a 50% RZ modulation scheme, RZ can be set to 0.5. Inserting equation (4.9) and (4.10) in equation (4.11) leads to

$$\frac{(N-1)}{2} \cdot \frac{d \cdot |\sin(\theta_{i+1}) - \sin(\theta_i)|}{c} \leq RZ \cdot T_S \tag{4.12}$$

By rearranging the terms, the symbol transition condition is defined as

$$N \leq 1 + \frac{2 \cdot RZ \cdot T_S \cdot c}{d \cdot |\sin(\theta_{i+1}) - \sin(\theta_i)|} \tag{4.13}$$

To make the equation easier to use, some variables can be adapted. Thus, instead of using θ_i and θ_{i+1} for the user positions, let's consider the median steering angle θ_0 (angle between users i and $i+1$) and the angular spacing between users $\Delta\theta_{user} = \theta_{sector}/n_{users}$. θ_i and θ_{i+1} can thus be replaced by

$$\theta_i = \theta_0 - \frac{\Theta_{sector}}{2 \cdot n_{users}} \quad \text{and} \quad \theta_{i+1} = \theta_0 + \frac{\Theta_{sector}}{2 \cdot n_{users}} \tag{4.14}$$

Equation (4.13) thus becomes

$$N \leq 1 + \frac{2 \cdot RZ \cdot T_S \cdot c}{d \cdot \left|\sin\left(\theta_0 + \frac{\Theta_{sector}}{2 \cdot n_{users}}\right) - \sin\left(\theta_0 - \frac{\Theta_{sector}}{2 \cdot n_{users}}\right)\right|} \tag{4.15}$$

The worst-case scenario in equation (4.15) occurs when the denominator is maximal. This happens when $\theta_0 = 0$, and inserting this value into (4.15) leads to **the symbol transition condition**

$$N \leq 1 + \frac{RZ \cdot T_S \cdot c}{d \cdot \left| \sin \left(\frac{\theta_{\text{sector}}}{2 \cdot n_{\text{users}}} \right) \right|} \tag{4.16}$$

where:

RZ is the return-to-zero duration $0 < RZ < 1$, T_S

T_S is the symbol duration at the transmitter data rate,

c is the speed of light

d is the antenna element spacing,

θ_{sector} is the size in [rad] of the sector, and

n_{users} is the number of user using the cell sector.

In the case of a PAA based on phase shifters, the symbol transition condition cannot be understood in the same way. Indeed, the phase shifter will not delay the signal, therefore ISI will not take place in the feeder. However, another problem arises. To have constructive interferences at the users in different directions, two conditions must be met: 1) the waves must constructively interfere at the user with the correct phases. 2) the energy transmitted by the different antennas must reach the users within the symbol duration. Using tunable phase shifters, the phase front can easily be adjusted. The second condition is however more challenging. Indeed, when transmitting ultra-short pulse, it could happen that the energies from the various antennas do not reach the user at the same time. The delay between the pulses exactly corresponds to the true time delay that is required to steer a beam in a particular direction, see equation (4.9). To ensure that the energy is, at least partially received simultaneously the maximum delay error between two antennas is limited by the symbol duration, thus an equation analog to (4.11) can be written

$$\left| \Delta t_{p,i} - \Delta t_{-p,i} \right| \leq \Gamma \cdot T_S \tag{A.17}$$

with Γ, the allowed overlap mismatch with $0 < \Gamma < 1$. Note that this condition does not anymore depend on the users i but on the position of the antenna at the edge of the PAA $\pm p$. Replacing equation (4.9) and (4.10) in (A.17) leads to a **symbol transition condition for phase shifters**

$$N \leq 1 + \frac{\Gamma \cdot T_S \cdot c}{d \cdot |\sin(\theta_i)|}. \tag{A.18}$$

It can thus be concluded that the steering angle $\theta_i \approx \theta_{\text{sector}}/2$ is fairly limited if one needs a minimum time overlap between the pulses reaching the users. Yet, simulations have shown that one can tolerate worse conditions at the

antenna array edges. Indeed, the antennas close to the center of the array will perform very well in a phase shifter based PAA while those at the edge will suffer more from this limitation. The behavior of Eq. (A.18)is similar to the one of Eq. (4.16), it provides a very good estimation of the TSDM limitations during the conceptual design of the system. Yet, for both cases full time domain simulations are recommended to ensure proper operation. In addition to the limitation from Eq. (A.18), an array antenna based on phase shifters will also produce beam squint. Various frequencies are sent in different directions. However, this effect is negligible in our case as 1) the beamwidth is relatively large, 12° for 10 users sharing a 120° sector, and 2) the transmission distances are relatively small, from tens to a few hundreds of meters.

4.2.3   The Frame Transition Condition

The third condition implies that "a pause has to be performed at the end of a frame transmission to scan the beam from its outmost angle back to its original transmission angle". As already explained, it is better to use TSDM with consecutive angles between users and large angular steering at the end of a frame transmission to go back to the original angle. The consequence is however that very large delays compared to the symbol duration will be required to scan back through the whole sector. Thus, ISI can be avoided by performing a pause in the data transmission.

The frame transition condition is derived starting with equation (4.13), see above:

$$N \leq 1 + \frac{2 \cdot RZ \cdot T_S \cdot c}{d \cdot |\sin(\theta_{i+1}) - \sin(\theta_i)|} \tag{4.19}$$

In the case of the frame transition condition, the beam must be steered from the last user position (largest angle) back to the first user position (smallest angle). Therefor θ_i and θ_{i+1} can be replaced by

$$\theta_{i,i+1} = \pm \left(\frac{\theta_{\text{sector}}}{2} - \frac{\theta_{\text{sector}}}{2 \cdot n_{\text{user}}} \right) \tag{4.20}$$

with θ_{sector} the size of the cell sector. Replacing (4.19) in (4.13) lead to

$$N \leq 1 + \frac{RZ \cdot T_S \cdot c}{d \cdot \left| \sin \left(\frac{(n_{\text{user}} - 1) \cdot \theta_{\text{sector}}}{2 \cdot n_{\text{user}}} \right) \right|} \tag{A.21}$$

but instead of having a maximum allowed delay of $RZ \cdot T_S < T_S$, a pause in transmission can be performed replacing RZ by an integer ($n_{\text{slot}} - n_{\text{users}}$) corresponding to the number of empty symbols to be transmitted during the steering of the beam. Thus, the **frame transition condition is**

$$N \leq 1 + \frac{(n_{\text{slot}} - n_{\text{users}}) \cdot T_S \cdot c}{d \cdot \left| \sin \left(\frac{(n_{\text{user}} - 1) \cdot \theta_{\text{sector}}}{2 \cdot n_{\text{user}}} \right) \right|} \tag{4.22}$$

where n_{slot} is the length of the transmitted frames (including both active and "empty" users), n_{users} is the number of user in the cell, T_S is the symbol duration at the transmitter, c is the speed of light, and θ_{sector} is the size of the sector in radians.

4.2.4   Summary and Supported Area

The supported area of a TSDM setup can be computed using the three conditions described in the previous sections. For the sake of clarity, they are provided again here:

- The beamwidth condition, equation (4.8)

$$N \geq 1 + \frac{2 \cdot \text{acosh}(A_{SL})}{\text{asech} \left(\cos \left(\sin \left(\frac{\theta_{\text{sector}}}{n_{\text{users}}} \right) \cdot \frac{\pi \cdot d}{\lambda_{\text{RF}}} \right) \right)}$$

- The symbol transition condition, equation (4.16)

$$N \leq 1 + \frac{\Gamma_{ISI} \cdot T_S \cdot c}{d \cdot \left| \sin \left(\frac{\theta_{\text{sector}}}{2 \cdot n_{\text{users}}} \right) \right|}$$

- The frame transition condition, equation (4.22)

$$N \leq 1 + \frac{(l_{\text{Frame}} - n_{\text{users}}) \cdot T_S \cdot c}{d \cdot \left| \sin \left(\frac{(n_{\text{user}} - 1) \cdot \theta_{\text{sector}}}{2 \cdot n_{\text{user}}} \right) \right|}$$

Using these conditions, the ideal working point of a TSDM setup can be plotted. As an example, consider a 60 GHz ($\lambda_{\text{RF}} = 5$ mm) mobile cell split in three sectors of 120° ($\theta_{\text{sector}} = 120°$). Dolph-Chebyshev tapering is implemented for an array with half wavelength spacing ($d = 2.5$ mm). In addition, the receiver symbol rate is set to 2 GBd in order to be compatible with the channels of the IEEE 802.11ad standard at 60 GHz.

In the following figures, the transmitter symbol rate is set to 10, 22, and 36 GBd corresponding to frame length of 5, 11, and 18 time slots, respectively.

In Fig. 4.11, the ideal working point for a transmitter symbol rate of 10 GBd (frame length of 5 time slots) is found by using a PAA with 13 antennas and 4 active users. This corresponds to a total cell capacity enhancement of a factor 4 without impacting 802.11ad user equipment.
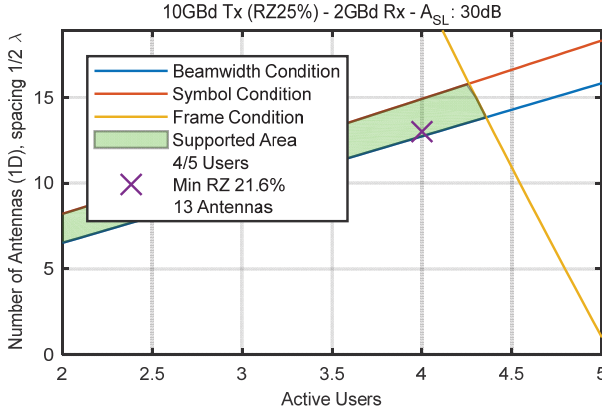
Fig. 4.11 - Supported area with a 10 GBd transmitter. The ideal working point for this configuration is found with a PAA comprising 13 elements and 4 actives users in frame of 5 times slots.

In Fig. 4.12, the ideal working point for a transmitter symbol rate of 22 GBd (frame length of 11 time slots) is found by using a PAA with 23 antennas and 8 active users. This corresponds to a total cell capacity enhancement of a factor 8 without impacting 802.11ad user equipment.
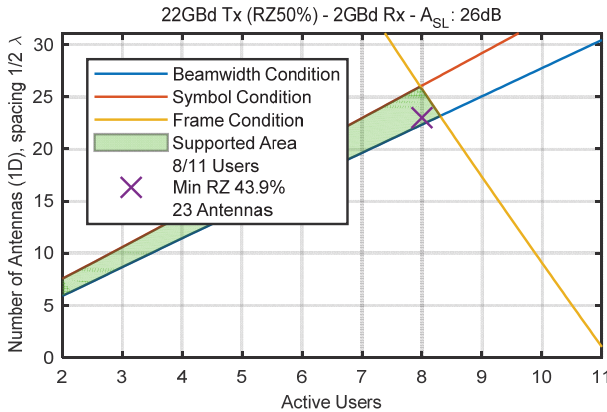
Fig. 4.12 - Supported area with a 22 GBd transmitter. The ideal working point for this configuration is found with a PAA comprising 23 elements and 8 actives users in frame of 11 times slots.

In Fig. 4.13, the ideal working point for a transmitter symbol rate of 36 GBd (frame length of 18 time slots) is found by using a PAA with 28 antennas and 11 active users. This corresponds to a total cell capacity enhancement of a factor 11 without impacting 802.11ad user equipment.
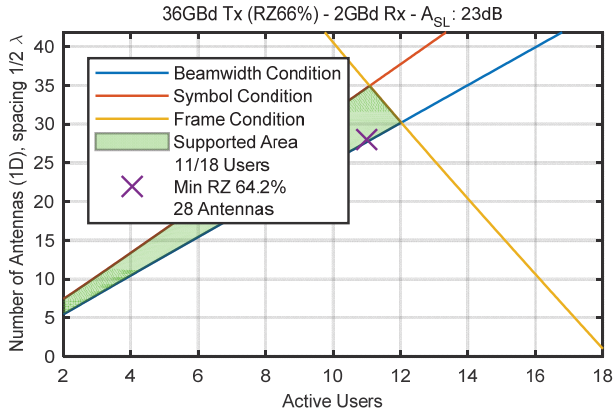
Fig. 4.13 - Supported area with a 36 GBd transmitter. The ideal working point for this configuration is found with a PAA comprising 28 elements and 11 actives users in frame of 18 times slots.

4.3 Optimizations to reach Tb/s Capacity

To reach Tb/s cell capacity as presented in the above sections, the TSDM parameters have been set according to those summarized in Table 4.2. These parameters define the structure of the TSDM frame that should be implemented.

Table 4.2 - TSDM parameters for a 60 GHz Tb/s mobile cell.

Tx Rate [GBd]	*36*
Return-to-Zero	66%
Frame length	18
Active users	11
Rx Rate [GBd]	2
Antennas (1D)	37
Channel [GBd]	22
Total Cell [Gb/s]	1056

Yet, there are other system parameters not related to the TSDM frame structure that require optimization in order to reach the desired capacity.

In this section, the impact of the following variables is discussed:

- The roll-off factor (ROF) of the transmitter's filter
- The roll-off factor (ROF) of the receiver's filter
- The Dolph-Chebyshev side lobe level of the array tapering
- The return-to-zero factor at the transmitter

It is important to note that independent optimization of the aforementioned variables greatly improves the results. Indeed, these variables are strongly tied to each other. Therefore, the optimizations in the following sub-sections are performed by sweeping at least two variables in a single simulation.

In parallel to these variables, other aspects of a communication system also influence the performance of TSDM. System specifications such as pulse shape, modulation format, matched filter type, array geometry, antenna spacing, equalizer training, or frequency and phase recovery algorithm equally play a role in the results. However, their impact and optimization methods are comparable to standard communication systems. Therefore, they are not discussed in the following. The focus of this section lies in effects that are specifically tied to TSDM.

4.3.1 Receiver Roll-off

Ideally in communication systems, one tries to use a matched filter in the receiver. For the TSDM case, this is however not possible as the transmitter filter is altered through the time-varying effect of the delay lines. In order to still be able to optimize the performance of TSDM, different filter types have been tried. The best results were found using a square-root raised cosine filter. In Fig. 4.14, EVM results for different roll-off factors versus the receiver filter bandwidth are depicted. Different effects are noticeable

- For Tb/s cell simulation, the frame length is 18 slots (see Table 4.2). Therefore the 2 GHz bandwidth of the receiver corresponds to 5.55 % (1/18) of the transmitter bandwidth. This value on the plot corresponds to the first minimum in the EVM curve. If a filter with a bandwidth lower than 2 GHz is used, ISI starts to appear from the next transmitted symbol (assigned to the user under investigation).

- Between 5.55 % and about 25 % receiver bandwidth, the curves for 0.1 and 0.5 roll-off factors show ripples. The zeros of these ripples are located at multiples of 5.55 %. The reason is that the Nyquist ISI criterion is partially fulfilled, e.g. partially fulfilled at 11 % means that one over two zeros of the filters shape lies at Rx symbols time slots.

- For the roll-off factor of 1, these ripples are barely noticeable as the tails of the filter (in time domain) are relatively flat. In other words, the Nyquist ISI criterion for the Rx symbol is always fulfilled.

- For filter bandwidth >25 %, the EVM increases again as 1) more noise is added and 2) ISI at the Tx symbol rate starts to play a role.
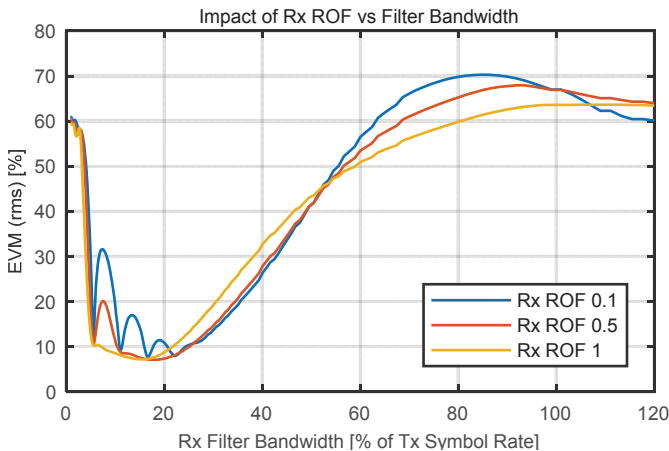
Fig. 4.14 - Impact of receiver roll-off factor for various filter bandwidth. The first minimum EVM occurs at 5.5 % of the transmitters bandwidth, i.e. 2 GHz. At other values, different effects deteriorate the performances.

4.3.2   Dolph-Chebyshev Sidelobe Level

The array radiation pattern (see section 2.2.2) is in TSDM, as for all other SDM schemes, significant for the cross-talk effects between the users. There are two aspects of the array pattern that lead to cross-talk:

- If the beamwidth is too large, the beam addressed to a user will extend to neighboring users. This will lead to a perturbation analog to inter-symbol interference.

- If the sidelobes are too high, a high "noise floor" will appear in the array pattern, i.e. this effect is not limited to the direct neighbor. Due to the many perturbations received from multiple beams, the effect of sidelobes that are too high can be considered as added noise.

As explained in section 2.2.5, the array pattern can be optimized by performing a tapering of the array. Applying a taper on an array means that not all the antennas of the PAA emit with the same power. A convenient way to adapt the array pattern is to use Dolph-Chebyshev tapering. Its main advantage is that the trade-off between beamwidth and sidelobe level can be easily adapted.

Fig. 4.15 shows the effects of various sidelobe level in TSDM. The best results are obtained with a Dolph-Chebyshev sidelobe level parameter of 25 dB as it provides a good trade-off between beamwidth and sidelobes. With <25 dB, the beamwidth is smaller and thus the ripples in the first part of the curve are attenuated. However, the "noise floor" is higher due to the sidelobe contribution. For a sidelobe level of >25 dB, the noise floor is reduced (see right part of the plot). Yet, the EVM is worth for the range 0-20%, where it matters. This is due to the interference of the direct neighbor.
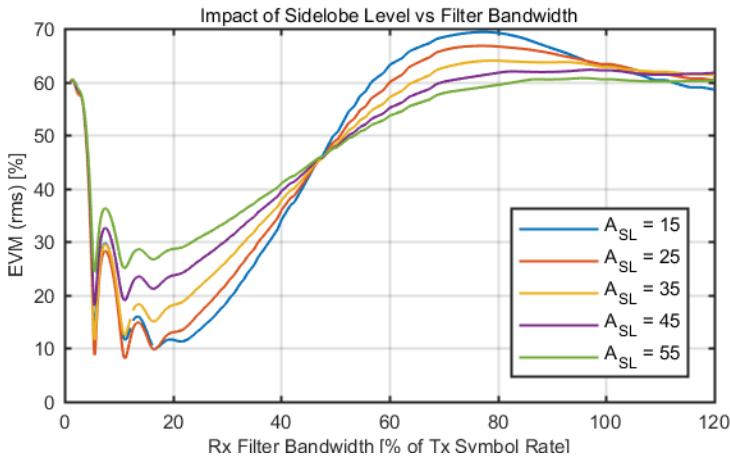
Fig. 4.15 - Impact of sidelobe level in TSDM. A good trade-off between sidelobe levels and beamwidth is crucial in the design of the PAA for TSDM as both effects lead to perturbations.

4.3.3   Return-to-Zero Percentage

In the previous section, the impact of the sidelobe level on the performance of TSDM was discussed. From Fig. 4.15, some trends can be observed when a good trade-off between sidelobe level and beamwidth is not found. Yet, the discussion above depends on other parameters, the main one being the return-to-zero (RZ) percentage defined in the transmitter.

If the beamwidth is large, it takes slightly more time at a given angular velocity for the active user to be out of sight of the beam addressed to the next user. Therefore, the RZ percentage defined in the transmitter plays a major role. If the off-time is increased, the beam has more time to switch from one user to the next. Due to this observation, better EVM values are expected for higher RZ modulation. In addition, it is obvious that energy has to be transmitted. Thus, RZ cannot be too large.

The cross-influence between RZ value and sidelobe level is depicted on Fig. 4.16. Obviously, these results largely depend on other parameters, but one can see that the area in which TSDM works best is limited.
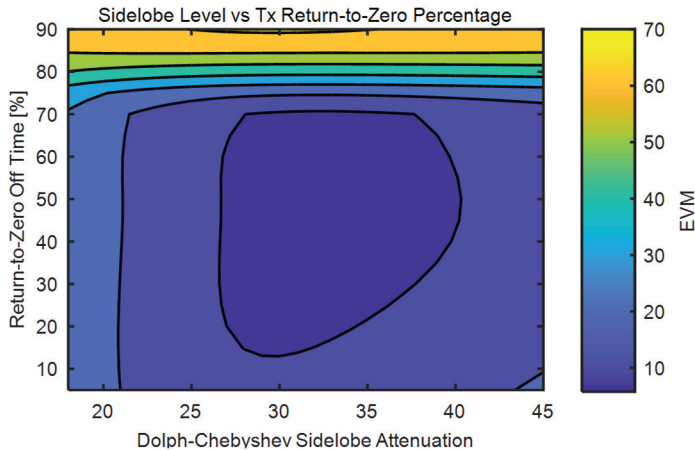
Fig. 4.16 - Sidelobe level and return-to-zero percentage. The area with low EVM (dark blue) is limited by the influence of the sidelobe level and the chosen percentage of the return-to-zero modulation scheme.

4.3.4   Roll-off Factor of Transmitter and Bandpass Filtering

In section 4.3.1 above, the impact of the receiver roll-off factor was discussed. There are however two additional aspects that need to be discussed. First the impact of the transmitter roll-off factor and second and more important, the influence of the TSDM architecture.

First, let's examine a TSDM implementation with lowpass filter (LPF) in the receiver, see Fig. 4.3. In such a case, depicted on Fig. 4.17, the EVM is mainly influenced by the transmitter roll-off factor. Indeed, the variations along the Y axis of the plots are almost negligible. The reason is that the receivers only receive return-to-zero signals. Therefore, the tails of the filter response (defined by the receiver ROF) in time domain do not play a large role in the receiver.
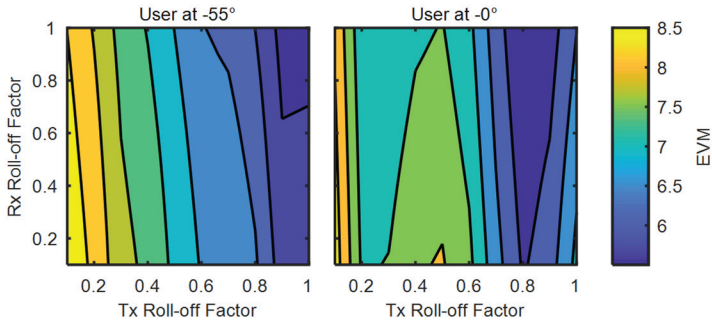
Fig. 4.17 - Transmitter versus receiver roll-off factors for a LPF configuration. It can be seen that in a LPF configuration, the results are mainly impacted by the roll-off factor of the transmitter.

In the case of a bandpass filter (BPF) TSDM configuration as described in Fig. 4.4, the situation drastically changes. As it can be seen from Fig. 4.18, the results are now mainly influenced by the receiver roll-off factor.
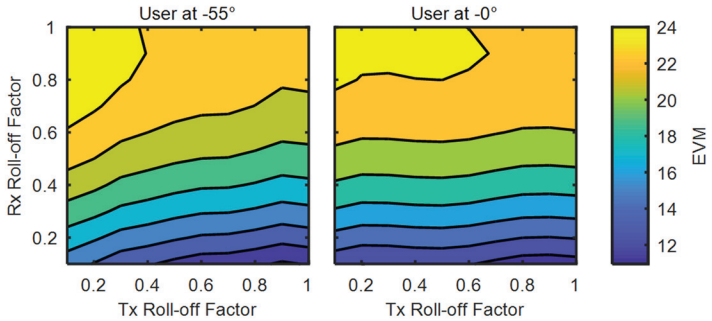
Fig. 4.18 - Transmitter versus receiver roll-off factors for a BPF configuration. It can be seen that in a BPF configuration, the results are mainly impacted by the roll-off factor of the receiver.

4.4 Ultra-fast Beam Steering Simulation

The simulation results on ultra-fast beam steering presented in previous sections are based on multiple optimizations that have been performed using a specially developed MATLAB environment. This simulation environment has been initially developed by Samuel Welschen in [57]. In this section, a short summary of the developed simulation environment is provided.

Section 4.4 is adapted from work presented in [57]:

Simulation of Ultra-Fast Beam Steering Systems

S. Welschen, Master Thesis No. 70,
Supervisors: R. Bonjour, Prof. Dr. J. Leuthold
Institute of Electromagnetic Fields (IEF), ETH Zurich, 2016.

4.4.1 Goals of the Simulation Environment

To be able to simulate the influence of various parameters in ultra-fast beam steering systems, a dedicated MATLAB environment has been developed. The environment is able to perform end-to-end BER simulations and leverage parallel computing to allow a fast analysis of the system performances through parameter sweeps.

The simulations are implemented in the time domain to enable the analysis and optimization of the simulated signals. A time domain implementation is also necessary to implement the time-varying responses of delay elements

4.4.2 Features of the Simulation Environment

The MATLAB environment has the following features:

- Preparation and evaluation of parallel simulations and variable sweeps using HTCondor (ETH D-ITET)
- Support for on-off keying (OOK), BPSK, QPSK and QAM modulation.
- Support for TTD, phase shifter, and various CPSS implementations.
- 2D beam steering for an adjustable number of receivers
- OFDM and LDPC encoding according to the IEEE 802.11ad standard
- Support for different transmitter and receiver filters
- Support for signal detection using a matched filter
- Analysis of BER, EVM and received power
- Generation of BER maps and variable sweep plots
- Generation of signal plots and eye diagrams

4.4.3   Overview of the Simulation Environment

Fig. 4.19 shows an overview of the MATLAB simulation implemented in [57]. As can be seen from the figure, the main stages are:

1. Data and signal generation in the baseband followed by pulse shaping and frequency up-conversion

2. Delay elements, modelled using the time varying impulse response

3. Transmission with modelling of free space path loss and propagation delay

4. Reception of the signal and addition of AWGN noise

5. Frequency down-conversion and lowpass filtering in the receiver

6. Signal detection and de-mapping

7. Calculation of the BER and saving of the simulation sweep

If parallel simulations are performed, input files with the simulation settings are generated before the simulations are executed on simulation hosts. After completion of the simulations, the outputs are collected and evaluated.

As discussed in 4.1.3, the lowpass filter in the receiver can be replaced by a bandpass filter in the transmitter to avoid the power loss associated with the restriction of the simulation bandwidth.
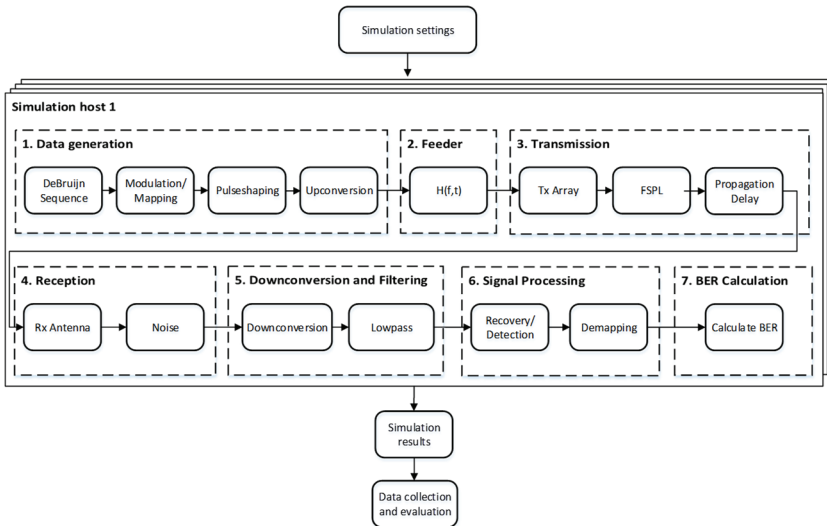
Fig. 4.19 - Flowchart of the ultra-fast beam steering MATLAB simulation environment.

5   Demonstrations of ultra-fast Beam Steering

One of the main advantage of MWP technologies compared to standard microwave techniques is its potential for ultra-fast settling times. Thanks to this increase in controlling speed, MWP enables phased array systems with capacities never demonstrated before.

The potential of ultra-fast beam steering in the field of wireless communication is detailed in chapter 4. Yet, in order to prove the feasibility of ultra-fast beam steering and its associated multiplexing concept, experimental demonstrations in the laboratory were required. This chapter combines two demonstrations of ultra-fast beam steering; one using the proposed CPSS concept and one using integrated photonics.

Section 5.1: Ultra-fast Millimeter Wave Beam Steering

The publication of section 5.1 presents a first demonstration of ultra-fast beam steering using a phased array antenna driven by the proposed complementary phase shifted spectra (CPSS) technique, see section 3.1. The key results of this experiment, i.e. a settling time of the beam direction lower than 50 fs, is still unmatched by orders of magnitude in other publications worldwide. These results demonstrate that CPSS provided, as assumed, new capabilities to phased array antenna systems based on MWP.

Section 5.2: Plasmonic Phased Array Feeder enabling ultra-fast Beam Steering at Millimeter Waves

In section 5.2, an ultra-fast beam steering demonstration is presented relying on an integrated plasmonic array feeder. The utilization of plasmonic enables the smallest MWP phased array feeder ever published. This work, awarded best student paper award at AVFOP & MWP conference 2016 (Long Beach USA), not only offers a small footprint but also sets a new settling time record for integrated MWP array feeders.

5.1 Ultra-fast Millimeter Wave Beam Steering

Abstract: In this paper, we demonstrate ultra-fast millimeter wave beam steering with settling times below 50 ps. A phased array antenna with two elements is employed to realize beam steering. The phased array feeder is implemented with a recently introduced time delay line that provides, at the same time, ultra-fast tunability, broadband operation and continuous tuning. Our implementation is used to perform symbol-by-symbol steering. In our demonstration, the beam direction is switched between two sequentially transmitted symbols towards two receivers placed 30° apart. We show successful symbol-by-symbol steering for data streams as fast as 10 GBd. The suggested scheme shows that ultrafast beam steering is becoming practical and might ultimately enable novel high-bit rate multiple access schemes.

5.1.1 Introduction

To meet the relentlessly growing bandwidth of wireless communication, moving carrier frequencies towards millimeter wave (mmWave) is a promising path [13, 68, 149]. However, higher carrier frequencies experience higher free space path loss [21], increasing the total losses of the wireless link. This drawback can be compensated by using phased array antennas (PAAs) [67]. Besides providing higher reach and reduced crosstalk [150], PAAs enable beam steering in order to direct the energy to multiple users. Non-mechanical and thus fast beam steering is achieved by implementing active feeder networks (FNs) in front of the PAAs [63]. The FNs create and delay copies of the signal using true-time delays (TTDs). If the elements used to delay the signals are not ideal, beam squint will occur, i.e. different frequencies will be steered in different directions.

Millimeter wave PAA systems call for a large fractional bandwidth which makes implementation of TTDs in electronics difficult. Conversely, microwave photonics (MWP) where the signal processing is done relying on photonic technologies rather than electronics offers ample bandwidth. Several MWP PAA architectures have been proposed lately. Such devices could be based on spatial light modulators (SLM) [91-95], ring-resonators [96-101], switched delays [102, 103], semiconductor optical amplifier (SOA) [104, 105], gratings [82, 83, 100, 106-110], dispersive fibers [111-116] and tunable phase shifters [117]. While all these devices are optimized for specific applications, none

provide large bandwidth, continuous tuneability, and low settling times as needed for ultra-fast beam steering.

In this paper, we demonstrate an ultra-fast beam steering concept relying on microwave photonics processing. The delay lines in the FN are based on a novel microwave photonics true-time delay scheme called Complementary Phase Shifted Spectra (CPSS) which we recently published in [138]. The advantages of ultra-fast beam steering are demonstrated with a proof-of-concept mmWave radio-access network leveraging symbol-by-symbol steering. This technique enables highly flexible bandwidth allocation. Thanks to that, the cost and power consumption of the receiver electronics can be strongly reduced. The demonstration is performed for a transmitting antenna array, but the same concept could be applied to receiving arrays in a similar way. Moreover, the proposed solution can be fully integrated on photonics platforms as it only relies on standard components such as couplers, waveguides, and phase modulators.

This paper is organized as follows. A short review on the main challenges in next generation mmWave communication systems is provided in section5.1.2. In section 5.1.3, we detailed the architecture of our ultra-fast beam steering scheme. The proof of concept demonstration with beam steering between 10 GBd symbols is described in section 5.1.4. Finally, we draw our conclusions in section 5.1.5.

5.1.2   Challenges in Millimeter Wave Communications

The use of mmWave carrier frequencies for communication links brings a number of challenges that will be discussed in this section.

Free Space Propagation Losses

Increasing the carrier frequency comes at the price of higher free space path losses [21]. The power budget in a wireless link can be derived from the Friis formula [88]

$$P_{\text{out}} - P_{\text{in}} = L + G_t + G_r + FSPL \tag{5.1}$$

where P_{in} and P_{out} are the input and output power of the transmitting and receiving antenna, respectively, while L corresponds to the link losses. G_t and G_r are the gain of the transmitting and receiving antennas, respectively, whereas $FSPL$ is the free space path loss defined as

$$FSPL = -20 \cdot log_{10} \left(\frac{4\pi \cdot d \cdot f_{\text{RF}}}{c} \right), \tag{5.2}$$

where f_{RF}, d and c are the carrier frequency, the distance between the antennas, and the speed of light in the propagation medium, respectively. Combining the FSPL and the atmospheric losses provides a good estimate for the required specification of the various components in the link. Assuming an attenuation of 17 dB/km for 50 mm/s rain [150], the total transmission losses

for a 60 GHz system are reported in Table 5.1 for different distances. The losses are as high as 103 dB for a 50 m link. Doubling the distance further increases the losses by 7 dB.

Table 5.1 - Losses for a 60 GHz Link.

d [m]	10	20	50	100	200
L_{link} [dB]	88	94	103	110	117

To overcome these high losses the power margin $P_{\text{out}} - P_{\text{in}}$ from Eq. (5.1) should be maximized. This can be achieved by increasing the transmitted power and reducing the minimum power required in the receiver. More importantly, high directivity antennas have to be implemented in order to focus the beam, i.e. increasing G_t and G_r in Eq. (5.1).

Point-to-Multipoint

To support point to multipoint transmission, directive beams from high gain antennas have to be steerable in order to combine both high reach and spatial flexibility. PAAs with active FNs are a solution to this challenge [45]. PAAs are realized by driving n tunable time delay elements with an equally split source signal [151], see Fig. 5.1. It can be deducted from Fig. 1 that two adjacent antennas require a time delay difference $\Delta t = -x/c = -\sin\theta \cdot d/c$, where c represents the speed of light. [63]. The propagation direction can be controlled by adjusting the signal delay Δt in each radiating antenna element [151].
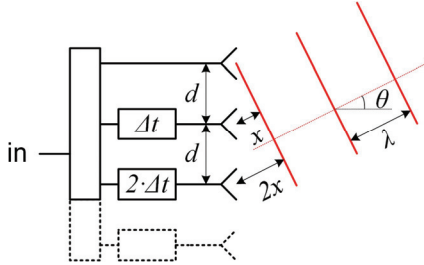
Fig. 5.1 - Principle of phased array antenna (PAA). In the feeder network of the PAA, the input signal is first split into n copies. Each of the copies is delayed with an appropriate value Δt such that the interferences after radiation point towards the desired direction θ [151].

5.1.3 Ultra-Fast Beam Steering

To enable broadband ultra-fast symbol-by-symbol beam steering, a PAA is needed in which each antenna in the feeder network (FN) requires a well-defined TTD. An ideal TDD provides a frequency independent unitary power response and a linear phase response. Varying the delay value changes the slope of the phase response [138]. In practical systems, TTDs are approximated by various methods. In order to compare various TTDs implementations, we have performed simulations [151]. Our study provides a simple metric to assess the performances of FNs with the various TTDs. Here, we highlight the two most relevant approaches from [151] enabling ultra-fast steering.

Array Feeder based on Phase Shifters

FNs can be built by replacing the TTDs in each of the antenna elements with phase shifters [127].When approximating TTD with phase shifters, the phase response as a function of frequency is constant instead of linear [138]. Due to this approximation, beam squint will occur. Different spectral components will be steered in different directions.
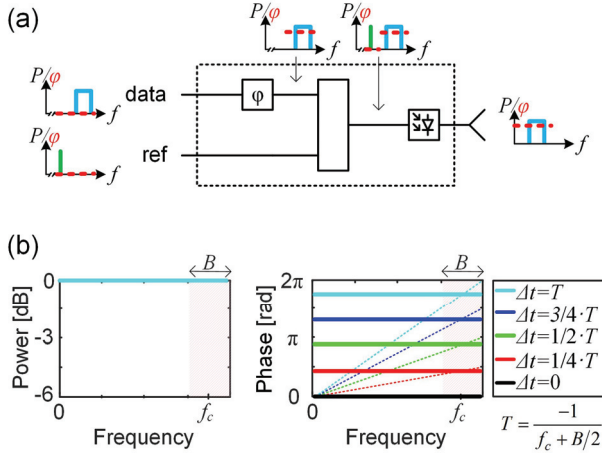
Fig. 5.2 - PAA feeder based on a TTD approximated by phase shifters. (a) Array element consisting of a phase modulator, a combiner and a photodiode that down-converts the optical signals into an RF signal before being fed to the antenna. (b) The TTD delay approximated by phase shifters features an ideal power frequency response (left) without any loss compared to its ideal counterpart. Yet the phase response (solid lines in right plot) shows errors when compared to the ideal TTD (dashed lines). This will lead to a beam squint in the PAA. [151]

An element of a MWP PAA based on a phase shifter is schematically depicted in Fig. 5.2(a). Here, the phase shifters are placed on the input port carrying the data laser. The phase shift will delay the beating of the reference and data

signal in the photodiode. Fig. 5.2(b) shows that the power frequency response is perfectly constant across all frequencies. The phase response corresponds to a constant phase offset applied to all frequencies equally, Fig. 5.2(b). In the frequency band of the signal (shaded area in Fig. 5.2(b)), the phase error is directly proportional to the fractional bandwidth, i.e. a system with a fractional bandwidth of e.g. 25% will have a phase error of up to 25% for $\Delta t = \Delta t_{\max}$. This error needs to be compared to the ideal TTD phase response - see dashed lines in Fig. 5.2(b) - and will lead to beam squint.

Array Feeder based on CPSS-SCT

In this section we describe a FN based on tunable delay units providing ultra-fast, broadband, and continuous tuning [138]. The technique called complementary phase shifted spectra (CPSS) imitates an ideal TTD. The principle of CPSS time delay can be understood with the help of Fig. 5.3. In this figure we plot the amplitude and phase response as well the phasors of a signal at various stages of the TTD element. First, the input signal is spectrally split using a delay interferometer into two complementary spectra (CS), see the phase and frequency responses at the upper and lower arms behind the delay interferometer. Secondly, one of the CS receives an additional phase shift from a phase modulator. When the two CS are recombined one obtains a phase frequency response close to the ideal phase response of the ideal TTD.
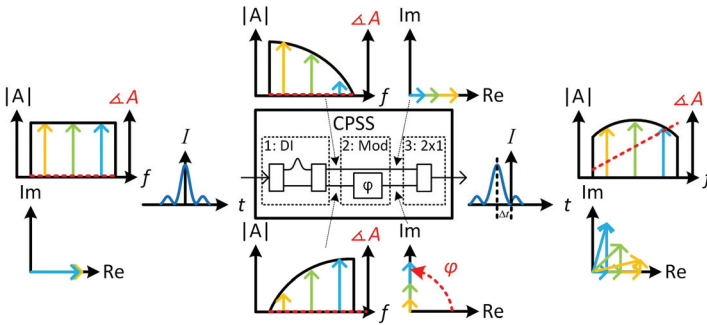
Fig. 5.3 - Ultra-fast tunable TTD based on complementary phase shifted spectra (CPSS). The input signal is first split into two complementary spectra using a delay interferometer (DI). Before being recombined, one of the signals is phase shifted by an optical phase modulator. The result is an almost ideal phase response. [138]

Such a CPSS delay element can be arranged into a PAA feeder by combining the CPSS signal with a reference laser, see Fig. 5.4(a). Once both lasers are combined they are directly sent to the photodiode, generating the microwave signals.

To improve the performance of the scheme, the CPSS scheme can be combined with a separate phase tuning of the reference laser [151]. This can

be obtained by adding a phase-modulator to the reference laser. This so-called separate carrier tuning (SCT) [152, 153] technique allows to add an offset phase to each PAA elements. While the CPSS gives the possibility to control the slope of the phase response, the SCT adds and offset so that the unit can be operated at higher frequencies. The resulting power and phase frequency responses are plotted in Fig. 5.4(b) for a filter optimized with a fractional bandwidth of 25% (shaded area). The phase response in the shaded area is close to ideal (dashed lines) which mean that beam squint should not occur.
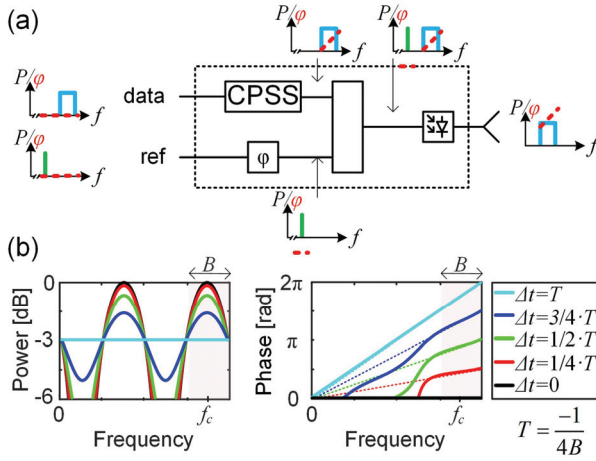
Fig. 5.4 - PAA feeder using CPSS-SCT. (a) An array element based on the CPSS-SCT scheme is built by applying the CPSS scheme on the laser carrying data and, in parallel, adjusting the phase of the reference laser by another phase shifter. (b) The power response (left) shows variations of about 1.5 dB in the bandwidth of interest while tuning the delay. The phase response (solid lines) is close to the ideal TDD response (dashed lines) for a designed fractional bandwidth of 25% (shaded area). [151]

Scheme Comparison

To assess PAA FN based on either phase-shifters or CPSS-SCT tuning we compare the 3 dB supported range [151] for both implementation and for various array sizes. We define the 3 dB supported range as the range within which beam steering for a given fractional bandwidth can be achieved with a gain flatness better than 3 dB, see Fig. 5.5. The dashed lines correspond to a PAA based on simple phase shifters (Fig. 5.2) while the solid lines correspond to a PAA FN relying on CPSS-SCT (Fig. 5.4).

For a PAA with 16×16 elements (green curves) providing a gain of 24 dB, CPSS-SCT allows a steering range of 120° for a fractional bandwidth up to 17%. A PAA FN relying on simple phase shifters would only support a steering range of 85°.

In our ultra-fast beam steering demonstration, we use CPSS without SCT. This simplification has been done in order to demonstrate both ultra-fast steering and CPSS with on-the-shelf components. This will not reduce the functionality but only come at the expense of the steering range [151].
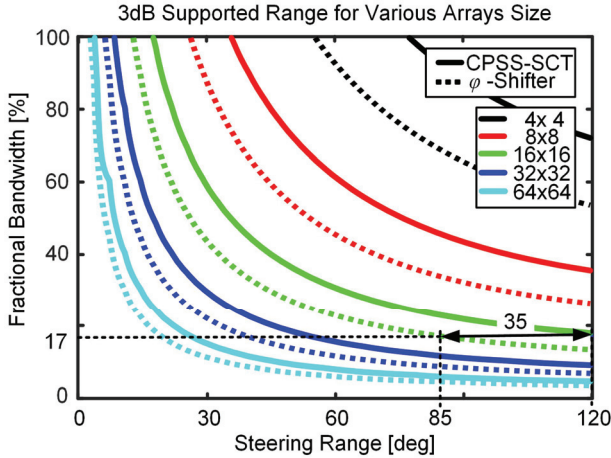
Fig. 5.5 - Simulated 3 dB supported range. The curves show for various array sizes (various colors), the area in which the gain flatness is better than 3 dB for a particular fractional bandwidth and steering angle. FN based on CPSS-SCT (solid curves) provides larger steering range compare to phase shifter (dashed lines) in all cases. For an exemplary V-band communication link using frequencies from 54 to 64 GHz (17% fractional bandwidth) CPSS-SCT provides steering up to 120° while phase shifter FNs are limited to 85°. [151]

Another analysis of the CPSS-SCT array feeder is performed in Fig. 5.6. It shows how the roll-off factor of a squared root raised cosine filter in the transmitted signal impacts the performance of a communication link based on a 16x16 array at 35 GHz. The simulations are performed in time domain by transmitting for each data point 1 million symbols. The receiver has been implemented with a matched filter and the corresponding roll-off factor. The results show that the smaller the roll-off, the better. This is due to the fact that larger roll-off factors require a larger bandwidth.
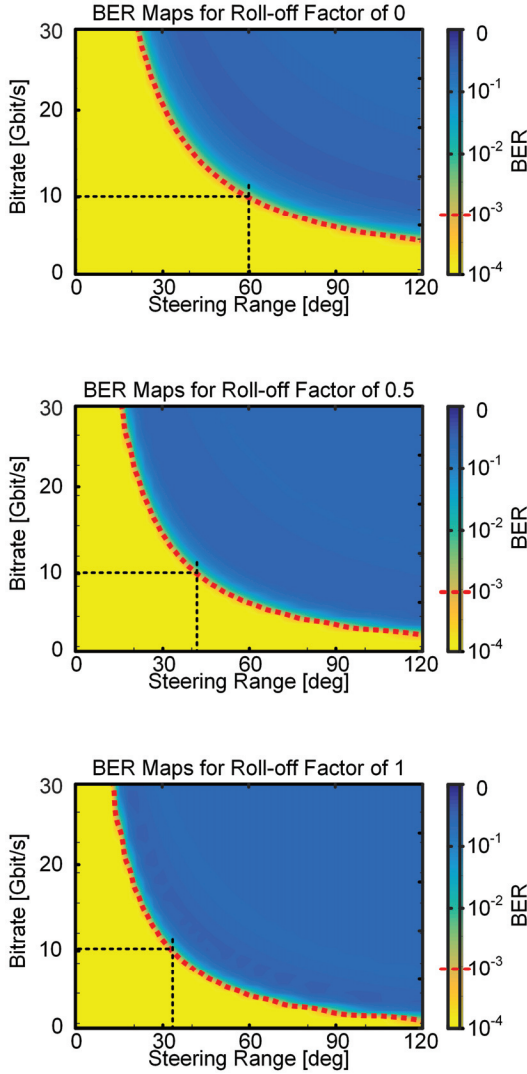
Fig. 5.6 - Impact of roll off factor on CPSS-SCT array feeders performances. The simulations are performed for a 16x16 element array at a carrier frequency of 35 GHz. The black dashed line corresponds to the 10 Gb/s experiment with a fractional bandwidth of 29% as discussed further below. It can be see that increasing the roll-off factor decreases the steering range. This can be interpreted by the fact that increasing the roll-off factor increases the bandwidth of the signal.

5.1.4 Demonstration of Ultra-Fast Beam Steering

Subsequently, we demonstrate ultrafast beam-steering in an access network scenario by performing symbol-by-symbol beam steering. Symbol-by-symbol beam steering is a kind of time space division multiplexing and provides two main advantages. First, it enables beamforming in the remote phased array antenna (PAA) which extends the reach of the link. Second, the data rate received by the end-user is linearly reduced by the number of user equipment (UE). Therefore, the hardware complexity and cost are strongly reduced and can rely on cheaper receiver (Rx) electronics. Ultra-fast beam steering is achieved based on microwave photonics as explained in the previous section. For the sake of simplicity, we will confine ourselves to a PAA FN with only 2 antennas and to a CPSS implementation without a SCT-scheme. This will only limit the tuning range but not degrade the functionality.

RAN leveraging Symbol-by-Symbol steering

Our proposed TSDM based MWP radio access network (RAN) implementation is depicted in Fig. 5.7 [154]. A transmitter located in the central office generates a radio-over-fiber (RoF) data signal and a steering control (SC) signal, see Fig. 5.7(a). The spectrum of the RoF signal is displayed in Fig. 5.7(b). The desired microwave carrier frequency f_{RF} corresponds to the frequency difference between a reference and a carrier laser, f_1 and f_2 respectively [67]. The data for the different UEs and the SC signals are generated by a digital signal processor (DSP) within the transmitter. The CO needs to know the exact position of the UEs in order to steer the signals correctly in the remote antenna unit (RAU) of the BS. This information could be provided actively by the UEs or measured in the RAU using direction of arrival (DoA) in a duplex implementation of our concept.

The RAUs, Fig. 5.7(c), are built using a MWP PAA with ultra-fast tunable delay line elements (CPSS). The SC is transmitted to the RAU on a separate optical channel. The time delays for each element of the PAA are set in the feeder network of the RAU using the SC signal.

As depicted in Fig. 5.7(d), the UEs require first an RF front end to down-convert the wireless signals. A low pass filter is included to reduce the bandwidth of the signal. The signal processing can be performed in a low-cost receiver as the UEs only receive during their assigned time slots.

Fig. 5.7 - Concept of mmWave RAN based on ultra-fast beam steering. The central office (CO) in (a) sends time division multiplexed (TDM) data frames to multiple users via a remote antenna unit (RAU). The radio-over-fiber (RoF) signal is shown in (b). The RAU (c) uses the steering control signal sent from the CO to steer the time slots of the symbol based TDM signal to different directions, acting as a spatial demultiplexer. The user equipment (UE) is based on an RF front end that down-converts the signal to baseband. A low pass filter (LPF) is implemented to reduce the noise level. In the receiver of the UE, low cost analog-to-digital converters (ADC) and digital signal processors (DSP) can be used as the UE only receives signals during its predefined time slot. If a 10 Gb/s TDM is demultiplexed to 3 users, the UEs will only require 3.3 Gb/s receivers. To prevent transmission outage if the line-of-sight condition is lost, multiple BS have to covers the same area. This also increases further the available bandwidth per area while inter-cell-interferences are prevented by the directed beams.

As with other mmWave RAN schemes, the transmission from the BS to the UEs works well with line-of-sight (LoS) conditions. If the LoS is interrupted by obstacles or simply because the users turning around, the transmission will be reduced. A solution to this problem was already proposed [15]. It relies on a multi-hop relaying where multiple BS covers the same area. In Fig. 5.7, this is exemplarily realized with BS on both side of the river. Increasing the BS density also increase the available bandwidth per area while inter-cell-interferences are prevented by the directed beams.

Experimental Setup

We experimentally demonstrate ultra-fast beam steering using the setup depicted in Fig. 5.8. The architecture of the proposed system consists mainly of two parts, a RoF transmitter and a PAA in the RAU with two antennas. A 10 Gb/s TDM data signal is generated by an arbitrary waveform generator (AWG M8195A). A root-raised cosine pulse shape with a roll-off of 0.8 is used. The data modulates the intensity of a CW laser with frequency f_2 by means of an external lithium niobate (LiNbO$_3$) Mach-Zehnder modulator. The output of the modulator is combined with a second laser of frequency f_1. The two laser carriers are separated with a frequency difference corresponding to the desired millimeter wave carrier, i.e. $f_{RF} = f_2 - f_1 = 35$ GHz. The optical spectrum is shown in Fig. 5.7(b). The phase fluctuations between the two free running lasers are not impacting the results as this first proof-of-concept is realized with on-off-keying signal.

At the RAU, the combined signal is split and fed to a 2x1 array feeder. On antenna 1, a CPSS filter is used to tune the delay based on the control signal

it receives directly from the AWG. The control signal for this proof-of-concept demonstration is transmitted through a RF cable rather than through a parallel optical channel as proposed in Fig. 5.7. However, proper calibration to synchronize the data and the control signal is required. On the path to antenna 2, a fixed time delay (TD) line is used to compensate any length difference between the two paths to the two antennas. In both paths, the out-of-band noise mainly from the EDFAs is removed by an optical band-pass filter. The photonic mixing of the two lasers at the two 40 GHz photodetectors (PDs) from Albis Opto generate the 35 GHz RF-signal. RF amplifiers are used to boost the electrical signals form the PDs to the required 10 dBm. Finally, the electrical signals are fed to two specially designed Vivaldi antennas, see Fig. 5.9. At the UEs, two horn antennas separated by 30° receive the RF signals, which are analyzed using a real-time oscilloscope (DSO-X 96204Q).

For the system to function properly, synchronization of the signals on the paths to the two transmitter antennas and the steering control is critical. The steering control signal of inset Fig. 5.8(a) must be synchronized with the transmitted signal shown in the inset Fig. 5.8(b) to enforce steering only at the symbol transitions rather than in the middle of the symbol. After the CPSS modules, the signal (c) is an overlap of a delayed and an undelayed copy. The second signal for antenna 2, inset (d), is synchronized to that of antenna 1 using the fixed time delay (TD). Then, the PAA transmits (c) and (d) to the two UEs. The received eye diagrams are depicted by insets (e) and (f). These eye diagrams show the case of symbol-by-symbol steering as evidenced by their complementary nature. When one antenna receives a symbol, the second receives nothing. This way, the effective data rate is reduced to 5 Gb/s corresponding to a 50 % RZ signal.
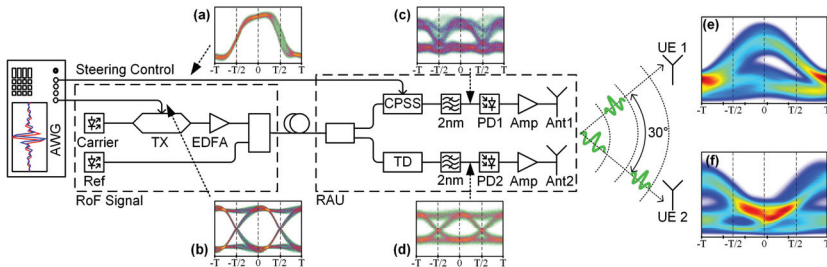
Fig. 5.8 - Experimental setup. An AWG generates two signals; a CPSS drive signal (a) and a PRBS15 NRZ TDM signal (b) which is encoded onto a carrier. The amplified carrier is combined with the reference line and fed to the remote antenna unit (RAU). In the RAU the signal is split into two paths, one is guided through the CPSS tunable true time delay (c) and the second through a fixed time delay (TD) line (d). The TD compensates the path difference between the two arms. Finally, the photodiodes (PD) 1 and 2 generate the 35 GHz RF carrier through photonic mixing. (e) and (f) show exemplary eye diagrams of the received signal at the two users. They demonstrate the symbol-by-symbol switching capacity.
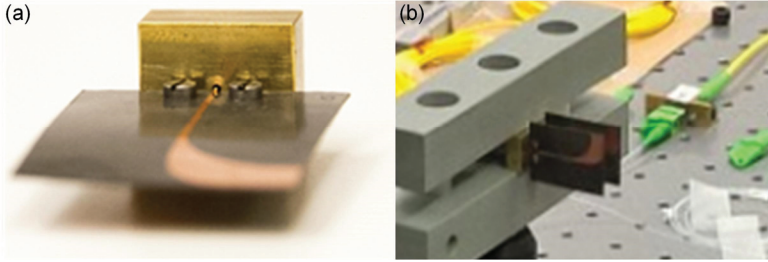
Fig. 5.9 - The 2x1 array of the RAU is made of two custom designed Vivaldi antennas. (a) Picture of the Vivaldi antenna used for the experimental demonstration. The antennas are designed to support frequencies from 30 to 40 GHz. (b) Antennas arranged in a 2x1 array with an antenna spacing of λ.

Results

For reference, we first measured the steering capability of our implementation with frame based TDM sequence. A 10 Gb/s signal on a 35 GHz carrier is steered to deliver 8-symbol frames to the users. Fig. 5.10(a) shows the received signal for the two UEs. The white and gray backgrounds show the time slots where either only User 1 (white slots) or User 2 (gray slots) receives the signal. The inset shows a sample of the transition where the beam is steered from User 1 to 2. The slight cross talk seen in case of User 2 is due to angular misalignment which can be avoided. The power suppression between the users is of about 6 dB between User 1 and 2. This could be largely improved by using an array with more antennas.

Further, we investigated the performances of our scheme using symbol-by-symbol steering. Fig. 5.10(b) shows the quality factor Q^2 [dB] at UE 1 for two different receiver bandwidths while the transmitter transmits 10 Gb/s. The black curve corresponds to a 10 Gb/s RX and the red curve to a 5 Gb/s Rx. The good match between the curves shows that receivers with lower bandwidths (5 GHz instead of 10 GHz) can be used without degradation of the signal quality. The small inset in Fig. 5.10 (b) depicts the eye diagram after the 5 Gb/s Rx. Fig. 5.10(c) shows how the Q^2 [dB] gradually degrades when the transmission distance is increased to 5 m. The reach limitations are due to the low gain offered by the 2x1 phased array.
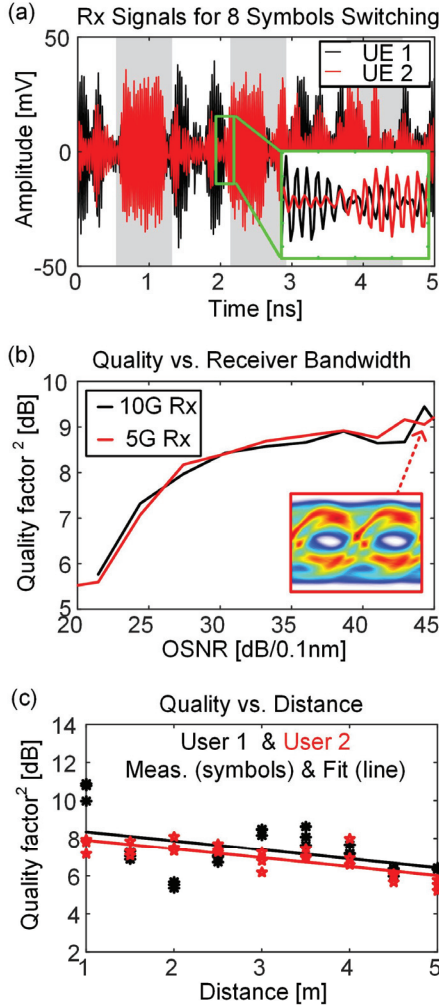
Fig. 5.10 - Experimental results. (a) Time signal measured at user 1 and 2 for 8-symbol frame steering. The inset shows a zoom in on the transition between the users. It can be seen how at UE2 the UE 2 dominates whereas the signal form UE1 is diminished and the other way around in UE 1. (b) Transmission of a 10 Gb/s TSDM signal with 5 Gb/s for UE 1 and 5 Gb/s capacity for UE2. It is shown how the quality factor vs OSNR (of the RoF signal) for symbol-by-symbol for UE 1, with either a 10 or a 5 GHz receiver bandwidth is similar. The good match between the curves shows that a reducing the receiver bandwidth does not decrease the signal quality. In both cases the 5 Gb/s of UE 1 is received. (c) Quality factor for symbol-by-symbol steering for distances up to 5 m. The quality decreases with higher distance due to higher losses

5.1.5   Conclusion

We have introduced and demonstrated an ultra-fast beam steering scheme capable of symbol-by-symbol steering at 10 GBd. The settling time of the system while changing the steering angle is therefore below 50 ps. Such high steering speed are achieve using a microwave photonics approach to generate and delay the signals of the phased array antenna.

Our setup was exemplary used in a millimeter wave radio access network based on a new multiplexing scheme. Beside the reduced costs of the user equipment, our scheme also has the potential to increase the reach and in addition to reduce the inter-cell interference of the radio access network. Both advantages are provided by the beamforming taking place in the remote antenna unit.

The setup demonstrated in this paper could also be used in a receiving array to provide the same flexible bandwidth allocation advantages to a duplex system. Moreover, our demonstration focuses on communication links but other applications such as tracking, or scanning could also benefit from ultra-fast beam steering.

5.2 Plasmonic Phased Array Feeder enabling ultra-fast Beam Steering at Millimeter Waves

Section 5.2 has been published in [RB4]:

Plasmonic phased array feeder enabling ultra-fast beam steering at millimeter waves

R. Bonjour, *et al.*, *Opt. Express,* vol. 24, no. 22, pp. 25608-25618, 2016.

For consistency with the rest of this thesis, some variables have been adapted from the original publication.

Abstract: In this paper, we demonstrate an integrated microwave photonics phased array antenna feeder at 60 GHz with record-low footprint. Our design is based on ultra-compact plasmonic phase modulators (active area <2.5µm2) that not only provide small sizes but also ultra-fast tuning speed. In our design, the integrated circuit footprint is in fact only limited by the contact pads of the electrodes and by the optical feeding waveguides. Using the high speed of the plasmonic modulators, we demonstrate beam steering with less than 1 ns reconfiguration time, i.e. the beam direction is reconfigured in-between 1 GBd transmitted symbols.

5.2.1 Introduction

Steerable phased array antennas (PAA) are a key technology for next generation radio access network (5G-RAN) [155], satellite payloads [156], and novel sensing applications [16]. But in order to cope with the requirements of novel network architectures [21, 157] or millimeter wave (mmWave) systems [15, 158, 159], PAAs need to be integratable on a single platform with least possible footprint, offering ultra-fast reconfigurability, and featuring broadband characteristics [49, 138].

Many mmWave concept demonstrations have already been performed with discrete components [24, 25, 49, 69]. However, these experiments will only reveal their full potential and become economically attractive once fully integrated [42]. Over the past few years, this challenge has been addressed in many publications within the context of integrated microwave photonics (IMWP). To this point, remarkable results have been achieved with integration platforms that include [42]: indium phosphide [110, 160], Silica glass planar lightwave circuits (PLCs) [161], silicon photonics [44], and silicon nitride [43]. Yet, with these platforms mmWave PAAs have typically provided footprints of a few cm^2 [43], slow reconfigurability based on thermal [162] or wavelength tuning [110], and bandwidth limitations of a few tens of GHz [101]. Among the fastest beam steering demonstrations, concepts relying on fiber-based Lithium Niobate (LiNbO3) modulators offer reconfiguration time

in the order of ns [49, 163]. Interesting work has also been made using advanced simulations [164, 165].

In this paper we demonstrate for the first time a mmWave multi-GBd beam steering system based on integrated plasmonic technology that offers (1) ultra-fast capability with >1ps tuning speeds and (2) an ultra-compact size, with modulator area of only a few μm^2. This technology enables the creation of completely integrated array feeders, capable of steering mmWave arrays of hundreds of antenna elements at ultra-high speed on an extremely reduced footprint, opening the path towards a fully-monolithic realization and therefore a reduction of unit costs.

5.2.2   Context of Application

A possible utilization of photonics in next generation 5G wireless communication systems is depicted in Fig. 5.11. In this example, microwave photonics is used to increase the capacity of the mobile cells without impacting the complexity of the user equipment [49]. The signals for multiple users are generated in the basement of the building using digital signal processing (DSP) and high-end electronic front-ends, see Fig. 5.11(a). This base band unit (BBU) then sends the mmWave signal over fibers to the remote radio head (RRH) of the access network. In this scenario, the users are time division multiplexed (TDM) in the DSP of the BBU. In the RRH, see Fig. 5.11(b), the optical signal enters a phased array feeder (PAF) which generates multiple copies with phase offsets that will allow to steer the beam in a particular direction. Steering is done in such a way that the beam is sent towards one user position via a steering control signal sent in parallel to the data signal in the optical fiber. In the scenario from Fig. 5.11, the PAA in the RRH is used to realize a time-to-space mapping of the TDM symbol by switching the beam direction in a symbol-by-symbol fashion, i.e. switching the beam direction between each transmitted symbols [49]. This is actually an example where high-speed beam steering might enable high speed data distribution without increasing the complexity in the user electronics [49], Fig. 5.11(d). However, this concept, or any other MWP solutions, requires integration on a reliable, cost effective, and compact platform [42, 155].

Our proposal relies on the integration of a phased array feeder (PAF) based on plasmonic phase modulators [166-169] to build the PAA in the RRH. This solution enables integration of array feeders on very small footprints. Fig. 5.11(c) shows a 4×1 phased array feeder with an active area of the plasmonic phase modulators of only 2.5 µm2. The utilization of phase shifters instead of true-time delays in the array feeder is justified by [170]. It has been demonstrated that for applications with limited fractional bandwidth (<15%), phase shifters perform as good as more advanced true-time delays while lowering the system complexity.
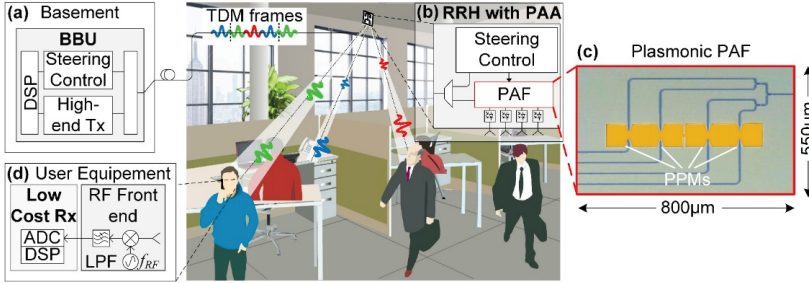
Fig. 5.11 - Symbol-by-symbol beam steering scenario. (a) The baseband unit (BBU) in the basement of the building sends time division multiplexed (TDM) data to multiple users via (b) a remote radio head (RRH). The RRH uses a steering control signal from the BBU to steer the single TDM symbols in different directions, acting as a spatial de-multiplexer. (c) Here, the RRH comprises of a plasmonic phased array feeder (PAF). (d) Since the user only receives a tributary of the TDM signal, the user equipment can be based on slow and low cost electronics.

5.2.3 Plasmonic Phased Array Feeder

The key element of our ultra-fast steering demonstration is a plasmonic phased array feeder (plasmonic PAF), Fig. 5.12(a). It is composed of an array [169] of 4 plasmonic phase modulators (PPMs) [171], Fig. 5.12(b). Plasmonic modulators are based on the generation and control of surface plasmon polaritons (SPPs) [172], which are electromagnetic surface waves created at a dielectric-metal interface. Recent reviews on plasmonic modulators for applications in optical communications are given in [167, 169]. In our demonstration, PPMs are employed to electrically control the phase of the microwave photonic signal radiated by the antennas of a linear antenna array, Fig. 5.12(c). As plasmonic modulators offer highest speed modulation on a µm²-scale footprint [167, 169], PPMs give access to ultra-fast beam steering capabilities in combination with an ultra-compact size (short structures of tens of µm length). This will enable highest integration densities on a small footprint.

Each PPM consists of a 25 µm-long plasmonic metal-insulator-metal (MIM) slot waveguide created by 100 nm separated gold (Au) electrodes, see Fig. 5.12(b). An organic nonlinear optical (NLO) material with a large electro-optic coefficient [173, 174] is deposited in the slots by spin-coating to enable phase modulation based on the linear electro-optic effect (Pockels effect). The voltage applied to the electrodes induces a refractive index change in the material in the slot, and thus, the phase of the optical signal is shifted proportional to the applied voltage. The Au electrodes are fabricated on an SOI wafer by e-beam evaporation and a lift-off process. The silicon access waveguides are fabricated via e-beam lithography and dry etching. An advantage of PPMs compared to other integrated photonic phase modulators is that the modulation of the phase does not impact the amplitude of the signal, i.e. there is no associated amplitude modulation. The propagation

losses per unit length in the PPMs amount to approximately ~0.5 dB/μm. This is a high value compared to other technologies. Nonetheless, these losses are mitigated by the much shorter device lengths [166] that can be achieved with plasmonic-organic-hybrid modulators. Recent progresses in organic electro-optic materials [175] even promises more efficient devices.

Four PPMs are arranged in parallel and electrically connected in series to allow for push-pull operation [169]. The required footprint per phase modulators is a few μm², as can be seen in Fig. 5.12(b). The size of the chip layout is limited only by the standard electrical test probes that are available, in ground-signal-ground configuration with a 100 μm pitch.

The operation principle of the plasmonic PAF is illustrated with the help of Fig. 5.12. An optical reference laser (narrow-linewidth) at frequency v_R enters the chip via a silicon grating coupler, Fig. 5.12(d). A 1×4 splitter is used to distribute the optical reference laser to the 4 PPMs. The silicon feeding waveguides are tapered down to excite surface plasmon polaritons (SPP) in the plasmonic slot waveguide [176]. The phases of the SPPs are shifted proportionally to the voltages applied to the modulator electrodes, see Fig. 5.12(e). After the PPMs, the light is converted back to the photonic domain and guided in silicon waveguides. Each phase-shifted copies of the reference laser are then combined with the optical carrier in 2×1 MMI couplers. The optical carrier is at a frequency $v_C = v_R + 60$ GHz and carry the modulated data signal. The optical carrier is depicted in Fig. 5.12(f) and the combined output spectra with the optical signal in phasor representation are shown in Fig. 5.12(g). The radio-over-fiber (RoF) signals exit the chip by means of silicon grating couplers. Each Radio-over-Fiber (RoF) output signal is then fed into a photodetector, where mmWave signals are generated. The signal generation is based on photonic beating [70], i.e. a copy of the data will be generated at the frequency difference between the two lasers (60 GHz). Changing the relative phase shift induced by the PPMs changes the phase of the generated mmWave signal, thus allowing to control the beam propagation direction of the antenna array.

The beam steering angle depends on the relative phase difference between neighboring PPMs. More specifically, in order to steer the main lobe of radiation to the angular direction θ, the electrical phase at the n-th antenna element is given by Eq. (5.3) [62].

$$a_n = -n \frac{2\pi f_{RF}}{c_0} d \cdot \cos \theta \qquad (5.3)$$

where f_{RF} is the central mmWave frequency, c_0 is the speed of light in air, and d is the antenna spacing of the array.
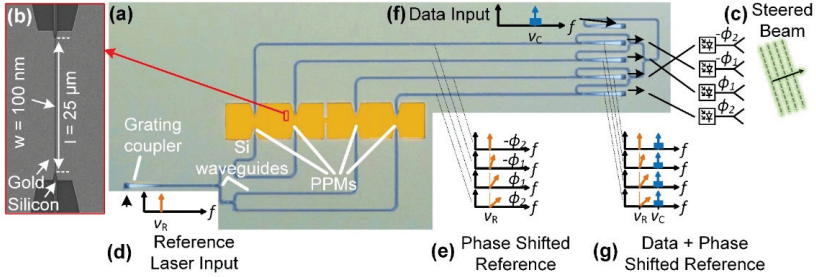
Fig. 5.12 - Plasmonic phased array feeder. (a) Colorized SEM image of a the plasmonic phased array feeder (PAF). The plasmonic phase modulators (PPM) used in the PAF are composed of a 25 µm-long and 100 nm-wide metal-insulator-metal (MIM) slot waveguides. The slot is filled with a second-order nonlinear material to allow for phase modulation based on the Pockels effect. (b) Microscope image of a low footprint PPM used in the PAF.

High-speed electro-optic tests were conducted on the PPMs. The broadband modulation capability of the PPMs employed is shown in Fig. 5.13. The device was driven by a -3 dBm sinusoidal RF signal with frequency swept from 10 GHz up to 70 GHz. The results measured with an optical spectrum analyzer show that the PPMs offer a flat frequency response up to frequencies of at least 70 GHz, limited by the measurement equipment. Only ±1.5 dB modulation ripples can be seen in the frequency response. By analyzing the ratio between the optical carrier and the modulation sidebands, the $V_{\pi, RF}/2$, as needed in push-pull operation, can be estimated to be in the order of 8.5 V±2 V across the complete 10-70 GHz band.
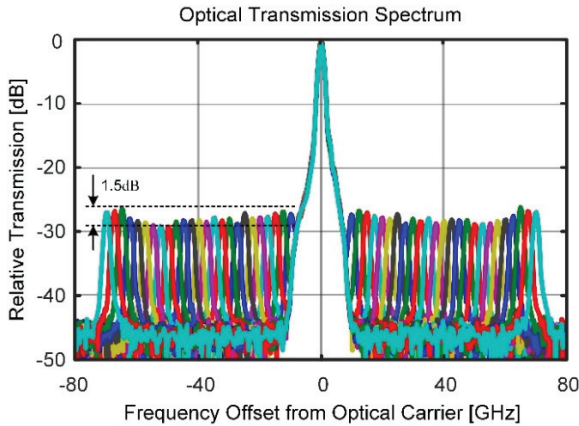
Fig. 5.13 - Measured optical transmission spectrum for -3 dBm RF modulation of the PPM used in the system experiments, from 10 GHz to 70 GHz. The higher sidebands at large frequencies are related to variations in the impedance matching between the pico-probe and the device through the measurement bandwidth.

5.2.4   Experimental Setup

For the experimental demonstration, we use the phased array feeder (PAF) described in the previous section to build a 2x1 antenna RRH. A 4x1 array would have been fully supported by the plasmonic PAF but the available RF equipment allowed us simultaneous operation of only two antennas. The experimental setup is detailed in Fig. 5.14. The experimental setup comprises of three parts. (a) The BBU with the signal generation, (b) the RRH with the plasmonic feeder, and (c) the user equipment (UE) with bandwidth tunable receivers (digital filtering).

The signals are generated in the BBU, see Fig. 5.14(a). An arbitrary wave form generator (AWG) is used to generate a pseudorandom binary sequence (PRBS) of length $2^{11}-1$ with 1 and 2 GBd and various modulation formats (BPSK, QPSK). The data are then encoded onto a narrow linewidth laser (< 100 kHz linewidth at a frequency v_C) by means of an IQ modulator. The optical signal is then amplified (EDFA) and filtered with an optical band-pass filter (0.6 nm). The power level of the carrier at the output of the BBU is -2 dBm. In parallel, a second, narrow linewidth reference laser with a frequency (v_R) offset against the carrier laser of $f_{RF} = 60$ GHz, is part of the BBU. The reference laser has a power of 16 dBm. The power of the reference laser is much higher in order to compensate for the excess losses in the integrated plasmonic feeder in the RRH.

The RRH is realized as a phased array antenna (PAA) comprising of a plasmonic PAF and a millimeter wave front end, Fig. 5.14(b). In the plasmonic PAF, the reference laser is first split onto 4 arms. The arms are then phase modulated to induce the progressive phase delay needed for beam steering. Finally, the phase shifted copies of the reference laser are combined with the data signal in a coupler stage within the PAF. The two outputs of the plasmonic PAF form the two RoF signals entering the mmWave front end. The mmWave front ends consist of a low noise EDFA to boost the signal, an optical delay line (DL) to compensate the fixed fiber length difference, an optical filter to remove the out-of-band noise of the EDFA, a variable optical attenuator (VOA), a 70 GHz photodiode performing the optical to mmWave conversion, an amplifier to boost the mmWave signal, and finally a horn antenna (20 dBi). The antenna spacing is ~2 cm. The two users are spatially separated by 30° (~ angle between maximum and null of the array pattern) and placed at a distance of 3 m from the PAA.

Ideally for our demonstration, the UEs at the receiver side, see Fig. 5.14(c), should be built with commercial components fulfilling mobile communication standards (such as 802.11ad). As depicted in Fig. 5.11(d), commercial UEs should include: a 60 GHz antenna, a mixer with f_{LO} at 60 GHz directly providing IQ baseband signals, a low pass filter (LPF), and the digital signal processing (DSP) stage. However, we have not used such UEs because we need the flexibility of a research setup to switch the bandwidth of the LPF from 0.7 to 1.4 GHz in order to demonstrate the advantage of symbol-by-symbol steering. Our bandwidth tunable UEs are therefore implemented as

following: First, the 60 GHz mmWave signals are received by Huber&Suhner Sencity Matrix antennas and amplified by V-band amplifiers. An intermediate frequency (IF) conversion stage is then used to shift the signals down to 11 GHz. This stage is implemented in order to enable direct recording with our digital storage oscilloscope (DSO) having a limited measurement bandwidth. The IF signals are, after recording with the DSO, processed with a
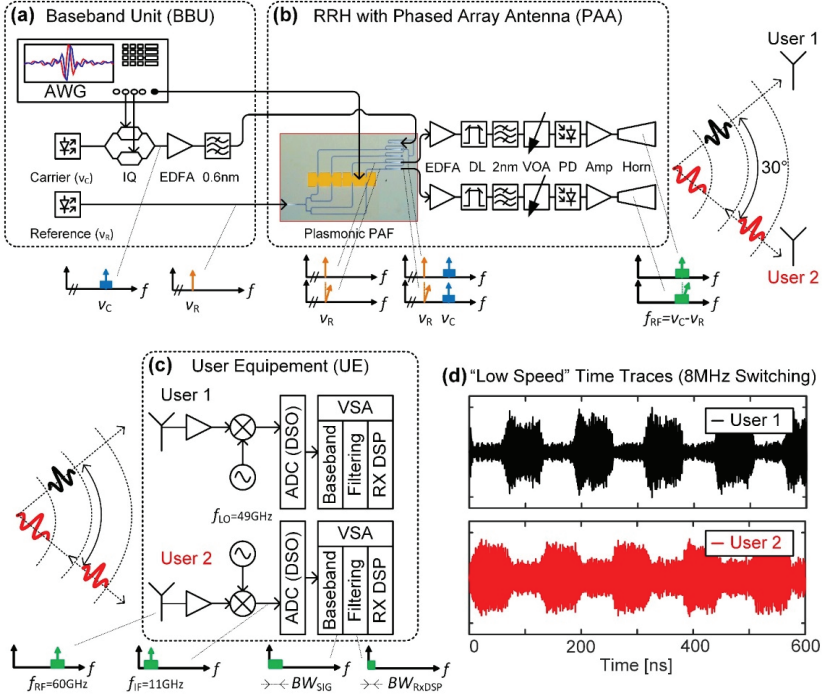
Fig. 5.14 - Experimental setup. (a) In the BBU, data from AWG are encoded by means of an IQ modulator onto a carrier laser (at frequency v_C). After optical amplification, the carrier laser is transmitted to the RRH. A second reference laser (at frequency v_R) having a frequency difference corresponding to the desired millimeter wave frequency (60 GHz) is fed to the RRH as well. (b) In the RRH the two lasers are combined within the plasmonic PAF chip and mapped onto photodiodes, where they are converted to millimeter wave (mmWave) signals. (c) To emulate a 0.7 and 1.4 GHz bandwidth UE (at a carrier of 60 GHz) we use a high-bandwidth DSO. For this, we receive the signal with 60 GHz high-gain antenna and down-convert the signal to an intermediate frequency (IF) of 11 GHz. The DSO is then used to perform the recording. The IF signals are then analyzed with a vector software analyzer (VSA) performing: the down-conversion to IQ baseband signals, low pass filtering to emulate a 0.7 and 1.4 GHz bandwidth UE, and digital signal processing (DSP) with standard recovery algorithm (timing, carrier, equalization). (d) The plot shows time traces right after the ADC (without DSP) for a "low" steering speed of 8 MHz, i.e. frames of 62 symbols are steered towards user 1 or 2 alternatively.

commercial vector software analyzer (VSA) for both users in parallel. In the VSA, the signals are first down-converted numerically into IQ baseband signals. The IQ baseband signals are then filtered using tunable digital filters with bandwidth BW_{RxDSP}. In our symbol-by-symbol demonstration in the next section, the bandwidth of this digital filter is switched from 1.4 GHz to 0.7 GHz in order to emulate UEs with lower processing bandwidth. Finally, a digital signal processing (DSP) chain applies the different recovery algorithms (timing, carrier, equalization) as needed for demodulation.

Fig. 5.15 depicts the experimental setup used in our laboratory. The pictures detail the mmWave paths after the RRH with the transmitting PAA, see inset (a), the 3m channel (main picture), and the two users. See inset (b) for close up on the receiver chain of user 2.

Before testing ultra-fast steering, we performed "low speed" characterization of the setup, i.e. instead of steering symbol-by-symbol, we steered the beam frame-by-frame. The result for a switching rate of 8 MHz between the two users is depicted in Fig. 5.14(d). At 8 MHz, the beam is steered every 62.5 ns corresponding to frames containing 62 symbols (at a symbol rate of 1 GBd). In Fig. 5.14(d), the received signals are depicted without any DSP processing (right after the ADCs). Time traces for user 1 and 2 are plotted in black and red, respectively. The result shows that the frames are indeed transmitted either towards user 1 or towards user 2. The reception was limited by the amplifiers noise with a worth case extinction ratio of 3 -5 dB. Measurements at various switching rates have shown that the extinction ratio does not depend on the switching speed but is rather related to the quality of the mmWave components.
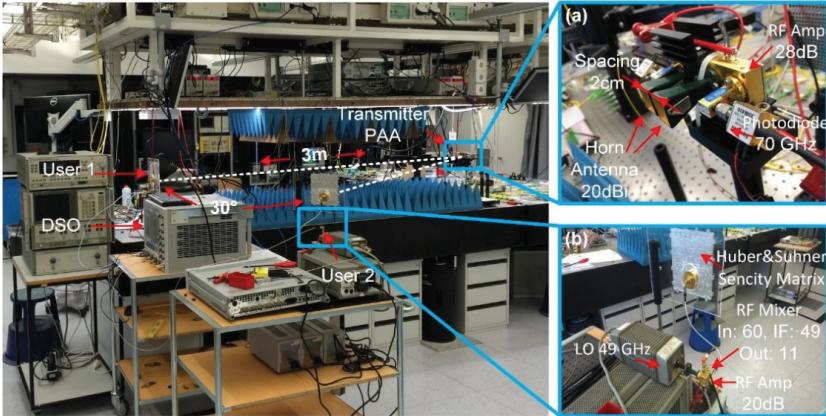
Fig. 5.15 - Picture of the experiment setup. The PAA, zoom in inset (a), is built with two photodiodes (70 GHz), two amplifiers (28 dB gain), and two horn antennas (directivity of 20 dBi) and antenna spacing of 2 cm. The two users are 3m apart from the transmitter PAA and separated by 30°. In the inset (b), the mmWave components used for user 2 are detailed the antenna, an amplifier (20 dB gain), and an RF mixer (LO at 49 GHz). The signals of the two users at an intermediate frequency of 11 GHz are directly recorded with a DSO.

For ultra-fast beam steering, synchronization between the transmitted data sequence and the steering control signal was needed. For instance, for symbol-by-symbol beam steering one needs to steer the beam in between symbol transitions and not during a symbol transmission and thus requires time synchronization with about 10% of the symbol duration. To calibrate the length of the mobile backhauling fibers, we used an auto-correlation based method. This worked as follow: the same PRBS pattern is sent on both channels (data and control sequence). The data are then modulated via the IQ modulator in the BBU while the phase shifter of the PAA will be modulated in the RRH. The physical distance difference between the two modulators (~80 m of fiber) leads to a superposition of the PRBS sequences on the output signals. By performing an auto-correlation of the signal in the receiver, the absolute delay difference between the two modulators can be derived from the correlation peaks.

5.2.5 Ultra-fast Beam Steering Results

After the aforementioned low-speed testing we moved on to ultra-fast symbol-by-symbol measurements. Here, the phased array antenna is reconfigured between each symbol transmission in order to steer every symbol in a different direction. This way the user will only receive one tributary out of a larger number of data and therefore operate at lower symbol rates [49]. This symbol-by-symbol steering experiment has been performed with a mmWave signal at a frequency of $f_r =$60 GHz. In opposite to Fig. 5.14(d), the results plotted in this section leverage the full DSP chain of the UEs, explaining the better signal qualities.

In a first step, we performed measurements with user equipment (UE) having a processing bandwidth corresponding to the full transmitted symbol rate, i.e. the digital filter bandwidth BW_{RxDSP} in Fig. 5.14(c) is set to ~1.4 GHz for a transmitted signal of 1 GBd (with roll-off factor of 0.35). Fig. 5.16 shows the received eye and constellation diagrams for the two users after the symbol-by-symbol transmission. It can be seen that there is always a null between symbols as each user receives only every second symbol. As a matter of fact, the transmitted 1 GBd (period of 1 ns) QPSK sequence is converted into two 50% return-to-zero bit streams (period of 2 ns) at the receivers by ultra-fast symbol-by-symbol steering. The resulting EVMs are 24.4% and 25.1% for user 1 and 2, respectively. We thereby verify beam switching times smaller than 1 ns, i.e. smaller than the symbol duration.
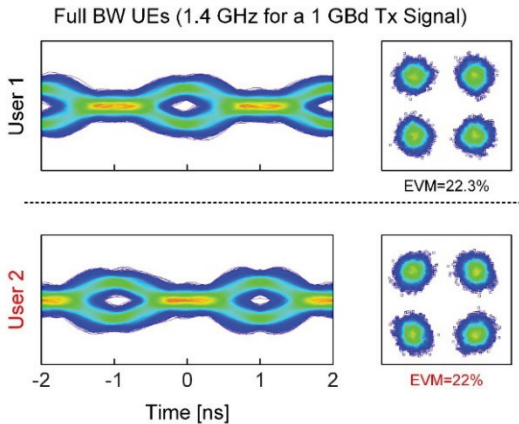
Fig. 5.16 - Received signals for 1GBd transmitted QPSK signal received as two independent 0.5GBd bit streams in full bandwidth receivers (1.4 GHz).

In a second step, we reduced the UEs BW by a factor two in order to demonstrate the key advantage of symbol-by-symbol steering. The UEs DSP bandwidth is now sets to 0.7 GHz by adapting the resampling in our commercial vector signal analyzer. The results plotted in Fig. 5.17 show that the signals can still be detected with a good EVM (24.4% for user 1 and 25.1% for user 2). In fact, the EVM penalty is only ~4% when reducing the UEs BW by a factor two. In this scenario, the bandwidth can be reduced from 1.4 GHz to 0.7 GHz. The receiver bandwidth matches the received symbol rate times the roll-off factor of 0.35 for both cases.
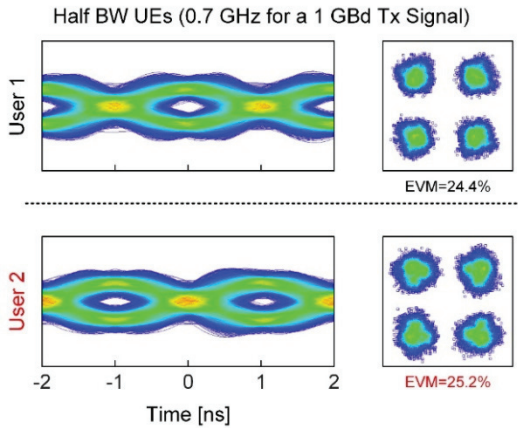
Fig. 5.17 - Received signals for receivers with only half the bandwidth of the transmitter (~700 MHz), compared to Fig. 5.16 the quality degradation is low.

Finally, the symbol-by-symbol steering results for various modulation formats and symbol rates are summarized in Fig. 5.18. We show experimental results for 1 GBd BSPK and 1 and 2 GBd QPSK. In a commercial system one could optimize the various EVM values by using a larger array, optimizing the RXs filter shapes (rectangular in this case), and by optimizing the shape of the control signal. These results show that reducing the bandwidth of the receivers works for advanced modulation formats at different symbols rates. As we are switching the beam between two users, the bandwidth can be reduced by a factor two. It is worth noting that the symbol rate of the demonstration is not limited by the PPMs bandwidth but rather by the limited SNR of the full millimeter wave setup. The performances of the receivers were limited by the standard pulse shaping used in this experiment. In order to improves the results, a possible path is to develop custom types of "matched filters" specially designed for symbol-by-symbol steering.
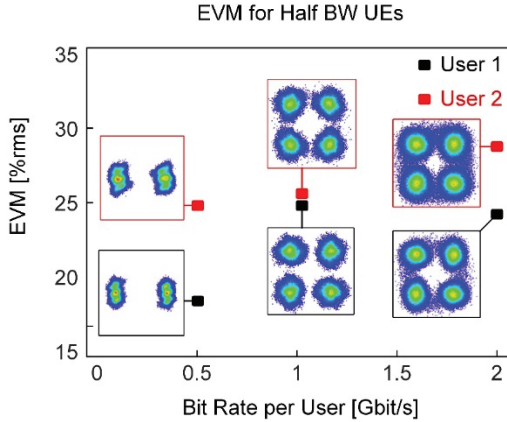
Fig. 5.18 - EVM Results for BPSK at 1GBd, QPSK at 1 and 2 GBd (symbol rate of the transmitted signal). For simplicity, the corresponding bitrate per user is used on the x-axis of the plot.

5.2.6   Conclusion

In this paper, we demonstrated an integrated phased array feeder for millimeter wave communication based on ultra-compact plasmonic phase modulators. The paper shows how the plasmonic platform can empower the development of future beam steering schemes by offering (1) ultra-compact size of the active area and thus large integration density and (2) ultra-fast beam steering with reconfiguration times of less than 1 ns. The wireless experiment has been performed at carrier frequency of 60 GHz and shown beam steering with beam steering reconfiguration in less than 1 ns. In other words, we were able to adjust the beam direction in between 1 GBd symbols. This method called symbol-by-symbol steering provides the advantage of shifting the complexity of the electronics away from the user equipment. The demonstration shows how the plasmonic platform may pave the way for complex system-on-chip schemes while providing larger bandwidth and smaller footprint compared to other platforms.

5.2.7   Funding

5.2.8   Acknowledgments

6   H<small>IGH</small> C<small>APACITY</small> W<small>IRELESS</small> L<small>INKS</small>

In parallel to the work directly related to the steering of mmWave with microwave photonics (MWP). A state-of-the MWP wireless communication setup had to be built to test the concepts presented in the previous chapters. This setup did not only enable successful demonstration of ultra-fast beam steering but also provided record in terms of spectral efficiency of a 60 GHz wireless link.

In this chapter, a publication made with this setup is presented to showcase the achievement performed at the system level during this thesis.

Section 6.1: Pre-equalization Technique enabling 70 Gb/s Photonic-Wireless Link at 60 GHz

In the publication of Section 6.1, a wireless link achieving 70 Gb/s at a carrier of 60 GHz is presented. This work, published by Felix Abrecht in collaboration with the author of this thesis, sets a new record of data transmission at 60 GHz. The challenge of this work was to increase wireless link capacity while relying on equipment that is compatible with the commercial technologies at 60 GHz. The main advantage of the presented experiment is the implementation of commercial off-the-shelf (COTS) components. In addition, the technologies, such as the one-shot equalization technique, used in this work have been leveraged in other publications of the group.

6.1 Pre-equalization Technique enabling 70 Gb/s Photonic-Wireless Link at 60 GHz

Abstract: In this paper, we demonstrate a 70 Gb/s photonic-based wireless link at 60 GHz using a single RF carrier and a single polarization. This high capacity is achieved by using 32QAM modulation with a symbol rate of 14 GBd. We show a novel pre-equalization technique that enables usage of such very high bandwidths at 60 GHz. Our work indicates that the consumer oriented 60 GHz band could be a viable alternative to more expensive E-band or sub-THz links for high capacity photonic wireless transmission, mobile backhauling and last-mile high-capacity connections.

6.1.1 Introduction

High capacity point-to-point wireless links at millimeter wave (mmWave) frequencies are expected to be an essential part of mobile backhauling for 5G networks [177]. In fact, speeds beyond 100 Gb/s will be needed in the backhaul network to support the increasing bandwidth demands [177]. Yet, the generation of these high frequency signals in the electrical domain is challenging [177].

An elegant solution may rely on microwave photonics (MWP) [32-35], where the millimeter wave signals are generated by optical heterodyning in a photodiode [36-38]. MWP enables larger bandwidth, lightweight structures, offer immunity to electromagnetic interference and larger inter-connection distances while simplifying the installation of the system [33]. Recently demonstrated photonic-based wireless links have shown impressive data rates in several frequency bands from 31 GHz up to 245 GHz carrier frequency. At 31 GHz, a 44.3 Gb/s transmission experiment revealed that very high transmission speeds can be achieved at smaller carrier frequencies when employing pre-equalization to improve the signal quality [178]. At 60 GHz, data rates have been limited to 25 Gb/s/polarization [179]. In the W-band (75-110 GHz) data rates achieved are 50 Gb/s/polarization over a 1.2 m wireless link [180], 40 Gb/s/polarization for a distance of 300 m [181] and even 10 Gb/s/polarization for 1.7 km transmission [182]. At 245 GHz, data rates beyond 100 Gb/s have been demonstrated [32]. However: broad adoption of MWP based solutions in next generation backhauling require: 1)

A capacity larger than 50 Gb/s/polarization after forward error correction. 2) Use of frequency bands for which the hardware costs are low (e.g. at 60 GHz, driven by IEEE 802.11ad WiGig standard). 3) Excellent signal quality to enable use of higher order modulation formats (i.e. 32QAM and higher).

In this paper, we demonstrate a data rate of 70 Gb/s on a single carrier and single polarization at 60 GHz. This high capacity is made possible by an efficient pre-equalization method which is enabled by a one-shot characterization method of the end-to-end system and that ultimately allows the effective use of 14 GBd signals with up to 32QAM. With the consumer oriented IEEE 802.11ad WiGig standard as the mayor driver for 60 GHz technology [183-185], the availability of components for 60 GHz communications could make high-capacity wireless links at 60 GHz affordable and may result in a cost-advantage over more expensive E-band or sub-THz links.

6.1.2   Application Scenario

Fig. 6.1 depicts a possible scenario for high capacity photonics-based wireless links. We envision a densely populated area with a large number of small cells. In such an environment, the diversity of small cells is needed to deal with the growing capacity requirements and number of users [18]. While each small cell base station could theoretically be deployed with an individual fiber connection to the backhaul network, this may call for expensive and time consuming construction work, and sometimes may not even be possible. Instead, the connection could be established wirelessly from a remote antenna unit (RAU) which is connected to the central office and which provides network access to several small cells, see Fig. 6.1. Thereby, deploying costly fiber links could be avoided.
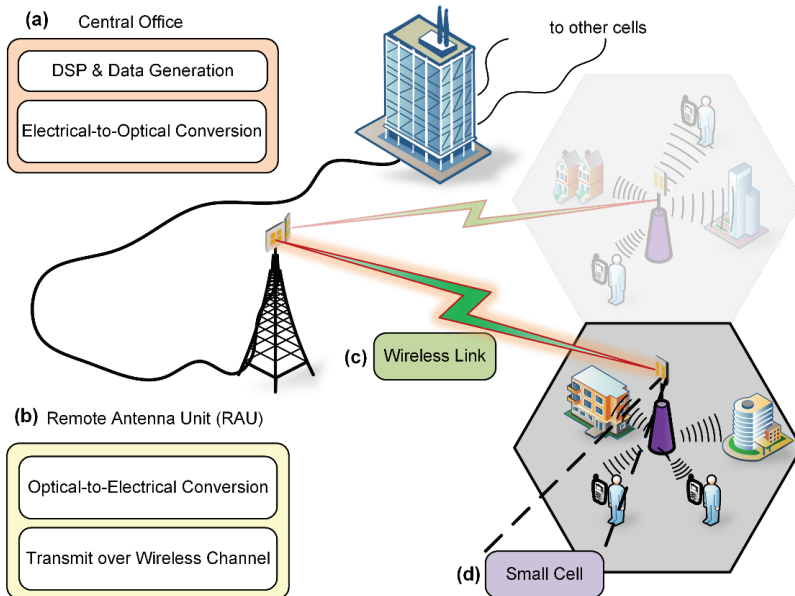
Fig. 6.1 - Mobile backhauling employing high capacity wireless links at 60 GHz. (a) In the central office digital signal processing (DSP) is performed on the mobile communications signals which are then transmitted as optical signals over a fiber. (b) In the remote antenna unit (RAU) signals are converted from the optical domain to the electrical domain and converted to the microwave domain. (c) Wireless transmission link and (d) the small cell base station

6.1.3 Experimental Setup

Following the concept of Fig. 6.1, our experimental setup is composed of four parts: an optical transmitter, an optical-to-RF converter, a wireless link and an RF receiver mimicking the central office, the remote antenna unit (RAU), the wireless link, and the small cell. The setup is detailed in Fig. 6.2. The concept has been employed and described in several previous works [32, 178-182] as stated in section 6.1.1.
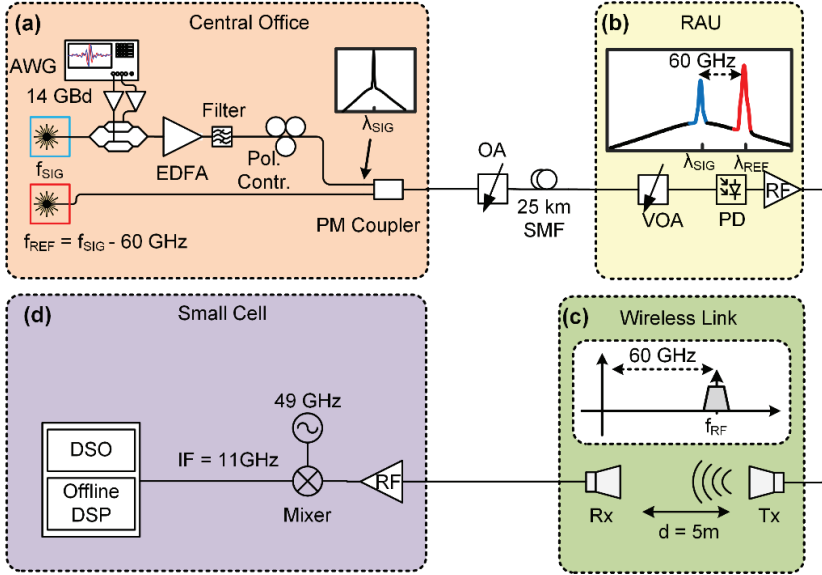
Fig. 6.2 - Experimental setup of the wireless link. (a) In the central office, an IQ modulator driven by an AWG modulates a laser (blue). The data signal is combined with a 60 GHz detuned reference laser (red) and sent to a remote location through 25 km of single-mode fiber. (b) In the remote antenna unit (RAU), a photodiode generates the RF signals which are transmitted over the wireless link (c). (d) In the receiving RAU, the signal is down-converted to an intermediate frequency and recorded with a digital sampling oscilloscope (DSO).

The central office, Fig. 6.2(a), generates the baseband data with a 65 GS/s arbitrary waveform generator (AWG). The data is fed to separate broadband amplifiers for the in-phase and quadrature components. The amplified signals drive an optical IQ modulator, which encodes the data onto a laser at 1550.12 nm (f_{SIG}), see inset Fig. 6.2(a). Afterwards, the data signal is boosted by two cascaded erbium doped fiber amplifiers (EDFA) with subsequent optical filters. The filters have bandwidths of 0.6 nm. The schematic only shows one EDFA- for the sake of simplicity. Subsequently, the data signal is recombined with a reference laser ($f_{REF} = f_{Sig} - 60\,\text{GHz}$) detuned by 60 GHz. A polarization controller is used to ensure that the data signal and the reference laser are on the same polarization. It should be noted, that the

two lasers are not locked to each other. Thus, the receiver requires the standard DSP algorithms of coherent communications to handle the frequency drift and phase noise of the lasers. Next, the signals are sent across 25 km of standard single mode fiber (SMF) to the RAU. Additionally, an optical attenuator (OA) is used to control the launch power to the fiber.

At the RAU, Fig. 6.2(b), the data and the reference laser are fed to a 70 GHz photodiode. The optical input power to the photodiode is controlled with a variable optical attenuator (VOA). The inset of Fig. 6.2(b) shows the measured spectra of the signal and reference laser in front of the photodiode with respective power levels of -8 dBm and 0.9 dBm. Through optical heterodyning in the photodiode, a copy of the data signal will be generated at the desired 60 GHz RF carrier. Unwanted signal copies at twice the optical frequency are cut-off by the photodiode while the subsequent V-band low noise amplifier suppresses the baseband copy. The V-band amplifier offers 23 dB gain at 60 GHz.

The wireless link, Fig. 6.2(c) consists of two high gain antennas by Huber&Suhner, which are set apart by 5 meters. These antennas offer a gain of 38 dBi which is helpful to compensate the added path loss at 60 GHz. Thereby, the link distance of 5 meters is rather limited by the dimensions of our laboratory then by the power budget.

In the small cell base station, Fig. 6.2(d), the signal is amplified directly after the antenna with a V-band amplifier offering 20 dB gain at 60 GHz. Further, the signal is electrically down-converted to an intermediate frequency of $f_{IF} = 11$ GHz using an RF mixer. This is necessary to ensure that the signal lies within the bandwidth of the receiver. Downconversion to baseband can then be realized digitally. Ultimately, the signal is recorded by a digital storage oscilloscope (DSO) and processed offline.

Fig. 6.3 shows a picture of some parts of the setup in our lab. The main photograph shows the wireless transmission path with the transmitter antenna in the foreground and the receiving antenna in the background. One can instantly see that the RAU only consists of a photodiode, a V-band amplifier and the antenna, compare Fig. 6.2(b). This setup is very simple since the complexity can be moved to the central office. The inset zooms in on the receiving antenna and reveals a view of the small cell receiver, compare Fig. 6.2(d). The V-band amplifier and the mixer used for IF down conversion can be identified as well as the digital sampling scope sitting in the background.
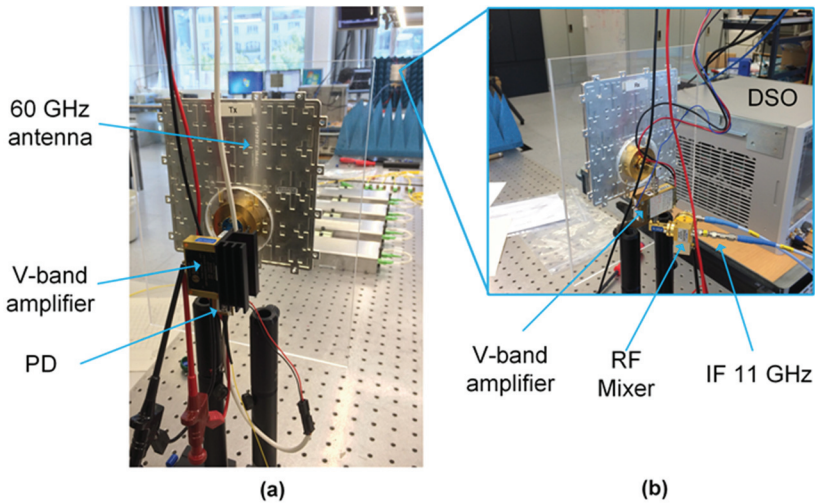
Fig. 6.3 - Photographs of the experimental setup. Figure (a) shows the RAU including photodiode (PD), V-band amplifier and 60 GHz antenna. At 60 GHz, the antenna provides 38 dBi gain while the gain of the amplifier is 23 dB. After 5 meter of wireless transmission the signal reaches the small cell that can be identified in the background and is magnified in the inset on the right hand side (b). Here, the 60 GHz signal is collected by an antenna that is identical to the one at the transmitting RAU. After boosting the signal with an amplifier with 20 dB gain at 60 GHz, it is down converted by an RF mixer to an intermediate frequency (IF) and recorded with a digital storage oscilloscope (DSO).

6.1.4   Pre-equalization Technique

The overall system performance may be impaired by any component in the signal chain. In our case, the frequency response of the channel is affected by the RF components such as the amplifiers and the antennas. In Fig. 6.4(a), the received normalized spectrum of a 14 GBd 16QAM signal (roll-off = 0.15) is depicted. The different noise levels to the left and the right of the signal spectrum are due to the low pass characteristics of the RF components. Ideally, the spectrum should be flat but power variations of up to 7 dB can be seen. The post equalizer in the receiver cannot recover the data without pre-equalization, i.e. the decision directed equalizer does not converge [178] because preceding receiver algorithms (e.g. timing and carrier recovery) do not work properly with an overly distorted signal. The demodulation fails under such conditions and data cannot be retrieved, see Fig. 6.4(a) inset. It should be noted, that the smaller variations in the spectrum are caused by the random character of the data.

In literature, pre-equalization or pre-distortion is well known to counteract limitations imposed by the optical transmitter [186-188]. However, pre-equalizing the signal in the transmitter according to the whole system impairments can be used to achieve a flat frequency response at the receiver and make the entire bandwidth usable. To perform pre-equalization, accurate channel response information is needed. A precise channel response can be obtained by offline S-parameter measurement of each RF component individually [178]. However, such an implementation is time consuming. In turn, inline-channel measurements are of great interest as they allow for characterization of a channel without a need for disassembling the link and compensating the measurement equipment's effects.

For the demonstration in this paper, an inline, one-shot, pre-equalization method was used, which works according to the steps depicted in Fig. 6.4(d). (1) The AWG generates a frequency comb which is encoded with a random phase pattern to limit the peak-to-average power ratio (PAPR). Note that the random phase pattern is set once, saved and kept for the whole measurement sequence. The frequency spacing as well as the spectral width of the comb can be varied according to the setup specifications. For our measurements, we used a spectral width slightly larger than the desired signal bandwidth and a spacing of 60 MHz for the comb lines, which provided optimal results for the channel pre-equalization. (2) The comb is sent through the system, where it is upconverted and sent through the wireless link while no changes on the setup configuration are made. (3) A sampling oscilloscope acquires the output signal in the receiver and down conversion to the baseband is performed. (4) The peaks of the various comb components are detected in the signal spectrum and used to compute the amplitude response by interpolation. In this work, we used a shape-preserving piecewise cubic interpolation. (5) The linear phase ramp (corresponding to the delay of the system) and the random phase pattern added in the transmitter are removed to extract the phase response. (6) The algorithm output is a complex channel

response (amplitude and phase response) that can be used for pre-equalization at the transmitter.

Fig. 6.4(b) shows the channel response of our 60 GHz link before equalization obtained using our one-shot measurement algorithm. The channel measurement was performed over a bandwidth of 20 GHz. The performance of the system is limited by the channel for various reasons, which can be seen from the complex channel response. First, strong amplitude variations (in some cases more than ±5 dB over 2 GHz) in the magnitude response can be identified. These variations are prone to the RF components, namely the amplifiers and antennas have a big influence on the spectral characteristic. For example, we found that exchanging the V-band amplifier at the transmitter antenna with one of the same models changes the spectral shape significantly. Second, the available bandwidth is limited due to the cut-off of the RF components at around 16 GHz. Third, the phase response shows a very strong dispersion (3000° difference across the full bandwidth).

In Fig. 6.4(c), the result of wireless transmission after applying this equalization technique is depicted. It can be clearly seen that the spectrum of the 16QAM signal at a symbol rate of 14 GBd (56 Gb/s) shows less distortions compared to the spectrum without pre-equalization, Fig. 6.4(a). The filter taps of the decision-directed post-equalizer in the receiver can now converge and the data be recovered, see Fig. 6.4(c) inset with the constellation diagram. Consequently, our pre-equalization technique counteracts linear distortions in the system to enable usage of standard digital signal processing (DSP) algorithms in the receiver such as timing and carrier recovery or the above mentioned decision-directed post-equalizer. If desired, an additional equalizer to tackle non-linear distortions could be added in the receiver DSP chain. It is worth noting that the pre-equalization technique is not exclusive to applications in V-band and can in principle be used to characterize any system under test.
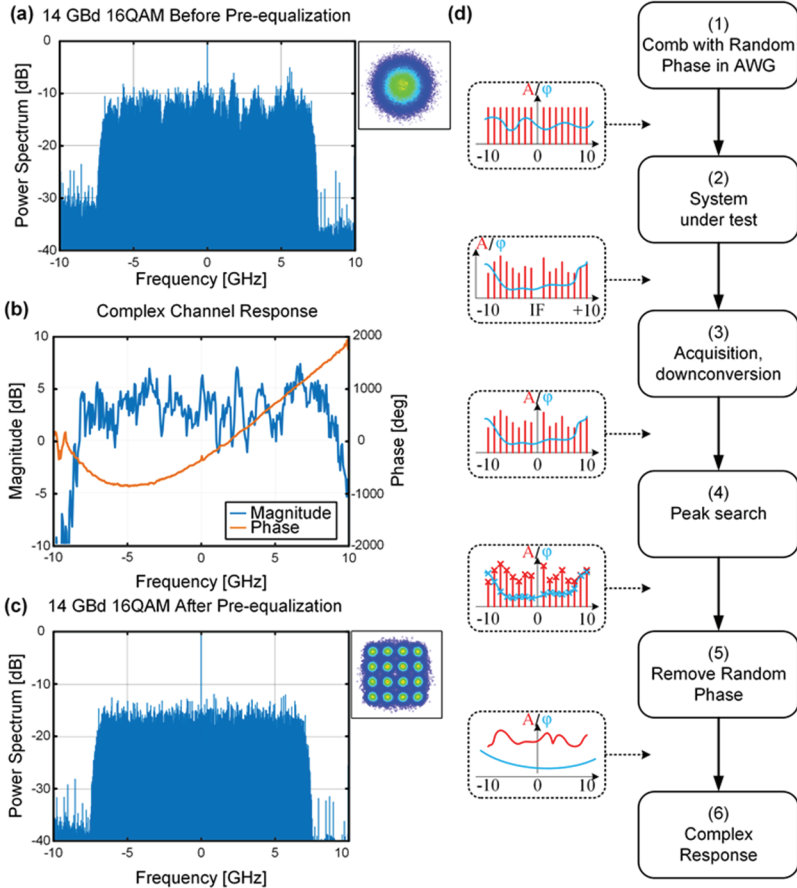
Fig. 6.4 - Impact of the one-shot pre-equalization technique and process flow. (a) Received data signal (14 GBd 16QAM) without pre-equalization, strong power variations can be seen in the spectrum (b) Complex channel response (magnitude and phase) measured with our algorithm. (c) Received data signal (14 GBd 16QAM) with pre-equalization. A flat channel spectrum for the received signal is found after applying the complex channel response as a pre-equalization filter. (d) The pre-equalization used in this experiment allows a "single-shot" measurement of the complex response of the system under test. The process consists of the following steps: (1) A frequency comb is generated digitally and sent to an AWG, a random phase is then added to every frequency component to avoid large PAPR. (2) The comb goes through the system, following the very same path that the data will encounter. (3) The comb is acquired by an oscilloscope at the receiver, down-converted, and an FFT is performed. (4) The amplitude peaks of the spectrum are found with a specialized algorithm to recover the frequency components of the comb. (5) The random phase is removed from the results. (6) The complex response of the system is provided. It enables complex pre-equalization of a system under test

6.1.5   Results

To test the scheme in an experiment, we used root-raised-cosine shaped signals and a 0.15 roll-off with data patterns generated with a DeBruijn-11 sequence. The results presented in this section were obtained with RF components not perfectly suited for this experiment. Yet, thanks to our pre-equalization method very high data rates have been demonstrated. One may however assume that the data rate would be even higher with RF components chosen specifically for the purpose of the demonstration.

First, we analyzed our system performance for various symbol rates and modulation formats. Fig. 6.5 depicts the error vector magnitude (EVM) for BPSK (red), QPSK (yellow), 16QAM (green), 32QAM (light blue), and for a 16QAM reference measurement without the wireless link (back-to-back, violet). Please note that we used the convention where the EVM is normalized to the power of the outermost ideal constellation point [189, 190]. As expected, the signal quality slowly decreases for all modulation formats when increasing the symbol rate, i.e. the average EVM increases. We found that BPSK and QPSK formats were able to perform well up to 15 GBd, 16QAM and 32QAM up to 14 GBd. This is due to the fact that the usable bandwidth is limited to approximately 16 GHz by the RF components. Additionally, BPSK and QPSK have a higher noise tolerance compared to 16QAM and 32QAM which is why they still work up to 15 GBd. The back-to-back case for 16QAM shows that by removing the wireless link from the transmission path, reception of 15 GBd signals is still possible. So, from a technical point of view, using 14 GBd signals is reasonable and doable at 60 GHz. It is yet another question if such bandwidths will be made available by regulation bodies.
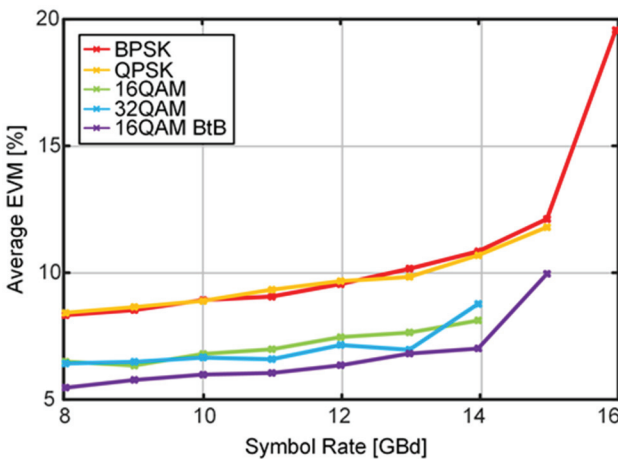
Fig. 6.5 - EVM for different symbol rates using pre-equalization. Measurements were performed with 4 dBm launch power to the 25 km fiber.

As a next step, we investigated the influence on the signal quality of the optical power fed to the photodiode. Fig. 6.6 shows the result for 10 GBd, 12 GBd, and 14 GBd 16QAM signals. A 14 GBd 16QAM measurement without the antennas is included for reference (back-to-back, blue). The signal will initially obtain a better EVM as the optical power increases. Crossing a certain power threshold (between -3.5 dBm and -2 dBm) causes the RF amplifiers at the receiver to go into saturation and distorting the signal. The excess power margin available in this experiment shows that our system will have sufficient power to cover even a larger wireless distance once the limitation of the laboratory room size is removed. We estimate that the wireless link can be extended to 20 meters while keeping the power at the receiver the same by increasing the optical input power by roughly 6 dB.

The plot in Fig. 6.6 further shows how the EVM increases for higher symbol rates when measured near the optimal input power. Note that the measured bit error rate (BER) close to the optimum is below 10^{-3} for all signals (10^5 bits were evaluated preventing statistically relevant claims below 10^{-3}). The EVM threshold to obtain a BER of 10^{-3} for 16QAM is 11% when additive white Gaussian noise is assumed [189, 190].
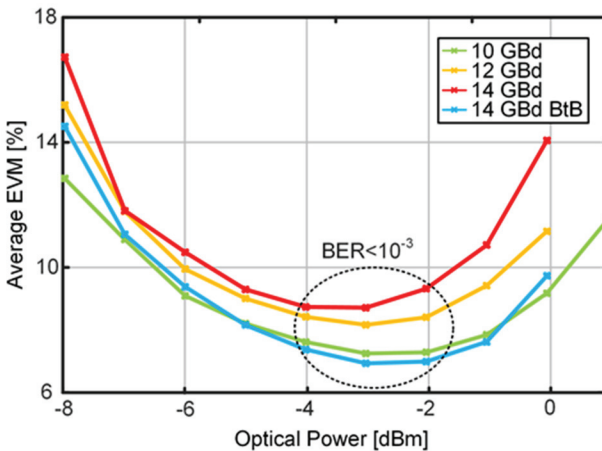
Fig. 6.6 - Results for 16QAM at symbol rates of 10, 12 and 14 GBd for various optical input powers to the photo diode. Launch power to the fiber was 8.6 dBm.

Finally, we evaluated the BER of 14 GBd signals for BPSK, QPSK, 16QAM and 32QAM. The received constellation and corresponding BER values can be observed in Fig. 6.7. For each measurement, at least 10 million bits were analyzed, i.e. BER of 10^{-5} can be stated at best. Both BPSK and QPSK did not reveal any errors within this recorded sequence (BER<10^{-5}) while 16QAM and 32QAM showed a BER of $7 \cdot 10^{-5}$ and $3.7 \cdot 10^{-3}$, respectively. These raw input BER values are below the threshold for error-free transmission when second-generation hard-decision FEC with 7% overhead is used [191]. In this case, an output BER of below $1 \cdot 10^{-15}$ may be expected if the FEC works correctly and limitations are only due to additive white Gaussian noise. The constellations also show some non-linear distortions which we suspect coming from the RF amplifiers and RF mixer.

The plot in Fig. 6.7 (d) shows a 14 GBd 32QAM transmission experiment. This results in a 70 Gb/s capacity for a single carrier, single polarization setup at 60 GHz. This is – to the best of our knowledge – the largest capacity so far transmitted in a V-band single polarization experiment.
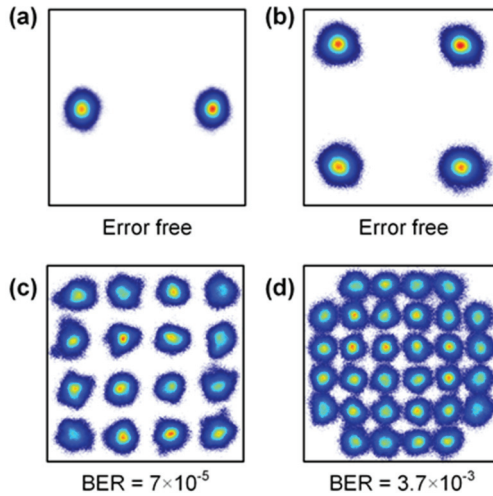
Fig. 6.7 - Constellation and measured BER for 14 GBd signals of (a) BPSK, (b) QPSK, (c) 16-QAM, (d) 32-QAM with more than $6 \cdot 10^6$ symbols.

6.1.6   Conclusion

We have successfully shown a 70 Gb/s photonic wireless link at 60 GHz on a single carrier and single polarization across 25 km of standard single mode fiber and a 5 m wireless transmission link. Usage of 14 GBd signals has been made possible by a pre-equalization technique. The pre-equalization relies on an efficient "single shot" frequency response characterization of the system that might be useful in future systems to repeatedly update the equalizer and thereby adapt to dynamic changes in the system. This work demonstrates that the 60 GHz band may be a good alternative to more expensive E-band or sub-THz links for >100 Gb/s mobile backhauling.

6.1.7   Funding

6.1.8   Acknowledgments

7 SUMMARY AND OUTLOOK

In this work, new technologies for microwave photonics have been combined with novel system level schemes. The key result is the introduction of time-to-space division multiplexing, a concept relying on ultra-fast beam steering to generate multiple beams with low hardware complexity. In parallel, the technological developments have led to several records mainly related to the settling time or the bitrate of the various investigated systems.

The outcome of this work and a short outlook for each achievement is provided here:

Ultra-fast tunable true-time delays

A scheme for *continuously tunable true-time delays with ultra-low settling time* [RB1] is demonstrated using a new concept called complementary phased shifted spectra (CPSS). This concept is the first to provide at the same time continuous operation and ultra-fast tunability for microwave photonic phased array applications.

In [RB1], CPSS is demonstrated using a fiber-based setup. CPSS could however be integrated on a photonic integrated circuit (PIC) to prove its full potential. Indeed, for phase array applications, it is not possible to implement bulky fiber based setup multiple times for all the delays, a low footprint solution is indeed needed. There are multiple potential PIC platforms, including the plasmonic one from the IEF, that could be used for such an integration. Early designs have already been performed and could be produced and tested.

Time-to-Space Division Multiplexing (TSDM)

In *Time-to-Space Division Multiplexing for Tb/s Mobile Cells* [RB7], a novel network scheme relying on ultra-fast beam steering is introduced and detailed. This scheme is able to generate multiple beams with limited hardware requirements.

While the main work of this thesis focuses on microwave photonic technologies, the concept of time-to-space division multiplexing is applicable to any other technologies.

The theoretical framework behind ultra-fast beam steering and time-to-space division provided in this thesis offers recommendations to design correctly a TSDM system. In combination with the developed simulation framework, these recommendations can be used to mitigate the effect of TSDM on the signal quality.

The theoretical framework provided in this thesis could be further enhanced based on information theory of wireless channels. Such a work has already been started in [52] and should be continued. The first results however already showed that the effect of TSDM on the signal is analog to the effect of multi-path fading in standard wireless communication systems. Thus, implementing standard fading mitigation techniques, i.e. techniques such as time or frequency diversity, in TSDM would improve the signal quality and therefore the bitrate of the cells.

Demonstration of ultra-fast beam steering

In *Ultra-fast millimeter wave beam steering* [RB3], time-division multiplexing is experimentally demonstrated using the true-time delays presented [RB1]. This paper still represents the beam steering demonstration with the fastest steering time ever reported (settling time below 50 ps).

In *Plasmonic phased array feeder enabling ultra-fast beam steering at millimeter waves* [RB4], time-division multiplexing is demonstrated with an array feeder based on plasmonic phase modulators. This demonstration not only shows integrated ultra-fast beam steering but also the microwave photonic feeder with the smallest footprint ever reported.

A larger scale demonstration of time-to-space division multiplexing relying on a phased array with more elements should be performed. The work in [RB3] and [RB4] serves as a technology demonstrator but a higher integration level could be leveraged to experimentally demonstrate a mobile cell effectively reaching Tb/s capacity.

High spectral efficiency wireless links

In *Pre-equalization technique enabling 70 Gb/s photonic-wireless link at 60 GHz* [RB5], high capacity wireless links are demonstrated in the V-band (~60 GHz) with components off-the-shelf. This contrasts with the trend of moving to THz frequencies, where the losses are higher, and the technologies are far less mature.

The work in [RB5] could be extended to include dual polarization transmission. This would double the achievable bitrate and demonstrate that 100 Gb/s, as needed for future mobile backhauling, can be implemented in a frequency band that is compatible with commercially available components.

The advantages of the above-mentioned achievements can only integrate products once a reliable, high performances photonic integration platform is available. To this end, the team of the Institute of Electromagnetic Field will continue the work towards this platform through projects such as the ERC Grant "Plasilor", and the EU projects PlasmoFab and PlasCMOS.

Appendix A SIMPLIFICATION OF THE ARRAY FACTOR

In the derivation of the array factor and array pattern, the received radiation E_P at the observation point $P(r)$ is derived by summing up the radiations originating from all antenna elements in the array. In section 2.2.2 Eq. (2.52), E_P is defined as

$$E_P(r) = \sum_i a_i \cdot D_i(\theta, \phi) \cdot \frac{1}{|\mathbf{R}_i|} e^{-ik|\mathbf{R}_i|}. \tag{A.1}$$

In this appendix, the simplification of this equation is detailed. The simplification is based on the replacement of the propagation vector $\mathbf{R}_i$ between the antenna elements and the observation point by [63, 64]

$$\mathbf{R}_i = \mathbf{r} - \mathbf{r}_i. \tag{A.2}$$

with $\mathbf{r} = [x, y, z]$ the position of the observation point P and $\overrightarrow{\mathbf{r}_i = [x_i, y_i, z_i]}$ the position of the i antenna element, see Fig. 2.11 for more details on the coordinates system. Thus $|\mathbf{R}_i|$ in Eq. (B.9) can be simplified as follow

$$
\begin{aligned}
|\mathbf{R}_i| &= |\mathbf{r} - \mathbf{r}_i| \\
|\mathbf{R}_i| &= \sqrt{(x - x_i)^2 + (y - y_i)^2 + (z - z_i)^2} \\
|\mathbf{R}_i| &= \sqrt{x^2 - 2xx_i + x_i^2 + y^2 - 2yy_i + y_i^2 + z^2 - 2zz_i + z_i^2}
\end{aligned} \tag{A.3}
$$

Assuming $|\mathbf{r}| \gg |\mathbf{r}_i|$, the terms x_i^2, y_i^2, and z_i^2 can be neglected. Thus

$$|\mathbf{R}_i| = \sqrt{x^2 - 2xx_i + y^2 - 2yy_i + z^2 - 2zz_i} \tag{A.4}$$

which can be rewritten

$$
\begin{aligned}
|\mathbf{R}_i| &= \sqrt{x^2 + y^2 + z^2 - 2(xx_i + yy_i + zz_i)} \\
|\mathbf{R}_i| &= \sqrt{|\mathbf{r}|^2 - 2(\mathbf{r} \cdot \mathbf{r}_i)} \\
|\mathbf{R}_i| &= \sqrt{|\mathbf{r}|^2 \left(1 - 2\frac{\mathbf{r} \cdot \mathbf{r}_i}{|\mathbf{r}|^2}\right)} \\
|\mathbf{R}_i| &= |\mathbf{r}| \sqrt{1 - 2\frac{\mathbf{r} \cdot \mathbf{r}_i}{|\mathbf{r}|^2}}
\end{aligned} \tag{A.5}
$$

using Taylor expansion $\sqrt{1 + x} = 1 + x/2 - \cdots$ lead to (first order is sufficient as $(\mathbf{r} \cdot \mathbf{r}_i)/|\mathbf{r}|^2 \ll 1$)

$$
\begin{aligned}
|\mathbf{R}_i| &= |\mathbf{r}| \left(1 - \frac{\mathbf{r} \cdot \mathbf{r}_i}{|\mathbf{r}|^2}\right) \\
|\mathbf{R}_i| &= |\mathbf{r}| - \frac{\mathbf{r} \cdot \mathbf{r}_i}{|\mathbf{r}|}
\end{aligned} \tag{A.6}
$$

Replacing $r/|r| = \hat{r}$, i.e. the unit vector of r finally lead to

$$|\mathbf{R}_i| = |r| - \hat{r} \cdot r_i. \tag{A.7}$$

Eq. (B.9), i.e. Eq. (2.52), can thus be rewritten as

$$E_P(\vec{r}) = \sum_i a_i \cdot D_i(\theta, \phi) \cdot \frac{1}{|r| - \hat{r} \cdot r_i} e^{-ik(|r| - \hat{r} \cdot r_i)}. \tag{A.8}$$

Eq. (A.8) is further used and simplified in 2.2.2 as Eq. (2.55).

Appendix B SIMPLIFICATION OF THE BEAMWIDTH CONDITION

The beamwidth condition, equation (4.8) in section 4.2.1, if found by rearranging the terms of equation (4.7). Equation (4.7) provides the number of users n_{users} that can share a sector size Θ_{sector} assuming an ISI-free beamwidth of $\Theta_{DC\_SL}(N)$, N being the number of antenna element in the steering direction of the PAA. Equation (4.7) in section 4.2.1 is defined by

$$n_{users} = \frac{\Theta_{sector}}{\Theta_{DC\_SL}(N)} \tag{B.9}$$

with $\Theta_{DC\_SL}(N)$ found from equation (2.72):

$$\Theta_{DC\_SL}(N) = \frac{\pi}{2} - acos\left(acos\left(\frac{1}{z_0(N, A_{SL})}\right) \cdot \frac{\lambda_{RF}}{\pi \cdot d}\right) \tag{B.10}$$

and $z_0(N, A_{SL})$ found from equation (2.73):

$$z_0(N, A_{SL}) = \cosh\left(\frac{2}{N-1} acosh(A_{SL})\right). \tag{B.11}$$

Equation (B.9) should however be rearranged in order to provide the minimum number of antenna N required for a number of users n_{users}. Replacing (B.11) and (B.10) in (B.9) leads to:

$$n_{users} = \frac{\Theta_{sector}}{\frac{\pi}{2} - acos\left(acos\left(\frac{1}{\cosh\left(\frac{2}{N-1} acosh(A_{SL})\right)}\right) \cdot \frac{\lambda_{RF}}{\pi \cdot d}\right)} \tag{B.12}$$

Rearranging the terms:

$$acos\left(acos\left(\frac{1}{\cosh\left(\frac{2}{N-1} acosh(A_{SL})\right)}\right) \cdot \frac{\lambda_{RF}}{\pi \cdot d}\right) = \frac{\pi}{2} - \frac{\Theta_{sector}}{n_{users}} \tag{B.13}$$

Applying cosine on both sides:

$$acos\left(\frac{1}{\cosh\left(\frac{2}{N-1} acosh(A_{SL})\right)}\right) \cdot \frac{\lambda_{RF}}{\pi \cdot d} = \cos\left(\frac{\pi}{2} - \frac{\Theta_{sector}}{n_{users}}\right) \tag{B.14}$$

Using the identity $\cos(\pi/2 - x) = \sin(x)$

Simplification of the Beamwidth Condition

$$\mathrm{acos}\left(\frac{1}{\cosh\left(\frac{2}{N-1}\mathrm{acosh}(A_{SL})\right)}\right)\cdot\frac{\lambda_{\mathrm{RF}}}{\pi\cdot d}=\sin\left(\frac{\Theta_{\mathrm{sector}}}{n_{\mathrm{users}}}\right)\qquad(B.15)$$

Rearranging the terms and applying cosine on both sides:

$$\cos\left(\sin\left(\frac{\Theta_{\mathrm{sector}}}{n_{\mathrm{users}}}\right)\cdot\frac{\pi\cdot d}{\lambda_{\mathrm{RF}}}\right)=\frac{1}{\cosh\left(\frac{2}{N-1}\mathrm{acosh}(A_{SL})\right)}\qquad(B.16)$$

Rearranging the terms:

$$\cosh\left(\frac{2}{N-1}\mathrm{acosh}(A_{SL})\right)=\frac{1}{\cos\left(\sin\left(\frac{\Theta_{\mathrm{sector}}}{n_{\mathrm{users}}}\right)\cdot\frac{\pi\cdot d}{\lambda_{\mathrm{RF}}}\right)}\qquad(B.17)$$

Applying "acosh" on both sides:

$$\frac{2}{N-1}\mathrm{acosh}(A_{SL})=\mathrm{acosh}\left(\frac{1}{\cos\left(\sin\left(\frac{\Theta_{\mathrm{sector}}}{n_{\mathrm{users}}}\right)\cdot\frac{\pi\cdot d}{\lambda_{\mathrm{RF}}}\right)}\right)\qquad(B.18)$$

Using the identity $\mathrm{acosh}(1/x)=\mathrm{asech}(x)$

$$\frac{2}{N-1}\mathrm{acosh}(A_{SL})=\mathrm{asech}\left(\cos\left(\sin\left(\frac{\Theta_{\mathrm{sector}}}{n_{\mathrm{users}}}\right)\cdot\frac{\pi\cdot d}{\lambda_{\mathrm{RF}}}\right)\right)\qquad(B.19)$$

Rearranging the terms finally lead to:

$$N=1+\frac{2\cdot\mathrm{acosh}(A_{SL})}{\mathrm{asech}\left(\cos\left(\sin\left(\frac{\Theta_{\mathrm{sector}}}{n_{\mathrm{users}}}\right)\cdot\frac{\pi\cdot d}{\lambda_{\mathrm{RF}}}\right)\right)}\qquad(B.20)$$

Thus, the beamwidth condition can be stated as:

$$N\geq1+\frac{2\cdot\mathrm{acosh}(A_{SL})}{\mathrm{asech}\left(\cos\left(\sin\left(\frac{\Theta_{\mathrm{sector}}}{n_{\mathrm{users}}}\right)\cdot\frac{\pi\cdot d}{\lambda_{\mathrm{RF}}}\right)\right)}\qquad(B.21)$$

In other word, the number of antenna N of the PAA should be larger or equal to the minimum number of antenna required to support the number of user n_{users}.

Equation (B.21) is further used in section 4.2.1 as equation (4.8).

Appendix C   TABLE OF FIGURES

Table of Figures

185

Appendix D REFERENCES

[1] Cisco, "Cisco Visual Networking Index: Forecast and Methodology," 2017.

[2] P. Salva-Garcia, J. M. Alcaraz-Calero, R. M. Alaez, E. Chirivella-Perez, J. Nightingale, and Q. Wang, "5G-UHD: Design, prototyping and empirical evaluation of adaptive Ultra-High-Definition video streaming based on scalable H.265 in virtualised 5G networks," *Computer Communications,* 2017/12/02/ 2017.

[3] M. Xiao *et al.*, "Millimeter Wave Communications for Future Mobile Networks," *IEEE Journal on Selected Areas in Communications,* vol. 35, no. 9, pp. 1909-1935, 2017.

[4] J. G. Proakis, *Digital Communications*. McGraw-Hill, 2001.

[5] D. Tse and P. Viswanath, *Fundamentals of Wireless Communication*. Cambridge University Press, 2005.

[6] (20.01.2018). *Cell Sizes*. Available: http://www.wirelesscommunication.nl/reference/chaptr04/cellplan/cellsize.htm

[7] F. Boccardi, R. W. Heath, A. Lozano, T. L. Marzetta, and P. Popovski, "Five disruptive technology directions for 5G," *IEEE Commun. Mag.,* vol. 52, no. 2, pp. 74-80, 2014.

[8] S. K. Biswash and D. N. K. Jayakody, "The Device Centric Communication System for 5G Networks," *Journal of Physics: Conference Series,* vol. 803, no. 1, p. 012023, 2017.

[9] Y. Mehmood, N. Haider, M. Imran, A. Timm-Giel, and M. Guizani, "M2M Communications in 5G: State-of-the-Art Architecture, Recent Advances, and Research Challenges," *IEEE Communications Magazine,* vol. 55, no. 9, pp. 194-201, 2017.

[10] M. Baker, "From LTE-advanced to the future," *IEEE Commun. Mag.,* vol. 50, no. 2, pp. 116-120, 2012.

[11] E. Larsson, O. Edfors, F. Tufvesson, and T. Marzetta, "Massive MIMO for next generation wireless systems," *IEEE Commun. Mag.,* vol. 52, no. 2, pp. 186-195, 2014.

[12] L. Lu, G. Y. Li, A. L. Swindlehurst, A. Ashikhmin, and R. Zhang, "An overview of massive MIMO: Benefits and challenges," *IEEE J. Sel. Topics Signal Process.,* vol. 8, no. 5, pp. 742-758, 2014.

[13] G. Shen, J. Liu, D. Wang, J. Wang, and S. Jin, "Multi-hop relay for next-generation wireless access networks," *Bell Labs Tech. J,* vol. 13, no. 4, pp. 175-193, 2009.

[14] C. Dehos *et al.*, "Millimeter-wave access and backhauling: the solution to the exponential data traffic increase in 5G mobile communications systems?," *IEEE Commun. Mag.,* vol. 52, no. 9, pp. 88-95, 2014.

[15] S. Rangan, T. S. Rappaport, and E. Erkip, "Millimeter-wave cellular wireless networks: potentials and challenges," *Proc. IEEE,* vol. 102, no. 3, pp. 366-385, 2014.

[16] T. S. Rappaport *et al.*, "Millimeter wave mobile communications for 5G cellular: It will work!," *IEEE Access,* vol. 1, pp. 335-349, 2013.

[17] S. Shu and T. S. Rappaport, "Wideband mmWave channels: Implications for design and implementation of adaptive beam antennas," in *Microwave Symposium (IMS), 2014 IEEE MTT-S International*, 2014, pp. 1-4.

References

[18] R. Waterhouse and D. Novak, "Realizing 5G: Microwave photonics for 5G mobile wireless systems," *IEEE Microw. Mag.,* vol. 16, no. 8, pp. 84-92, 2015.

[19] W.-F. Alliance. (2015, October). *WiGig® and the future of seamless connectivity*. Available: http://www.wi-fi.org/discover-wi-fi/wigig-certified

[20] A. Alkhateeb, J. Mo, N. Gonzalez-Prelcic, and R. W. Heath, "MIMO precoding and combining solutions for millimeter-wave systems," *IEEE Commun. Mag.,* vol. 52, no. 12, pp. 122-131, 2014.

[21] S. Shu, T. S. Rappaport, R. W. Heath, A. Nix, and S. Rangan, "MIMO for millimeter-wave wireless communications: beamforming, spatial multiplexing, or both?," *IEEE Commun. Mag.,* vol. 52, no. 12, pp. 110-121, 2014.

[22] ITU, "Multiple gigabit wireless systems in frequencies around 60 GHz," *ITU Report,* vol. M.2227-1, 2014.

[23] E. TSGR, "LTE: Evolved Universal Terrestrial Radio Access (E-UTRA)," *Multiplexing and channel coding (3GPP TS 36.212 version 10.3. 0 Release 10) ETSI TS,* vol. 136, no. 212, p. V10, 2011.

[24] S. Koenig *et al.*, "Wireless sub-THz communication system with high data rate," *Nat Photon,* Letter vol. 7, no. 12, pp. 977-981, 2013.

[25] T. Nagatsuma, G. Ducournau, and C. C. Renaud, "Advances in terahertz communications accelerated by photonics," *Nat Photon,* Review vol. 10, no. 6, pp. 371-379, 2016.

[26] X. Li, J. Yu, z. Zhang, and Y. Xu, "Field Trial of 80-Gb/s PDM-QPSK Signal Delivery over 300-m Wireless Distance with MIMO and Antenna Polarization Multiplexing at W-Band," in *Optical Fiber Communication Conference Post Deadline Papers*, Los Angeles, California, 2015, p. Th5A.5: Optical Society of America.

[27] C. Yang, X. Li, J. Xiao, N. Chi, and J. Yu, "Fiber-wireless integration for 80 Gbps polarization division multiplexing −16QAM signal transmission at W-band without RF down conversion," *Microw. Opt. Technol. Lett,* vol. 57, no. 1, pp. 9-13, 2015.

[28] F. Rusek *et al.*, "Scaling up MIMO: Opportunities and challenges with very large arrays," *IEEE Signal Processing Magazine,* vol. 30, no. 1, pp. 40-60, 2013.

[29] K. Haneda *et al.*, "5G 3GPP-like channel models for outdoor urban microcellular and macrocellular environments," in *Vehicular Technology Conference (VTC Spring), 2016 IEEE 83rd*, 2016, pp. 1-7: IEEE.

[30] E. Bjornson, P. Zetterberg, M. Bengtsson, and B. Ottersten, "Capacity limits and multiplexing gains of MIMO channels with transceiver impairments," *IEEE Communications Letters,* vol. 17, no. 1, pp. 91-94, 2013.

[31] C.-S. Choi, "RF impairment models for 60GHz-band SYS/PHY simulation," *IEEE 802.15-06-0477-01-003c,* 2006.

[32] S. Koenig *et al.*, "Wireless sub-THz communication system with high data rate," *Nat. Photon.,* Letter vol. 7, no. 12, pp. 977-981, Dec. 2013.

[33] J. Capmany and D. Novak, "Microwave photonics combines two worlds," *Nat. Photon.,* vol. 1, no. 6, pp. 319-330, 2007.

[34] J. Yao, "Microwave photonics," *J. Lightwave Technol.,* vol. 27, no. 3, pp. 314-335, 2009.

[35] T. Nagatsuma, G. Ducournau, and C. C. Renaud, "Advances in terahertz communications accelerated by photonics," *Nat. Photon.,* vol. 10, no. 6, pp. 371-379, 2016.

[36] A. J. Seeds, H. Shams, M. J. Fice, and C. C. Renaud, "Terahertz photonics for wireless communications," *J. Lightwave Technol.,* vol. 33, no. 3, pp. 579-587, 2015.

[37] J. A. Nanzer, P. T. Callahan, M. L. Dennis, T. R. Clark, D. Novak, and R. B. Waterhouse, "Millimeter-wave wireless communication using dual-wavelength photonic signal generation and photonic upconversion," *IEEE Trans. Microw. Theory Techn.,* vol. 59, no. 12, pp. 3522-3530, 2011.

[38] J. Capmany, J. Mora, I. Gasulla, J. Sancho, J. Lloret, and S. Sales, "Microwave photonic signal processing," *J. Lightwave Technol.,* vol. 31, no. 4, pp. 571-586, 2013.

[39] R. W. Heath, N. Gonzalez-Prelcic, S. Rangan, W. Roh, and A. M. Sayeed, "An overview of signal processing techniques for millimeter wave MIMO systems," *IEEE journal of selected topics in signal processing,* vol. 10, no. 3, pp. 436-453, 2016.

[40] R. Bonjour, M. Singleton, P. Leuchtmann, and J. Leuthold, "Comparison of steering angle and bandwidth for various phased array antenna concepts," *Opt. Commun.,* vol. 273, pp. 35-43, 2015.

[41] G. Grosskopf, B. Kuhlow, R. Eggemann, G. Przyrembel, and D. Rohde, "Photonic beam-forming for millimeter-wave mobile communications," in *Lasers and Electro-Optics Society, 2003. LEOS 2003. The 16th Annual Meeting of the IEEE*, 2003, vol. 2, pp. 859-860 vol.2.

[42] D. Marpaung, C. Roeloffzen, R. Heideman, A. Leinse, S. Sales, and J. Capmany, "Integrated microwave photonics," *Laser Photon. Rev.,* vol. 7, no. 4, pp. 506-538, 2013.

[43] C. G. H. Roeloffzen *et al.*, "Silicon nitride microwave photonic circuits," *Optics Express,* vol. 21, no. 19, pp. 22937-22961, 2013/09/23 2013.

[44] R. Soref, "Silicon Photonics: A Review of Recent Literature," *Silicon,* journal article vol. 2, no. 1, pp. 1-6, 2010.

[45] M. Burla *et al.*, "On-chip, CMOS-compatible, hardware-compressive integrated photonic beamformer based on WDM," in *Int. Topical Meeting on Microwave Photonics (MWP)*, 2013, pp. 41-44.

[46] O. E. Ayach, S. Rajagopal, S. Abu-Surra, Z. Pi, and R. W. Heath, "Spatially sparse precoding in millimeter wave MIMO systems," *IEEE Trans. Wireless Commun.,* vol. 13, no. 3, pp. 1499-1513, 2014.

[47] D. Astely, E. Dahlman, A. Furuskar, Y. Jading, M. Lindstrom, and S. Parkvall, "LTE: the evolution of mobile broadband," *IEEE Commun. Mag.,* vol. 47, no. 4, pp. 44-51, 2009.

[48] R. Bonjour *et al.*, "Plasmonic phased array feeder enabling ultra-fast beam steering at millimeter waves," *Opt. Express,* vol. 24, no. 22, pp. 25608-25618, 2016.

[49] R. Bonjour *et al.*, "Ultra-fast millimeter wave beam steering," *IEEE J. Quant. Electron.,* vol. pp, no. 99, pp. 1-8, 2015.

References

[50] E. Greco, "Integrated System for ultra-fast Beam Steering," Semester Thesis, Institute of Electromagnetic Fields (IEF), ETH Zurich, 2014.

[51] M. Jost, "Regulation of delay interferometer for ultra-fast tunable true time delays," Semester Thesis, Institute of Electromagnetic Fields (IEF), ETH Zurich, 2016.

[52] L. Authier, "Theoretical Analysis of a Phased Array Antenna System for Ultra-Fast Beam Steering," Semester Thesis, Institute of Electromagnetic Fields (IEF), ETH Zurich, 2017.

[53] P. S. Gani Aliguzhinov, and Thomas Benz, "RF Board for Photonic Chip Evaluation," Group Project, Institute of Electromagnetic Fields (IEF), ETH Zurich, 2016.

[54] M. B. Noa Melchior, and Lukas Bieri, "Development of a Measurement Setup for Through the Wall Sensing," Group Project, Institute of Electromagnetic Fields (IEF), ETH Zurich, 2017.

[55] S. S. Dash, "Simulation of High Speed Optical Beam Steering Systems for next generation Fiber Over Radio communication link," Master Thesis, Institute of Electromagnetic Fields (IEF), ETH Zurich, 2013.

[56] M. Singleton, "Ultrafast beam steering demonstrator," Master Thesis, Institute of Electromagnetic Fields (IEF), ETH Zurich, 2014.

[57] S. Welschen, "Simulation of Ultra-Fast Beam Steering Systems," Master Thesis, Institute of Electromagnetic Fields (IEF), ETH Zurich, 2016.

[58] P. Mousel, "Passive Radar-From Quality Criteria to Coverage Optimization," Master Thesis, Institute of Electromagnetic Fields (IEF), ETH Zurich, 2017.

[59] M. Seimetz, *High-order modulation for optical fiber transmission*. Springer Berlin Heidelberg, 2009.

[60] E. M. Purcell, *Electricity and Magnetism*. Cambridge University Press, 2013.

[61] A. Ghosh, J. Zhang, J. G. Andrews, and R. Muhamed, *Fundamentals of LTE*. Prentice Hall Press, 2010, p. 464.

[62] R. E. Collin, *Antennas and radiowave propagation*. McGraw-Hill, 1985.

[63] R. J. Mailloux, *Phased array antenna handbook*, 2nd ed. (Artech House antennas and propagation library). Artech House, 2005, p. 496 S.

[64] R. S. Simon, *Antennas and propagation for wireless communication systems*, 2nd ed. ed. Chichester: Chichester : Wiley, 2007.

[65] C. A. Balanis, *Antenna theory: Analysis and Design, 3rd ed.* Wiley India Pvt. Limited, 2009.

[66] R. A. Minasian, "Photonic signal processing of microwave signals," (in English), *IEEE Transactions on Microwave Theory and Techniques,* vol. 54, no. 2, pp. 832-846, Feb 2006.

[67] J. Capmany and D. Novak, "Microwave photonics combines two worlds," (in English), *Nat Photonics,* vol. 1, no. 6, pp. 319-330, 2007.

[68] J. Wells, "Faster than fiber: The future of multi-G/s wireless," *IEEE Microwave,* vol. 10, no. 3, pp. 104-112, 2009.

[69] J. Yao, "Microwave photonics," *J. Lightwave Technol.,* vol. 27, pp. 314-335, 2009.

[70] J. Yao, "A tutorial on microwave photonic filters," *IEEE Photonics Society Newsletters,* 2012.

[71] (2018.01.08). *Waveguide Sizes*. Available: https://www.everythingrf.com/tech-resources/waveguides-sizes

[72] M. Burla, *Advanced integrated optical beam forming networks for broadband phased array antenna systems*. University of Twente, 2013.

[73] D. A. I. Marpaung, "High dynamic range analog photonic links: design and implementation," Twente University Press, 2009.

[74] T. Nagatsuma, "Photonic generation of extreme broadband RF signals for communications and sensing," in *Microwave Photonics (MWP), 2013 International Topical Meeting on*, 2013, pp. 104-107.

[75] E. H. Armstrong, "A New System of Short Wave Amplification," *Proceedings of the Institute of Radio Engineers,* vol. 9, no. 1, pp. 3-11, 1921.

[76] S. A. Malyshev and A. L. Chizh, "p-i-n Photodiodes for Frequency Mixing in Radio-Over-Fiber Systems," *Journal of Lightwave Technology,* vol. 25, no. 11, pp. 3236-3243, 2007.

[77] S. F. Jacobs, "Optical heterodyne (coherent) detection," *American Journal of Physics,* vol. 56, no. 3, pp. 235-245, 1988.

[78] J. Leuthold, *Lecture Notes: Optical Communication Fundamentals*. Institute of Electomagnetic Fields (IEF) ETH Zurich, 2017.

[79] G. P. Agrawal, *Fiber-optic communication systems*, 4. ed. (Wiley series in microwave and optical engineering). Hoboken N.J.: Wiley, 2010, p. 603 S.

[80] M. Razeghi, *Fundamentals of Solid State Engineering*. Kluwer Academic Publishers, 2002.

[81] W. Freude, *Optische Nachrichtentechnik*. Springer-Verlag, 2005.

[82] M. Burla, L. Romero Cortés, M. Li, X. Wang, L. Chrostowski, and J. Azaña, "On-chip programmable ultra-wideband microwave photonic phase shifter and true time delay unit," *Optics Letters,* vol. 39, no. 21, pp. 6181-6184, 2014/11/01 2014.

[83] C. Caucheteur *et al.*, "All-fiber tunable optical delay line," *Optics Express,* vol. 18, no. 3, pp. 3093-3100, 2010/02/01 2010.

[84] D. Marpaung *et al.*, "Low-power, chip-based stimulated Brillouin scattering microwave photonic filter with ultrahigh selectivity," *Optica,* vol. 2, no. 2, pp. 76-83, 2015/02/20 2015.

[85] J. Sancho *et al.*, "Tunable and reconfigurable multi-tap microwave photonic filter based on dynamic Brillouin gratings in fibers," *Optics Express,* vol. 20, no. 6, pp. 6157-6162, 2012/03/12 2012.

[86] W. Wei, L. Yi, Y. Jaouën, and W. Hu, "Software-defined microwave photonic filter with high reconfigurable resolution," *Scientific Reports,* Article vol. 6, p. 35621, 10/19/online 2016.

[87] "IEEE Standard for Definitions of Terms for Antennas," *IEEE Std 145-2013 (Revision of IEEE Std 145-1993),* pp. 1-50, 2014.

[88] H. T. Friis, "A Note on a Simple Transmission Formula," *Proceedings of the IRE,* vol. 34, no. 5, pp. 254-256, 1946.

[89] (19.01.2018). *Antenna aperture*. Available: https://en.wikipedia.org/wiki/Antenna_aperture

References

[90]   R. Bonjour, Y. Salamin, S. Gebrewold, P. Leuchtmann, and J. Leuthold, "Verteilte Antennen für Through Wall Sensing - Report September 2014," Aramis-Number: 041-19, Institute of Electromagnetic Fields (IEF), ETH Zurich, 2014.

[91]   T. Akiyama, A. Satoh, K. Nishizawa, S. Yamamoto, S. Itakura, and Y. Hirano, "Fourier Transform Optically Controlled Phased Array Antenna in Receiving Operation," in *MWP 2009*, 2009, pp. 322-325.

[92]   X. Yi, T. X. H. Huang, and R. A. Minasian, "Photonic Beamforming Based on Programmable Phase Shifters With Amplitude and Phase Control," *IEEE Photonics Technology Letters,* vol. 23, no. 18, pp. 1286-1288, 2011.

[93]   T. Akiyama *et al.*, "Spatial light modulator based optically controlled beamformer for variable multiple-spot beam antenna," in *MWP 2011*, 2011, pp. 401-404.

[94]   X. Yi, L. Li, T. X. Huang, and R. A. Minasian, "Programmable multiple true-time-delay elements based on a Fourier-domain optical processor," *Optics Letters,* vol. 37, no. 4, pp. 608-10, Feb 15 2012.

[95]   L. Jofre *et al.*, "Optically beamformed wideband array performance," (in English), *Ieee Transactions on Antennas and Propagation,* vol. 56, no. 6, pp. 1594-1604, Jun 2008.

[96]   F. N. Xia, L. Sekaric, and Y. Vlasov, "Ultracompact optical buffers on a silicon chip," (in English), *Nature Photonics,* vol. 1, no. 1, pp. 65-71, Jan 2007.

[97]   A. Meijerink *et al.*, "Novel Ring Resonator-Based Integrated Photonic Beamformer for Broadband Phased Array Receive Antennas - Part I: Design and Performance Analysis," *Lightwave Technology, Journal of,* vol. 28, no. 1, pp. 3-18, 2010.

[98]   L. Zhuang *et al.*, "Novel Ring Resonator-Based Integrated Photonic Beamformer for Broadband Phased Array Receive Antennas - Part II: Experimental Prototype," *Lightwave Technology, Journal of,* vol. 28, no. 1, pp. 19-31, 2010.

[99]   L. Zhuang *et al.*, "Ring resonator-based on-chip modulation transformer for high-performance phase-modulated microwave photonic links," *Optics Express,* vol. 21, no. 22, pp. 25999-26013, 2013/11/04 2013.

[100] L. Zhuang *et al.*, "On-chip microwave photonic beamformer circuits operating with phase modulation and direct detection," *Optics Express,* vol. 22, no. 14, pp. 17079-17091, 2014/07/14 2014.

[101] C. Roeloffzen *et al.*, "Integrated Optical Beamformers," in *Optical Fiber Communication Conference*, Los Angeles, United States, 2015, p. Tu3F.4: Optical Society of America.

[102] J. Byung-Min, K. Dong-Hyun, J. In-Pyung, S. Sang-Jin, and K. Hyoung-Joo, "Optical true time-delay beamformer based on microwave photonics for phased array radar," in *Synthetic Aperture Radar (APSAR)*, 2011, pp. 1-4.

[103] B.-M. Jung, J.-D. Shin, and B.-G. Kim, "Optical True Time-Delay for Two-Dimensional X-Band Phased Array Antennas," *Photonics Technology Letters, IEEE,* vol. 19, no. 12, pp. 877-879, 2007.

[104] J. Mørk, R. Kjær, M. van der Poel, and K. Yvind, "Slow light in a semiconductor waveguide at gigahertz frequencies," *Optics Express,* vol. 13, no. 20, pp. 8136-8145, 2005/10/03 2005.

[105] P. Berger, J. Bourderionnet, F. Bretenaker, D. Dolfi, and M. Alouini, "Time delay generation at high frequency using SOA based slow and fast light," *Optics Express,* vol. 19, no. 22, pp. 21180-21188, 2011/10/24 2011.

[106] W. Zhang and J. Yao, "Photonic Generation of Millimeter-Wave Signals With Tunable Phase Shift," *IEEE Photonics Journal,* vol. 4, no. 3, pp. 889-894, 2012.

[107] S. Blais and J. Yao, "Photonic True-Time Delay Beamforming Based on Superstructured Fiber Bragg Gratings With Linearly Increasing Equivalent Chirps," (in English), *Lightwave Technology, Journal of,* vol. 27, no. 9, pp. 1147-1154, May 1 2009.

[108] D. B. Hunter, M. E. Parker, and J. L. Dexter, "Demonstration of a continuously variable true-time delay beamformer using a multichannel chirped fiber grating," (in English), *Ieee Transactions on Microwave Theory and Techniques,* vol. 54, no. 2, pp. 861-867, Feb 2006.

[109] M. Burla, L. R. Cortés, M. Li, X. Wang, L. Chrostowski, and J. Azaña, "Integrated waveguide Bragg gratings for microwave photonics signal processing," *Optics Express,* vol. 21, no. 21, pp. 25120-25147, 2013/10/21 2013.

[110] Z. Cao *et al.*, "Integrated remotely tunable optical delay line for millimeter-wave beam steering fabricated in an InP generic foundry," *Opt. Lett.,* vol. 40, no. 17, pp. 3930-3933, 2015/09/01 2015.

[111] R. Soref, "Optical dispersion technique for time-delay beam steering," *Applied Optics,* vol. 31, no. 35, pp. 7395-7397, 1992/12/10 1992.

[112] M. Y. Chen, "Hybrid Photonic True-Time Delay Modules for Quasi-Continuous Steering of 2-D Phased-Array Antennas," *Lightwave Technology, Journal of,* vol. 31, pp. 910-917, 2013.

[113] H. Lee, H.-b. Jeon, and J.-w. Jung, "Optical true time-delay beam-forming for phased array antenna using a dispersion compensating fiber and a multi-wavelength laser," in *Fly by Wireless Workshop (FBW), 2011 4th Annual Caneus*, 2011, pp. 1-4.

[114] B. Vidal *et al.*, "Simplified WDM optical beamforming network for large antenna arrays," *Photonics Technology Letters, IEEE,* vol. 18, pp. 1200-1202, 2006.

[115] S. Namiki, "Wide-Band and -Range Tunable Dispersion Compensation Through Parametric Wavelength Conversion and Dispersive Optical Fibers," *Lightwave Technology, Journal of,* vol. 26, no. 1, pp. 28-35, 2008.

[116] N. Alic *et al.*, "Microsecond Parametric Optical Delays," *Lightwave Technology, Journal of,* vol. 28, no. 4, pp. 448-455, 2010.

[117] S. Shouyuan *et al.*, "Conformal ultra-wideband optically addressed transmitting phased array and photonic receiver systems," in *Int. Topical Meeting on Microwave Photonics (MWP)*, 2013, pp. 221-224.

[118] P. F. McManamon *et al.*, "A Review of Phased Array Steering for Narrow-Band Electrooptical Systems," (in English), *Proceedings of the Ieee,* vol. 97, no. 6, pp. 1078-1096, Jun 2009.

[119] J. L. Corral, J. Marti, J. M. Fuster, and R. I. Laming, "True time-delay scheme for feeding optically controlled phased-array antennas using chirped-fiber gratings," (in English), *Photonics Technology Letters, IEEE,* vol. 9, no. 11, pp. 1529-1531, Nov 1997.

References

[120] J. Capmany and D. Novak, "Microwave photonics combines two worlds," (in English), *Nature Photonics,* vol. 1, no. 6, pp. 319-330, Jun 2007.

[121] J. Wells, "Faster than fiber: The future of multi-G/s wireless," *Microwave Magazine, IEEE,* vol. 10, no. 3, pp. 104-112, 2009.

[122] Y. Okawachi *et al.*, "Large tunable delays using parametric mixing and phase conjugation in Si nanowaveguides," (in English), *Optics Express,* vol. 16, no. 14, pp. 10349-10357, Jul 7 2008.

[123] E. Choi, J. H. Na, Y. Ryu, G. Mudhana, and B. H. Lee, "All-fiber variable optical delay line for applications in optical coherence tomography: feasibility study for a novel delay line," (in English), *Optics Express,* vol. 13, no. 4, pp. 1334-1345, Feb 21 2005.

[124] G. N. Pearson, K. D. Ridley, and D. V. Willetts, "Chirp-pulse-compression three-dimensional lidar imager with fiber optics," (in English), *Applied Optics,* vol. 44, no. 2, pp. 257-265, Jan 10 2005.

[125] J. Xie, L. Zhou, Z. Li, J. Wang, and J. Chen, "Seven-bit reconfigurable optical true time delay line based on silicon integration," *Optics Express,* vol. 22, no. 19, pp. 22707-22715, 2014/09/22 2014.

[126] S. Fathpour and N. A. Riza, "Silicon-photonics-based wideband radar beamforming: basic design," *Optical Engineering,* vol. 49, no. 1, pp. 018201-7, 2010.

[127] S. Shi, J. Bai, G. Schneider, and D. Prather, "Optical phase feed network and ultra-wideband phased array," in *Photonics Conference, IEEE*, 2012, pp. 372-373.

[128] J. Li *et al.*, "Tunable free space optical delay interferometer for demodulation of differential phase shift keying signals," in *Optical Fiber Communication (OFC), collocated National Fiber Optic Engineers Conference, 2010 Conference on (OFC/NFOEC)*, 2010, pp. 1-3.

[129] J. Leuthold *et al.*, "100 Gbit/s all-optical wavelength conversion with integrated SOA delayed-interference configuration," (in English), *Electronics Letters,* vol. 36, no. 13, pp. 1129-1130, Jun 22 2000.

[130] F. Séguin and F. Gonthier, "Tuneable All-Fiber® Delay-Line Interferometer for DPSK Demodulation," in *Optical Fiber Communication Conference and Exposition and The National Fiber Optic Engineers Conference*, Anaheim, California, 2005, p. OFL5: Optical Society of America.

[131] M. V. Drummond, P. P. Monteiro, and R. N. Nogueira, "Photonic True-Time Delay Beamforming Based on Polarization-Domain Interferometers," *Lightwave Technology, Journal of,* vol. 28, no. 17, pp. 2492-2498, 2010.

[132] Z. Li *et al.*, "Impact of Phase Perturbation on Passive Phase-Locking Coherent Beam Combination," *Photonics Technology Letters, IEEE,* vol. 24, no. 8, pp. 655-657, 2012.

[133] H. Q. Lam, P. Shum, L. N. Binh, and Y. Gong, "Electrically ultra-fast tunable optical filter employing HiBi fiber and phase modulator," *Optics Communications,* vol. 283, no. 13, 7/1/ 2010.

[134] A. Ortigosa-Blanch *et al.*, "Highly birefringent photonic crystal fibers," *Optics Letters,* vol. 25, no. 18, pp. 1325-1327, 2000/09/15 2000.

[135] P. A. Morton and J. B. Khurgin, "Microwave Photonic Delay Line With Separate Tuning of the Optical Carrier," *Photonics Technology Letters, IEEE,* vol. 21, no. 22, pp. 1686-1688, 2009.

[136] S. Koenig *et al.*, "Wireless sub-THz communication system with high data rate," *Nat Photon,* Letter vol. 7, no. 12, pp. 977-981, 12//print 2013.

[137] S. Shouyuan *et al.*, "Conformal ultra-wideband optically addressed transmitting phased array and photonic receiver systems," in *Microwave Photonics (MWP), 2013 International Topical Meeting on*, 2013, pp. 221-224.

[138] R. Bonjour *et al.*, "Time-space division multiplexing enabled by ultra-fast beam steering," in *Microwave Photonics (MWP), 2015 International Topical Meeting on*, 2015, pp. 1-3.

[139] R. Bonjour, S. A. Gebrewold, D. Hillerkuss, C. Hafner, and J. Leuthold, "Ultra-Fast Tunable True-Time Delay Using Complementary Phase-Shifted Spectra (CPSS)," in *Optical Fiber Communication Conference*, Los Angeles, California, 2015, p. W2A.67: Optical Society of America.

[140] P. A. Morton and J. B. Khurgin, "Microwave Photonic Delay Line With Separate Tuning of the Optical Carrier," *PTL,* vol. 21, no. 22, pp. 1686-1688, 2009.

[141] M. Burla *et al.*, "On-chip CMOS compatible reconfigurable optical delay line with separate carrier tuning for microwave photonic signal processing," *Optics Express,* vol. 19, no. 22, pp. 21475-21484, 2011/10/24 2011.

[142] P. Zhouyue and F. Khan, "An introduction to millimeter-wave mobile broadband systems," *Communications Magazine, IEEE,* vol. 49, no. 6, pp. 101-107, 2011.

[143] M. Burla *et al.*, "Multiwavelength-integrated optical beamformer based on wavelength division multiplexing for 2-D phased array antennas," *J. Lightwave Technol.,* vol. 32, no. 20, pp. 3509-3520, 2014.

[144] T. Kleine-Ostmann and T. Nagatsuma, "A review on terahertz communications research," *J. Infrared Millim. Terahertz Waves,* vol. 32, no. 2, pp. 143-171, 2011.

[145] F. C. Abrecht *et al.*, "Pre-equalization technique enabling 70 Gbit/s photonic-wireless link at 60 GHz," *Opt. Express,* vol. 24, no. 26, pp. 30350-30359, 2016.

[146] S. Han, C. l. I, Z. Xu, and C. Rowell, "Large-scale antenna systems with hybrid analog and digital beamforming for millimeter wave 5G," *IEEE Commun. Mag.,* vol. 53, no. 1, pp. 186-194, 2015.

[147] W. Hong, K. H. Baek, Y. Lee, Y. Kim, and S. T. Ko, "Study and prototyping of practically large-scale mmWave antenna systems for 5G cellular devices," *IEEE Commun. Mag.,* vol. 52, no. 9, pp. 63-69, 2014.

[148] W. Roh *et al.*, "Millimeter-wave beamforming as an enabling technology for 5G cellular communications: theoretical feasibility and prototype results," *IEEE Commun. Mag.,* vol. 52, no. 2, pp. 106-113, 2014.

References

[149] S. Koenig *et al.*, "Wireless sub-THz communication system with high data rate," *Nat Photonics,* Letter vol. 7, no. 12, pp. 977-981, 2013.

[150] C. Dehos *et al.*, "Millimeter-wave access and backhauling: the solution to the exponential data traffic increase in 5G mobile communications systems?," *Communications Magazine, IEEE,* vol. 52, no. 9, pp. 88-95, 2014.

[151] R. Bonjour, M. Singleton, P. Leuchtmann, and J. Leuthold, "Comparison of Steering Angle & Bandwidth for Various Phased Array Antenna Concepts," *Optics Communications,* vol. to be published.

[152] P. A. Morton and J. B. Khurgin, "Microwave Photonic Delay Line With Separate Tuning of the Optical Carrier," *IEEE Photonics Technol. Lett.,* vol. 21, no. 22, pp. 1686-1688, 2009.

[153] M. Burla *et al.*, "On-chip CMOS compatible reconfigurable optical delay line with separate carrier tuning for microwave photonic signal processing," *Opt. Express,* vol. 19, no. 22, pp. 21475-21484, 2011.

[154] R. Bonjour *et al.*, "Time-Space Division Multiplexing Enabled by Ultra-Fast Beam Steering," in *Microwave Photonics (MWP), 2015 International Topical Meeting on*, 2015.

[155] R. Waterhouse and D. Novak, "Realizing 5G: Microwave Photonics for 5G Mobile Wireless Systems," *Microwave Magazine, IEEE,* vol. 16, no. 8, pp. 84-92, 2015.

[156] S. Pan *et al.*, "Satellite Payloads Pay Off," *Microwave Magazine, IEEE,* vol. 16, no. 8, pp. 61-73, 2015.

[157] E. Larsson, O. Edfors, F. Tufvesson, and T. Marzetta, "Massive MIMO for next generation wireless systems," *Communications Magazine, IEEE,* vol. 52, no. 2, pp. 186-195, 2014.

[158] T. Bai, A. Alkhateeb, and R. W. Heath, "Coverage and capacity of millimeter-wave cellular networks," *IEEE Commun. Mag.,* vol. 52, no. 9, pp. 70-77, 2014.

[159] F. Boccardi, R. W. Heath, A. Lozano, T. L. Marzetta, and P. Popovski, "Five disruptive technology directions for 5G," *Communications Magazine, IEEE,* vol. 52, no. 2, pp. 74-80, 2014.

[160] L. A. Coldren *et al.*, "High Performance InP-Based Photonic ICs - A Tutorial," *J. Lightwave Technol.,* vol. 29, no. 4, pp. 554-570, 2011.

[161] C. L. Callender *et al.*, "Compact silica-on-silicon planar lightwave circuits for high speed optical signal processing," in *SPIE Photonics West 2012*, San Francisco, United States, 2012, vol. 8257, pp. 82570P-82570P-10: Society of Photographic Instrumentation Engineers.

[162] A. Meijerink *et al.*, "Novel Ring Resonator-Based Integrated Photonic Beamformer for Broadband Phased Array Receive Antennas - Part I: Design and Performance Analysis," *J. Lightwave Technol.,* vol. 28, no. 1, pp. 3-18, 2010.

[163] J. Bai *et al.*, "Optically Driven Ultrawideband Phased Array With an Optical Interleaving Feed Network," *IEEE Antenn. Wireless Propag. Lett.,* vol. 13, pp. 47-50, 2014.

[164] T. Cao, G. Zheng, and S. Wang, "Chemical control of continuous light-steering using an array of gradient Au/Bi2Se3/Au strips," *RSC Advances,* 10.1039/C5RA13366A vol. 5, no. 85, pp. 69319-69324, 2015.

[165] T. Cao, G. Zheng, S. Wang, and C. Wei, "Ultrafast beam steering using gradient Au-Ge2Sb2Te5 -Au plasmonic resonators," *Optics Express,* vol. 23, no. 14, pp. 18029-18039, 2015/07/13 2015.

[166] A. Emboras *et al.*, "Electrically Controlled Plasmonic Switches and Modulators," *IEEE Journal of Selected Topics in Quantum Electronics,* vol. 21, no. 4, pp. 276-283, 2015.

[167] C. Haffner *et al.*, "All-plasmonic Mach–Zehnder modulator enabling optical high-speed communication at the microscale," *Nat Photon,* Letter vol. 9, no. 8, pp. 525-528, 08//print 2015.

[168] C. Hoessbacher *et al.*, "Dense Plasmonic Mach-Zehnder Modulator Array for High-Speed Optical Interconnects," in *Advanced Photonics 2015*, Boston, United States, 2015, p. IM2B.1: Optical Society of America.

[169] W. Heni *et al.*, "High speed plasmonic modulator array enabling dense optical interconnect solutions," *Optics Express,* vol. 23, no. 23, pp. 29746-29757, 2015/11/16 2015.

[170] R. Bonjour, M. Singleton, P. Leuchtmann, and J. Leuthold, "Comparison of steering angle and bandwidth for various phased array antenna concepts," *Optics Communications,* 2015.

[171] A. Melikyan *et al.*, "High-speed plasmonic phase modulators," *Nat Photon,* Letter vol. 8, no. 3, pp. 229-233, 03//print 2014.

[172] T. Nikolajsen, K. Leosson, and S. I. Bozhevolnyi, "Surface plasmon polariton based modulators and switches operating at telecom wavelengths," *Applied Physics Letters,* vol. 85, no. 24, pp. 5833-5835, 2004.

[173] W. Jin *et al.*, "Benzocyclobutene barrier layer for suppressing conductance in nonlinear optical devices during electric field poling," *Applied Physics Letters,* vol. 104, no. 24, p. 243304, 2014.

[174] W. Heni *et al.*, "Optimizing Plasmonic Modulators for In-Device Nonlinearities of up to 275 pm/V," in *Advanced Photonics 2016 (IPR, NOMA, Sensors, Networks, SPPCom, SOF),*, Vancouver, Canada, 2016, p. ITu1A.1: Optical Society of America.

[175] W. Jin *et al.*, "Structure-function relationship exploration for enhanced thermal stability and electro-optic activity in monolithic organic NLO chromophores," *J. Mater. Chem.,* 10.1039/C6TC00358C vol. 4, no. 15, pp. 3119-3124, 2016.

[176] C. Haffner *et al.*, "Plasmonic Organic Hybrid Modulators - Scaling Highest Speed Photonics to the Microscale," *Proceedings of the IEEE,* vol. pp, no. 99, pp. 1-18, 2016.

[177] S. E. Alavi, M. R. K. Soltanian, I. S. Amiri, M. Khalily, A. S. M. Supa'at, and H. Ahmad, "Towards 5G: A photonic based millimeter wave signal generation for applying in 5G access fronthaul," *Sci. Rep.,* Article vol. 6, p. 19891, Jan. 2016.

[178] T. Umezawa *et al.*, "31-GHz single-carrier, 44.6-Gbps photonic wireless transmission using a wide-bandwidth high power photodetector and a pre-distortion technique," in *Optical Fiber Communication Conference and Exhibition (OFC)*, Anaheim, California, 2016, p. M3B.3: Optical Society of America.

References

[179] C.-H. Ho *et al.*, "50-Gb/s radio-over-fiber system employing MIMO and OFDM modulation at 60 GHz," in *Optical Fiber Communication Conference and Exhibition (OFC)*, Los Angeles, California, 2012, p. OM2B.3: Optical Society of America.

[180] X. Pang *et al.*, "100 Gbit/s hybrid optical fiber-wireless link in the W-band (75–110 GHz)," *Opt. Express,* vol. 19, no. 25, pp. 24944-24949, Dec. 2011.

[181] X. Li, J. Yu, z. Zhang, and Y. Xu, "Field trial of 80-Gb/s PDM-QPSK signal delivery over 300-m wireless distance with MIMO and antenna polarization multiplexing at W-band," in *Optical Fiber Communication Conference and Exhibition (OFC)*, Los Angeles, California, 2015, p. Th5A.5: Optical Society of America.

[182] X. Li, J. Xiao, and J. Yu, "Long-distance wireless mm-wave signal delivery at W-band," *J. Lightwave Technol.,* vol. 34, no. 2, pp. 661-668, Jan. 2016.

[183] WiGig-Alliance, "Wireless communications white paper," July 2010.

[184] R. C. Daniels, J. N. Murdock, T. S. Rappaport, and R. W. Heath, "60 GHz wireless: Up close and personal," *IEEE Microw. Mag.,* vol. 11, no. 7, pp. 44-50, 2010.

[185] T. Nitsche, C. Cordeiro, A. B. Flores, E. W. Knightly, E. Perahia, and J. C. Widmer, "IEEE 802.11 ad: directional 60 GHz communication for multi-Gigabit-per-second Wi-Fi [Invited Paper]," *IEEE Comm. Mag.,* vol. 52, no. 12, pp. 132-141, 2014.

[186] P. W. Berenguer *et al.*, "Nonlinear digital pre-distortion of transmitter components," *J. Lightwave Technol.,* vol. 34, no. 8, pp. 1739-1745, 2016.

[187] R. I. Killey, P. M. Watts, V. Mikhailov, M. Glick, and P. Bayvel, "Electronic dispersion compensation by signal predistortion using digital processing and a dual-drive Mach-Zehnder modulator," *IEEE Photon. Technol. Lett.,* vol. 17, no. 3, pp. 714-716, 2005.

[188] T. Sugihara, T. Kobayashi, T. Fujimori, and T. Mizuochi, "Electronic pre-equalization technologies using high-speed DAC," in *European Conference and Exposition on Optical Communications (ECOC)*, 2011, p. Tu6B.2: Optical Society of America.

[189] R. Schmogrow *et al.*, "Error vector magnitude as a performance measure for advanced modulation formats," *IEEE Photon. Technol. Lett.,* vol. 24, no. 1, pp. 61-63, 2012.

[190] R. Schmogrow *et al.*, "Corrections to "Error vector magnitude as a performance measure for advanced modulation formats" [Jan 1, 2012 61-63]," *IEEE Photon. Technol. Lett.,* vol. 24, no. 23, pp. 2198-2198, 2012.

[191] F. Chang, K. Onohara, and T. Mizuochi, "Forward error correction for 100 g transport networks," *IEEE Commun. Mag.,* vol. 48, no. 3, pp. S48-S55, 2010.

Appendix E GLOSSARY

Greek Symbols

Γ	Allowed overlap mismatch for phase shifters based array feeder
Γ_{ISI}	Delay overlap factor, used to prevent ISI in symbol-by-symbol steering
Δt	Time delay
$\Delta \theta$	Relative angular separation between the two directions
ε_0	Vacuum permittivity
ε_a	Efficiency of the antenna aperture
η	Quantum efficiency of a photodiode
λ	Wavelength
λ_{RF}	Wavelength at the millimeter wave frequency f_{RF}
λ_{RFmax}	Wavelength of the highest frequency component in the RF signal
$\Re$	Responsivity of a photodiode
φ	Phase shift
ϕ	Azimuth steering angel
θ	Elevation steering angle
Θ_{3dB}	3dB beamwidth for a uniform phased array tapering
$\Theta_{\mathrm{DC\_3dB}}$	3dB beamwidth for a Dolph-Chebyshev phased array tapering
$\Theta_{\mathrm{DC\_SL}}$	Beamwidth at side lobe level for a Dolph-Chebyshev phased array tapering
Θ_{sector}	Size of a sector in a mobile cell

Glossary

Latin Symbols

a_i	Complex weighting factor for antenna element i
A	Area
AF	Array factor
A_{eff}	Effective Area of the antenna
A_{iso}	Aperture size of an isotropic antenna
A_{phys}	Antenna physical aperture size
A_{SL}	Desired side lobe attenuation in a Dolph-Chebyshev phased array tapering
B	Bandwidth
c_0	Speed of light in vacuum
c	Speed of light in medium
$c(t)$	Complex data signal
C	Channel Capacity
C_{tot}	Aggregated capacity of a mobile cell
d	Distance between two elements of a uniform array
d_p	Position of the antenna for 1D PAA (scalar)
D_{A}	Largest size of the antenna, or size of the array.
$D_i(\theta, \phi)$	Antenna pattern
$D_{\mathrm{PAA}}(\theta, \phi)$	Array Pattern
E_P	Received radiation amplitude at the observation point $P(\boldsymbol{r})$
E_{opt}	Electromagnetic field amplitude
f	Frequency
f_{RF}	Carrier frequency at microwave or millimeter waves frequencies
f_{B}	Fractional bandwidth
F	Array Factor
F_{n}	Noise factor
FSR	Free spectral range
G	Gain
G_{A}	Antenna Gain
$G_{\mathrm{A\_Rx}}$	Gain of the receiving antenna

$G_{\text{A\_Tx}}$	Gain of the transmitting antenna
H	Frequency response
$\hbar h$	Plank constant
I_{PD}	Photocurrent generated by a photodiode
I_{RF}	RF part of the photocurrent generated by a photodiode
I_{s}	Power Density
k	Wavenumber
K	Scalar taking into account constants used in the conversion of electromagnetic field strength into optical power
L	Losses
L_{link}	Atmospheric link losses (attenuation & scattering)
n	Refractive index
n_{beams}	Number of beam generated in a space division multiplexing (SDM) scheme
n_{channel}	Number of frequency channels that can be used in a regulated frequency band
n_{sector}	Number of sector in a mobile cell
N	Number of element in a 1D phased array
N_0	
p	Relative position of the antenna in reference to d (antenna element spacing)
P	Power
P_{iso}	Received power using isotropic antennas
P_{opt}	Optical power
P_{RF}	RF Power
P_{Rx}	Received power (after receiving antenna)
P_{S}	Source power
P_{Tx}	Transmitted power (before transmitting antenna)
q	Elementary charge
r	Distance between the transmitter and the receiver
$\mathbf{r}$	Position of the observation point $P(\boldsymbol{r})$
$\boldsymbol{r}_i$	Position of the i antenna element
R_{b}	Bitrate

Glossary

$\mathbf{R}_i$	Propagation vector from antenna element i
R_{PD}	Load of a photodiode
R_{S}	Symbol rate
RZ	Return-to-zero duration
$\Re$	Responsivity of a photodiode
S_{21}	Transmission of scattering parameter S
SR	Supported range of steering
t	Time
T	Transfer matrix
T_{S}	Symbol duration
w_0	Optical noise spectral density
$\mathbb{Z}$	Integer numbers

Acronyms

ADC	Analog to digital converter
AWG	Arbitrary waveform generator
BBU	Base band unit
BER	Bit error rate
BPF	band pass filter
BS	Base station
CPSS	Complementary phased shifted spectra
CO	Central office
DAC	Digital to-analog converter
DL	Delay Line
DSO	Digital storage oscilloscope
DSP	Digital signal processing
EDFA	Erbium doped fiber amplifiers
EVM	Error vector magnitude
FDM	Frequency division multiplexing
FIR	Finite impulse response

FN	Feeder network
FSPL	Free-space path losses
HPBW	Half-power beamwidth
ISI	Inter-symbol interference
IQ	In-phase quadrature
LO	Local oscillator
LoS	Line of sight
LDPC	Low-density parity-check code
LPF	Low pass filter
MWP	Microwave Photonic
MIMO	Multiple-inputs multiple-outputs
mmWave	Millimeter waves
NG RAN	Next generation radio access network
OFDM	Orthogonal frequency division multiplexing
OSNR	Optical signal-to-noise ratio
PAA	Phased array antenna
PAF	Phased array feeder
PAPR	Peak-to-average power ratio
PIC	Photonic integrated circuits
PMF	Polarization maintaining fiber
PPM	Plasmonic phase modulator
PRBS	Pseudo-random binary sequence
PS	Phase shifters
QAM	Quadrature amplitude modulation
RAN	Radio access network
RAU	Remote antenna unit
RF	Radio-frequency, also sometime used in analogy for millimeter wave frequencies
RIN	Relative intensity noise
RoF	Radio-over-fiber

Glossary

ROF	Roll-off Factor
RRH	Remote radio head
RZ	Return-to-zero
SC	Steering control signal
SCT	Separate carrier tuning
SDM	Space division multiplexing
SMF	Single mode fiber
SNR	Signal-to-noise ratio
TDM	Time division multiplexing
TSDM	Time-to-space division multiplexing
TTD	True-time delay
UE	User equipment
VOA	Variable optical attenuator

LIST OF OWN PUBLICATIONS

Journal Articles

[RB1]   **R. Bonjour**, S. A. Gebrewold, D. Hillerkuss, C. Hafner, and J. Leuthold, "Continuously tunable true-time delays with ultra-low settling time," Optics Express, vol. 23, no. 5, pp. 6952-6964, 2015.

[RB2]   **R. Bonjour**, M. Singleton, P. Leuchtmann, and J. Leuthold, "Comparison of steering angle and bandwidth for various phased array antenna concepts," Optics Communications, vol. 373, pp. 35-43, 2016.

[RB3]   **R. Bonjour** et al., "Ultra-fast Millimeter Wave Beam Steering," IEEE Journal of Quantum Electronics, vol. 52, no. 1, p. 7358045, 2016.

[RB4]   **R. Bonjour** et al., "Plasmonic phased array feeder enabling ultra-fast beam steering at millimeter waves," Optics Express, vol. 24, no. 22, pp. 25608-25618, 2016.

[RB5]   F. C. Abrecht, **R. Bonjour** et al., "Pre-equalization technique enabling 70 Gbit/s photonic-wireless link at 60 GHz," Optics Express, vol. 24, no. 26, pp. 30350-30356, 2016.

[RB6]   **R. Bonjour**, S. Welschen, P. Leuchtmann, P. Wellig, and J. Leuthold, "Remote in-building motion detection using single frequency technique, "Electronics Letters, vol. 53, no. 15, pp. 997-1001, 2017.

[RB7]   **R. Bonjour**, S. Welschen, and J. Leuthold, "Time-to-Space Division Multiplexing for Tb/s Mobile Cells," IEEE Transactions on Wireless Communications, 2018.

[RB8]   S. A. Gebrewold, L. Marazzi, P. Parolari, R. Brenot, S. P. O. Duill, **R. Bonjour**, D. Hillerkuss, C. Hafner, and J. Leuthold, "Reflective-SOA Fiber Cavity Laser as Directly Modulated WDM-PON Colorless Transmitter," IEEE Journal of Selected Topics in Quantum Electronics, vol. 20, no. 5, p. 3100409, 2014.

[RB9]   K. G. Kraiczek, **R. Bonjour**, Y. Salvadé, and R. Zengerle, "Highly Flexible UV–Vis Radiation Sources and Novel Detection Schemes for Spectrophotometric HPLC Detection," Analytical chemistry, vol. 86, no. 2, pp. 1146-1152, 2014.

[RB10] S. A. Gebrewold, **R. Bonjour**, S. Barbet, A. Maho, R. Brenot, P. Chanclou, M. Brunero, L. Marazzi, P. Parolari, A. Totovic, D. Gvozdic, D. Hillerkuss, C. Hafner, and J. Leuthold, "Self-Seeded RSOA-Fiber Cavity Lasers vs. ASE Spectrum-Sliced or Externally Seeded Transmitters—A Comparative Study," Applied Sciences, vol. 5, no. 4, 2015.

[RB11] W. Heni, C. Hoessbacher, C. Haffner, Y. Fedoryshyn, B. Baeuerle, A. Josten, D. Hillerkuss, Y. Salamin, **R. Bonjour**, A. Melikyan, M. Kohl, D. L. Elder, L. R. Dalton, C. Hafner, and J. Leuthold, "High speed plasmonic modulator array enabling dense optical interconnect solutions," Optics Express, vol. 23, no. 23, pp. 29746-29757, 2015.

[RB12] Y. Salamin, W. Heni, C. Haffner, Y. Fedoryshyn, C. Hoessbacher, **R. Bonjour**, M. Zahner, D. Hillerkuss, P. Leuchtmann, D. L. Elder, L. R. Dalton, C. Hafner, and J. Leuthold, "Direct Conversion of Free Space Millimeter Waves to Optical Domain by Plasmonic Modulator Antenna," Nano Letters, vol. 15, no. 12, pp. 8342-8346, 2015.

[RB13] C. Haffner, W. Heni, Y. Fedoryshyn, A. Josten, B. Bäuerle, C. Hössbacher, Y. Salamin, U. Koch, N. Dordevic, P. Mousel, **R. Bonjour**, A. Emboras, D. Hillerkuss, P. Leuchtmann, D. L. Elder, L. R. Dalton, C. Hafner, and J. Leuthold, "Plasmonic Organic Hybrid Modulators - Scaling Highest Speed Photonics to the Microscale," Proceedings of the IEEE, vol. 104, no. 12, pp. 2362-2379, 2016.

[RB14] S. Gebrewold, **R. Bonjour**, R. Brenot, D. Hillerkuss, and J. Leuthold, "Bit- and Power-Loading—A Comparative Study on Maximizing the Capacity of RSOA Based Colorless DMT Transmitters," Applied Sciences, vol. 7, no. 10, p. 999, 2017.

Conference Contributions

[RB15] **R. Bonjour** et al., "Ultra-Fast Tunable True-Time Delay Using Complementary Phase-Shifted Spectra (CPSS)," presented at the Optical Fiber Communication Conference and Exposition, OFC 2015, Los Angeles, CA, USA, March 22-26, 2015

[RB16] **R. Bonjour** et al., "Time-space division multiplexing enabled by ultra-fast beam steering," presented at the International Topical Meeting on Microwave Photonics (MWP 2015), Paphos, Cyprus, October 26-29, 2015

[RB17] **R. Bonjour** et al., "Plasmonic phased array feeder enabling symbol-by-symbol mm-wave beam steering at 60 GHz," presented at the 2016 IEEE International Topical Meeting on Microwave Photonics (MWP), Long Beach, CA, USA, October 31 - November 3, 2016

[RB18] F. C. Abrecht, **R. Bonjour** et al., "70 Gbit/s Photonic Wireless Link at 60 GHz," presented at the IEEE International Topical Meeting on Microwave Photonics, MWP 2016, Long Beach, CA, USA, October 31 - November 10, 2016,

[RB19] M. Burla, **R. Bonjour** et al., "Ultrafast optical signal processing enabled by plasmonics," presented at the SPIE/COS Photonics Asia, Beijing, China, October 12-14, 2016, 2016

[RB20] M. Burla, **R. Bonjour** et al., "Plasmonics: A Novel Approach for Microwave Photonics Integrated Circuits," presented at the International Conference on Optoelectronics and Microelectronics Technology and Applications, OMTA2016, Shanghai, October 10-12, 2016

[RB21] M. Burla, **R. Bonjour** et al., "Microwave Plasmonics: Plasmonic Modulators for RF Photonics and mm-Wave Wireless Communications," presented at the Photonics North Conference 2016, Québec, Canada, May 24-26, 2016

[RB22] M. Burla, **R. Bonjour** et al., "Microwave Plasmonics: A Novel Platform for RF Photonics," presented at the IEEE International Topical Meeting on Microwave Photonics, MWP 2016, Long Beach, CA, USA, October 31 - November 3, 2016

[RB23] S. A. Gebrewold, **R. Bonjour**, R. Brenot, D. Hillerkuss, C. Hafner, and J. Leuthold, "Adaptive Subcarrier Multiplexing Maximizing the Performance of a Bandwidth-Limited Colorless Self-Seeded Reflective-SOA," presented at the 2015 International Conference on Photonics in Switching (PS), Florence, Italy, September 22-25, 2015, 2015

[RB24] C. Haffner, W. Heni, Y. Fedoryshyn, B. Baeuerle, A. Josten, Y. Salamin, **R. Bonjour**, C. Hoessbacher, A. Emboras, D. L. Elder, P. Leuchtmann, D. Hillerkuss, L. R. Dalton, C. Hafner, and J. Leuthold, "Ultra-Compact Plasmonic IQ-Modulator," presented at the European Conference on Optical Communication (ECOC) 2015, Valencia, Spain, September 27 - October 1, 2015, 2015

[RB25] J. Leuthold, **R. Bonjour**, S. A. Gebrewold, S. Dash, W. Heni, C. Hoessbacher, C. Haffner, Y. Salamin, B. Baeuerle, A. Josten, P. Ma, P. Leuchtmann, Y. Fedoryshyn, D. Hillerkuss, and C. Hafner, "The Path towards 100 Gbit/s Wireless Communications," presented at the 36th Symposium on Progress in Electromagnetics Research (PIERS 2015), Prague, Czech Republic, July 6-9, 2015, 2015

[RB26] Y. Salamin, **R. Bonjour**, W. Heni, C. Haffner, C. Hoessbacher, Y. Fedoryshyn, M. Zahner, D. L. Elder, L. R. Dalton, C. Hafner, and J. Leuthold, "Antenna Coupled Plasmonic Modulator," presented at the Frontiers in Optics 2015, San Jose, CA, USA, October 18-22, 2015, 2015

[RB27] B. Baeuerle, A. Josten, **R. Bonjour**, D. Hillerkuss, and J. Leuthold, "Effect of Transmitter Impairments on Nyquist-FDM Signals with Increasing Sub-Band Granularity," presented at the Advanced Photonics 2016 (IPR, NOMA, Sensors, Networks, SPPCom, SOF), Vancouver, Canada, July 18–20, 2016, 2016

[RB28]   S. A. Gebrewold, R. Brenot, **R. Bonjour**, A. Josten, B. Baeuerle, D. Hillerkuss, C. Hafner, and J. Leuthold, "Colorless, Low-Cost RSOA Based Transmitters Optimized for Highest Capacity Through Bit- and Power-Loaded DMT," presented at the 2016 Optical Fiber Communications Conference and Exhibition, OFC 2016, Anaheim, CA, USA, March 20-24, 2016, 2016

[RB29]   J. Leuthold, C. Haffner, W. Heni, C. Hössbacher, Y. Salamin, U. Koch, Y. Fedoryshyn, **R. Bonjour**, A. Josten, B. Bäuerle, M. Burla, D. Hillerkuss, A. Emboras, C. Hafner, D. L. Elder, and L. R. Dalton, "Wired and Wireless High-Speed Communications Enabled by Plasmonics," presented at the 21st European Conference on Networks and Optical Communications, NOC 2016, Lisbon, Portugal, June 1-3, 2016, 2016

[RB30]   J. Leuthold, W. Heni, C. Hössbacher, C. Haffner, Y. Salamin, U. Koch, Y. Fedoryshyn, **R. Bonjour**, A. Josten, B. Bäuerle, D. Hillerkuss, and C. Hafner, "Plasmonics - a Technology for Microscale High-Speed Integrated Optics," presented at the 18th European Conference on Integrated Optics 2016 (ECIO 2016), Warsaw, Poland, May 18-20, 2016, 2016 Y. Salamin, W. Heni, Y. Fedoryshyn, C. Haffner, C. Hoessbacher, P. V. Johnston, D. L. Elder, **R. Bonjour**, M. Zahner, R. Cottier, A. F. Tillack, L. R. Dalton, C. Hafner, and J. Leuthold, "Direct RF-to-Optical Detection by Plasmonic modulator integrated into a four-leaf-clover antenna," presented at the CLEO: Science and Innovations 2016, San Jose, CA, USA, June 5-10, 2016, 2016

SUPERVISED THESES

This work would not have been possible without the crucial contributions of many students. Indeed, there is not a single achievement presented in this thesis that does not rely on their work.

By submission date order, the following theses have been supervised:

Soumya Sunder Dash, master thesis on *Simulation of high-speed optical beam steering systems for next generation fiber-over-radio communication link (2013), [55]*

Matthew Singleton, master thesis on *Ultrafast beam steering demonstrator* (2014), [56]

Emanuel Greco, semester thesis on *Integrated System for Ultra-Fast Beam Steering* (2014), [50]

Samuel Welschen, master thesis on *Simulation of Ultra-Fast Beam Steering Systems* (2016), [57]

Michael Jost, semester thesis on *Regulation of delay interferometer for ultra-fast tunable true-time delays* (2016), [51]

Gani Aliguzhinov, **Paul Scheffler**, and **Thomas Benz**, semester project on *RF Board for Photonic Chip Evaluation* (2016), [53]

Noa Melchior, **Matthias Binder**, and **Lukas Bieri**, semester project on *Development of a Measurement Setup for Through the Wall Sensing* (2017), [54]

Pol Mousel, master thesis on *Passive Radar – From Quality Criteria to Coverage Optimization* (2017), [58]

Léonard Authier, semester thesis on *Theoretical Analysis of a Phased Array Antenna System for Ultra-Fast Beam Steering* (2017), [52]

ACKNOWLEDGEMENT